

**SILICON-MICROMACHINED VIBRATORY
DIFFRACTION GRATINGS FOR MINIATURIZED
HIGH-RESOLUTION RAPID LASER SCANNING**

DU YU

(B. Eng., XIAN JIAOTONG UNIVERSITY, CHINA)

**A THESIS SUBMITTED
FOR THE DEGREE OF DOCTOR OF PHILOSOPHY
DEPARTMENT OF MECHANICAL ENGINEERING
NATIONAL UNIVERSITY OF SINGAPORE**

2012

To my parents and my wife for their love, support and encouragement

Acknowledgements

First and foremost I would like to extend my deepest gratitude to my supervisors, Assoc. Prof. Zhou Guangya, Assoc. Prof. Chau Fook Siong and Dr. Zhang Qingxin for their erudite knowledge, expert guidance and invaluable suggestions.

I would also like to thank my fellow lab mates in Micro and Nano Systems Initiative (MNSI) in National University of Singapore (NUS): Dr. Yu Hongbin, Dr. Tian Feng, Mr. Cheo Koon Lin, Mr. Wang Shouhua, Mr. Chew Xiong Yeu and Mr. Mu Xiaojing, for their selfless help and assistance as well as the generous sharing of their knowledge and expertise.

In addition, I would like to take this opportunity to express my appreciation to the leadership and support of other mentors and colleagues in the Institute of Microelectronics, A*Star (IME), including Prof. Kwong Dim-Lee, Dr. Feng Hanhua, Mr. Deng Wei, Mr. Li Hongbin and other IME staff members for their generous guidance and assistance during the micro fabrication process.

Finally, the love, support and encouragements from my parents and my wife have inspired me continuously to march forward in the research study.

Many thanks to you all,

Du Yu

NUS, Singapore

2012

Publications & Presentations

Journal Publications

- [1] **Y. Du**, G. Zhou, K.L. Cheo, Q. Zhang, H. Feng, B. Yang and F.S. Chau, “High speed laser scanning using MEMS driven in-plane vibratory grating: Design, modeling and fabrication” *Sensors and Actuators, A: Physical*, vol. 156, n 1, pp. 134-144, (2009).
- [2] **Y. Du**, G. Zhou, K.L. Cheo, Q. Zhang, H. Feng and F.S. Chau, “A 2-DOF circular-resonator-driven in-plane vibratory grating laser scanner” *IEEE/ASME Journal of Microelectromechanical Systems*, vol. 18, n 4, pp. 892-904, (2009).
- [3] **Y. Du**, G. Zhou, K.L. Cheo, Q. Zhang, H. Feng and F.S. Chau, “A high-speed MEMS grating laser scanner with a backside thinned grating platform fabricated using a single mask delay etching technique” *Journal of Micromechanics and Microengineering*, vol. 20, n 11, 115028 (2010).
- [4] **Y. Du**, G. Zhou, K.L. Cheo, Q. Zhang, H. Feng and F.S. Chau, “Double-layered vibratory grating scanners for high-speed high-resolution laser scanning” *IEEE/ASME Journal of Microelectromechanical Systems*, vol. 5, n 19, pp. 1186-1196 (2010).
- [5] **Y. Du**, G. Zhou, K.L. Cheo, Q. Zhang, H. Feng, and F.S. Chau, “A 21.5kHz High Optical Resolution Electrostatic Double-layered Vibratory Grating Laser Scanner” *Sensors and Actuators, A: Physical*, vol. 168, n 2, pp. 253-261, (2011).
- [6] F.S. Chau, **Y. Du** and G. Zhou, “A micromachined stationary lamellar grating interferometer for Fourier Transform spectroscopy” *Journal of Micromechanics and Microengineering*, vol. 18, n 11, 115028 (2010).
- [7] G. Zhou, **Y. Du**, Q. Zhang, H. Feng, and F.S. Chau, “High-speed, high-optical- efficiency laser scanning using a MEMS-based in-plane vibratory sub-wavelength diffraction grating” *Journal of Micromechanics and Microengineering*, vol. 18, n 8, 085013 (2008).

- [8] Q. Zhang, **Y. Du**, C.W. Tan, J. Zhang, M.B. Yu, W.G. Yeoh, G.Q. Lo, D.L. Kwong, “A silicon platform with MEMS active alignment function and its potential application in Si-photonics packaging” *IEEE Journal of Selected Topics in Quantum Electronics*, vol. 16, n 1, p 267-275, (2010).
- [9] Q. Zhang, **Y. Du**, C.W. Tan; J. Zhang, M. B. Yu, G. Q. Lo, D.L. Kwong, “A lens holder in conjunction with a MEMS platform for on-chip aligning and mechanical fixing of a ball lens in silicon photonics packaging” *IEEE Photonics Technology Letters*, vol. 23, n 9, p 588-590, (2011).
- [10] G. Zhou, K.L. Cheo, **Y. Du**, F.S. Chau, H. Feng, Q. Zhang, “Hyperspectral imaging using a microelectrical-mechanical-systems-based in-plane vibratory grating scanner with a single photodetector”, *Optics Letters*, vol. 34, n 6, p 764-766, (2009).
- [11] G. Zhou, K.L. Cheo, **Y. Du**, F.S. Chau, “An optically interrogated microgyroscope using an out-of-plane lamellar grating”, *Sensors and Actuators: A Physical*, vol. 154, n 2, p 269-274, (2009).

Conference Presentations

- [12] **Y. Du**, G. Zhou, K.L. Cheo, Q. Zhang, H. Feng and F.S. Chau, “A micromachined vibratory sub-wavelength diffraction grating laser scanner” *IEEE/LEOS International Conference on Optical MEMS and Nanophotonics*, pp. 98-99, (2008).
- [13] **Y. Du**, G. Zhou, Q. Zhang, H. Feng, K.L. Cheo, B. Yang and F.S. Chau “Micromachined high speed, high optical efficiency laser scanner using sub- wavelength diffraction grating” *22nd European Conference on Solid-State Transducers (Euroensors XXII)*, Dresden, Germany, pp. 1373-1376, (2008).
- [14] **Y. Du**, G. Zhou, K.L. Cheo, Q. Zhang, H. Feng and F.S. Chau, “Dynamic characterization of a 2-DOF circular resonator-driven vibratory grating scanner with geometric nonlinearity” *Proceedings of the SPIE-The International Society for Optical Engineering, 4th International Conference on Experimental Mechanics*, vol. 7522, 75221S (9 pp.), (2009).
- [15] **Y. Du**, G. Zhou, K.L. Cheo, Q. Zhang, H. Feng and F.S. Chau, “Synchronized laser scanning of multiple beams by MEMS gratings integrated resonant frequency fine tuning mechanisms” *IEEE/LEOS International Conference on Optical MEMS and Nanophotonics*, pp. 81-82, (2010).
- [16] **Y. Du**, G. Zhou, K.L. Cheo, Q. Zhang, H. Feng and F.S. Chau, “A 50 kHz micromachined electrostatic driven vibratory grating laser scanner” *Physics Procedia, International Conference on Optics in Precision Engineering and Nanotechnology (ICOPEN 2011)*, vol. 19, pp. 308-314, (2011).
- [17] **Y. Du**, G. Zhou, K.L. Cheo, Q. Zhang, H. Feng and F.S. Chau, “A high-speed electrostatic double-layered vibratory grating scanner with very high optical resolution” *16th International Solid-State Sensors, Actuators and Microsystems Conference (TRANSDUCERS'11)*, pp. 2546-2549, (2011).

- [18] G. Zhou, **Y. Du** and F.S. Chau, “MEMS gratings for nondispersive optical phase modulation” *IEEE 21st International Conference on Micro Electro Mechanical Systems*, pp. 136-139, (2008).
- [19] G. Zhou, **Y. Du**, K.L. Cheo, H. Yu, F.S. Chau, “Optical scanning with MEMS in-plane vibratory gratings and its applications” *IEEE/LEOS International Conference on Optical MEMS and Nanophotonics*, pp. 21-22, (2010).
- [20] Q.X. Zhang, **Y. Du**, C.W. Tan, J. Zhang, M. Yu, G.O. Lo, D.L. Kwong, “A MEMS platform for 2-D fine-positioning and locking of optical ball-lens in silicon photonics packaging” *Photonics Global Conference (PGC 2010)*, (2010).
- [21] Q.X. Zhang, **Y. Du**, C.W. Tan, J. Zhang, M. Yu, G.O. Lo, D.L. Kwong, “A novel MEMS configuration for three dimensional fine positioning and mechanical fixing of a ball lens in the packaging of silicon photonics” *16th International Solid-State Sensors, Actuators and Microsystems Conference (TRANSDUCERS'11)*, pp. 1795-1798, (2011).
- [22] G. Zhou, **Y. Du**, K.L. Cheo, F.S. Chau, “MEMS-driven diffraction gratings for rapid scanning of laser beams with very high optical resolution” *Proceedings of the SPIE - The International Society for Optical Engineering*, vol. 8191, 819105 (10 pp.), (2011).
- [23] G. Zhou, K.L. Cheo, **Y. Du** and F.S. Chau, “A novel optical lamellar grating out-of-plane microgyroscope” *IEEE 21st International Conference on Micro Electro Mechanical Systems*, pp. 864-867, (2008).
- [24] G. Zhou, K.L. Cheo, **Y. Du** and F.S. Chau, “Hyperspectral imaging using a micro-machined in-plane vibratory grating scanner” *15th International Conference on Solid-State Sensors, Actuators and Microsystems (TRANSDUCERS 2009)*, pp. 1377-1380, (2009).
- [25] G. Zhou, K.L. Cheo, **Y. Du** and F.S. Chau, “Built-in optical angular position sensing mechanism for high-resolution vibratory grating scanner” *Proceedings of the 16th International Conference on Optical MEMS & Nanophotonics*, pp. 17-18, (2011).

Table of Contents

Acknowledgements	I
Publications & Presentations	II
Table of Contents	VI
Summary	X
List of Tables	XIII
List of Figures	XV
List of Symbols and Acronyms	XXV
Chapter 1 Introduction	1
1.1 Introduction to laser scanning technology	1
1.2 Overview of major laser scanning technologies	4
1.3 MEMS technology empowered miniaturized laser scanners	8
1.3.1 MEMS based micromirror laser scanners	8
1.3.2 MEMS based vibratory grating scanners	10
1.4 Objectives and organization of the dissertation	12
Chapter 2 Literature Review	15
2.1 Structure of MEMS micromirror scanners	15
2.2 Electrostatic actuation mechanisms	18
2.2.1 Rotating plate electrostatic actuators	20
2.2.2 Staggered vertical comb-drive actuators	21
2.2.3 Angular vertical comb-drive actuators	23
2.2.4 In-plane vertical comb-drive actuators	25

2.2.5 Lateral comb-drive actuators	25
2.2.6 Circular comb-drive actuators	26
2.3 Other actuation mechanisms	27
2.3.1 Piezoelectric actuation	27
2.3.2 Electrothermal actuation	28
2.3.3 Electromagnetic actuation	29
2.4 Dynamic flatness of micromirrors	31
2.5 Preliminary results on MEMS vibratory grating laser scanners	34
2.6 Summary	37
 Chapter 3 Micromachined vibratory grating scanners: theoretical study, optical efficiency optimization and modeling.....	 39
3.1 Theory of laser scanning with diffraction grating	39
3.2 Optical efficiency maximization by grating profile optimization	43
3.3 Actuation mechanisms for scanning gratings	50
3.4 Comprehensive dynamic models	53
3.4.1 Linear mode of a 2-DOF ELTR resonator	54
3.4.1.1 Simplified analytical model of the 2-DOF ELTR resonator	55
3.4.1.2 Weight influence of flexural beams	59
3.4.1.3 Influence of stress alleviation beams	62
3.4.1.4 Influence of micromachining imperfections	64
3.4.2 Linear modeling of a 2-DOF circular resonator	65
3.4.2.1 Modeling of connection flexural beams	66
3.4.2.2 Modeling of circular folded beam suspensions	68
3.4.2.3 Simplified model of the 2-DOF circular resonator	70
3.4.2.4 Weight influence of flexural beams	72
3.4.2.5 Influence of stress alleviation beams and fabrication imperfections	74

3.4.3 Modeling of a 2-DOF circular resonator considering geometric nonlinearities	75
3.5 Summary.....	81
 Chapter 4 Single-layered vibratory grating scanner: design, fabrication process and characterization	 83
4.1 Single-layered grating scanner driven by 2-DOF LTR resonator	83
4.1.1 Scanner design and simulation	84
4.1.2 Fabrication process	87
4.1.3 Experimental characterizations	89
4.2 Single-layered grating scanner driven by 2-DOF ELTR resonator	95
4.2.1 Single mask delay etching technique	95
4.2.2 Scanner design and simulation	102
4.2.3 Fabrication process	105
4.2.4 Experimental characterization	109
4.3 Single-layered grating scanner driven by 2-DOF circular resonator	114
4.3.1 Scanner design and simulation	114
4.3.2 Fabrication process	117
4.3.3 Experimental characterizations	118
4.4 Summary	122
 Chapter 5 Double-layered vibratory grating scanner: design, fabrication process and characterization	 125
5.1 Double-layered configuration	125
5.2 Scanner design and simulation	127
5.3 Fabrication process	132
5.3.1 Diffraction grating, grating platform and connection pillar	132
5.3.2 Electrostatic comb-driven 2-DOF circular resonator	137
5.3.3 Manual assembly process	138
5.4 Experimental characterizations	142

5.4.1 Dynamic characterizations	142
5.4.2 Optical quality of the scanned beam	146
5.5 Summary	154
 Chapter 6 Synchronized laser scanning of multiple MEMS	
diffraction gratings.....	156
6.1 Background	156
6.2 Design and fabrication	160
6.3 Characterization	165
6.4 Summary	169
 Chapter 7 Conclusion	170
 References	175

Summary

Scanned beam technology is highly desired in numerous display and imaging applications. A high quality display or imaging system based on scanned beam technology requires laser scanners with large aperture size, large optical scan angle and high scanning frequency. Microelectromechanical systems (MEMS) technology based micromirror laser scanners enabled the possibility of high frequency operations but its optical performance will degrade during high speed scanning due to non-rigid body dynamic deformation. An alternative laser scanning scheme, which utilize in-plane rotation of a diffraction grating rather than out-of-plane deflection of a reflective surface, is then proposed to overcome the performance limitation of the micromirror laser scanner at high frequency region.

This dissertation presents the working principle, design, modeling, fabrication and characterization of several novel MEMS vibratory grating laser scanners for high speed scanned beam display and imaging applications. The major achievements during the development are summarized as the follows:

High optical efficiency (around 80%) is achieved (close to that of a coated scanning mirror) using simple binary sub-wavelength gold-coated diffraction gratings with TM-polarized incident laser beam. The grating profile is optimized through rigorous coupled wave analysis (RCWA) simulations.

The in-plane rotation of the diffraction grating platform can be generated directly by electrostatic circular combdrive actuator or indirectly by two-degree-of-freedom (2-DOF) resonators. The electrostatic comb-driven 2-DOF lateral-to-rotational resonator, which couples the translational motion of two or more micro resonators to the rotational motion of the diffraction platform, is developed. This driving scheme overcomes the travel range limitation of the micro actuators. A high speed vibratory grating scanner driven by 2-DOF lateral-to-rotational resonator with 1mm aperture is capable of scanning at 50192Hz with an optical scanning angle of 14.1° .

To increase the mechanical rotation angle of the diffraction grating, the electrostatic comb-driven 2-DOF circular resonator is developed. Compared with 2-DOF lateral-to-rotational (LTR) resonator, the 2-DOF circular resonator is capable of increasing total stiffness of the suspensions without inducing excessive stress, thus ensuring large in-plane rotation angle at high scanning frequency. The prototype scanner with 1mm aperture size is capable of scanning at 20289Hz with a scanning angle of 25° .

To further increase the optical performance, the double-layered configured grating scanner, where the grating platform and the driving actuator are located in different planes, is developed. It is capable of increasing the aperture size and scanning angle simultaneously. The prototype double-layered scanner with a 2mm aperture is capable of scanning at 21591Hz with an optical scan angle of 33.5° . The corresponding optical resolution is 1460 pixels per

unidirectional scan and the scanned beam quality is proved to be good by using stroboscopic method and lateral shear interferometer.

Synchronized motion of multiple gratings is required for multi-wavelength collinear scanning applications. A mechanically synchronization scheme with frequency tuning mechanism is developed. The synchronized laser scanning by two diffraction gratings is experimentally demonstrated by the prototype scanner.

List of Tables

Table 2.1	Comparisons between typical electrostatic actuation mechanisms	19
Table 4.1	Material properties of single crystal silicon	85
Table 4.2	Comparison between theoretical predicted and FE simulated resonant frequencies as well as mode shapes of a 2-DOF LTR resonator driven single-layered grating scanner	87
Table 4.3	Summary of theoretically predicted, FE simulated and measured resonant frequencies as well as mode shapes of the prototype 2-DOF LTR resonator driven single-layered grating scanner	91
Table 4.4	DRIE process parameters of anisotropic silicon etching	96
Table 4.5	DRIE process parameters of isotropic silicon recess etching	99
Table 4.6	Structural parameters of the 2-DOF ELTR resonator driven single-layered vibratory grating scanner	103
Table 4.7	Comparison between theoretically predicted and FE simulated resonant frequencies as well as mode shapes of a 2-DOF ELTR resonator driven single-layered grating scanner	105
Table 4.8	Summary of theoretically predicted, FE simulated and measured resonant frequencies as well as mode shapes of the prototype 2-DOF ELTR resonator driven single-layered grating scanner	112
Table 4.9	Comparison between theoretically predicted and FE simulated resonant frequencies as well as mode shapes of a 2-DOF circular resonator driven single-layered grating scanner	116
Table 4.10	Summary of theoretically predicted, FE simulated and measured resonant frequencies as well as mode shapes of the prototype 2-DOF circular resonator driven single-layered grating scanner	122

Table 4.11 Performance parameters of the developed single-layered vibratory grating scanners	123
---	-----

List of Figures

Figure 1.1	Schematic illustration of raster-scanning laser projection display/TV	2
Figure 1.2	$\theta_{\text{Opt}}D$ product and scanning frequency requirements for different display format	3
Figure 1.3	Summarization of major laser scanning technologies	5
Figure 1.4	(a) Electrostatic gimbaled dual-axis micromirror scanner [38]; (b) Schematics showing the dynamic deformation of a micromachined mirror body	9
Figure 1.5	Working principles of (a) micromirror scanner and (b) vibratory grating scanner	11
Figure 2.1	Summarization of structures of current MEMS micromirror scanners ...	16
Figure 2.2	Summarization of typical electrostatic actuation mechanisms	18
Figure 2.3	Working principle of a bimorph thermal actuator	29
Figure 2.4	Schematic illustration of 1D scanning mirror driven by electromagnetic actuator	29
Figure 2.5	Schematic illustration of the working principle of the 2D electromagnetic driven scanning mirror [111]	30
Figure 2.6	Schematic illustration of mirror dynamic deformation while scanning	31
Figure 2.7	Schematic illustration of a thin mirror plate reinforced by a thick backside frame	33
Figure 2.8	Micromirrors suspended by single and multiple springs	33
Figure 2.9	Schematic illustration of a single-side driven scanning grating actuated by an electrostatic comb-drive actuator [124]	35

Figure 2.10 Schematic illustration of a symmetrical electrostatic comb-driven scanning grating [40]	36
Figure 2.11 (a) Dual laser beams with same incident angle and scanned collinearly by two diffraction gratings configured on a same platform; (b) Simulated scanned trajectories [41]	37
Figure 3.1 Schematic illustration showing operational principles of a scanning grating	39
Figure 3.2 Simulated scanning trajectories of the 1 st order diffraction beam with a grating period of 500nm	41
Figure 3.3 Simulated scanning trajectories of the 1 st order diffraction beam with varying grating period from 450nm to 4 μ m	42
Figure 3.4 Magnification ratios between the optical scanning angle and grating rotation angle with varying grating period from 450nm to 4 μ m	43
Figure 3.5 Diffraction efficiencies as a function of grating groove depths for (a) TE- and (b) TM-polarized incident light	45
Figure 3.6 Experimental setup for diffraction efficiency measurement	46
Figure 3.7 SEM images showing cross-sectional views of gratings with different groove depths: (a) 65nm, (b) 125nm, (c) 235nm and (d) 440nm	47
Figure 3.8 Simulated and measured diffraction efficiency of the optimal grating profile with a groove depth of 125nm as a function of grating in-plane rotation	49
Figure 3.9 Actuation mechanisms for in-plane rotation: (a) 1-DOF electrostatic circular comb-driven resonator; (b) 2-DOF electrostatic comb-driven LTR resonator; (c) 2-DOF electrostatic comb-driven ELTR resonator and (d) 2-DOF electrostatic comb-driven circular resonator	50

Figure 3.10 Schematic of a typical 2-DOF electrostatic comb-driven ELTR resonator	54
Figure 3.11 Schematic illustration of a simplified 2-DOF undamped spring-mass free vibration system	55
Figure 3.12 Local variables defined with respect to a suspension beam	56
Figure 3.13 Schematic of a deformed connection flexural beam	59
Figure 3.14 Schematic of a deformed folded beam suspension	60
Figure 3.15 FE simulated torque-angle relationships of flexural beams	62
Figure 3.16 FE simulation results showing a set of deformed stress alleviation beams	63
Figure 3.17 Cross-sectional profile model of the beam after DRIE process and SEM image showing an etched trench	64
Figure 3.18 Schematic illustration of a 2-DOF circular resonator	66
Figure 3.19 Model of the main flexural beam and its corresponding local variables	67
Figure 3.20 Schematic illustrations of a lateral folded beam and a circular folded beam suspension	69
Figure 3.21 Model of one set of circular folded beam suspension	70
Figure 3.22 Schematic illustration of a simplified 2-DOF circular resonator	71
Figure 3.23 Schematic of a deformed connection flexural beam	72
Figure 3.24 FE simulated torque-angle points and polynomial fitted curve of a connection flexural beam	76
Figure 3.25 Schematic illustration of a 2-DOF circular resonator with nonlinear connection suspensions	77

Figure 3.26 Theoretical predictions of the variation of resonant frequency with the optical scan angle of (a) the first and (b) the second resonating mode for different ε values	80
Figure 4.1 Schematic illustration of a single-layered vibratory grating scanner driven 2-DOF LTR resonator	84
Figure 4.2 Mode shapes of (a) 1 st and (b) 2 nd resonating mode during vibration obtained using FE simulation	86
Figure 4.3 Fabrication process of the prototype 2-DOF LTR resonator driven single-layered vibratory grating scanner	88
Figure 4.4 SEM images showing (a) sub-wavelength diffraction grating with a period of 500nm and a duty cycle of 50%; (b) center part of the prototype 2-DOF LTR resonator driven single-layered vibratory grating scanner	89
Figure 4.5 Photograph shows the scanning trajectory and the inset shows a schematic illustration of the experimental setup	90
Figure 4.6 Frequency responses of prototype 2-DOF LTR resonator driven single-layered grating scanner at frequency regions near the resonant frequencies of (a) 1 st and (b) 2 nd resonating modes	91
Figure 4.7 Schematic illustration of experimental setup to investigate the scanned-beam quality and optical resolution using stroboscopic method	92
Figure 4.8 Photograph of actual experimental setup investigating the scanned-beam quality and optical resolution using stroboscopic method	93
Figure 4.9 Light intensity distribution of the focal spots captured by CCD camera	94
Figure 4.10 Average etching rates (over 4 hours) as a function of the trench width	96

Figure 4.11 White light interferometer measured bottom profiles of trenches with different trench widths, which are formed by a 4 hour DRIE process	97
Figure 4.12 Schematic of the multi-level step structures on a SOI wafer formed using the SMDE technique	98
Figure 4.13 Circular cavities with different step heights formed using the SMDE technique	99
Figure 4.14 Three-level circular step structure formed using the SMDE technique	100
Figure 4.15 Polygonal cavities with different shapes formed using the SMDE technique	100
Figure 4.16 An example showing (a) Non-uniform etching profile after a 4 hour DRIE process and (b) uniformity improved etching profile by using the SMDE technique	101
Figure 4.17 Schematic illustration of a 2-DOF ELTR resonator driven single-layered vibratory grating scanner with a backside thinned grating platform	103
Figure 4.18 FE simulation results showing the resonant frequencies and mode shapes of (a) the 1 st and (b) the 2 nd resonating mode	104
Figure 4.19 Fabrication process of the prototype 2-DOF ELTR resonator driven single-layered vibratory grating scanner	106
Figure 4.20 SEM image showing the cross-sectional view of the fabricated sub-wavelength diffraction grating with a grating period of 400nm	107
Figure 4.21 Microscopic image showing the whole view of the fabricated device	108
Figure 4.22 SEM images showing the (a) top view and (b) bottom view of the fabricated device	108

Figure 4.23 White light interferometer measurement results of the round cavity and circular reinforcement frame on the backside of the grating platform	109
Figure 4.24 Schematic of the experimental setup measuring the diffraction efficiency of the fabricated grating	110
Figure 4.25 (a) Measured 1 st order diffraction efficiency versus the polarization angle; (b) measured scanned beam efficiency versus the optical scan angle for TM-polarization	111
Figure 4.26 Schematic of the experimental setup for measurement of dynamic performances	112
Figure 4.27 (a) Measured frequency response of the prototype scanner in vacuum at the region near its first resonating mode; (b) photograph of the laser scanning trajectory of the prototype scanner on a projection screen	113
Figure 4.28 Schematic illustration of the micromachined 2-DOF electrical comb driven circular resonator driven in-plane vibratory grating scanner	115
Figure 4.29 Mode shapes of (a) 1 st and (b) 2 nd resonating mode during vibration obtained using FE simulation	116
Figure 4.30 Fabrication process flow of the prototype in-plane vibratory grating scanner	117
Figure 4.31 (a) Microscopic image showing the whole view and (b) SEM image showing the center part of the fabricated prototype scanner	118
Figure 4.32 Measured frequency responses of the prototype scanner in atmosphere at frequency regions near the resonant frequencies of (a) the 1 st and (b) the 2 nd modes	119
Figure 4.33 Measured frequency responses of the prototype scanner in vacuum at frequency regions near the resonant frequencies of (a) the 1 st and (b) the 2 nd modes	120

Figure 4.34	Photograph of the experimental setup for the prototype scanner	121
Figure 5.1	Schematic illustration of grating scanners with (a) single-layered and (b) double-layered configurations	126
Figure 5.2	Schematic illustration of an assembled double-layered vibratory grating scanner	128
Figure 5.3	Schematic illustration of the grating platform with connection pillar	128
Figure 5.4	Schematic illustration of the electrostatic 2-DOF circular resonator	129
Figure 5.5	FE simulation results showing the resonant frequencies and mode shapes of (a) the 1 st and (b) the 2 nd resonating mode	131
Figure 5.6	Theoretical predictions of resonant frequency variations of the 1 st resonating mode	132
Figure 5.7	Initial micromachining process used to fabricate the grating platform with the diffraction grating and the connection pillar	133
Figure 5.8	White light interferometer measured surface profile of the diffraction grating fabricated using SOI wafers	134
Figure 5.9	Improved micromachining process used to fabricate the diffraction grating, grating platform and connection pillar	135
Figure 5.10	(a) SEM image of the fabricated grating platform and the connection pillar; (b) white light interferometer measurement static deformation of the diffraction grating	136
Figure 5.11	Fabrication process flow of the electrostatic comb-driven 2-DOF circular resonator	137
Figure 5.12	Microscopic image of the fabricated electrostatic comb-driven 2-DOF circular resonator	138

Figure 5.13	Photograph of the in-house developed manual aligner	139
Figure 5.14	Schematic illustration of the manual assembly process	139
Figure 5.15	Images of the assembled prototype double-layered vibratory grating scanner	141
Figure 5.16	Microscopic images showing the backside of the assembled double-layered grating scanner and the magnified view of the epoxide resin anchor	141
Figure 5.17	White light interferometer measurement result of the parallelism between the diffraction grating and its driving actuator	142
Figure 5.18	Schematic illustration of the experimental setup for dynamic characterization	143
Figure 5.19	Photograph of the laser scanning trajectory of the prototype scanner on a projection screen	144
Figure 5.20	Measured frequency response of the prototype scanner in vacuum at frequency regions near the resonant frequencies of its 1 st resonating mode	145
Figure 5.21	Comparison of theoretical and experimental measured variations of normalized resonant frequencies with optical scan angles	146
Figure 5.22	(a) Schematic illustration and (b) photograph showing the experimental setup to investigate the scanned-beam quality using an in-house developed cyclic lateral shearing interferometer	147
Figure 5.23	Measured interferograms of the strobed spots at four different positions of the scan line using cyclic lateral shearing interferometer	149
Figure 5.24	(a) Schematic illustration and (b) photograph showing the experimental setup to investigate the scanned-beam quality using an in-house developed Mach-Zehnder interferometer	150

Figure 5.25 Measured interferograms of the strobed spots at different positions of the scan line using a Mach-Zehnder interferometer	151
Figure 5.26 (a) Schematic illustration and (b) photograph showing the experimental setup to investigate the optical resolution	152
Figure 5.27 CCD camera captured light intensity distribution of the focal spots at different positions of the scan line	153
Figure 6.1 Schematic illustration of multi-wavelengths collinear scanning of laser beams using multiple grating elements configured on (a) a common grating platform with and (b) multiple grating platforms with synchronized rotational motion	158
Figure 6.2 Schematic illustration of a mechanical synchronization scheme	159
Figure 6.3 Schematic illustration of MEMS vibratory grating scanner with two diffraction gratings and their integrated resonant frequencies fine-tuning mechanisms	161
Figure 6.4 Schematic illustrations of (a) the electrothermal driven resonant frequency fine-tuning mechanism and (b) working principle of the T-shaped stiffness variable flexure	162
Figure 6.5 Schematic illustration of the process flow fabricating the prototype scanner with two diffraction gratings	163
Figure 6.6 Microscopic image showing the whole view of the fabrication prototype scanner	164
Figure 6.7 SEM images of the prototype device showing (a) common electrostatic comb-driven resonator with one diffraction grating and (b) diffraction gratings with their resonant frequencies fine tuning mechanisms	164
Figure 6.8 Schematic illustration of the experimental setup measuring the resonant frequency tuning capabilities	165

Figure 6.9 Measured variations of the resonant frequency with respect to different tuning voltages	166
Figure 6.10 Schematic illustration of the experimental setup investigating the synchronized laser scanning of two beams using the stroboscopic method	167
Figure 6.11 Photograph of the actual experimental setup investigating the synchronized laser scanning of two beams using the stroboscopic method	167
Figure 6.12 Strobe spots from different positions of scanning trajectories (a) before and (b) after the resonant frequency tuning with tuning voltages of 0V and 3.87 V for two tuning actuators	168
Figure 7.1 Summarization of the scanning performances of developed vibratory grating scanners	171

List of Symbols and Acronyms

θ_{Opt}	Optical scan angle
θ_{max}	Maximum half mechanical deflection angle
θ_i	Incident angle
θ_d	Diffraction angle
θ_R	Grating rotation angle (angle between grating line and X-axis)
θ_o	Rotation angle of the outer circular resonator in 2-DOF circular resonators
λ	Wavelength
\vec{r}	Normalized wave-vector
\vec{e}_x	Unit vectors along X-axis
\vec{e}_y	Unit vectors along Y-axis
\vec{e}_z	Unit vectors along Z-axis
β_i	Coefficients of thermal expansion
α	Slope angle of a sidewall formed by DRIE
α_n	Slope angle of a sidewall at a notched area formed by DRIE
ρ	Material density
ρ_{Si}	Density of silicon
ε	Small parameter reflecting the degree of nonlinearity in flexural beams
φ	Mode ratio of the system
\tilde{E}_k	Modified total kinetic energy of the system considering the beam mass

ΔE_{k_c}	Kinetic energy of vibrating connection flexural beams
ΔE_{k_s}	Kinetic energy of vibrating supporting flexural beams
ΔE_{k_f}	Kinetic energy of vibrating folded beam suspensions
$\Delta \theta$	Tilt angle at the anchor of stress alleviation beams
δ_c	Stiffness reduction rate of connection flexures in 2-DOF ELTR resonators
δ_s	Stiffness reduction rate of supporting flexures in 2-DOF ELTR resonators
δ_{c1}	Stiffness reduction rate of type 01 connection flexural beams
δ_{c2}	Stiffness reduction rate of type 02 connection flexural beams
A_R	Rotational amplitude of the diffraction grating in 2-DOF circular resonators
A_o	Rotational amplitude of the outer resonator in 2-DOF circular resonators
C_{amp}	Magnification ratio between optical scan angle and mechanical rotation angle
c_i	Geometric coefficients
D	Beam diameter or scanner's aperture size
d	Grating pitch
E	Young's modulus
E_k	Total kinetic energy
E_p	Total potential energy

f	Frequency
f_{01}	Resonate frequency of the 1 st resonating mode
f_{02}	Resonate frequency of the 2 nd resonating mode
I_c	Area moment of inertia of the connection flexural beam
I_s	Area moment of inertia of the supporting flexural beam
I_f	Area moment of inertia of beams in a folded beam suspension
J_{in}	Moment of inertia of inner round platform in a 2-DOF resonator
J_o	Moment of inertia of the outer circular resonator in 2-DOF circular resonators
K_f	Total spring constant of a lateral resonator's suspension
$[k_c]$	Stiffness matrix of a connection flexure in 2-DOF ELTR resonators
$[k_s]$	Stiffness matrix of a supporting flexure in 2-DOF ELTR resonators
k_c	Spring constant of a connection flexure in a 2-DOF circular resonators
K_c	Total spring constant of connection flexures
\tilde{K}_c	Modified total spring constant of connection flexures
K_s	Total spring constant of supporting flexures
L_c	Length of connection a flexural beam
L_s	Length of supporting a flexural beam
L_f	Length of beams in a folded beam suspension
m	Diffraction order
m_o	Mass of lateral outer resonator
n_c	Number of connection flexural beams in a 2-DOF ELTR resonator

n_s	Number of supporting flexural beams in a 2-DOF ELTR resonator
n_{c1}	Number of type 01 connection flexures in a 2-DOF circular resonator
n_{c2}	Number of type 02 connection flexures in a 2-DOF circular resonator
n_f	Number of folded beams suspensions
W_c	Width of connection flexural beams
W_s	Width of supporting flexural beams
W_f	Width of beams in folded beams suspensions
W	Designed width of a flexural beam
\tilde{W}	Actual width of a flexural beam after etching
R_{in}	Radius of the inner round platform in a 2-DOF resonator
R_o	Radius of the outer circular resonator in 2-DOF circular resonators
S_1	Normalized resonate frequency of the 1 st resonating mode
S_2	Normalized resonate frequency of the 2 nd resonating mode
T	Thickness
T_n	Thickness of the notched area in a trench formed by DRIE
u_c	Vector of local variables of a connection flexural beam
u_s	Vector of local variables of a supporting flexural beam
x_o	Displacement of a lateral resonator
V_{pp}	Peak-to-Peak Voltages
1-DOF	One-Degree-Of-Freedom
2-DOF	Two-Degree-Of-Freedom
2D	Two Dimensional

3D	Three Dimensional
AC	Alternating Current
AO	Acousto-Optic
AOM	Acousto-Optic Modulator
BCB	Benzocyclobutene
BOE	Buffered Oxide Etchant
BOX	Buried OXide
CCD	Charge-Coupled Device
CO ₂	Carbon dioxide
Cr	Chromium
CTE	Coefficients of Thermal Expansion
DC	Direct Current
DRIE	Deep Reactive Ion Etching
ELTR	Enhanced-Lateral-To-Rotational
EO	Electro-Optic
FE	Finite Element
FWHM	Full-Width-Half-Maximum
He-Ne	Helium-Neon
HF	Hydrofluoride
IC	Integrated Circuit
LCD	Liquid Crystal Display
LIDAR	LIght Detection And Ranging

LPCVD	Low Pressure Chemical Vapor Deposition
LTR	Lateral-To-Rotational
KOH	Potassium hydroxide
MEMS	MicroElectroMechanical Systems
MOSBE II	Molded Surface Micro Machining and Bulk Etching Release
PEVCD	Plasma Enhanced Vapor Chemical Deposition
PLL	Phase Locked Loop
PZT	Lead Zirconate Titanate
QVGA	Quarter Video Graphics Array
RCWA	Rigorous Coupled Wave Analysis
RF	Radio Frequency
RIE	Reactive Ion Etching
SEM	Scanning Electron Microscope
SMDE	Single Mask Delay Etching
SOI	Silicon-On-Insulator
SUMMiT-V	Sandia's Ultra-planar Multilevel MEMS Technology-V
SVGA	Super Video Graphics Array
SXGA	Super eXtended Graphics Array
TE	Transverse Electric
TM	Transverse Magnetic
Ti	Titanium
USG	Undoped Silicate Glass

UV	Ultraviolet
VGA	Video Graphics Array
XGA	eXtended Graphics Array

Chapter 1 Introduction

1.1 Introduction to laser scanning technology

Laser scanning — a technology for image generation and acquisition — has been widely implemented in numerous applications in various fields including manufacturing, medicine, military hardware, information and communication systems. These applications include but are not limited to, raster-scanning laser projection displays/TVs for consumer markets [1-5]; laser scanning confocal microscopes [6-10] and optical coherence tomography (OCT) endoscopes [11-17] for biomedical and healthcare applications; laser printers for the computer industry [18]; terrestrial laser scanning for 3D visualizations and modeling [19]; laser barcode readers [20] and laser scanning 3D (three dimensional) imaging LIDAR (laser detection and ranging) for unmanned ground vehicles [21] and laser material processing for rapid prototyping [22].

Many of these applications require both high-speed and high-resolution scanning. As an example, consider the laser-scanning projection display/TV system shown schematically in Figure 1.1. As shown, beams from three laser sources with different wavelengths (Red, Green, and Blue) are combined to form a beam of white light, which is scanned rapidly across a projection screen. The system typically employs one biaxial or two uniaxial optical scanners where the horizontal scanner is operated at resonance, and the vertical scanner is driven by a saw-tooth waveform. The combined motions of the two scanners create a 2D sinusoidal raster. Images are created by modulating the intensities of the light sources according to the beam

position. This laser scanning projection display technology generates displays with a very wide color gamut of up to twice the range of colors that existing plasma and LCD TVs can offer. In addition, it is power efficient, bright, and can maintain full power output for the lifespan of the laser, resulting in a picture that does not progressively degrade over time compared to current plasma and LCD technology. This system is hailed by its developer as the next revolution in visual technology.

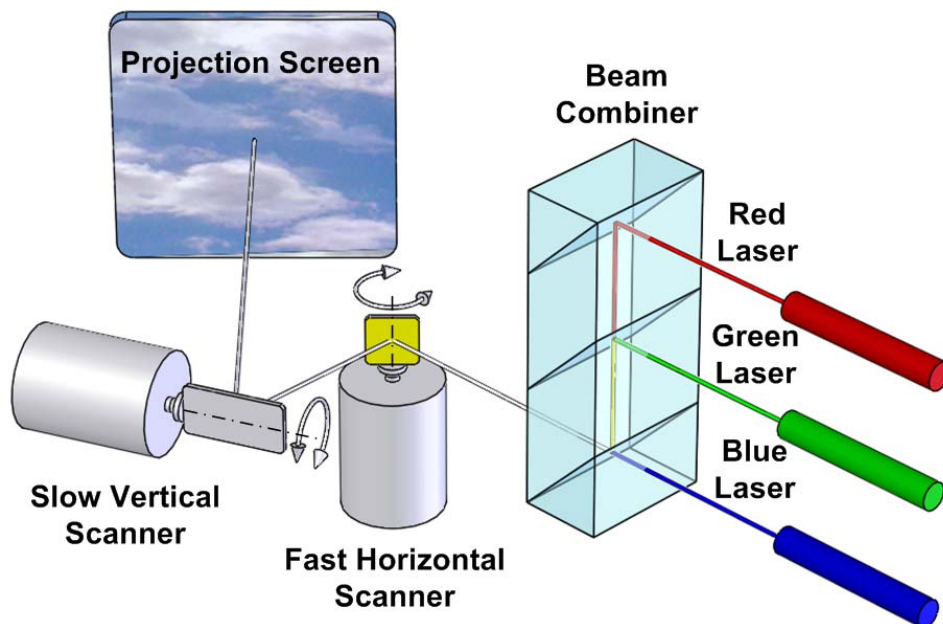


Figure 1.1 Schematic illustration of raster-scanning laser projection display/TV.

The performance characteristics of the laser scanners, such as scan frequency and optical resolution, are crucial to the laser projection system. Optical resolution — the number of resolvable spots/pixels per unidirectional scan — is defined as the ratio of the mirror scan angle to optical beam divergence. Theoretically, the scan resolution is proportional to the product of the maximum optical scan angle θ_{Opt} and beam diameter (or scanner's aperture size)

D. The $\theta_{\text{Opt}}D$ product and scanning frequency requirements for different display formats in a laser projection display system with a refresh rate of 60Hz are summarized in Figure 1.2.

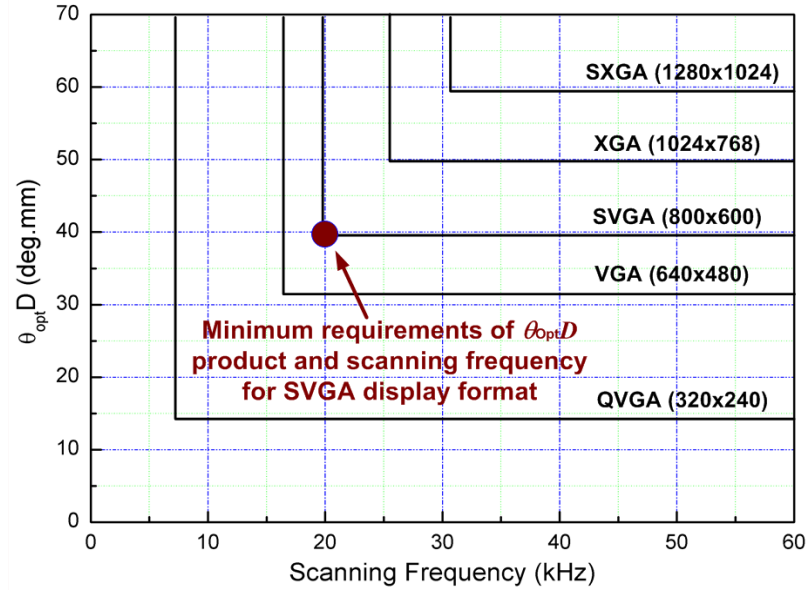


Figure 1.2 $\theta_{\text{Opt}}D$ product and scanning frequency requirements for different display formats with a refresh rate of 60Hz.

For example, to achieve a standard SVGA (Super Video Graphics Array) resolution, i.e. 800 pixels per line and 600 lines per frame at 60Hz frame refresh rate, the slow vertical scanner is required to operate at 60Hz. This can be easily implemented using most mechanical laser scanners in the market. However, the fast horizontal laser scanner in this system must be operated at about 20kHz (36,000 scans for display plus some time for vertical scanner to retrace, assuming bidirectional scanning, i.e. 2 scans per oscillation period). Since the scanner is to deliver an optical resolution of 800 pixels per scan, the $\theta_{\text{Opt}}D$ product of the scanner at 20kHz must be larger than 39 deg.mm, which is technically challenging. For example, if the diameter of the laser beam D is 1mm, the scanning amplitude of 39° is required at 20kHz. As

shown in Figure 1.2, for laser raster scanning display applications, the classification of the display thus depends largely on two important factors: the $\theta_{\text{opt}}D$ product and scanning frequency of the fast horizontal scanner. Clearly, a scanner with a large $\theta_{\text{opt}}D$ product (or higher resolution) and a high scanning speed is always preferred. Besides laser projection display, this is also true for many other applications, including laser printers and laser scanning confocal microscopes.

1.2 Overview of major laser scanning technologies

Present laser scanning technologies can be classified into two principal categories, namely “mechanical” and “nonmechanical”, according to their working principles [23]. Mechanical laser scanners can be further categorized according to their motions, for example, rotational and oscillatory, as shown in Figure 1.3.

Among “mechanical” rotational laser scanners, rotating polygon optical scanners are attractive for their high scan rate, velocity stability, wide scan angles, and simple saw-tooth scan pattern [24-26]. However, they also have many drawbacks. For example, each facet of the polygon must be substantially larger than the incident beam diameter; otherwise much of the duty-cycle would be wasted when the beam straddles two adjacent facets. This significantly increases the inertia of the rotating polygon. Besides, high-speed motor and pneumatic rather than mechanical bearings are required. Making the polygon into a high-speed centrifuge represents a significant safety hazard. Furthermore, each facets of the polygon is slightly different in reflectivity and angle with respect to the axis of rotation. Those

angular differences, known as pyramidal errors, combine with any wobble in the bearing to cause the beam to fluctuate in the direction perpendicular to the scan unless additional optical corrections are applied.

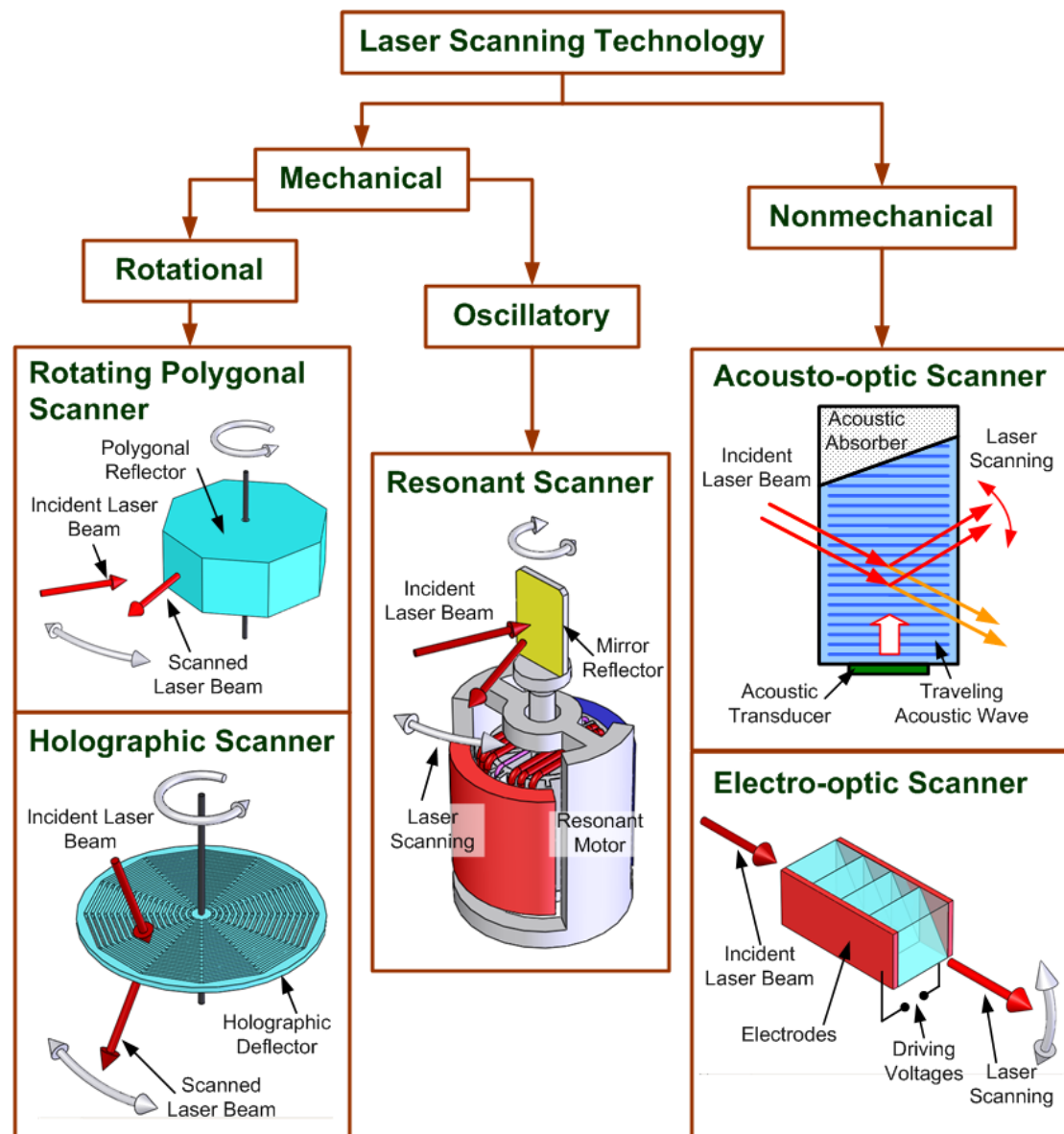


Figure 1.3 Summarization of major laser scanning technologies.

Holographic scanners (i.e. rotating diffraction gratings) are consumable to rotating polygons in utility and systematic performance, but offer additional advantages in Bragg angle wobble

correction and low aerodynamic loading [27-29]. Hence, when properly designed, holographic scanners can out-perform rotating polygons in terms of scanning speed. However, many of the drawbacks associated with rotating polygons still remain in holographic scanners, for example, the need for an air bearing system for high-speed operation, bulkier and high cost.

A resonant scanner typically consists of a suspended mirror that can be driven into torsional oscillation by introducing a periodic signal into coils around a magnetic core. It is operated at resonance to take advantage of both large vibration amplitude and high speed [23]. Compared with rotational mechanical scanners for example rotating polygons, resonant scanners have certain advantages which include being optically simple and relatively compact. They exhibit negligible pyramidal errors or other variations from one scan to the next, enable the scan angle to be adjusted over a range to suit different applications, and possess a flexure suspension, which eliminates long-term wear due to mechanical motion. The disadvantages of the resonant scanners mainly originate from the sinusoidal nature of scan, resulting in non-uniform scan velocity and restricted duty cycle. However, these disadvantages can be overcome through electronic compensation, for example, pixel linearization. Currently, the operating frequency of commercially-available resonant scanners is typically limited to several kilo hertz.

In contrast to “mechanical” laser scanners, which inherently have high inertia, the “nonmechanical” scanners are truly low inertia in performance. The electro-optic (EO) [30-31]

and acousto-optic (AO) [32-33] scanners shown in Figure 1.3 are two popular examples of “nonmechanical” laser deflectors. Without mechanical moving parts, they are capable of rendering rapid alteration of position, velocity or direction of the scanned beam. However, high cost, small scan angle and limited scan resolution are among the major drawbacks of these types of scanners. For electro-optic scanners, it is quite difficult to achieve a scan resolution greater than 100 pixels since most electro-optic coefficients are extremely low. For acousto-optic scanners, where ultrasonic waves are utilized to modify the direction of a laser beam passing through an acousto-optic material, the resolution is typically only a few hundreds of pixels per scan. Additional drawbacks of acousto-optic scanners include complicated driving electronics (RF signal is required to drive the ultrasonic waves) and variation of diffraction efficiency during scanning due to the fixed Bragg angle (per input beam angle and drive frequency). Generally, both of the “nonmechanical” laser scanners are seldom used in high-resolution scanning applications such as laser printers and projection displays.

In summary, for currently available commercial laser scanners, the conventional “mechanical” scanners have high scan resolutions but relative low scan speeds due to the high inertia of moving parts. On the contrary, the “nonmechanical” scanners are fast but have inherently low scan resolutions. In addition, all of these scanners for high-speed operation are bulky and expensive.

1.3 MEMS technology-empowered miniaturized laser scanners

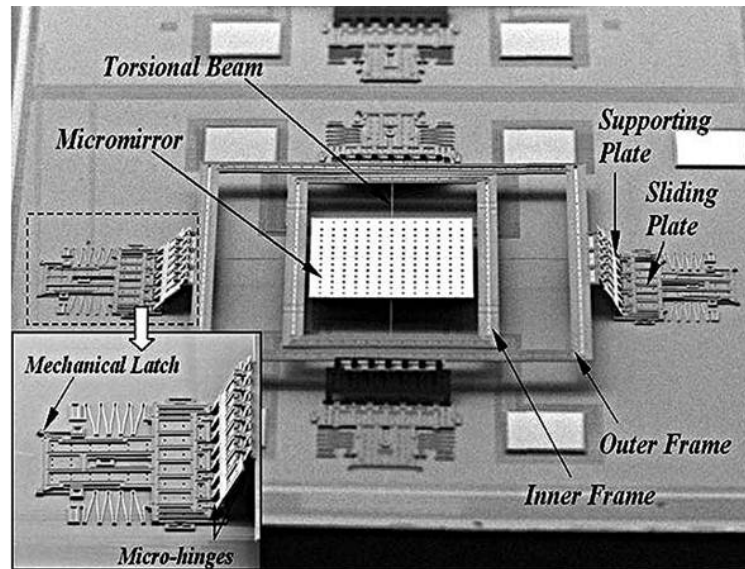
Microelectromechanical systems (MEMS) are small integrated devices or systems that combine electrical and mechanical components. They can range in size from the sub-micron level to the millimeter level in a particular system. MEMS extend the fabrication techniques developed for the integrated circuit (IC) industry to add mechanical elements such as beams, gears, diaphragms, and springs to devices [34].

In recent years, MEMS-based mechanical oscillatory optical scanners [35] have attracted much attention. Fabricated through silicon micromachining technology, these scanners operate in a fashion quite similar to that of resonant scanning mirrors except that they have a much lower inertia. As a result, MEMS-based scanners are capable of operating at much higher scan frequencies and yet consume significantly less electrical power. Other outstanding advantages over existing technologies include small form-factor, light-weight, and low per-unit-cost through IC-like batch fabrication. This technology can not only provide significant performance enhancements to existing applications but also form a technological basis for a wide range of new applications that require miniaturized laser scanning, such as scanning endoscopic probes for health-care applications [36] and raster-scanning retinal projection wearable displays for medical, military automotive and consumer markets [37].

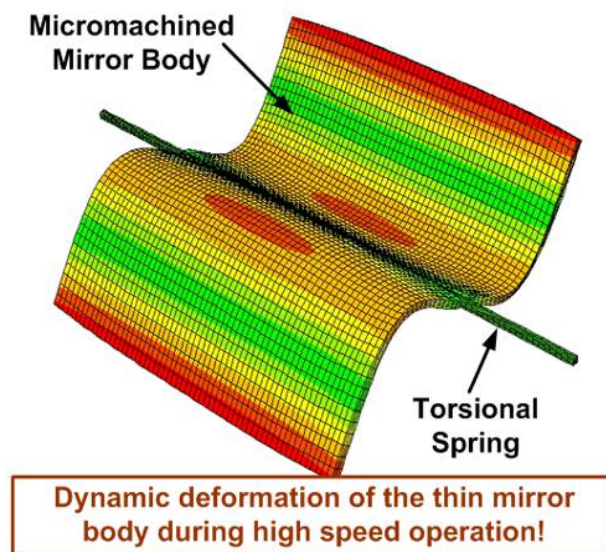
1.3.1 MEMS based micromirror laser scanners

Currently, the majority of research in the area of MEMS-based scanners has focused on micromirror scanners [1-5]. An example is shown in Figure 1.4(a). A micromachined reflector

is suspended by a double gimbaled structure and can rotate along two axes. While driven by electrostatic micro actuators, 2D laser scanning can be achieved.



(a)



(b)

Figure 1.4 (a) Electrostatic gimbaled dual-axis micromirror scanner [38]; (b) Schematics showing the dynamic deformation of a micromachined mirror body.

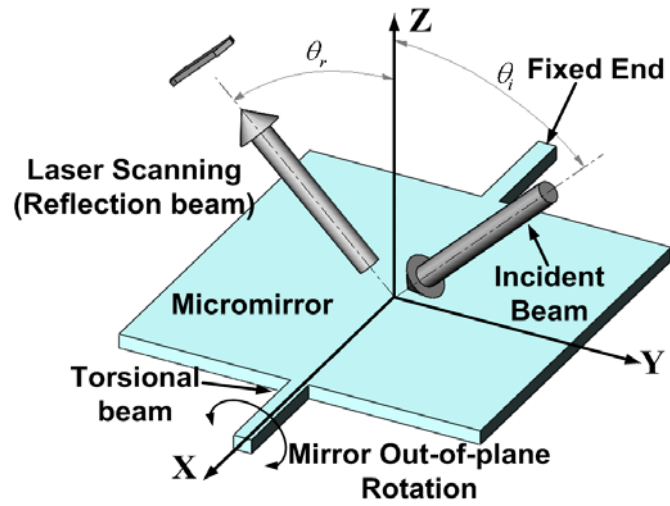
However, as shown in Figure 1.4(b), due to the nature of fabrication processes, micromirrors are normally much thinner than conventional macro-scanning mirrors, and therefore, at high scan frequencies, the mirror plate loses its rigidity and tends to deform dynamically during scanning due to high out-of-plane acceleration forces. This introduces obvious dynamic aberrations into the optical system and seriously degrades its optical resolution [39]. Although using a thick micromirror can achieve a dynamic deformation within the Rayleigh limit ($\lambda/8$ mechanical), the moment of inertia will be increased significantly. In order to maintain a high scanning frequency, the stiffness of the mirror suspension has to be increased. This results in a very high driving voltage and considerable power consumption.

1.3.2 MEMS-based vibratory grating scanners

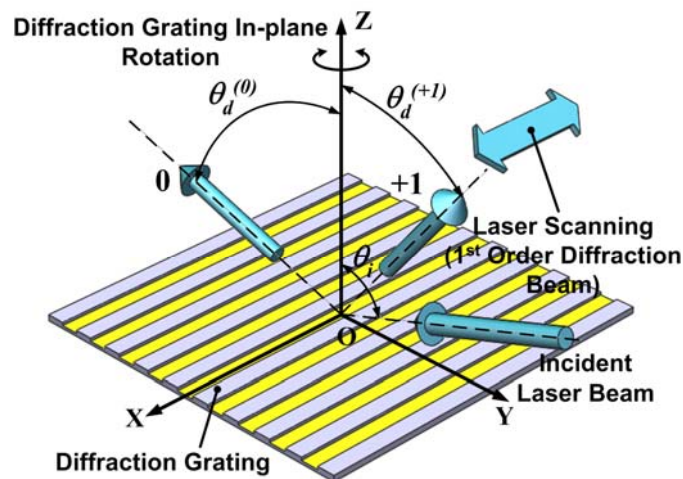
To overcome the drawbacks of the MEMS micromirror scanners stated above, an innovative MEMS high-speed laser scanning technology that uses a more mechanically stable in-plane motion of a diffraction grating to avoid the dynamic deformation at high scanning speeds is proposed [40-41]. Figures 1.5 (a) and (b) show the working principles of the conventional micromirror scanner and the proposed vibratory grating scanner respectively.

In a micromirror scanner shown in Figure 1.5(a), the mirror rotates along X-axis and an incident laser beam locates in YOZ plane. The out-of-plane deflection motion of the micromirror scans the reflected beam in YOZ plane. In contrast, vibratory grating scanners utilize rotational in-plane vibration of planar microstructures to change the orientation of the diffraction grating lines, hence causing the diffracted laser beams to scan, as shown in Figure

1.5(b). It is well known from elasto-dynamics that the dynamic non-rigid-body deformation of a thin plate under in-plane excitation is much smaller than that for rotational out-of-plane excitation. Hence, MEMS-based vibratory grating scanners have the potential to scan at high frequencies without optical performance degradation resulting from the dynamic non-rigid-body deformation prevalent in conventional high-speed out-of-plane torsional micromirror based scanners.



(a)



(b)

Figure 1.5 Working principles of (a) micromirror scanner and (b) vibratory grating scanner.

1.4 Objectives and organization of the dissertation

Although the MEMS grating scanning scheme utilizing in-plane rotational motion potentially has huge advantages in high-speed scanning applications, the performance of current grating scanners is not satisfactory [40-41]. The problems include low optical efficiency, low scanning resolution and relatively low scanning frequency. Thus a main objective of the project described in this dissertation is to enhance the performance of the micromachined high-speed vibratory grating scanner through optical design, scanner structure optimization and novel micromachining process development. This dissertation is organized as the follows:

Chapter 1 gives a general introduction to laser scanning technology and its applications, followed by an overview of major laser scanning technologies. Then two types of MEMS-based miniaturized laser scanners, namely micromirrors and vibratory gratings, are introduced and their advantages and disadvantages briefly reviewed. The objectives and organization of this dissertation are presented.

Chapter 2 provides an overview of existing literature and state-of-the-art of MEMS technology miniaturized laser scanners. Firstly, the structures and actuation mechanisms of various micromirror scanners are reviewed. Then the mirror body dynamic deformation problem and its solution are discussed. Finally, previous developments on vibratory grating scanners are introduced.

Chapter 3 provides some theoretical studies of MEMS vibratory grating scanners. Firstly, the working principle of laser scanning using a diffraction grating is introduced. Then, the optimization of grating profile using numerical rigors coupled wave analysis (RCWA) simulation for maximum optical efficiency is discussed. Finally, the development of comprehensive dynamic models for predicting the dynamic performance of 2-DOF electrostatic comb-driven LTR and circular resonators are presented.

Chapter 4 presents the design, simulation, fabrication process and characterization of three types of single-layered vibratory grating scanners, which are driven by 2-DOF LTR resonator, 2-DOF enhanced LTR resonator and 2-DOF circular resonator respectively. In addition, a novel single mask delay etching (SMDE) technique is introduced in detail.

Chapter 5 describes the design, development and demonstration of a novel double-layered vibratory grating scanner including structural simulation, fabrication process and experimental characterization.

Chapter 6 presents an effective method to achieve synchronized laser scanning of multiple beams by using MEMS diffraction gratings together with resonant frequency fine-tuning mechanisms. Multiple gratings are actuated in-plane by a common electrostatic comb-driven resonator and their resonant frequencies are fine-tuned to compensate for micromachining errors. Continuous and reversible resonant frequency tuning are experimentally demonstrated.

Chapter 7 concludes with the major contributions in the dissertation and proposes possible work in the future.

Chapter 2 Literature Review

In recent years, MEMS micromirror scanners have been mostly developed for various applications, due to their outstanding advantages, such as compact size, fast scanning speed, low power consumption and low per-unit cost. Micromirrors with various structures and actuation mechanisms, which can be classified as electrostatic, piezoelectric, electrothermal and magnetic actuation, have been developed. However, the dynamic deformation of the micromachined thin reflector has become a limiting factor for realizing high-speed high-resolution laser scanning, such as projection displays. MEMS vibratory grating scanners, which inherently subjected to less dynamic deformation, have the potential to scan at high frequency without optical performance degradation. In this chapter, typical structures of micromirrors, actuation mechanisms (electrostatic, piezoelectric, thermal and magnetic actuations), mirror body dynamic flatness and preliminary research on scanning grating will be reviewed in detail.

2.1 Structure of MEMS micromirror scanners

Structures of most micromirror scanners are summarized in Figure 2.1. As shown in Figure 2.1, based on the number of scanning axes current MEMS micromirror scanners can be classified as single-axis and dual-axes. Since the first micromirror proposed by Petersen (IBM, 1980) [43], a mirror plate tilting around the torsional suspension spring has become a standard design for a single-axis scanning micromirror, shown in Figure 2.1(a).

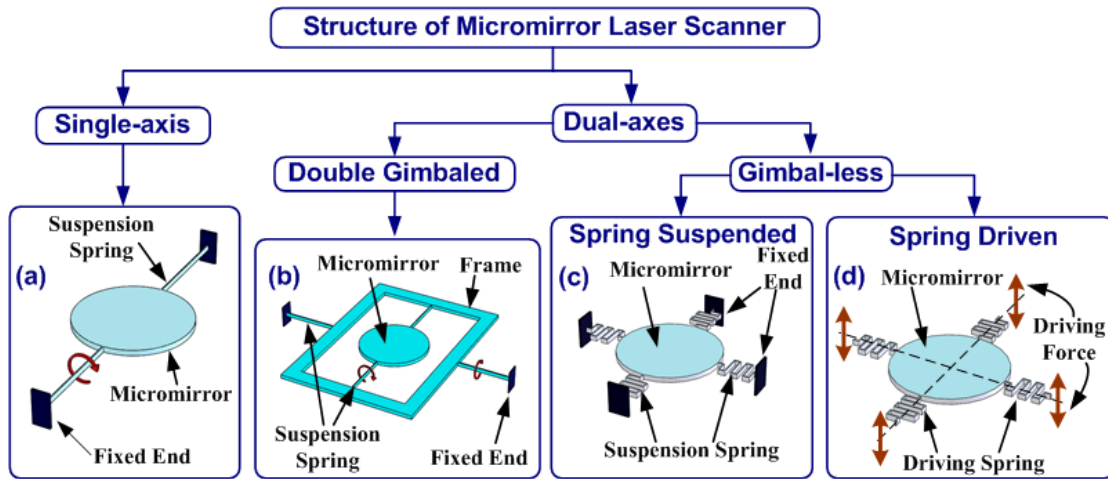


Figure 2.1 Summarization of structures of current MEMS micromirror scanners.

Dual-axes scanning mirrors which are able to realize 2D laser scanning have been extensively studied, which can be either double gimbaled or gimbal-less. Gimbal is a pivoted support that allows the rotation of an object about a single-axis. Double gimbals, where one mounted on the other with pivot axis orthogonal, can be used to allow the object mounted on the innermost gimbal to rotate freely along two directions regarding its support, as shown in Figure 2.1(b). Double gimbaled structure is the most common and effective way to implement 2D rotational motion thus dual-axes double gimbaled scanning micromirrors are very popular. For example a double gimbaled micromirror for optical cross-connects was demonstrated by V.A. Aksyuk et al. in 2000 [44]. Raster laser scanning can be easily achieved with double gimbaled scanners by simply designing two gimbals with different resonant frequencies. However, elimination of crosstalk between driving voltages, electrical isolation and mechanical coupling demand structure optimization as well as complex fabrication process. Besides, scanning frequency differences between two axes could affect its performance in high-speed scanning applications.

In contrast, gimbal-less scanners have uniform suspensions and will not encounter the cross-talk problem. Besides two-axis scanning, most gimbal-less scanners are capable of realizing the piston motion. Moreover, symmetric structure design allows both axes to have similar angular rotation and speed, which is highly desirable for vector or non-raster scanning applications. Dual-axes gimbal-less scanners can be further categorized as spring suspended scanners and spring driven scanners. In a gimbal-less spring suspended scanner, the scanning mirror is connected to a fixed substrate through several suspension springs and the actuation forces directly act on the mirrors, as shown in Figure 2.1(c). J. Tsai et al. demonstrated a gimbal-less spring suspended micromirror with a hidden crossbar torsional spring and actuated by four terraced electrodes in 2005. In a gimbal-less spring driving scanner, suspension springs are not only used to support the micromirror but also acting as a media which transfer the actuation force from actuators to the mirror, as shown in Figure 2.1(d). The mechanical deflection of the mirror depends on the mechanical characteristics of all actuators as well as the actuation scheme. For example, prototype scanners with symmetric folded [46] and T-shape suspensions [47], which transfer the electrostatic torques generated by 1D vertical comb-driven rotation actuators, are developed by V. Milanovic et al. in 2004 and J. Tsai et al. in 2006, respectively. In 2005, J. Singh et al. demonstrated a micromirror suspended by four serpentine springs and driven by electrothermal bimorph actuators [48]. Besides, S.H. Sadat et al. in 2009 reported a micromirror, which is suspended by four spiral-shaped suspensions. The actuation force of the mirror is generated by using the zipping effect of the flexible beams [49].

2.2 Electrostatic actuation mechanisms

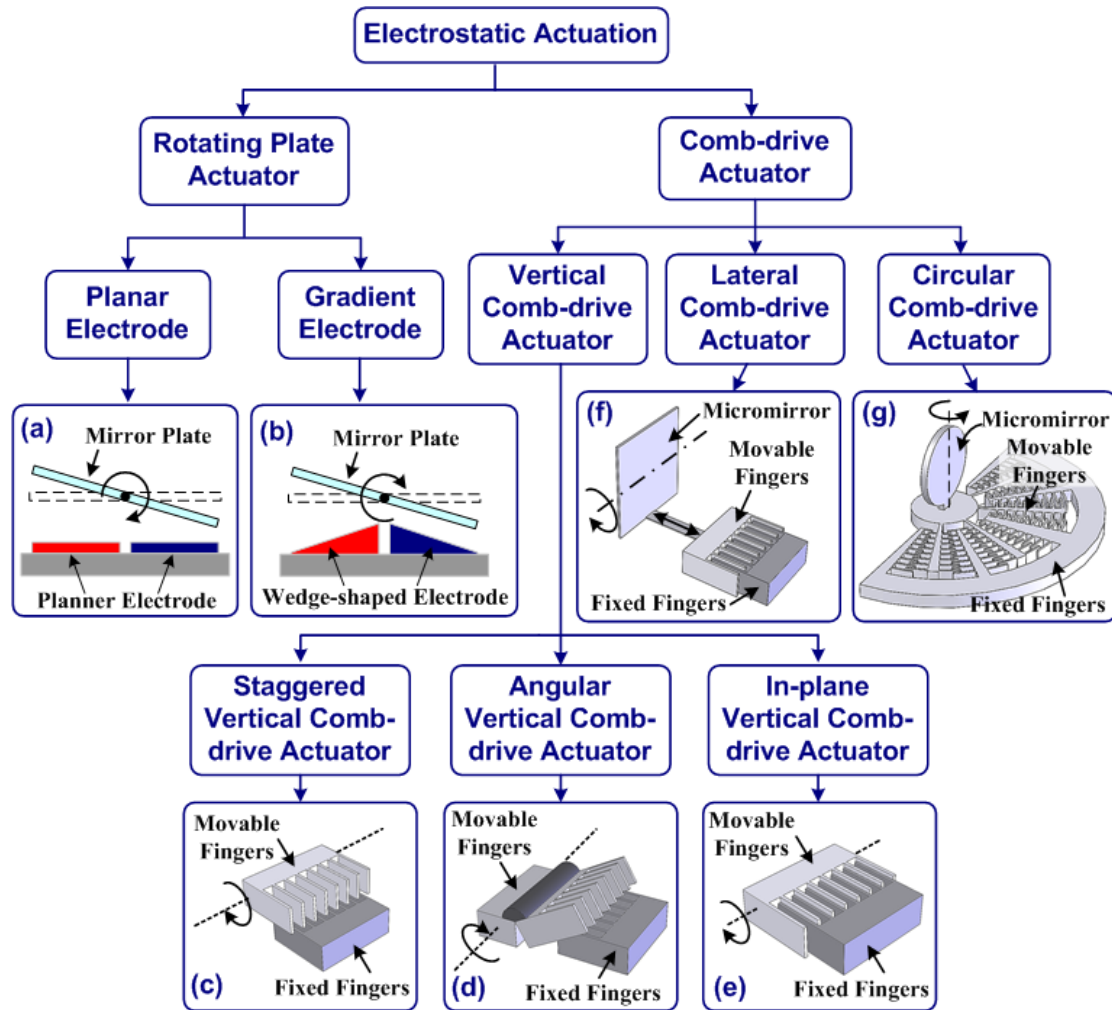


Figure 2.2 Summary of typical electrostatic actuation mechanisms.

Generally, an electrostatic actuation utilizes an attractive or a repulsive Coulomb force between electrically charged fixed and movable electrodes. The generated electrostatic force is proportional to the square of the applied voltage as well as the overlapping area and inversely proportional to the gap of the electrodes. Electrostatic force acting on the surface drastically increases with decreasing scale, compared with body forces such as gravity and inertia force. Electrostatic actuators have many outstanding advantages, such as little power consumption, zero heat dissipation due to zero steady-state current and structure simplicity

resulting in high compatibility with micro fabrication processes. Figure 2.2 summarizes typical electrostatic actuation mechanisms. As shown in Figure 2.2, current dominating electrostatic actuation mechanisms can be classified as rotating plate driven and comb-drive actuation, which vary the mutual distance and overlapping area, respectively.

Table 2.1 Comparisons between typical electrostatic actuation mechanisms.

Electrostatic Actuators		Advantages	Disadvantages
Rotating Plate Actuator	Planer Electrode	Simple structure High-fill factor COMS process compatible	Driving force will decrease when travel range increases.
	Gradient Electrode	Simple structure High-fill factor Lower driving voltages	Special process required to fabricate the gradient electrode
Vertical Comb-drive Actuator	Staggered	Large force density Large travel range Piston-tilt movement achievable	Complicated fabrication process
	Angular	Large force density Large travel range Suitable for rotational motion Simple fabrication process	Post assembly process required
	In-plane	Large force density Large travel range Simple fabrication process	Only suitable for resonant actuation
Lateral Comb-drive Actuator		Large force density Large travel range	Complicated fabrication process
Circular Comb-drive Actuator		Large force density Large travel range	Post assembly process required

Comb-drive actuators, which consist of many interdigitated electrodes (comb-fingers) with small gaps (normally several microns) between them, are generally more efficient compared to rotating plate actuators. According to the shape and motion of the comb-fingers, comb-drive actuator used for micromirror actuation can be further classified as vertical

comb-drive, lateral comb-drive and circular comb-drive actuators, as shown in Figure 2.2. Among these three types, vertical comb-drive actuators have been mostly developed due to their large force density resulting in low driving voltages and high resonant frequencies for large scanning angle [50]. There are three major designs of vertical comb-drive actuators, which are staggered, angular and in-plane vertical comb-drive actuators.

The relative advantages and disadvantages of the typical electrostatic actuation mechanisms are summarized in Table 2.1.

2.2.1 Rotating plate electrostatic actuators

In the rotating plate electrostatic actuator driven MEMS scanner, the mirror body acts as the movable electrode and the fixed electrodes are placed under the mirror. The planar electrodes are preferred in most of scanners due to its fabrication simplicity, as shown in Figure 2.2(a). The maximum mirror rotation angle depends on the initial gap due to the geometrical restriction. Larger initial gap results in larger scan angle, however requires higher driving voltages. This is a design trade-off. Therefore, the wedge-shaped electrodes, although its fabrication process is complex, are then developed to reduce the driving voltages while maintaining large scan angles (shown in Figure 2.2(b)) [44].

In one way, the mirror body and electrodes underneath can be fabricated on a common substrate using multi-layer surface micromachining processes [43]. To increase the maximum scanning angle, a post-assembly process is applied to elevate the mirror creating a larger gap

between mirror plate and driving electrodes, as shown in Figure 1.4(a) [51-54]. In the other way, the mirror body and its driving actuator can be fabricated separately using bulk-micromachining and then assembled together. For example a micromirror scanner has been developed by T.S. Kim et al. in 2002. The fabrication process combines the bulk micromachining and post assembly process, where the fixed and movable electrodes are self-aligned during the assembly [55].

2.2.2 Staggered vertical comb-drive actuators

In a staggered vertical comb-drive actuator, there is an initial vertical offset between movable and stationary fingers (shown in Figure 2.2(c)), which is used for continuous torque generation for both static and dynamic actuation. The alignment between top and bottom comb-figures is very critical because a small amount of misalignment may cause the side wall pull-in of comb-fingers. Various types of fabrication schemes have been applied to form the initial offset.

V. Milanovic et al. in 2002 proposed a novel fabrication process for multilevel beam SOI-MEMS devices, which is capable of fabricating staggered vertical comb-drive actuators [56-59]. Instead of using expensive SOI wafers, fabrication process based on monolithic silicon wafers were developed to reduce the fabrication cost. In 2002, J.H. Lee et al. demonstrated a staggered vertical comb-drive actuator fabricated using bulking micromachining and anodic wafer bonding process [60]. Later in 2005, Q. Zhang et al. proposed a low-cost micromachining process using single monolithic silicon wafer to

fabricate staggered vertical comb-drive actuators, which combines anisotropic and isotropic etching processes [61].

In the above fabrication processes, the alignment accuracy between upper and lower fingers is determined by the accuracy of mask alignment during the lithography process, where the misalignment error could be introduced. U. Krishnamoorthy et al. investigated the influence of the misalignment between comb-fingers on the performance of the vertical comb-drive actuator in 2003 and proposed a self-alignment fabrication process to eliminate the influence of the misalignment between fingers [62]. Later from 2004 to 2006, scanning micromirrors actuated by various self-aligned staggered vertical comb-drive actuators are demonstrated [46, 63-65].

Besides using bulk micromachining process, multi-layered surface micromachining process can also be used to fabricate staggered vertical comb-drive actuators. These micromirrors are mostly used in high-fill-factor mirror arrays. In 2003 and 2006, D. Hah et al. and J.C. Tsai et al. demonstrated their prototypes fabricated using Sandia's Ultra-planar Multilevel MEMS Technology-V (SUMMiT-V) process [66, 46]. SUMMiT-V is offered by Sandia National Laboratory, which consists of five polysilicon layers (one fixed and four movable) [67].

Bulk micromachining process could offer thick mirror body as well as comb-fingers and stiff torsional spring resulting in large angular displacement but high driving voltages. On the contrary, surface micromachining process could offer light weight mirror body, soft torsional

spring and thin comb-fingers, resulting in large dynamic deformation, small driving voltages but limited angular displacement. To fabricate a low-inertia micro scanning mirror with reinforced mirror body, soft torsional suspensions and thick comb-fingers, a novel process, namely Molded Surface Micro Machining and Bulk Etching Release (MOSBE II) process, was proposed by M.C. Wu et al. in 2004 [68-69].

Fabrication methods, other fabrication processes, which combine a simple micromachining and a post assembly process, were also reported to form staggered vertical comb-fingers. For example, K.H. Jeong et al. utilized the deformation of a bimorph cantilever to form the vertical gap between fix and movable comb-fingers, which are patterned initially in a same layer [70]. Similarly, M. Sasaki et al. utilized buckling of bimorph bridges to elevate movable fingers and form the initial vertical offset [71].

2.2.3 Angular vertical comb-drive actuators

In an angular vertical comb-drive actuator, there is an initial angular offset between movable and static fingers (shown in Figure 2.2(d)), unlike the staggered type discussed above. Generally, the movable and fixed comb-fingers are firstly fabricated in the same layer. Then the movable fingers are tilted upward by post assembly process, either manually or through a self-assembly process. Since all the fingers are patterned at the same time, they are inherently self-aligned. Moreover, angular vertical comb-drive actuator is capable of achieving larger maximum scanning angles, compared with staggered comb-finger configuration [72]. In angular vertical comb-drive actuators, the movable fingers can be deflected to form the initial

angular offset by various methods, such as deflection of multi-layered beam due to stress mismatch in different materials [72], surface tension of polymer hinges formed by recurring process [73-75], latching of mechanical hinges [76] and deformation of torsional suspensions [77-79].

In 2003, H. Xie et al. employed stress-induced curling of a multi-layered cantilever to form angular vertical comb-drive actuators [72]. Later in 2004, D. Hah et al. utilized the surface tension of a photoresist hinge during the reflow process to form the initial angular offset [73]. Instead of using photoresist hinge, M. Fujino et al. and H.D. Nguyen et al. reported prototype angular vertical comb-drives formed using photo-definable benzocyclobutene (BCB) polymer [74-75]. Then, W. Piyawattanametha et al. in 2005 demonstrated their 2D scanner actuated by four angular vertical comb-drive actuators with mechanical latching hinges. After that, J. Kim et al. demonstrated 1D [77-78] and 2D [79] scanning micromirrors in 2006, which are driven by angular vertical comb-drive actuators. The initial angular offset is formed using plastic deformation of torsional springs. All comb-fingers, torsional springs and the mirror body are patterned in a same layer. Then torsional springs are mechanically deformed while heated above the glass transition temperature, introducing a permanent plastic deformation. The torsional springs can be deformed by a selective stiction process [77], which utilizes the principle that residual non-CO₂ liquid could still cause stiction phenomena during the CO₂ critical point drying process [80]. The torsional springs can also be deformed using a predefined mold wafer with several pillar-like structures [78-79]. Using this method the amount of initial offset can be easily adjusted by changing the mold wafer.

2.2.4 In-plane vertical comb-drive actuators

Staggered or angular vertical comb-drive actuators with vertical or angular offsets between movable and fixed fingers, which are capable of producing continuous rotational torques, are required in static scanning applications, such as optical switches and optical attenuators. Generally, fabrication processes used to form initial offsets between comb-fingers are complicated. H. Schenk et al. proposed an in-plane vertical comb-drive actuator especially for resonant scanning applications as shown in Figure 2.2(e) [81-83], such as projection displays, which require high scanning speed with large scanning amplitudes.

In-plane vertical comb-drive actuators take advantages of capacitances variation between movable and fixed vertical comb-fingers during oscillation. The capacitance decreases with the out-plane-rotation of the mirror plate. The applied voltage between movable and fixed comb-fingers generates an electrostatic torque pulling the mirror plate to its rest position. Although all the fingers are pattern in a same plane, small asymmetries of the device still exist due to imperfections of micromachining process, which slightly differ the electrostatic and mechanical rest positions. Thus an AC driving signal with a frequency which is two times of the resonant frequencies of the micromirror, will excite the torsional oscillation of the mirror plate.

2.2.5 Lateral comb-drive actuators

Some scanning micromirrors are actuated by lateral comb-drive actuators by employing leverage mechanisms which transfer the lateral motion to rotational motion of mirror plate

(shown in Figure 2.2(f)). Lateral comb-drive actuation mechanisms were initially developed to overcome the scanning amplitudes limitation of surface micromachined micromirrors actuated by electrostatic rotating plate actuator [35, 84-87].

Lateral comb-drive actuated micromirrors based on SOI micromachining technology were demonstrated by V. Milanovic et al. and L. Zhou et al. in 2003 and 2006 [88-89]. Lateral comb-driven scanning mirrors overcome the alignment issue in staggered vertical comb-drive actuators and offer additional advantages, such as small moment of inertia and high actuation force resulting in large scanning angle and fast response. The lateral motion of comb-drive actuator is converted to rotation of micromirror through a leverage mechanism. The lateral pushing or pulling force is transferred along linkages and applies below the axes of rotation of the mirror torsion bars, resulting in mirror rotation [88]. Two fabrication processes were reported to fabricate the motion conversion mechanism, which are multi-level beam SOI-MEMS Fabrication process [88] and SOI/SOI wafer bonding process [89].

2.2.6 Circular comb-drive actuators

A circular comb-drive actuator contains two sets of circular-shaped comb-fingers and all comb-fingers are concentric. While operating, movable comb-fingers move in rotational motion with respect to stationary comb-fingers. Since the circular comb-drive actuator is initially designed for in-plane rotation, the mirror body is required to be either fabricated or assembled vertically with respect to the actuator plane (shown in Figure 2.2(g)). Thus the rotational axes of mirror and actuator are coincident. Scanning micromirrors driven by

circular comb-drive actuators are mostly developed for optical switching applications [90-92].

2.3 Other actuation mechanisms

Compared with electrostatic actuations, other types of actuators, such as piezoelectric, electrothermal and electromagnetic actuation, are capable of providing larger actuation forces but consuming more energy. In the following sections, examples of individual actuators are reviewed.

2.3.1 Piezoelectric actuation

Piezoelectric actuation in general is based on the bending of a bimorph beam or plate induced by an electric field. The induced strain is proportional to the applied electric field. Piezoelectric actuators are attractive because they are able to generate large stresses and high-energy density. Besides, they can be operated within a large bandwidth and potentially require low driving voltages. However, the actuation displacements of piezoelectric actuators is small and dedicate deposition process of piezoelectric material is required, which is generally complicated.

Various micromirror scanners driven by piezoelectric actuators with lead zirconate titanate (PZT) films have been developed [93-98]. F. Filhol et al. in 2005 demonstrated a 1D resonant torsional micromirror based on PZT thin film actuation. The prototype scanner is capable of scanning at 10.9kHz (less than 1V_{pp} driving voltages) with an optical scan angle of 78° in vacuum conditions [95]. Later in 2007, J.H. Park et al. demonstrated another 1D scanning

mirror, which is capable of scanning at 28kHz (60V_{pp} driving voltages) with an optical scan angle of 41° [97].

2.3.2 Electrothermal actuation

Thermal actuation takes advantage of the thermal expansion or contraction property of a material, which can be heated by passing a current through an embedded resistor (Joule heating). Thermal actuators can generate large actuation forces and their fabrication processes are simple. However, they are generally slow and require a large amount of thermal energy for their operation and therefore consume substantial electrical energy. High temperature and complicated thermal management are among the major considerations of these actuators. Moreover, the rest position of the mirror plate is significantly dependent on the ambient temperature which could raise problems for some applications. In mostly widely implemented thermal actuators for micromirror scanners, which are called bimorphs or multi-morphs, two or more layers of materials with different coefficients of thermal expansion (CTE) β_i are grown adjacently to each other and displacement is generated under temperature variation [48, 99-102], shown in Figure 2.3. S. Schweizer et al. demonstrated an electrothermal actuated scanning mirror in 1999. The rest position of the mirror can be adjusted through controlling the residual stress in films during processing. The prototype scanners are capable of achieving an optical scan angle of above 180° [99].

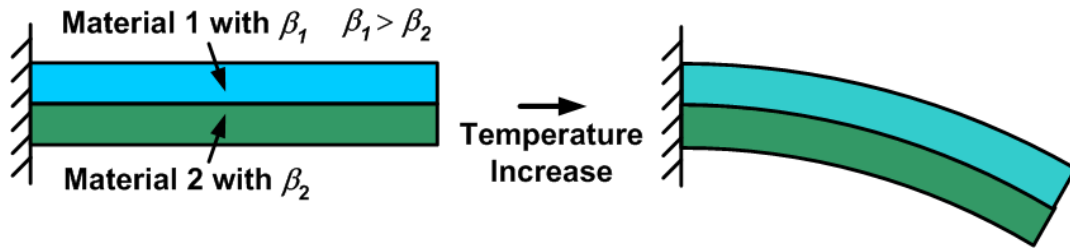


Figure 2.3 Working principle of a bimorph thermal actuator.

2.3.3 Electromagnetic actuation

Magnetically actuated micromirrors utilize the Lorentz forces. In general, a coil with one or more windings is fabricated on top of the mirror plate and placed in the field of an external permanent magnet or an electromagnet. Depending on the direction of the current passing through the coil, the mirror plate will deflect to the left or to the right, shown in Figure 2.4.

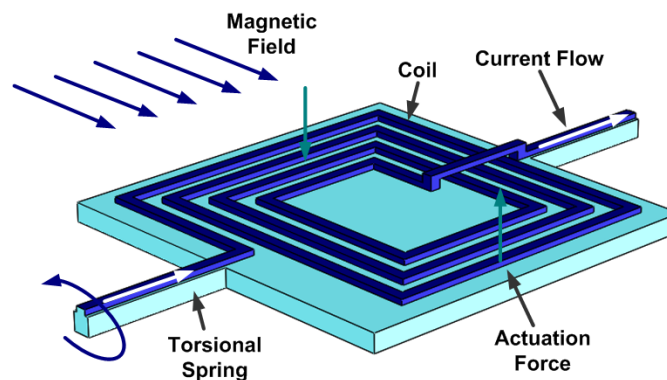


Figure 2.4 Schematic illustration of 1D scanning mirror driven by electromagnetic actuator.

Electromagnetic actuators are very attractive for scanning applications requiring large scanning angle, high scanning frequencies and large aperture size, because magnetic forces scale with the volume of external magnets. The major limiting factors for electromagnetic actuation used in miniaturized laser scanning applications are high power consumption and relatively large scanner overall size.

From 1991 onwards, various types of micromirrors driven by electromagnetic actuators were developed [104-116]. Significantly, A.D. Yalcinkaya et al. and D. Brown et al. reported an electromagnetic actuated 2D double-gimbaled resonant scanning micromirror in 2006 [111]. All driving coils are configured on gimbal structure instead of scanning mirror for better mirror flatness. The 2D scanning operation is based on superimposing the driving torques on two scanning directions. The actuation torque is applied at 45° relative to two scanning axes, shown in Figure 2.5.

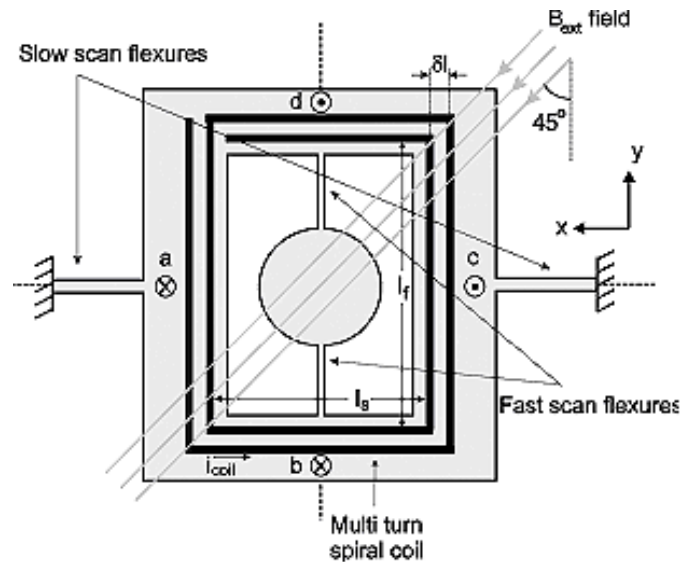


Figure 2.5 Schematic illustration of the working principle of the 2D electromagnetic driven scanning mirror [111].

The double-gimbal structure acts as a mechanical filter which separates the driving torque into two components. Torque components then stimulate the respective modal motions of the mirror along both axes according to their frequency response characteristics. Therefore, if an actuation signal, which is a combination of a high frequency sinusoidal and low frequency saw-tooth signals, is applied, pure sinusoidal motion of horizontal resonant scanning and

saw-tooth motion of vertical non-resonant scanning can be realized. The prototype scanner with a 1.5mm diameter mirror body is capable of achieving optical scan angles of 65° (horizontal scanning) and 53° (vertical scanning) with corresponding resonant frequencies of 21.3kHz and 60Hz.

2.4 Dynamic flatness of micromirrors

As discussed in Chapter 1, the dynamic deformation of the mirror body in micromirror scanners can be a limiting factor for them to realize high speed high resolution laser scanning applications (such as laser scanning displays), which typically require large aperture size, large optical scan angle and high scanning frequency. While scanning resonantly, the out-of-plane acceleration force bends the mirror body, shown in Fig 2.6.

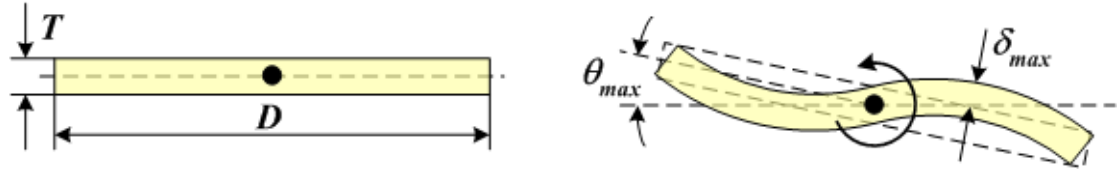


Figure 2.6 Schematic illustration of mirror dynamic deformation while scanning.

The maximum deformation will appear at the extreme position where the angular acceleration torque becomes the maximum. Since velocity of the mirror is zero at the extreme position, damping effect is not considered because damping force is proportional to velocity. Maximum dynamic deformation (δ_{\max}) of a solid micromirror with a rectangular shape (shown in Figure 2.31) can be calculated using Eq. 2.1 [117].

$$\delta_{\max} = 0.217 \frac{\rho f^2 D^5 \theta_{\max}}{ET^2} \quad (2.1)$$

where ρ is the material density; E is the Young's modulus; f is the scanning frequency; D and T are length and thickness of the mirror body; θ_{\max} is the maximum half mechanical deflection angle.

It can be concluded from Eq. 2.1 that the maximum dynamic deformation increases with the increase in scanning frequency, scanning amplitude, mirror size and decrease in mirror thickness. Therefore, scanning mirrors with large sizes and scanning amplitudes with high scanning frequency, which are required for many scanning applications, could suffer from considerable dynamic deformations. To address this, R.A. Conant et al. presented a design criterion in 2000 to find a combination of scanner dimension and resonant frequency for scanners with good optical quality [118].

Dynamic deformation can be reduced by increasing the rigidity of the mirror body through increasing mirror thickness, which is the most direct way. However, the moment of inertia of the mirror body will be increased considerably at the same time. The stiffness of the torsional springs that supports the mirror has to be increased to maintain the scanning frequency. This limits the scanning amplitude due to excessive stress induced. Therefore, a thin mirror plate with backside thick reinforcement frames, which increases the rigidity of the mirror body adversely without increasing the moment of inertia, have been widely adopted, as shown in Figure 2.7 [46, 68-69, 119-120].

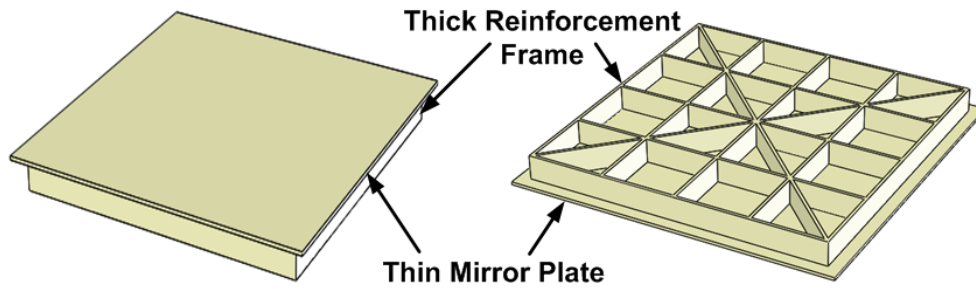


Figure 2.7 Schematic illustration of a thin mirror plate reinforced by a thick backside frame.

C.H. Ji et al. demonstrated an electrostatic scanning micromirror with diaphragm mirror plate and diamond-shaped reinforcement frame in 2006 [120]. A scanning micromirror with a $10\mu\text{m}$ thick, $1.5\text{mm}\times 1.5\text{mm}$ square diaphragm mirror plate is supported by an array of $110\mu\text{m}$ thick rhombic support frames. An optical scanning angle of 17° at a resonant frequency of 19.55kHz is achieved.

Besides increasing the rigidity of the mirror plate, A. Wolter et al. presented a method to reduce the dynamic deformation by changing configurations of mirror plate suspensions in 2006. The principle idea is to apply forces of the torsional springs to multiple points located at the edge of mirror plate rather than only to small regions through adopting multiple spring suspensions, shown in Figure 2.8 [121-122]. Dynamic deformation can be minimized through optimizing the stiffness of each spring.

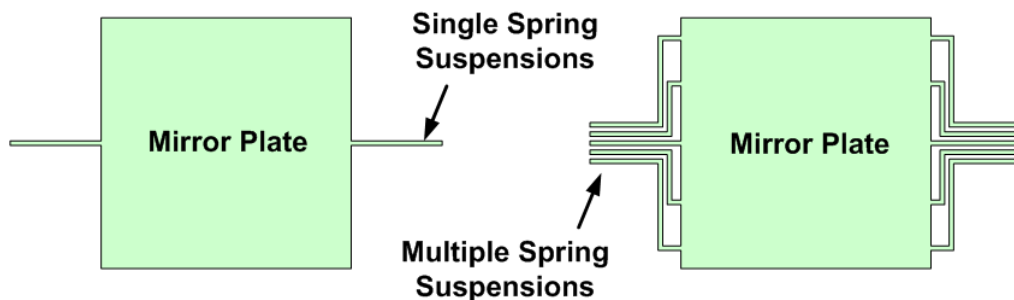


Figure 2.8 Micromirrors suspended by single and multiple springs.

2.5 Preliminary results on MEMS vibratory grating laser scanners

As discussed in Chapter 1, the grating scanning scheme will not suffer from the dynamic deformation problem and perform better in high speed scanning domain compared with micromirror scanner. Several prototype scanning gratings have been developed [40-41, 123-124].

A.A. Yasseen et al. reported the first miniaturized scanning gratings in 1999, which is driven by an electrostatic micro motor [123]. The prototype scanner is capable of achieving a scan rate of 347 scans per-second and an angular range of 360°. The in-plane rotation motion of the diffraction grating will introduce little out-of-plane dynamic deformation. However, scanning speed of the prototype scanner is limited by its actuation mechanism. The gap between the rotor and the bearing post could cause wobble of the rotor. Also, considerable heat could be generated by contact friction between the rotor and the substrate while scanning at high frequencies. Moreover, optical efficiency of the scanner is quite low, which is 5-7% for the 1st order diffraction beam. Consequently, scanning gratings actuated by micro motors have little comparative advantages to micromirror scanner because the dynamic deformation of a micromirror is not significant at low frequency region and micromirror scanners have higher reflection efficiency as well as more stable working condition. Nevertheless, this work represents the first MEMS driven grating scanner

In 2003, G. Zhou et al. proposed a novel grating scanner with vibratory motion, which is fabricated using three layer surface micromachining process [124]. The diffraction grating

platform is single-sided suspended and actuated by an electrostatic comb-driven lateral resonator, shown in Figure 2.9.

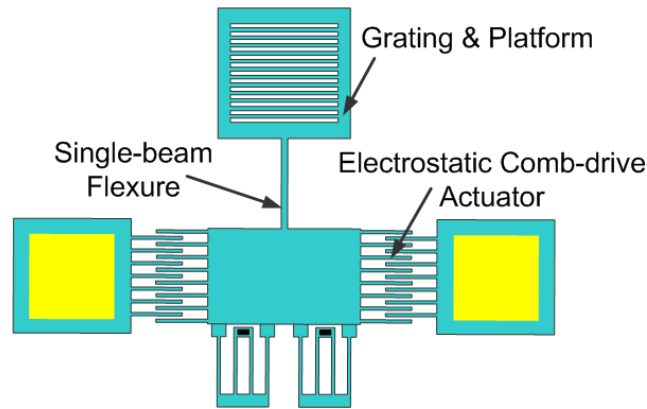


Figure 2.9 Schematic illustration of a single-side driven scanning grating actuated by an electrostatic comb-drive actuator [124].

This configuration inherently enables possibilities of higher speed scanning, compared with micro motor driven, due to negligible wear and tear. Besides, the in-plane vibratory motion suffers little from the dynamic deformation. The scanning frequency of the prototype is 7.67 kHz and the optical scan angle of 9th order bow-free scanning is 12-13°. However, optical efficiency of the prototype is quite low. Besides, the single-side driven structure could cause the rotational center of the grating platform to shift and the softening of the flexure beam during vibration.

Later in 2004, G. Zhou et al reported a grating scanner actuated by two symmetrically configured electrostatic comb-drive actuators, which is fabricated using SOI micromachining technology [40], shown in Figure 2.10. As shown in Figure 2.10, the diffraction grating is suspended symmetrically by two “T” shape suspensions. This configuration ensures the

diffraction grating rotating along a fixed center and has higher mechanical stability compared with the previous prototype [124]. However, the optical efficiency is still low. The prototype is capable of scanning at 8.34kHz with an optical scan angle of 15.9°.

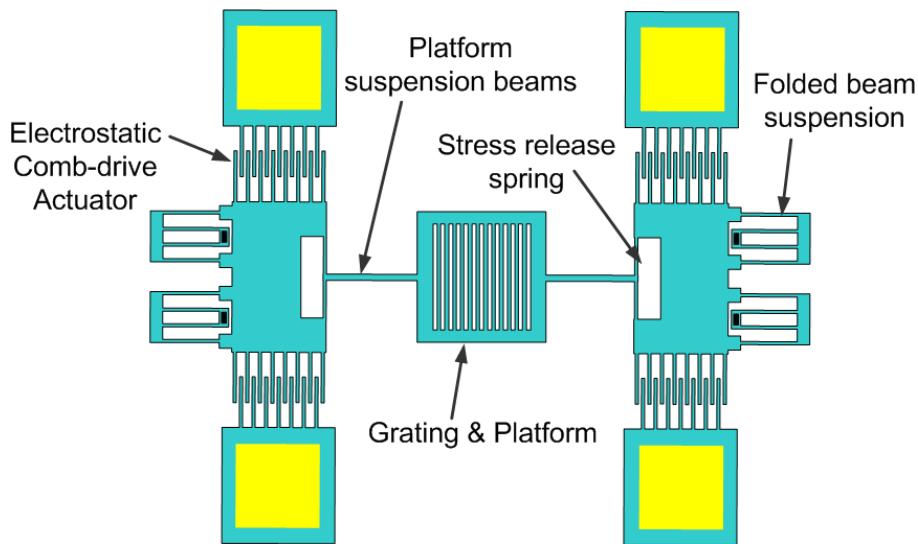


Figure 2.10 Schematic illustration of a symmetrical electrostatic comb-driven scanning grating [40].

Since the diffraction grating is a dispersive element, grating scanner with a single grating is quite suitable for narrow-band laser scanning but not suitable for the situation that requires multi-wavelength collinear scanning, such as colorful projection display. G. Zhou et al. provided a solution for multi-wavelength collinear scanning in 2006, which is integrating several gratings with different grating periods corresponding to laser beams with different wavelength [41]. Figure 2.11(a) shows the working principle of multi-wavelength collinear scanning by multiple gratings integrated on a same platform.

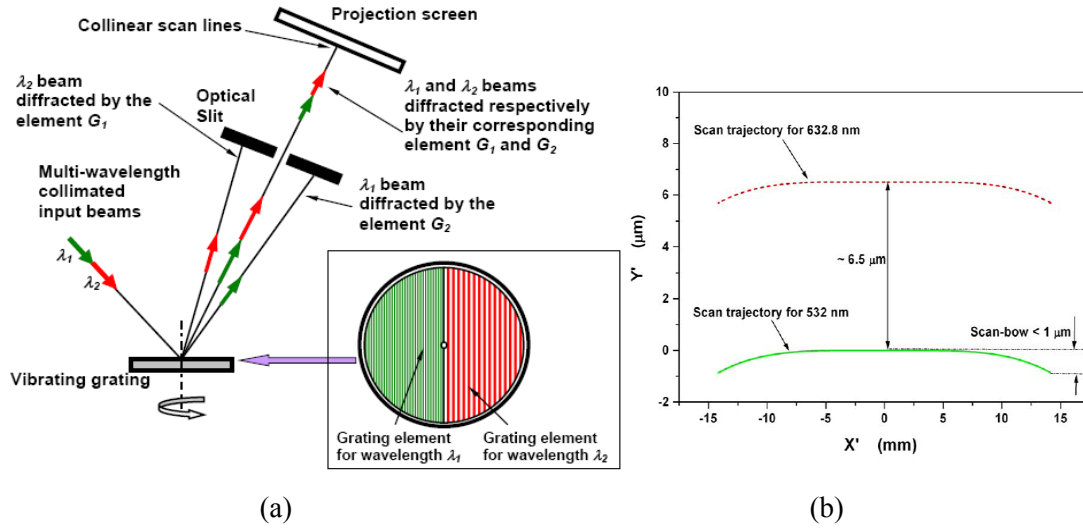


Figure 2.11 (a) Dual laser beams with same incident angle and scanned collinearly by two diffraction gratings configured on a same platform; (b) Simulated scanned trajectories [41].

As shown in Figure 2.11(a), two grating elements are placed on a same platform for two incident laser beams. Laser beams illuminate on the grating platform with same incident angles and each has two diffraction beams. Each laser beam diffracted by its corresponding grating element will have same diffraction angle, resulting in a collinear scanning trajectory. Simulated collinear scanning trajectories with a 6.5 μm spacing are shown in Figure 2.11(b). The drawback of this method is the low scanning efficiency due to multiple gratings configuration, which limits the aperture size for each grating element.

2.6 Summary

As discussed in above sections, micromirror scanners with various structures and actuation mechanisms have been mostly developed. Dynamic deformation is a limiting factor of micromirrors while implemented in high-speed, high-efficiency applications, such as projection displays. Dynamic deformation of scanning mirror can be reduced by either

increasing the rigidity of the mirror plate or changing the configurations of torsional springs. In-plane grating scanners inherently have little dynamic deformation during high-speed scanning. Considerable research processes have been achieved on the MEMS scanning gratings, such as stable vibration structure, bow-free scanning trajectories and multi-wavelength collinear scanning. However, performance of current prototypes are not satisfying, such as low optical efficiency, low scanning resolution and relatively low scanning frequency, which need to be increased for high-quality, high-speed laser scanning applications.

Chapter 3 Micromachined vibratory grating scanners: theoretical study, optical efficiency optimization and modeling

This chapter provides theoretical studies of MEMS vibratory grating scanners, which will be discussed in four parts. Firstly, theory of laser scanning by a diffraction grating is introduced. Secondly, grating profile optimization using numerical Rigors Coupled Wave Analysis (RCWA) simulations for obtaining maximum optical efficiency is discussed. Thirdly, different actuation mechanisms for driving the diffraction grating are introduced and compared. Finally, comprehensive dynamic models to predict scanners' dynamic performances are presented.

3.1 Theory of laser scanning with diffraction grating

The operational principle of a scanning diffraction grating is shown in Figure 3.1 below.

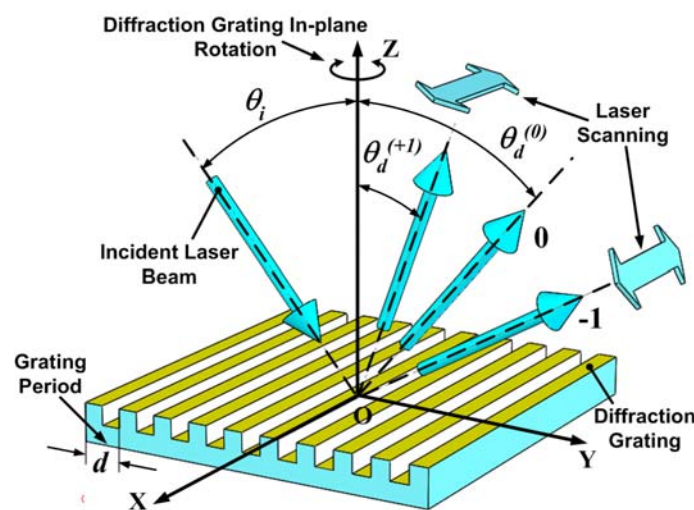


Figure 3.1 Schematic illustration showing operational principles of a scanning grating.

As shown in Figure 3.1, the grating lies in the XOY plane with its lines orientated parallel to the X-axis. An incident laser beam lies in the YOZ plane and illuminates the grating at an angle of incident θ_i . When the diffraction grating rotates about the Z-axis (in-plane rotation), the diffracted beams (except the zeroth order) scan accordingly. As reported by G. Zhou et al. in 2004, the normalized wave-vector \vec{r} pointing to the direction of the outgoing m^{th} order diffraction beam as a function of the grating rotation [41] is shown below:

$$\begin{aligned} \vec{r}(\theta_R) = & \left(-\frac{m\lambda}{d} \sin \theta_R \right) \vec{e}_x + \left(\sin \theta_i - \frac{m\lambda}{d} \cos \theta_R \right) \vec{e}_y \\ & + \left\{ 1 - \left(\frac{m\lambda}{d} \sin \theta_R \right)^2 - \left(\sin \theta_i - \frac{m\lambda}{d} \cos \theta_R \right)^2 \right\}^{1/2} \vec{e}_z \end{aligned} \quad (3.1)$$

where m is the diffraction order; λ is the wavelength of the incident beam; d is the pitch of the diffraction grating; θ_i is the angle of the incident beam; θ_R is the grating rotation angle (angle between grating line and X-axis); $\vec{e}_x, \vec{e}_y, \vec{e}_z$ are the unit vectors along X-, Y- and Z-axis, respectively.

Normally, some level of scan-line bow is present in MEMS-based diffraction grating scanners, which is not desirable for most scanning applications. However, the scan-bow, which is defined as the departure of the scan line from a perfect straight line, can be minimized to a negligible level. A diffraction-grating scanner will produce a virtually bow-free scanning trajectory when the incident angle θ_i , diffraction angles θ_d and diffraction order m satisfy Eq. 3.2 shown below [125]:

$$\begin{cases} \sin \theta_i = \frac{m\lambda}{d} - \frac{d}{m\lambda} \\ \sin \theta_d = \frac{d}{m\lambda} \end{cases} \quad (3.2)$$

To make sure Eq. 3.2 has a real solution, the ratio of grating period to diffraction order m should reside within a specific range, i.e. $0.618\lambda \leq \frac{d}{m} \leq \lambda$. It can be seen that either large grating pitch with high diffraction order or small grating pitch with low diffraction order can be selected for bow-free scanning. However, a lower order diffraction beam is always preferred for laser scanning because the diffraction efficiency decreases rapidly at higher diffraction orders. It is clear that the grating pitch must be smaller than the wavelength of incident beam so that a high-efficiency 1st order beam can be utilized to scan a bow-free line. For example, when illuminated with a laser beam with a wavelength of 632.8nm, the grating pitches could vary from 391nm to 632.8nm for bow-free scanning of 1st order diffraction beam. If the grating pitch is selected to be 500nm, the incident angle θ_i can be calculated to be 28.4° for bow-free scanning according to Eq. 3.2. Scanning trajectory of the 1st order diffraction beam on a projection screen is calculated based on Eq. 3.2 (grating pitch: 500nm; incident angle: 28.4°; grating rotation angle: $\pm 10^\circ$; screen to grating distance: 200mm), shown in Figure 3.2. X' and Y' are corresponding coordinates of the projection screen.

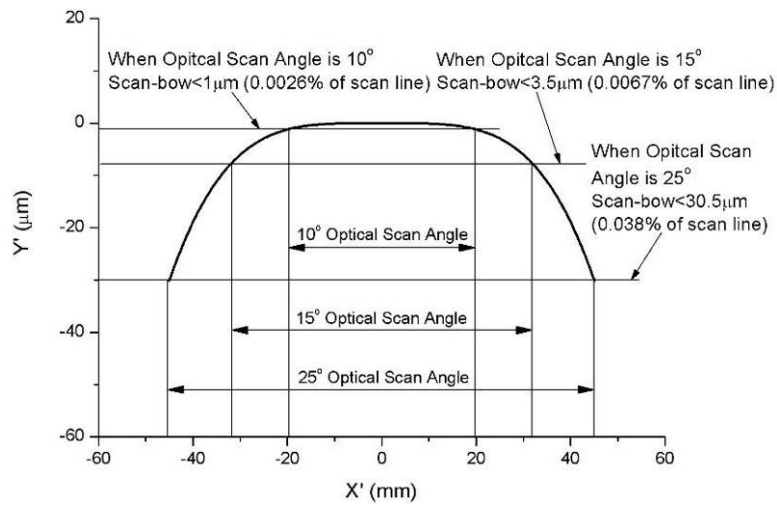


Figure 3.2 Calculated scanning trajectories of the 1st order diffraction beam with a grating period of 500nm.

As shown in the figure, the scan-bow increases with increasing scanning angle. The maximum deviations of the scan trajectory from the ideal straight line are $1\mu\text{m}$, $3.5\mu\text{m}$ and $30.5\mu\text{m}$ with optical scan angles of 10° , 15° and 25° , respectively. Deviations relative to total lengths of the scan trajectory are 0.0026%, 0.0067% and 0.038%, which can be ignored.

Figure 3.3 shows calculated scanning trajectories of the 1st order diffraction beam on a projection screen with varying grating period based on Eq. 3.1 (grating pitch: 500nm; incident angle: 28.4° ; grating rotation angle: $\pm 10^\circ$; screen to grating distance: 200mm). X' and Y' are corresponding coordinates of the projection screen. As shown in Figure 3.3, bow-like scanning trajectories are presented if the bow-free scanning condition (Eq. 3.2) is not satisfied.

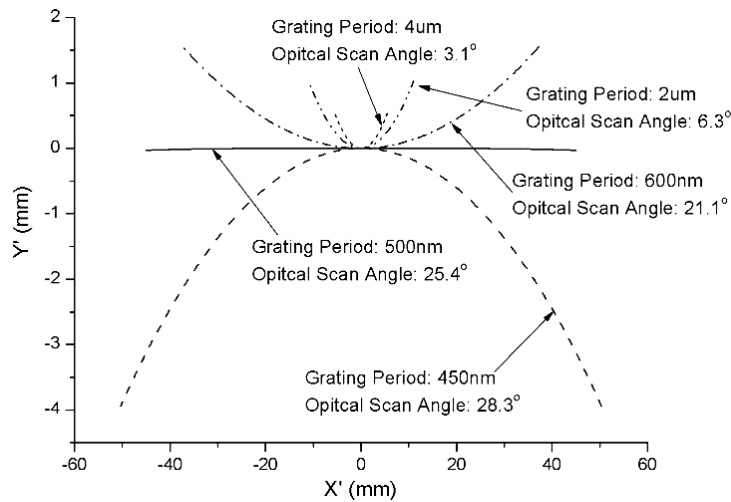


Figure 3.3 Calculated scanning trajectories of the 1st order diffraction beam with varying grating period from 450nm to $4\mu\text{m}$.

Moreover, it is observed that the optical scan angle increases when the grating period is

reduced. Magnification ratios between the optical scanning angle θ_{opt} and the grating rotation angle θ_R with varying grating period from 450nm to 4 μm are simulated, shown in Figure 3.4.

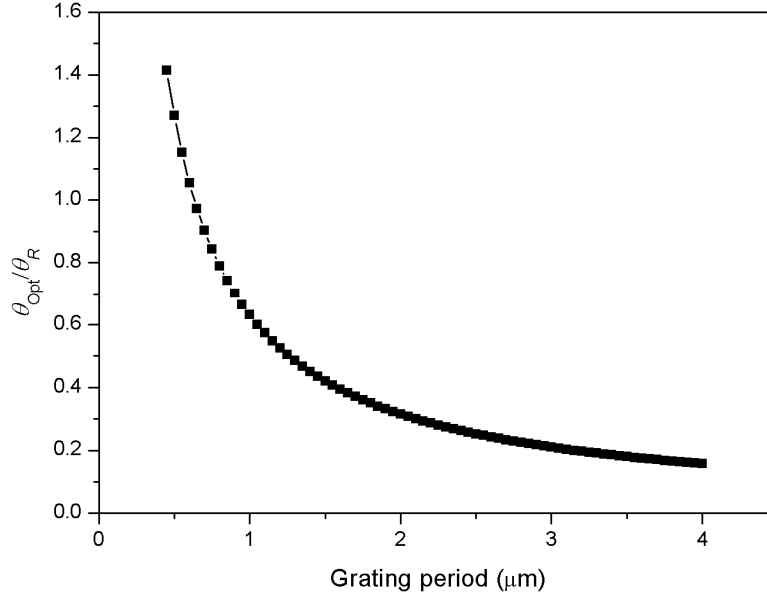


Figure 3.4 Magnification ratios between the optical scanning angle and grating rotation angle with varying grating period from 450nm to 4 μm .

3.2 Optical efficiency maximization by grating profile optimization

In this dissertation, sub-wavelength diffraction gratings with periods of 400nm and 500nm are used in all the prototypes. In this section, diffraction grating with a period of 500nm is taken as an example. While illuminating a laser beam with a wavelength of 632.8nm, the incident angle for bow-free scanning is calculated as 28.4°. According to the well-known grating equation, only two propagating diffraction orders exist, namely, the zeroth and the first order. It is noted that the non-diffracted zeroth-order beam will remain stationary during grating in-plane rotation. Hence, the objective is to maximize the diffraction efficiency of the first-order diffracted beam that is used for laser scanning. Although a diffraction grating can

theoretically achieve 100% diffraction efficiency for a selected diffraction order at a given wavelength, a continuous surface profile would be necessary, which is difficult to achieve using conventional silicon micromachining technology, especially when the grating period is small. A binary grating profile is adopted in this dissertation due to its simplicity and ease of fabrication using one-step photolithography and RIE process. The diffraction efficiency of the 1st order diffraction beam as a function of the grating groove depth is investigated while keeping the grating duty cycle fixed at 50% (250nm wide grooves and ridges).

Since the grating period is smaller than the wavelength of the incident laser beam, prediction of diffraction efficiency using the scalar diffraction theory is no longer valid. Numerical simulations using a more accurate RCWA method [126] are therefore performed to investigate the relationship between the diffraction efficiency of the scanner and the binary grating profile. RCWA is a numerical method that can provide a rigorous fully vectorial solution of Maxwell's equations and is suitable for analyzing the transmission, reflection and diffraction of periodic structures. In the simulations, the sub-wavelength binary grating is assumed to be made of gold with a complex refractive index of $0.13+3.16j$ at a wavelength of 632.8nm [127], in which the imaginary part indicates the extinction coefficient. A light beam with a wavelength of 632.8nm strikes the grating at the bow-free scanning incident angle of 28.4° . The grating is aligned such that its grooves and ridges are perpendicular to the plane containing the incident beam. TE-polarized light is defined as an incident light wave having an electric field vector parallel to the grating grooves, and TM-polarized light is defined as an incident wave having an electric field vector perpendicular to the grating grooves. Simulation

results show that the grating diffraction efficiency, which is defined as the ratio of optical power of the first diffraction order to the total incident power, is polarization dependent. Diffraction efficiencies as a function of the grating groove depths are plotted in Figures 3.5 (a) & (b) for TM- and TE-polarized incident light, respectively.

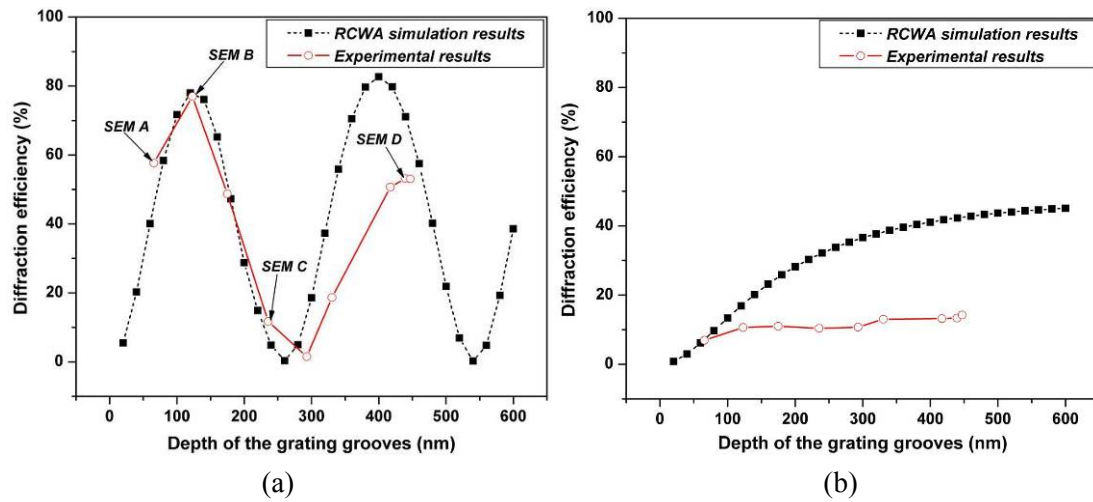


Figure 3.5 Diffraction efficiencies as a function of grating groove depths for (a) TM- and (b) TE-polarized incident light.

It is observed that for TM polarization, the diffraction efficiency of the grating varies in a sinusoidal pattern as the grating groove depth increases and can be as high as 80% as long as the depth of the grating grooves is properly set. For TE polarization, the diffraction efficiency increases monotonically with increasing depth of the grating grooves and saturates at about 45% for the simulated results using RCWA. From the simulation results, it is noted that high optical efficiencies (close to that of a coated mirror) can indeed be achieved with a simple binary metallic sub-wavelength grating, provided that the grating groove depth is precisely controlled in the fabrication process and a TM-polarized incident laser beam is utilized for illumination during the scanner operation.

To verify the simulation results, a set of diffraction gratings with the same period of 500nm but different groove depths were fabricated using deep-UV lithography and RIE of silicon wafers. The duty cycle of the diffraction grating was designed to be 50%, which may slightly vary during the fabrication process. Nevertheless, for a diffraction grating, a slightly change in duty cycle has little influence on its performance. A 10nm thick chromium layer followed by an 80nm thick gold layer was then deposited on the wafer surface using a sputtering process to increase the reflectivity. Diffraction efficiencies of fabricated gratings are then measured with a linearly polarized He-Ne laser, shown in Figure 3.6.

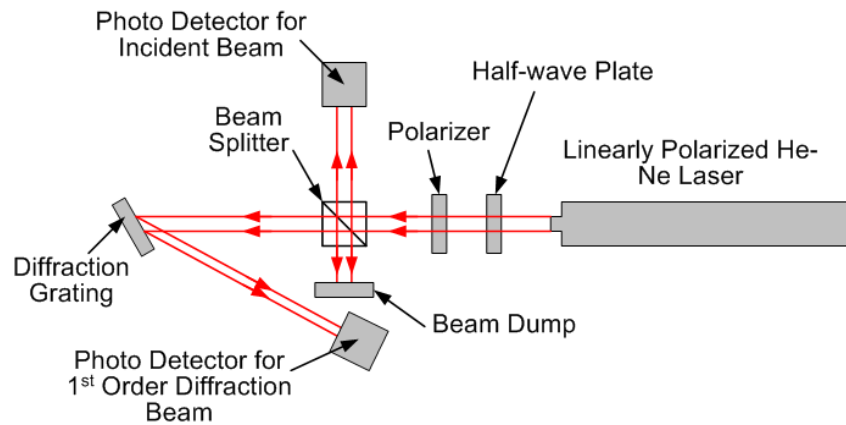


Figure 3.6 Experimental setup for diffraction efficiency measurement.

As shown in Figure 3.6, the polarization state of the He-Ne laser beam is rotated by a half-wave plate with an angle of 45° with respect to the horizontal reference. A linear polarizer is then used to provide TE- or TM-polarized incident light beam. The incident beam is then uniformly split into two beams by a beam splitter. The intensity of one beam is directly measured by a photo detector. The other beam illuminates on the diffraction grating and the intensity of diffraction beam is measured by another photo detector. Measured grating

efficiencies as a function of the grating groove depths are plotted as open circles in Figures 3.5(a) & (b) for TM- and TE-polarized light respectively. It is observed that the experimental results are in good agreement with the simulation results at small groove depths. However, significant discrepancy occurs when the grating groove depth is large. This is because the diffraction gratings in our simulations had been assumed to be made of gold whereas the actual gratings used in our experiment were made of silicon and then coated with an optically thick gold layer. Figures 3.7 (a) to (d) show the cross-sectional SEM images of the gratings with different groove depths.

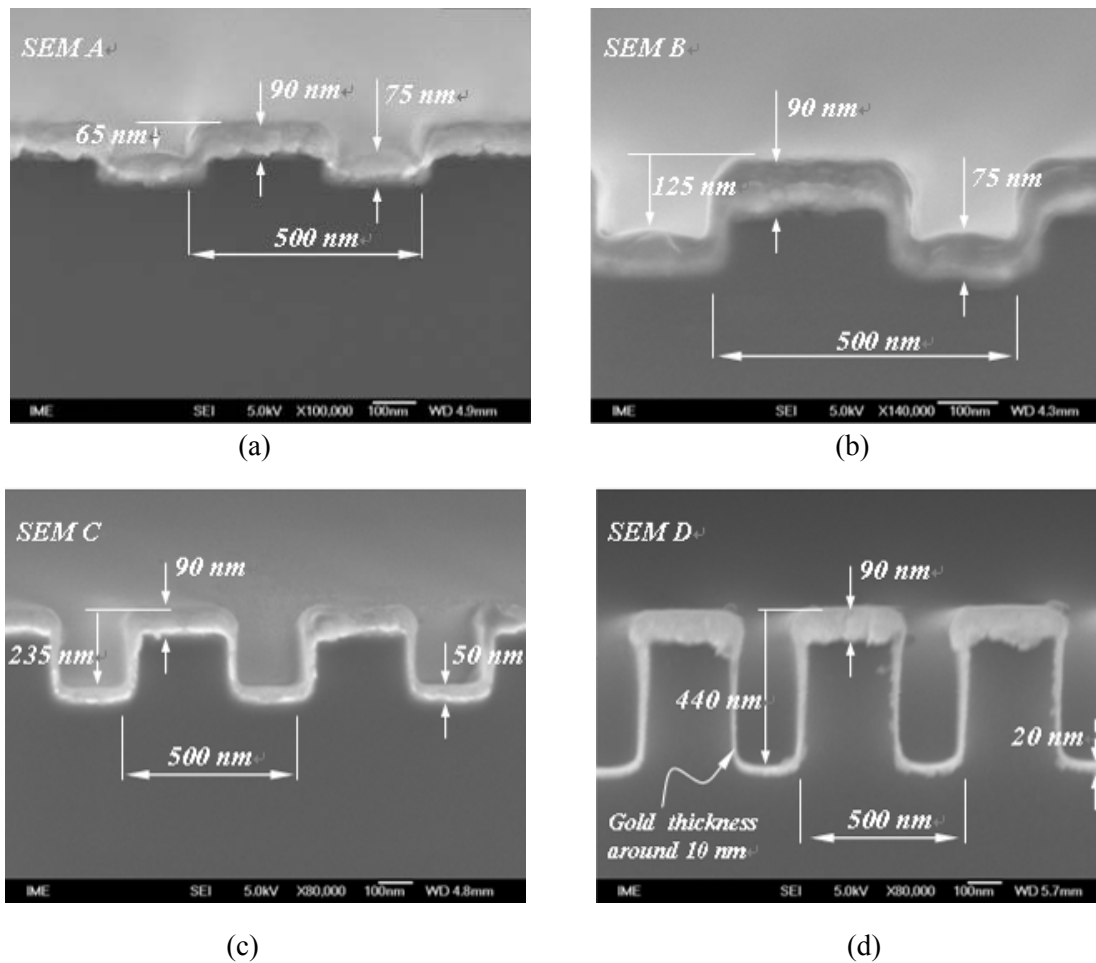


Figure 3.7 SEM images showing cross-sectional views of gratings with different groove depths: (a) 65nm, (b) 125nm, (c) 235nm and (d) 440nm.

As shown in Figure 3.7, relatively conformal step coverage of gold layers is achieved using the sputtering process for shallow grating grooves. Since gold films on the sidewalls and bottom surfaces of shallow grating grooves are optically thick, the assumption that the diffraction gratings are made wholly of gold in RCWA simulations is valid. However, as the grating groove depth increases, step coverage deteriorates accordingly and the gold films on side walls and bottom surfaces of grating grooves are no longer optically thick. As a result, part of the incident light energy can be transmitted through the gold layer and absorbed by the silicon layer underneath causing a reduction in total diffracted optical energy. Nevertheless, regardless of the discrepancy between simulation and experiment at large groove depths, we note that a diffraction efficiency of more than 75% is experimentally achieved for TM polarization with shallow grating grooves at an optimal groove depth of 125nm. This is closed to the reflective efficiency of a mirror with the same metal coating, which was measured to be around 90%.

Since optical scanning is achieved with a linearly polarized incident laser beam in conjunction with an in-plane vibratory sub-wavelength grating, of which the diffraction efficiency is polarization dependent, variation of the scan beam intensity with scan angle is expected. The uniformity of the scan-beam intensity is investigated both experimentally and numerically with the RCWA method. Figure 3.8 shows the simulated and measured diffraction efficiency of the optimal grating profile with a groove depth of 125nm as a function of grating in-plane rotation. The TM-polarized laser beam was used and the grating lines were initially aligned perpendicular to the plane of incidence. It is observed that the measurement results agree well

with the simulation results. The diffraction efficiency, and hence output scan-beam intensity when incident light power is stabilized, decreases slightly from the center to the end of scan. The intensity drop was found to be less than 8% with the grating in-plane rotation angle of $\pm 20^\circ$, which corresponds to an optical full scan angle of 51° . This is acceptable for many laser-scanning applications. For applications requiring highly uniform intensity of a scanned-beam, two methods can be utilized to overcome the problem. They are using a randomly or circularly polarized incident light or employing an active electro-optic feedback system to adjust the incident light power by sensing the non-scanning zeroth-order diffracted beam. The first method achieves uniform intensity at the expense of a decrease in total diffraction efficiency since low efficiency TE-polarized light is present in the system, while the second method eliminates scan intensity variation at the expense of increased system complexity and cost.

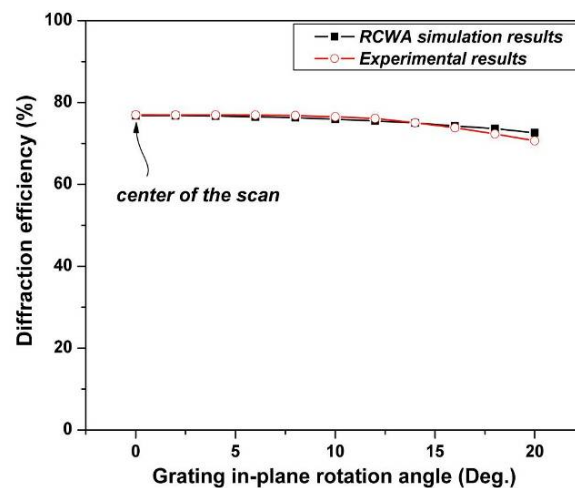


Figure 3.8 Simulated and measured diffraction efficiency of the optimal grating profile with a groove depth of 125nm as a function of grating in-plane rotation.

3.3 Actuation mechanisms for scanning gratings

Electrostatic comb-drive actuators are adopted in this study due to their outstanding advantages, such as high force density with little power consumption and zero heat dissipation due to zero steady-state current; structure simplicity resulting in high compatibility with micro fabrication process.

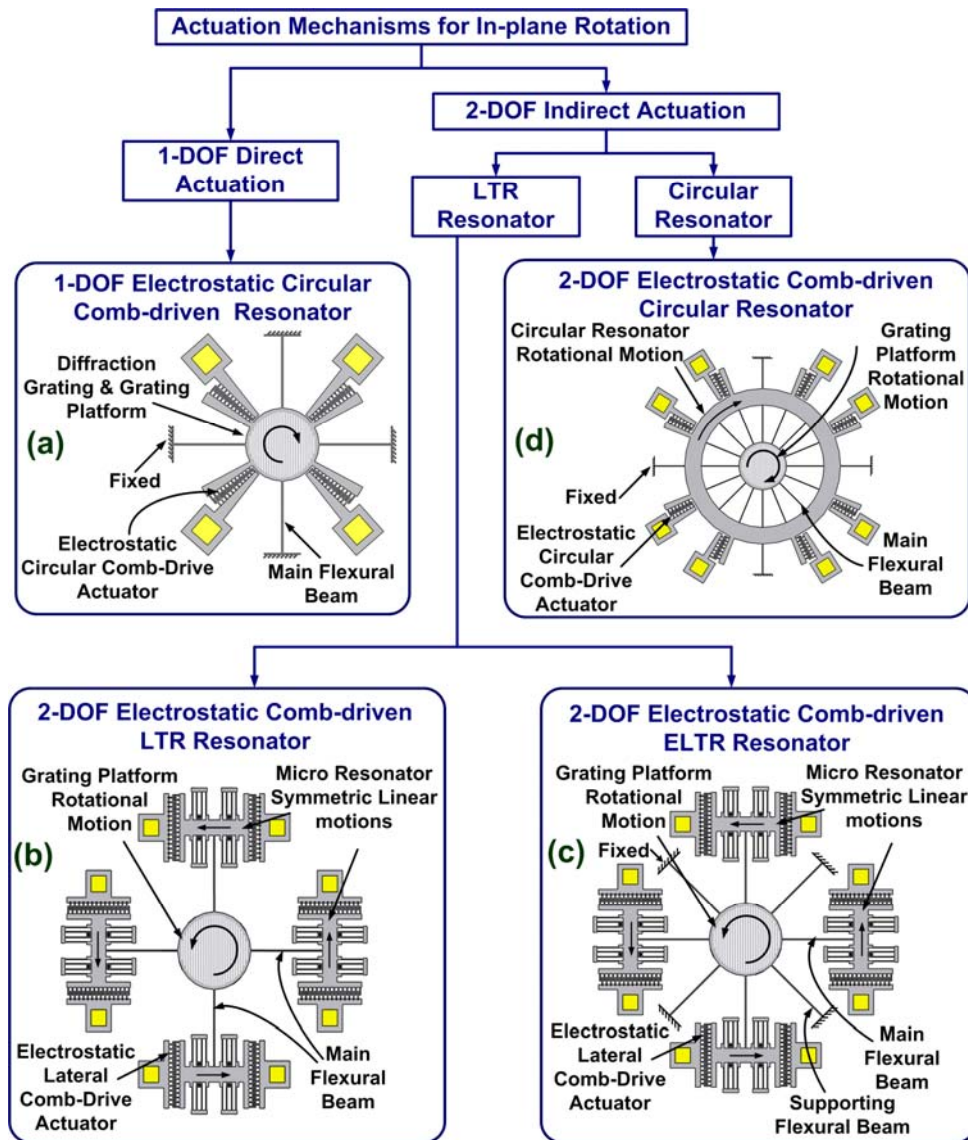


Figure 3.9 Actuation mechanisms for in-plane rotation: (a) 1-DOF electrostatic circular comb-driven resonator; (b) 2-DOF electrostatic comb-driven LTR resonator; (c) 2-DOF electrostatic comb-driven ELTR resonator and (d) 2-DOF electrostatic comb-driven circular resonator.

Figure 3.9 summarizes various actuation mechanisms, which can be used to generate in-plane rotational motion of the diffraction grating. As shown in Figure 3.9, micromachined diffraction gratings can be actuated either directly by one-degree-of-freedom (1-DOF) resonators or indirectly by 2-DOF resonators. Using a 1-DOF electrostatic circular comb-drive resonator (shown in Figure 3.9(a)) is the most straight forward method to generate the in-plane rotation. In a 1-DOF resonator, a diffraction grating platform is connected to substrate through several flexures and actuated directly by several sets of electrostatic circular comb-drive actuators. The in-plane rotational range of the grating platform is determined by the travel range of the circular comb-drive actuator, which is limited owing to pull-in of comb-fingers. This actuation mechanism will inevitably lead to small scanning angles with a large diameter diffraction grating. However, in many optical scanning applications, larger beam size is always preferred to achieve higher optical resolution.

In a 2-DOF resonator (shown in Figure 3.9 (b) to (d)), the diffraction grating platform is actuated by an outer resonator through several flexures. The outer resonator is suspended by several flexures and directly driven by electrostatic comb-drive actuators. Compared with 1-DOF resonators, the rotational range of the grating platform is no longer determined by the travel range of micro actuators but by the mode shape, which is defined as the ratio between the displacements/rotation angles of grating platform and outer resonator at the resonance, can be easily predefined by varying stiffness of flexures. The rotational range of the grating platform is then determined by the maximum allowable deformation of the flexural

suspension beams, which is the deformation when the internal maximum stress reaches their rupture limit. Without changing the total stiffness, hence maintaining the same resonant frequency, the internal maximum stress can be reduced by reducing the width of each flexural beam and increasing the total number of suspension beams.

According to the motion of the outer resonator, 2-DOF resonators can be further categorized as lateral-to-rotational (LTR) and circular types, as shown in Figure 3.9. In a LTR resonator, the rotational motion of the grating platform is excited by the synchronized linear motions of several electrostatic lateral comb-driven outer resonators through several flexural beams, shown in Figure 3.9(b). The LTR resonator has strong driving capability because the actuation force supplied by the lateral resonator can be easily increased by increasing the number of comb-fingers. Thus, it is very suitable for high-speed scanning. However, due to space limitation, the numbers of outer resonators and flexural suspensions are typically limited resulting in relatively small rotational range of the grating platform. This can be slightly improved by an enhanced LTR (ELTR) resonator, in which some extra supporting springs are added, shown in Figure 3.9(c). In addition, due to uncertainties and imperfections of the micro fabrication process, the resonant frequencies of the micro resonators are typically different, which can cause a variation of the diffraction grating's rotational center and marked performance deviations from the original design. Although this problem can be solved by adding feedback control to each individual micro-resonator, the complexity of the system will significantly increase.

The 2-DOF circular resonator is then developed to further increase the rotational range of the grating platform, shown in Figure 3.9(d). Under this driving scheme, the rotational motion of the grating platform is excited by outer circular resonator's rotation. The internal maximum stress in each flexural beam can be much lower because increasing the number of main flexural beams for this driving method is feasible. This results in a further increased rotational range of the grating platform. In addition, since only one micro resonator is adopted as compared to several symmetrically configured micro resonators, it will not encounter resonant frequency mismatch problem due to uncertainties and imperfections in the micro fabrication process. However, the 2-DOF circular resonator has a lower driving capability compared with the 2-DOF LTR resonator due to limited circular comb-fingers in the outer resonator.

In this dissertation, vibratory grating scanners actuated by 2-DOF LTR, ELTR and circular resonator are demonstrated in the following chapters.

3.4 Comprehensive dynamic models

Simplified analytical models and finite element (FE) simulations are two frequently used tools in the design of most MEMS devices. Simplified models could provide rapid performance predictions with limited accuracy. FE simulations of the whole structure are accurate but less efficient. In this section, comprehensive dynamic models of 2-DOF ELTR (also applicable to 2-DOF LTR resonators) and circular resonators, which could accurately and efficiently predict the dynamic performances, are established for scanner's structure

optimization. A simplified dynamic model based on ideal situation, such as weightless suspension springs, small and linear beam deformation and perfect fabrication process, is firstly established. Then, the model is modified by considering effects of practical factors, such as weight influence of micro suspension springs, fabrication imperfections and large deformation geometry nonlinearities.

3.4.1 Linear mode of a 2-DOF ELTR resonator

Figure 3.10 shows a typical 2-DOF electrostatic comb-driven ELTR resonator. As shown in the figure, a round platform is connected to the substrate through several supporting springs. Several electrostatic comb-drive resonators are attached symmetrically to the grating platform through one connection flexural beam on each of them. The lateral resonator is suspended by several fold-beam suspensions. Besides, each connection suspension spring contains a main flexural beam with several perpendicularly connected stress alleviation beams, which are used to reduce the axial stress of the main flexural beam during large deformation [128].

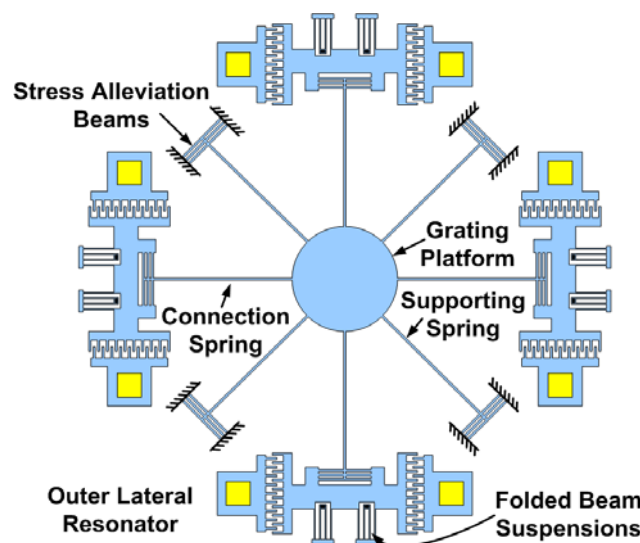


Figure 3.10 Schematic of a typical 2-DOF electrostatic comb-driven ELTR resonator.

3.4.1.1 Simplified analytical model of the 2-DOF ELTR resonator

The dynamics of a 2-DOF ELTR resonator can be simplified to a 2-DOF undamped spring-mass free vibration system under the following assumptions:

- 1) Deformations of all beams are small and linear.
- 2) All suspension springs are considered to be weightless.
- 3) Stress alleviation beams are considered to be ideal, which release the axial stress but have little influence on the total spring constant.

Figure 3.11 shows the 2-DOF undamped spring-mass free vibration system. The total kinetic energy of the system during vibration is:

$$E_k = n_c \frac{1}{2} m_o \dot{x}_o^2 + \frac{1}{2} J_{in} \dot{\theta}_R^2 \quad (3.3)$$

where n_c , m_o and x_o are the number, individual mass and displacement of lateral resonators respectively; J_{in} and θ_R are the moment of inertia and rotational angle of the grating platform.

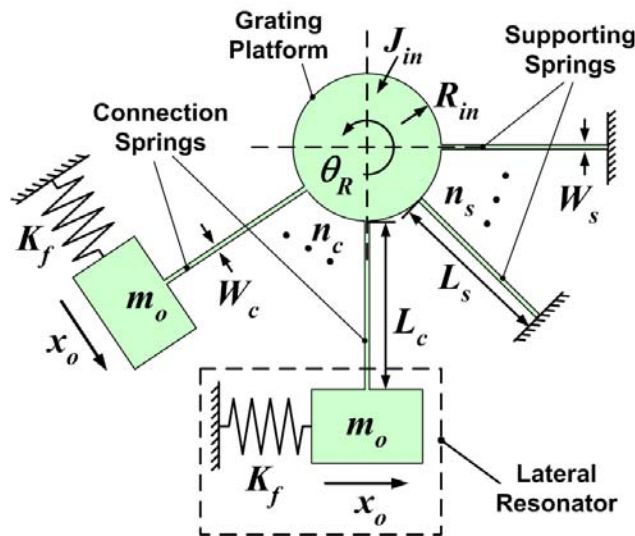


Figure 3.11 Schematic illustration of a simplified 2-DOF undamped spring-mass free vibration system.

Stiffness matrix of a single beam is adopted to calculate the potential energy of the suspension beam under deformation. Figure 3.12 shows the local variables defined for a single suspension beam.

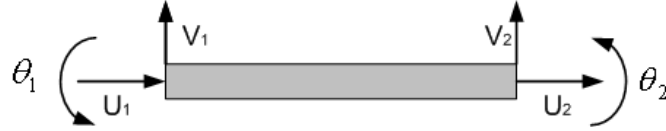


Figure 3.12 Local variables defined with respect to a suspension beam.

The stiffness matrix of the above beam is:

$$[k] = \frac{EI}{L^3} \begin{bmatrix} \frac{AL^2}{I} & 0 & 0 & -\frac{AL^2}{I} & 0 & 0 \\ 0 & 12 & 6L & 0 & -12 & 6L \\ 0 & 6L & 4L^2 & 0 & -6L & 2L^2 \\ -\frac{AL^2}{I} & 0 & 0 & \frac{AL^2}{I} & 0 & 0 \\ 0 & -12 & -6L & 0 & 12 & -6L \\ 0 & 6L & 2L^2 & 0 & -6L & 4L^2 \end{bmatrix} \quad (3.4)$$

where L , I and A are length, second moment and cross-sectional area of the beam and E is the Young's modulus of the material.

The corresponding vector of local variables is then:

$$\bar{u} = [u_1 \quad v_1 \quad \theta_1 \quad u_2 \quad v_2 \quad \theta_2]^T \quad (3.5)$$

Vectors of local variables for both connection beam and supporting beam under small deformation assumption are:

$$\begin{cases} \bar{u}_c = [0 & -x_o & 0 & 0 & -R_{in}\theta_R & \theta_R]^T \\ \bar{u}_s = [0 & 0 & 0 & 0 & -R_{in}\theta_R & \theta_R]^T \end{cases} \quad (3.6)$$

where R_{in} is the radius of the grating platform.

With everything in place, the potential energy E_p of the system is then:

$$E_p = n_c \frac{1}{2} K_f x_o^2 + n_c \frac{1}{2} \bar{u}_c^T [k_c] \bar{u}_c + n_s \frac{1}{2} \bar{u}_s^T [k_s] \bar{u}_s \quad (3.7)$$

where, K_f is the total spring constant of a lateral resonator's suspension; \bar{u}_c and \bar{u}_s are vectors of local variables of a connection and a supporting flexural beam; n_c and n_s are number of connection and supporting flexural beams; $[k_c]$ and $[k_s]$ are stiffness matrixes of a connection and a supporting flexural beam, shown below:

$$[k_c] = \frac{EI_c}{L_c^3} \begin{bmatrix} \frac{AL_c^2}{I_c} & 0 & 0 & -\frac{AL_c^2}{I_c} & 0 & 0 \\ 0 & 12 & 6L_c & 0 & -12 & 6L_c \\ 0 & 6L_c & 4L_c^2 & 0 & -6L_c & 2L_c^2 \\ -\frac{AL_c^2}{I_c} & 0 & 0 & \frac{AL_c^2}{I_c} & 0 & 0 \\ 0 & -12 & -6L_c & 0 & 12 & -6L_c \\ 0 & 6L_c & 2L_c^2 & 0 & -6L_c & 4L_c^2 \end{bmatrix}$$

and

$$[k_s] = \frac{EI_s}{L_s^3} \begin{bmatrix} \frac{AL_s^2}{I_s} & 0 & 0 & -\frac{AL_s^2}{I_s} & 0 & 0 \\ 0 & 12 & 6L_s & 0 & -12 & 6L_s \\ 0 & 6L_s & 4L_s^2 & 0 & -6L_s & 2L_s^2 \\ -\frac{AL_s^2}{I_s} & 0 & 0 & \frac{AL_s^2}{I_s} & 0 & 0 \\ 0 & -12 & -6L_s & 0 & 12 & -6L_s \\ 0 & 6L_s & 2L_s^2 & 0 & -6L_s & 4L_s^2 \end{bmatrix}$$

Since folded beam suspensions are used to suspend the lateral resonator, the total spring constant K_f can be expressed as:

$$K_f = n_f \frac{12EI_f}{L_f^3} \quad (3.8)$$

where, L_f and I_f are length and Second moment of area of beams in a folded beam suspension; n_f is the number of folded beams suspensions.

Applying the Euler-Lagrange formulation, the simplified model of the system is obtained:

$$\begin{bmatrix} n_c m_o & 0 \\ 0 & J_{in} \end{bmatrix} \begin{bmatrix} \ddot{x}_o \\ \ddot{\theta}_R \end{bmatrix} + \begin{bmatrix} n_c K_f + \frac{K_c}{c_2} & -\frac{c_1 K_c}{c_2} \\ -\frac{c_1 K_c}{c_2} & K_s + K_c \end{bmatrix} \begin{bmatrix} x_o \\ \theta_R \end{bmatrix} = 0 \quad (3.9)$$

where, K_c , K_s denote the rotational spring constants of all connection and supporting flexural beams, respectively:

$$K_c = n_c \frac{12EI_c}{L_c^3} (R_{in}^2 + L_c R_{in} + \frac{L_c^2}{3}) \quad \text{and} \quad K_s = n_s \frac{12EI_s}{L_s^3} (R_{in}^2 + L_s R_{in} + \frac{L_s^2}{3});$$

c_1 , c_2 are geometric coefficients:

$$c_1 = R_{in} + \frac{L_c}{2} \quad \text{and} \quad c_2 = R_{in}^2 + L_c R_{in} + \frac{L_c^2}{3};$$

I_c and I_s are area moment of inertia of connection and supporting flexural beams; W_c and W_s are beam widths of the connection and supporting flexural beams; T is the thickness of all flexural beams:

$$I_c = \frac{1}{12} W_c^3 T \quad \text{and} \quad I_s = \frac{1}{12} W_s^3 T.$$

where T is the thickness of the beam.

3.4.1.2 Weight influence of flexural beams

In a multiple springs suspended 2-DOF ELTR resonator, ignoring the mass of flexural beams can introduce significant errors while estimating resonant frequencies and mode shapes of the system. A FE simulation shows that if we ignore the mass of the flexural beams, the grating platform's moment of inertia estimation error increases from 18.4% to 51.1% when the number of the main flexural beams increases from 4 to 40.

In this section, the weight influence of flexural beams are modeled and added into the simplified analytical model shown in Eq. 3.9. Weight influence of connection flexural beams is investigated first. Figure 3.13 shows a schematic of a deformed connection flexural beam.

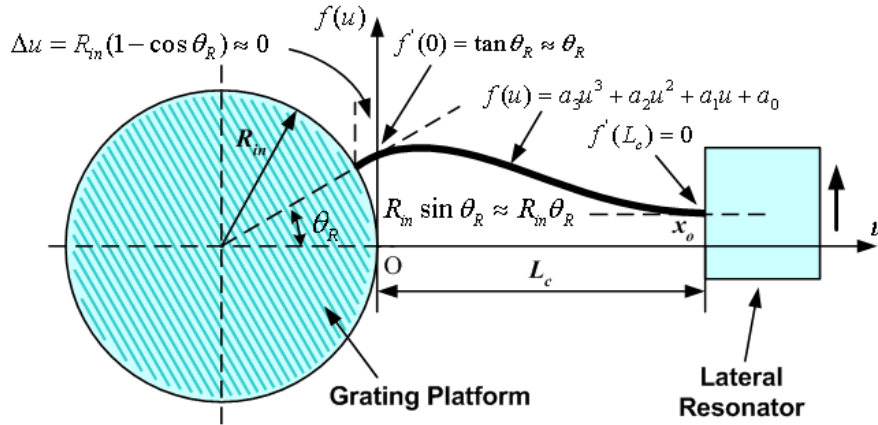


Figure 3.13 Schematic of a deformed connection flexural beam.

The deflection of the connection spring is approximated by a third order polynomial expression that fulfills the boundary conditions of the beam given below:

$$\begin{cases} f(0) = R_{in} \sin \theta_R \approx R_{in} \theta_R \\ f(L_c) = x_o \\ f'(0) = \tan \theta_R \approx \theta_R \\ f'(L_c) = 0 \end{cases} \quad (3.10)$$

The resultant deflection along the beam is a function of x_o and θ_R :

$$f(u) = \left(\frac{(2R_{in} + L_c)u^3}{L_c^3} - \frac{u^3}{L_c^2} - \frac{u^3}{L_c^2} + u + R_{in} \right) \theta_R + \left(\frac{3u^2}{L_c^2} - \frac{2u^3}{L_c^3} \right) x_o \quad (3.11)$$

The kinetic energy of vibrating connection flexural beams can be obtained:

$$\begin{aligned} \Delta E_{k_c} &= n_c \int_0^{L_c} \frac{1}{2} \dot{f}^2(u) dm = n_c \frac{1}{2} \rho_{Si} W_c T \int_0^{L_c} \dot{f}^2(u) du \\ &= n_c \frac{1}{2} \rho_{Si} W_c T L_c \left[\left(\frac{13}{35} R_{in}^2 + \frac{1}{105} L_c^2 + \frac{11}{105} L_c R_{in} \right) \dot{\theta}_R^2 - \frac{13}{35} \dot{x}_o^2 + \left(\frac{13}{210} L_c + \frac{9}{35} R_{in} \right) \dot{x}_o \cdot \dot{\theta}_R \right] \end{aligned} \quad (3.12)$$

The kinetic energy of vibrating supporting flexural beams can be obtained by letting $x_o = 0$:

$$\Delta E_{k_s} = n_s \frac{1}{2} \rho_{Si} W_s T L_s \left(\frac{13}{35} R_{in}^2 + \frac{1}{105} L_s^2 + \frac{11}{105} L_s R_{in} \right) \dot{\theta}_R^2 \quad (3.13)$$

Weight influence of folded beam suspensions can be obtained using similar method. A

deformed folded beam suspension is shown in Figure 3.14.

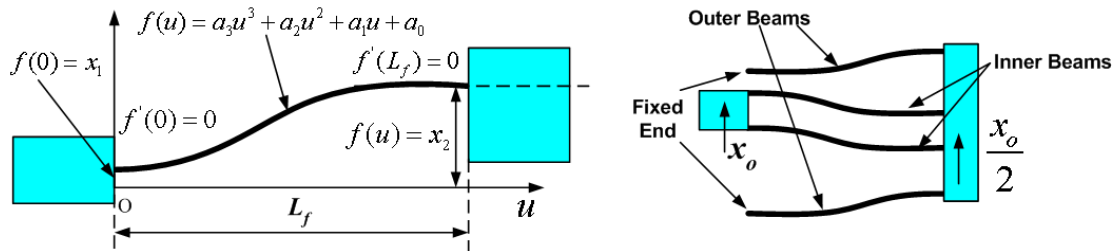


Figure 3.14 Schematic of a deformed folded beam suspension.

Deflection of the beam is also approximated by a third order polynomial expression that fulfills the boundary condition shown below:

$$\begin{cases} f_{inner}(0) = x_o, & f_{inner}(L_f) = \frac{x_o}{2} \\ f'_{inner}(0) = 0, & f'_{inner}(L_f) = 0 \end{cases} \text{ and } \begin{cases} f_{outer}(0) = 0, & f_{outer}(L_f) = \frac{x_o}{2} \\ f'_{outer}(0) = 0, & f'_{outer}(L_f) = 0 \end{cases} \quad (3.14)$$

The resultant deflection profile along the beam can be expressed as a function of x_o :

$$f_{inner}(u) = \left(\frac{2u^3}{L_f^3} - \frac{3u^2}{L_f^2} + 2 \right) \frac{x_o}{2} \text{ and } f_{outer}(u) = \left(\frac{3u^2}{L_f^2} - \frac{2u^3}{L_f^3} \right) \frac{x_o}{2} \quad (3.15)$$

The kinetic energy of vibrating folded beam suspensions can be computed as:

$$\begin{aligned} \Delta E_{k_f} &= 2n_f \int_0^{L_f} \frac{1}{2} [\dot{f}_{inner}^2(u) + \dot{f}_{outer}^2(u)] dm = n_f \rho_{St} W_f T \int_0^{L_f} [\dot{f}_{inner}^2(u) + \dot{f}_{outer}^2(u)] du \\ &= n_f \frac{1}{2} \rho_{St} W_f T L_f \frac{48}{35} \dot{x}_o^2 \end{aligned} \quad (3.16)$$

The modified total kinetic energy of the system \tilde{E}_k is then:

$$\tilde{E}_k = E_k + \Delta E_{k_c} + \Delta E_{k_s} + \Delta E_{k_f} \quad (3.17)$$

Applying the Lagrange formulation with the modified kinetic energy, dynamic model considering weight influence of flexural beams is obtained:

$$\begin{bmatrix} n_c m_o + n_c \Delta m_o & \Delta M \\ \Delta M & J_{in} + \Delta J_{in} \end{bmatrix} \begin{bmatrix} \ddot{x}_o \\ \ddot{\theta}_R \end{bmatrix} + \begin{bmatrix} n_c K_f + \frac{K_c}{c_2} & -\frac{c_1 K_c}{c_2} \\ -\frac{c_1 K_c}{c_2} & K_s + K_c \end{bmatrix} \begin{bmatrix} x_o \\ \theta_R \end{bmatrix} = 0 \quad (3.18)$$

where:

$$\Delta m_o = \rho_{Si} T \left(\frac{13}{35} W_c L_c + n_f \frac{48}{35} W_f L_f \right), \quad \Delta M = n_c \frac{1}{2} \rho_{Si} W_c T L_c \left(\frac{13}{210} L_c + \frac{9}{35} R_{in} \right),$$

$$\Delta J_{in} = \rho_{Si} T \left[n_c W_c L_c \left(\frac{13}{35} R_{in}^2 + \frac{1}{105} L_c^2 + \frac{11}{105} L_c R_{in} \right) + n_s W_s L_s \left(\frac{13}{35} R_{in}^2 + \frac{1}{105} L_s^2 + \frac{11}{105} L_s R_{in} \right) \right]$$

3.4.1.3 Influence of stress alleviation beams

Several stress alleviation beams were designed to release the axial stress of the main flexural beam by permitting some translational motion. This can help to eliminate the nonlinearity of the scanner. In an ideal case, the stress alleviation beams should have no effect on the linear harmonic solution. This is necessary as the rotation of the grating platform introduces tension in the suspension beams. Figure 3.15 shows FE simulation results of the improved torque-angle relationships with and without the addition of these stress alleviation beams compared to the ideal linear spring model.

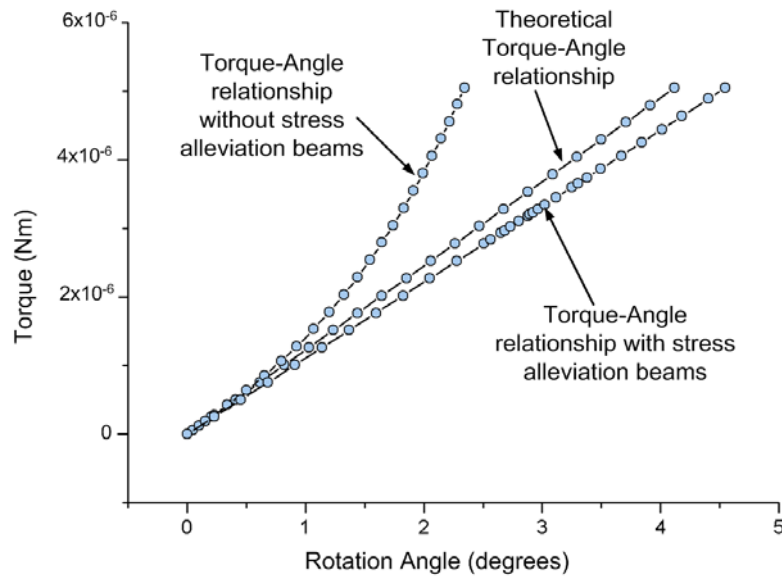


Figure 3.15 FE simulated torque-angle relationships of flexural beams.

Figure 3.16 shows FE simulation results of a set of deformed stress alleviation beams, which illustrates how the stress alleviation beams help in reducing stress at the anchor locations. More importantly, it shows a small tilt angle at the non-rigid anchor position, which reduces stiffness of flexural suspensions, thus affecting resonant frequencies of the system.

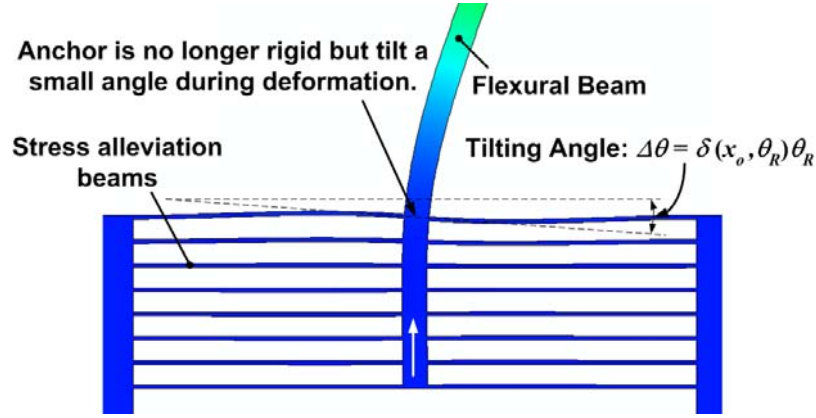


Figure 3.16 FE simulation results showing a set of deformed stress alleviation beams.

The stiffness reduction of suspension springs can be expressed using spring constant reduction coefficient, which are $\delta_c(x_o, \theta_R)$ and $\delta_s(\theta_R)$ for connection and supporting flexural beams, respectively. Although the reduction rate is a function of x_o and θ_R , it can be approximated by a constant and easily obtained through a simple FE simulation. Considering the stiffness reduction of flexural beams, the modified dynamic model (shown in Eq. 3.18) becomes:

$$\begin{bmatrix} n_c m_o + n_c \Delta m_o & \Delta M \\ \Delta M & J_{in} + \Delta J_{in} \end{bmatrix} \begin{bmatrix} \ddot{x}_o \\ \ddot{\theta}_R \end{bmatrix} + \begin{bmatrix} n_c K_f + \frac{\delta_c K_c}{c_2} & -\frac{c_1 \delta_c K_c}{c_2} \\ -\frac{c_1 \delta_c K_c}{c_2} & \delta_s K_s + \delta_c K_c \end{bmatrix} \begin{bmatrix} x_o \\ \theta_R \end{bmatrix} = 0 \quad (3.19)$$

3.4.1.4 Influence of micromachining imperfections

Fabrication imperfection is another very important issue needed to be addressed. The imperfections [129] in plasma etching process (such as etching slope, undercut and notching effect) will change the dimensions and area moment of the beams. This can induce significant change in the stiffness of the suspension beams and finally introduce significant error to the predictions of the natural frequency and mode shape. Figure 3.17 shows a cross-sectional profile model of the beam after DRIE process and a SEM image showing an etched trench obtained from pre-calibration processes. The etching undercut (ΔW_1) and the sidewall etching slope (α) have been included in this cross-sectional model. In addition, this cross-sectional model attempts to account for the notching effect as well, which is expressed by the thickness (T_n) and sidewall slope (α_n) of the notching area. Generally all the trenches at the both sides of suspension beams are designed to be the same to ensure the uniformity during the fabrication process. Hence, the parameters in the model can be directly obtained or calculated by using the measured width of the trench at different positions.

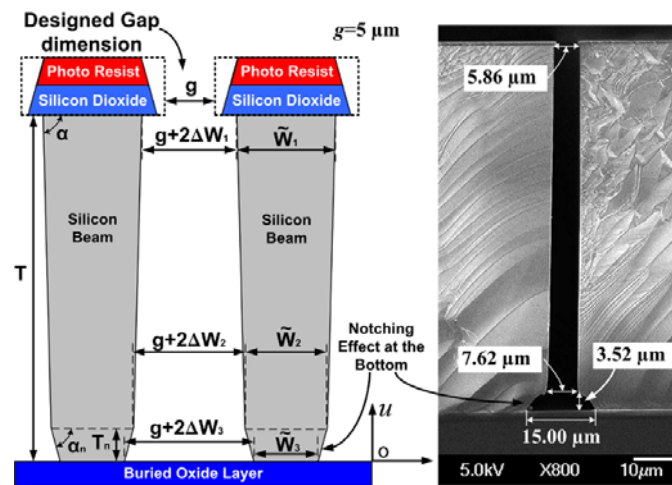


Figure 3.17 Cross-sectional profile model of the beam after DRIE process and SEM image showing an etched trench.

As shown in the SEM image in Figure 3.17, the width of the trench at its top, bottom, upper boundary and thickness of the notching area are measured so that actual widths \tilde{W}_i at different position of the beam can be calculated:

$$\tilde{W}_i = W - 2\Delta\tilde{W}_i \quad i = 1, 2, 3 \quad (3.20)$$

where, W is the designed width of the beam.

Slope angles at sidewall and notching area are calculated:

$$\begin{cases} \alpha = \arctg\left(\frac{T - T_n}{\Delta\tilde{W}_2 - \Delta\tilde{W}_1}\right) \\ \alpha_n = \arctg\left(\frac{T_n}{\Delta\tilde{W}_3 - \Delta\tilde{W}_2}\right) \end{cases} \quad (3.21)$$

Then, the actual beam width $W(u)$ can be expressed as a function of beam thickness:

$$\begin{cases} W(u) = \tilde{W}_3 + 2u \cdot \text{ctg}\alpha_n & 0 \leq u < T_n \\ W(u) = \tilde{W}_2 + 2u \cdot \text{ctg}\alpha & T_n \leq u < T \end{cases} \quad (3.22)$$

Therefore, the modified area moment of inertia \tilde{I} based on the above model is expressed as:

$$\tilde{I} = \frac{1}{96} \text{tg}\alpha_n (\tilde{W}_2^4 - \tilde{W}_3^4) + \frac{1}{96} \text{tg}\alpha (\tilde{W}_1^4 - \tilde{W}_2^4) \quad (3.23)$$

By using the modified area moment of inertia in the dynamic model, influence of fabrication imperfections is included.

3.4.2 Linear modeling of a 2-DOF circular resonator

Figure 3.18 shows a schematic illustration of 2-DOF circular resonator. As shown in Figure

3.18, a round inner platform is connected to the outer resonator through several connection flexural beams. Each of them has several pairs of perpendicularly connected stress alleviation beams, which are used to reduce its axial stress during large deformation. Among connection flexural beams, some of them are designed to be longer than the others in order to save space, namely type01 and type02 connection flexural beams. The outer circular resonator is suspended by symmetrically configured circular folded beam suspensions and driven by electrostatic circular comb-drive actuators.

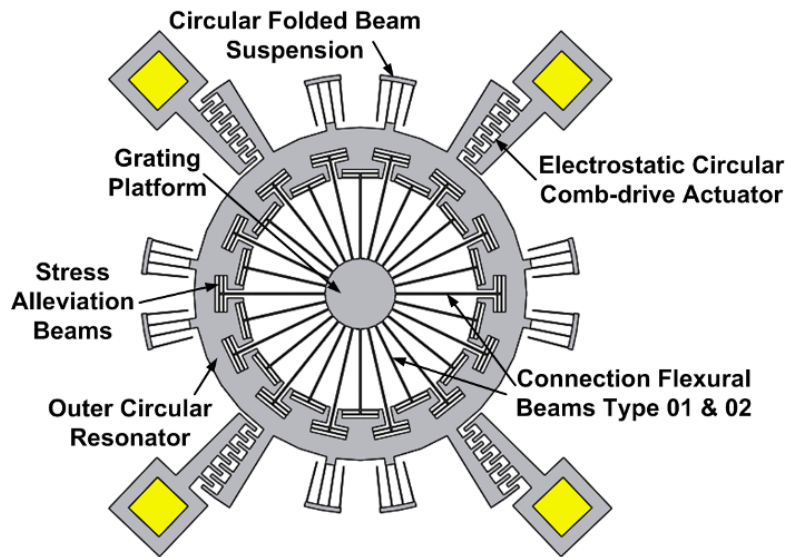


Figure 3.18 Schematic illustration of a 2-DOF circular resonator.

3.4.2.1 Modeling of connection flexural beams

We take advantage of the stiffness matrix (Eq. 3.4) of a single beam to obtain the model of the connection flexural beam. Figure 3.19 shows a model of a connection flexural beam and its corresponding local variables.

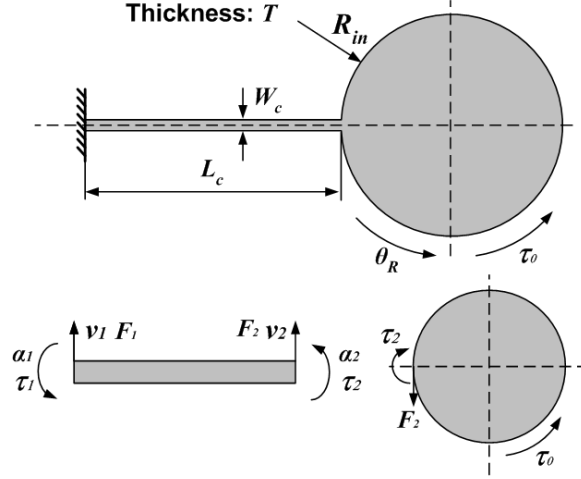


Figure 3.19 Model of the main flexural beam and its corresponding local variables.

As shown in Figure 3.19, when an external torque τ_0 is applied, the grating platform with a radius of R_{in} will rotate an angle of θ_R . The spring constant of one flexural beam can be expressed as the ratio of τ_0 to θ_R . The beam is assumed to have small deformations so that the axial deformation is ignored and the stress alleviation springs are not considered at the moment. The relationship between the local variables of force (F_1 , τ_1 , F_2 and τ_2) and displacement (v_1 , α_1 , v_2 and α_2) for a single beam can be expressed as:

$$\begin{bmatrix} F_1 \\ \tau_1 \\ F_2 \\ \tau_2 \end{bmatrix} = \frac{EI_c}{L_c^3} \begin{bmatrix} 12 & 6L_c & -12 & 6L_c \\ 6L_c & 4L_c^2 & -6L_c & 2L_c^2 \\ -12 & -6L_c & 12 & -6L_c \\ 6L_c & 2L_c^2 & -6L_c & 4L_c^2 \end{bmatrix} \begin{bmatrix} v_1 \\ \alpha_1 \\ v_2 \\ \alpha_2 \end{bmatrix} \quad (3.24)$$

where, L_c and I_c are beam length and area moment of inertia of the beam; E is the Young's modulus of the material.

Apply the boundary conditions shown in Figure 3.19 into Eq. 3.24, we can get:

$$\begin{bmatrix} F_1 \\ \tau_1 \\ F_2 \\ \tau_2 \end{bmatrix} = \frac{EI_c}{L_c^3} \begin{bmatrix} 12 & 6L_c & -12 & 6L_c \\ 6L_c & 4L_c^2 & -6L_c & 2L_c^2 \\ -12 & -6L_c & 12 & -6L_c \\ 6L_c & 2L_c^2 & -6L_c & 4L_c^2 \end{bmatrix} \begin{bmatrix} 0 \\ 0 \\ -R_{in}\theta_R \\ \theta_R \end{bmatrix} \quad (3.25)$$

Since the grating platform is in rotational equilibrium (shown in Figure 3.20), the external torque τ_0 can be expressed as:

$$\tau_0 = \tau_2 - F_2 R_{in} = \frac{EI_c}{L_c^3} (12R_{in}^2 + 12R_{in}L_c + 4L_c^2)\theta_R \quad (3.26)$$

Hence, the spring constant for one connection flexural beam k_c is:

$$k_c = \frac{EI_c}{L_c^3} (12R_{in}^2 + 12R_{in}L_c + 4L_c^2) \quad (3.27)$$

Since two types of the main flexural beams are adopted, the spring constant for each type, which is expressed as k_{ci} , is shown below:

$$k_{ci} = \frac{EI_{ci}}{L_{ci}^3} (12R_{in}^2 + 12R_{in}L_{ci} + 4L_{ci}^2) \quad (3.28)$$

Therefore, the total spring constant of all connection flexural beams, which is expressed as K_c , is shown below:

$$K_c = n_{c1}k_{c1} + n_{c2}k_{c2} \quad (3.29)$$

where, n_{c1} and n_{c2} are numbers of each type of connection flexural beams.

3.4.2.2 Modeling of circular folded beam suspensions

In a 2-DOF circular resonator, the outer resonator is suspended by circular folded beam suspensions. Figure 3.20 shows the schematic illustrations of a lateral folded beam and a

circular folded beam suspension.

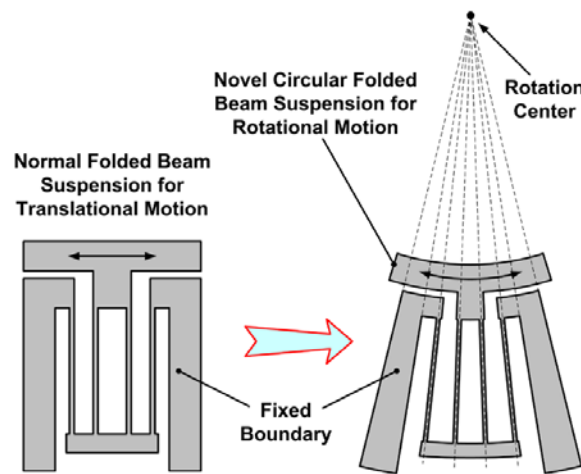


Figure 3.20 Schematic illustrations of a lateral folded beam and a circular folded beam suspension.

As shown in Figure 3.20, similar to the lateral folded beam suspension, one set of circular folded beam suspension is composed of four identical single beam flexures with one end connected to each other through a rigid truss structure. Two of them are connected to the movable structure and the other two are connected to the fixed boundary. However, the axial lines of the four beams are no longer parallel to each other but coincident with the rotation center and the rigid truss structure is also changed from a rectangular shape to a sector-annular shape.

Figure 3.21 shows the model of one set of circular folded beam suspension. As shown in Figure 3.21, beams numbered 1 & 2, 3 & 4 are connected in series respectively and the two sets of the serially connected beams are then connected in parallel. Since the dimensions of the four beams are same, the rotational spring constant of one set of circular folded-beam

suspension is equivalent to that of one single beam.

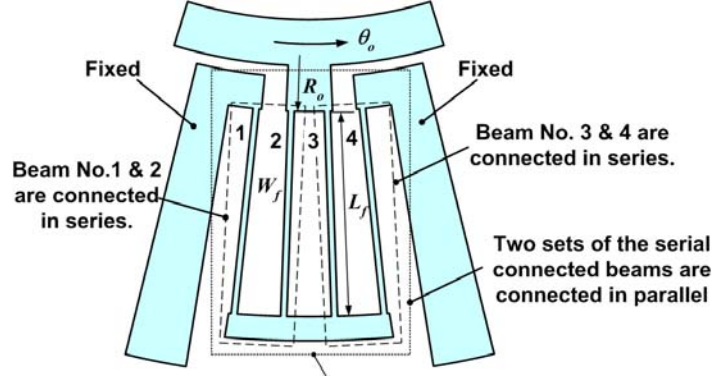


Figure 3.21 Model of one set of circular folded beam suspension.

According to Eq. 3.27, the total spring constant of circular folded beam suspensions is:

$$K_f = n_f \frac{EI_f}{L_f^3} (12R_o^2 + 12R_oL_f + 4L_f^2) \quad (3.30)$$

where L_f and I_f are length and area moment of inertia of the beam in circular folded beam suspension; R_o is the radius of outer circular resonator and n_f is the number of circular folded beam suspensions.

3.4.2.3 Simplified model of the 2-DOF circular resonator

Similar to 2-DOF ELTR resonators, the dynamics of 2-DOF circular resonators can be simplified to 2-DOF undamped spring-mass free vibration systems, shown in Figure 3.22, based on the following assumptions:

- 1) Deformations of all beams are small and linear.
- 2) All suspension springs are considered to be weightless.

- 3) Stress alleviation beams are considered to be ideal, which release the axial stress but have little influence on the total spring constant.

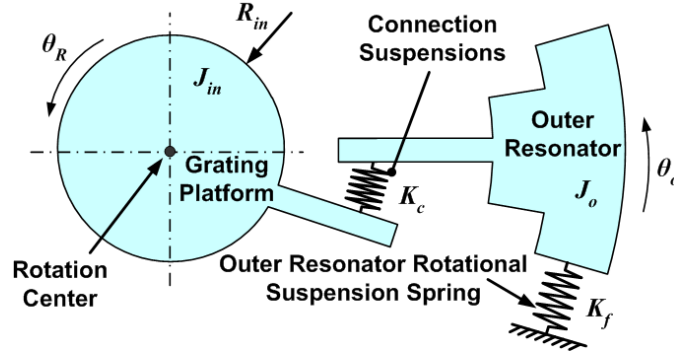


Figure 3.22 Schematic illustration of a simplified 2-DOF circular resonator.

The total kinetic and potential energy of the system during vibration, which are expressed as

E_k and E_p , respectively, are shown below:

$$\begin{cases} E_k = \frac{1}{2} J_{in} \dot{\theta}_R^2 + \frac{1}{2} J_o \dot{\theta}_o^2 \\ E_p = \frac{1}{2} K_c (\theta_R - \theta_o)^2 + \frac{1}{2} K_f \theta_o^2 \end{cases} \quad (3.31)$$

where J_{in} , R_{in} and θ_R are moment of inertia, radius and rotation angle of the inner grating platform and J_o , R_o and θ_o are moment of inertia, radius and rotation angle of the outer circular resonator.

Then, the simplified model of the system is obtained by applying the Euler-Lagrange formulation:

$$\begin{bmatrix} J_{in} & 0 \\ 0 & J_o \end{bmatrix} \begin{bmatrix} \ddot{\theta}_R \\ \ddot{\theta}_o \end{bmatrix} + \begin{bmatrix} K_c & -K_c \\ -K_c & K_f + K_c \end{bmatrix} \begin{bmatrix} \theta_R \\ \theta_o \end{bmatrix} = 0 \quad (3.32)$$

3.4.2.4 Weight influence of flexural beams

As discussed in section 3.4.1.2, ignoring the mass of flexural beams in a multiple springs suspended 2-DOF ELTR resonator can introduce significant errors while estimating dynamic performance of the system. The estimation error can be more significant for a 2-DOF circular resonator due to the increased number of connection flexural beams.

In this section, the mass of connection flexural beams and circular folded beam suspensions will be included into the dynamic model. Similar with section 3.4.1.2, the deformation profile of the beam suspension due to the rotation of both the grating platform and the outer circular resonator is considered. Figure 3.23 shows a deformed connection flexural beam.

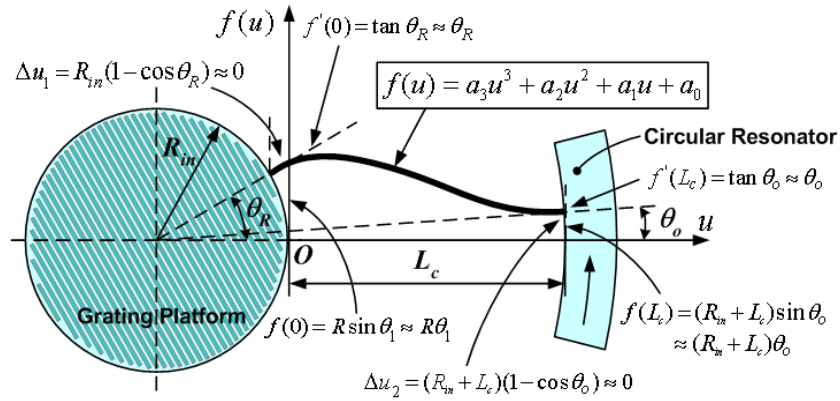


Figure 3.23 Schematic of a deformed connection flexural beam.

As shown in Figure 3.23, the deflection profile of a main flexural beam is approximated by a third order polynomial expression that satisfies the boundary conditions given below, where all the angles are assumed to be very small.

$$\begin{cases} f(0) = R_{in} \sin \theta_R \approx R_{in} \theta_R \\ f(L_c) = (R_{in} + L_c) \sin \theta_o \approx (R_{in} + L_c) \theta_o \\ f'(0) = \tan \theta_R \approx \theta_R \\ f'(L_c) = \tan \theta_o \approx \theta_o \end{cases} \quad (3.33)$$

The resultant deflection profile as a function of θ_R and θ_o is shown below:

$$f(u) = \left(\frac{2R_{in} + L_c}{L_c^3} u^3 - \frac{3R_{in} + 2L_c}{L_c^2} u^2 + u + R_{in} \right) \theta_R + \left(\frac{3R_{in} + 2L_c}{L_c^2} u^2 - \frac{2R_{in} + L_c}{L_c^3} u^3 \right) \theta_o \quad (3.34)$$

The kinetic energy brought by the vibrating connection flexural beams ΔE_k are:

$$\Delta E_k = \int_0^{L_c} \frac{1}{2} \dot{f}^2(u) dm = \frac{1}{2} \rho_{Si} W_c T \int_0^{L_c} \dot{f}^2(u) du \quad (3.35)$$

The total kinetic energy of connection flexural beams ΔE_{k_c} is then shown below:

$$\begin{aligned} \Delta E_{k_c} = & \frac{1}{2} \rho_{Si} T \sum_{i=1}^2 n_{ci} W_{ci} L_{ci} \left[\left(\frac{13}{35} R_{in}^2 + \frac{11}{105} R_{in} L_{ci} + \frac{1}{105} L_{ci}^2 \right) \dot{\theta}_R^2 \right. \\ & \left. + \left(\frac{13}{35} R_{in}^2 + \frac{67}{105} R_{in} L_{ci} + \frac{29}{105} L_{ci}^2 \right) \dot{\theta}_o^2 + \left(\frac{9}{70} R_{in}^2 + \frac{9}{70} R_{in} L_{ci} + \frac{1}{42} L_{ci}^2 \right) \dot{\theta}_R \dot{\theta}_o \right] \end{aligned} \quad (3.36)$$

The kinetic energy of the vibrating circular folded beam suspensions ΔE_{k_f} can be obtained

easily using Eq. 3.36 by applying corresponding boundary conditions:

$$\Delta E_{k_f} = \frac{1}{2} \rho_{Si} W_f T L_f \left(\frac{87}{70} R_o^2 + \frac{41}{42} R_o L_f + \frac{67}{210} L_f^2 \right) \dot{\theta}_o^2 \quad (3.37)$$

The modified total kinetic energy of the system \tilde{E}_k is then:

$$\tilde{E}_k = E_k + \Delta E_{k_c} + \Delta E_{k_f} \quad (3.38)$$

Applying the Lagrange formulation with the modified kinetic energy, a dynamic model

considering weight influence of flexural beams is obtained:

$$\begin{bmatrix} J_{in} + \Delta J_{in} & \Delta J \\ \Delta J & J_o + \Delta J_o \end{bmatrix} \begin{bmatrix} \ddot{\theta}_R \\ \ddot{\theta}_o \end{bmatrix} + \begin{bmatrix} K_c & -K_c \\ -K_c & K_f + K_c \end{bmatrix} \begin{bmatrix} \theta_R \\ \theta_o \end{bmatrix} = 0 \quad (3.39)$$

where:

$$\begin{aligned} \Delta J_{in} &= \rho_{Si} T \sum_{i=1}^2 n_{ci} W_{ci} L_{ci} \left(\frac{13}{35} R_{in}^2 + \frac{11}{105} R_{in} L_{ci} + \frac{1}{105} L_{ci}^2 \right), \\ \Delta J &= \rho_{Si} T \sum_{i=1}^2 n_{ci} W_{ci} L_{ci} \left(\frac{9}{70} R_{in}^2 + \frac{9}{70} R_{in} L_{ci} + \frac{1}{42} L_{ci}^2 \right), \\ \Delta J_o &= \rho_{Si} T \left[\sum_{i=1}^2 n_{ci} W_{ci} L_{ci} \left(\frac{13}{35} R_{in}^2 + \frac{67}{105} R_{in} L_{ci} + \frac{29}{105} L_{ci}^2 \right) + n_f W_f L_f \left(\frac{87}{70} R_o^2 + \frac{41}{42} R_o L_f + \frac{67}{210} L_f^2 \right) \right] \end{aligned}$$

3.4.2.5 Influence of stress alleviation beams and fabrication imperfections

Stress alleviation beams, which permit some translational motion, can help to release the tensile stress along the flexural beam without changing its stiffness, as discussed in section 3.4.1.3. However, the actual stress alleviation beams could reduce the stiffness of the beam due to the small tilt angle at the non-rigid anchor position.

To include the influence of stress alleviation beams, spring constant reduction coefficients of both types of connection beams are introduced into the dynamic model shown in Eq. 3.39. In 2-DOF circular resonators, spring constant reduction coefficients δ_{c1} and δ_{c2} can be easily obtained through simple FE simulations of a single connection flexural beam. The total spring constant of connection beams (Eq. 3.29) changes to:

$$\tilde{K}_c = n_{c1} \delta_{c1} k_{c1} + n_{c2} \delta_{c2} k_{c2} \quad (3.40)$$

Hence, the dynamic model considering the influence of stress alleviation beams is shown below:

$$\begin{bmatrix} J_{in} + \Delta J_{in} & \Delta J \\ \Delta J & J_o + \Delta J_o \end{bmatrix} \begin{bmatrix} \ddot{\theta}_R \\ \ddot{\theta}_o \end{bmatrix} + \begin{bmatrix} \tilde{K}_c & -\tilde{K}_c \\ -\tilde{K}_c & K_f + \tilde{K}_c \end{bmatrix} \begin{bmatrix} \theta_R \\ \theta_o \end{bmatrix} = 0 \quad (3.41)$$

Fabrication imperfections, such as the well-known under-cut, notching effect in plasma etching process, will also influence the dynamic performance of the system. Area moment of inertias of all fabricated flexural beams differ from their designed value. The modified area moment of inertia, shown in Eq. 3.23, has been worked out in section 3.4.1.3. By using the modified area moment of inertia, the influence of fabrication imperfections is included in the dynamic model.

3.4.3 Modeling of a 2-DOF circular resonator considering geometric nonlinearities

Although the stress alleviation beams can help to release the axial tensile stress in the connection flexural beams, the geometric nonlinearity cannot be fully eliminated when the rotational angle of the grating platform is large. A FE simulation was conducted to estimate restoring torques of a connection flexural beam at different half mechanical rotational angles of the grating platform. Both linear and nonlinear analyses were conducted and simulation results are shown in Figure 3.24. The geometric nonlinearity due to large deformation of the flexures was considered in the nonlinear analyses. Simulation results indicate that, as expected, when the rotational angle is small, the restoring torque remains linear and the geometric nonlinearity can be fully ignored. However, when the rotational angle is larger than 0.1arc (5.73°), the nonlinearity of the restoring torque appears and the geometric nonlinearity can no longer be ignored. The equation for nonlinear restoring torques as a function of rotation angle can be acquired by fitting polynomials to the simulated data points, which is

shown below:

$$\tilde{\tau} = k_c \theta + k_c \varepsilon \theta^3 \quad (3.42)$$

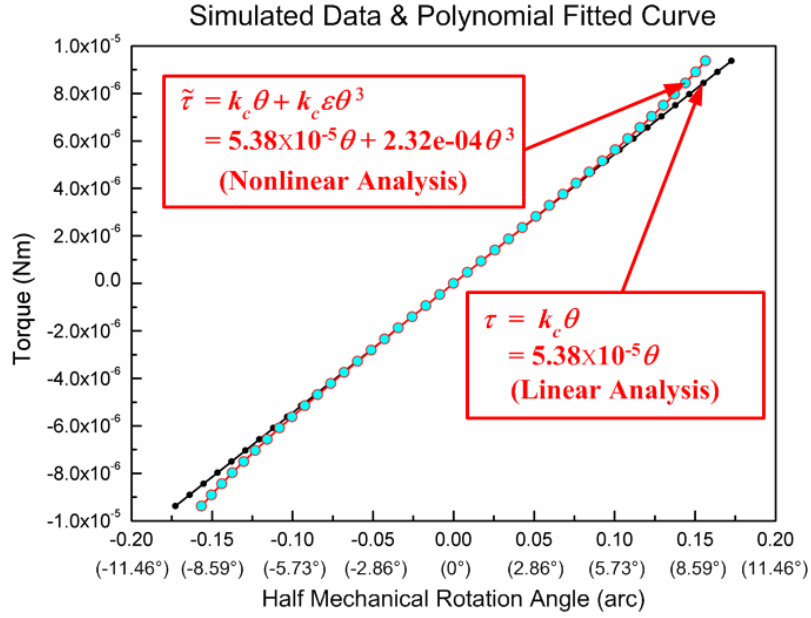


Figure 3.24 FE simulated torque-angle points and polynomial fitted curve of a connection flexural beam.

For 2-DOF circular resonators, which are designed for large scanning amplitudes, considerations of the geometric nonlinearity in the connection flexural beams are necessary.

In this section, a perturbation analysis is conducted to analyze the effects of the weakly nonlinear spring.

Figure 3.25 shows the schematic of a 2-DOF circular resonator with nonlinear connection suspensions.

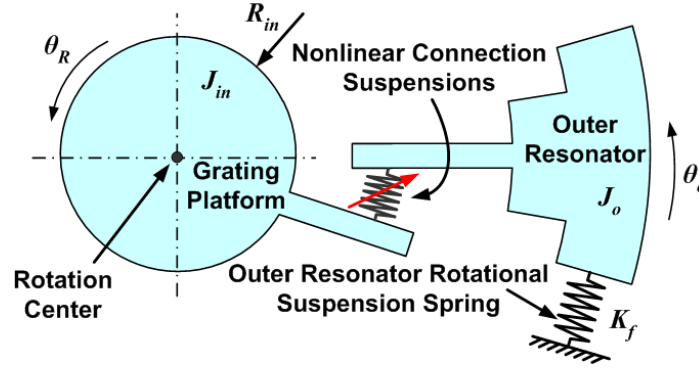


Figure 3.25 Schematic illustration of a 2-DOF circular resonator with nonlinear connection suspensions.

Generally, two types of connection beams are configured in a 2-DOF circular resonator and their corresponding nonlinear restoring torques are shown below:

$$\begin{cases} \tilde{\tau}_1 = k_{c1}\theta + k_{c1}\varepsilon_1\theta^3 \\ \tilde{\tau}_2 = k_{c2}\theta + k_{c2}\varepsilon_2\theta^3 \end{cases} \quad (3.43)$$

Then, the total nonlinear restoring torque $\tilde{\tau}$ for a given relative rotational angle θ between the diffraction grating and the outer resonator is shown below:

$$\tilde{\tau} = n_{c1}\tilde{\tau}_1 + n_{c2}\tilde{\tau}_2 = \tilde{K}_c\theta + \tilde{K}_c\varepsilon\theta^3 \quad (3.44)$$

where, the defined small parameter ε reflects the degree of nonlinearity in flexural beams; \tilde{K}_c is simulated spring constant of all connection flexural beams, which has included the influence of the stress alleviation beams. Besides, the influence of the fabrication imperfections can also be included by applying the etched beam profile in the FE model.

Then, the dynamic model considering geometric nonlinearity can be derived from Eq. 3.39 and Eq. 3.44 by replacing the total linear restoring torque with the total nonlinear restoring torque, shown below:

$$\begin{cases} J_{in}\ddot{\theta}_R + \Delta J\ddot{\theta}_o + \tilde{K}_c(\theta_R - \theta_o) + \tilde{K}_c\mathcal{E}(\theta_R - \theta_o)^3 = 0 \\ J_o\ddot{\theta}_o + \Delta J_c\ddot{\theta}_R + K_f\theta_o + \tilde{K}_c(\theta_o - \theta_R) + \tilde{K}_c\mathcal{E}(\theta_o - \theta_R)^3 = 0 \end{cases} \quad (3.45)$$

Defining $\omega_{10}^2 = \frac{\tilde{K}_c}{J_{in}}$, $\omega_{20}^2 = \frac{K_f}{J_o}$, $\mu_1 = \frac{\Delta J}{J_{in}}$ and $\mu_2 = \frac{J_o}{J_{in}}$, Eq. 3.45 can be expressed as:

$$\begin{cases} \ddot{\theta}_R + \mu_1\ddot{\theta}_o + \omega_{10}^2(\theta_R - \theta_o) + \omega_{10}^2\mathcal{E}(\theta_R - \theta_o)^3 = 0 \\ \ddot{\theta}_o + \frac{\mu_1}{\mu_2}\ddot{\theta}_R + \omega_{20}^2\theta_o + \frac{\omega_{10}^2}{\mu_2}(\theta_o - \theta_R) + \frac{\omega_{10}^2}{\mu_2}\mathcal{E}(\theta_o - \theta_R)^3 = 0 \end{cases} \quad (3.46)$$

The harmonic balance method [130] is used to solve Eq. 3.46. The periodic solutions are assumed to exist and expanded using Fourier series with ω_0 and only keeping the 1st order harmonic, which are shown below:

$$\begin{cases} \theta_R(t) = A_R \cos \omega_0 t \\ \theta_o(t) = A_o \cos \omega_0 t \end{cases} \quad (3.47)$$

where, A_R and A_o denote the rotational amplitudes of the diffraction grating and the outer resonator respectively.

Substitute Eq. 3.47 into Eq. 3.46, we have:

$$\begin{cases} \left[-A_R\omega_0^2 - A_o\omega_0^2\mu_1 + \omega_{10}^2(A_R - A_o) \right] \cos \omega_0 t + \omega_{10}^2\mathcal{E}(A_R - A_o)^3 \cos^3 \omega_0 t = 0 \\ \left[-A_o\omega_0^2 - A_R\frac{\mu_1}{\mu_2}\omega_0^2 + \omega_{20}^2 + \frac{\omega_{10}^2}{\mu_2}(A_o - A_R) \right] \cos \omega_0 t + \frac{\omega_{10}^2}{\mu_2}\mathcal{E}(A_o - A_R)^3 \cos^3 \omega_0 t = 0 \end{cases} \quad (3.48)$$

The item $\cos^3 \omega_0 t$ can be expanded to:

$$\cos^3 \omega_0 t = \frac{3}{4} \cos \omega_0 t + \frac{1}{4} \cos 3\omega_0 t \quad (3.49)$$

Substitute Eq. 3.49 into Eq. 3.48, we have:

$$\left\{ \begin{aligned} & \left[-A_R \omega_0^2 - A_0 \omega_0^2 \mu_1 + \omega_{10}^2 (A_R - A_0) + \frac{3}{4} \omega_{10}^2 \varepsilon (A_R - A_0)^3 \right] \cos \omega_0 t \\ & \quad + \frac{1}{4} \omega_{10}^2 \varepsilon (A_R - A_0)^3 \cos 3\omega_0 t = 0 \\ & \left[-A_0 \omega_0^2 - A_R \frac{\mu_1}{\mu_2} \omega_0^2 + \omega_{20}^2 + \frac{\omega_{10}^2}{\mu_2} (A_0 - A_R) + \frac{3\omega_{10}^2}{4\mu_2} \varepsilon (A_0 - A_R)^3 \right] \cos \omega_0 t \\ & \quad + \frac{\omega_{10}^2}{4\mu_2} \varepsilon (A_0 - A_R)^3 \cos 3\omega_0 t = 0 \end{aligned} \right. \quad (3.50)$$

The symbol φ is then defined to represent the mode ratio of the system, which is shown in Eq.

3.51 below:

$$A_R = \varphi A_o \quad (3.51)$$

Then, Eq. 3.52 below can be obtained by substituting Eq. 3.51 into Eq. 3.50 and order all the coefficients of the first harmonic component to be zero.

$$\left\{ \begin{aligned} & -\omega_0^2 \varphi - \omega_0^2 \mu_1 + \omega_{10}^2 (\varphi - 1) + \frac{3}{4} \omega_{10}^2 \varepsilon (\varphi - 1)^3 A_o = 0 \\ & -\omega_0^2 - \frac{\mu_1}{\mu_2} \omega_0^2 \varphi + \omega_{20}^2 + \frac{\omega_{10}^2}{\mu_2} (1 - \varphi) + \frac{3\omega_{10}^2}{4\mu_2} \varepsilon (1 - \varphi)^3 A_o = 0 \end{aligned} \right. \quad (3.52)$$

Solution of Eq. 3.52 yields the resonant frequencies f , rotational amplitudes A_{in} and A_o of the diffraction grating and the outer circular resonator as well as the optical scan angle θ_{opt} , as shown in Eq. 3.53 below:

$$\left\{ \begin{aligned} & f = \frac{\omega_0}{2\pi} = \frac{\omega_{20}}{2\pi} \sqrt{\frac{\mu_2}{\varphi + \mu_1 + \mu_2 + \mu_1 \varphi}} \\ & A_{in} = \varphi A_o \\ & A_o = \sqrt{\frac{\varphi^2 + \frac{(\mu_2 - 1)\omega_{10}^2 - \mu_2 \omega_{20}^2}{(1 + \mu_1)\omega_{10}^2} \varphi + \frac{(\mu_1 + \mu_2)\omega_{10}^2 + \mu_1 \mu_2 \omega_{20}^2}{(1 + \mu_1)\omega_{10}^2}}{\frac{3\varepsilon}{4} (\varphi + \frac{\mu_1 + \mu_2}{1 + \mu_1})(1 - \varphi)^3}} \\ & \theta_{opt} = 2C_{amp} A_{in} \end{aligned} \right. \quad (3.53)$$

where, C_{amp} is the magnification ratio between optical scan angle and the mechanical rotational angle of the diffraction grating, which can be obtained from Figure 3.4.

The calculated resonant frequencies with different optical scan angles are then normalized by their linear resonant frequencies f_{01} and f_{02} for both the first and the second resonating modes for easy comparison. The normalized resonant frequencies of both the resonating modes are denoted by S_1 and S_2 , which are shown in Eq. 3.54 below:

$$\begin{cases} S_1 = f / f_{01} \\ S_2 = f / f_{02} \end{cases} \quad (3.54)$$

The theoretical model predicts the variations for the resonant frequencies with different ε values of both the first and second resonating modes, which are shown in Figure 3.26.

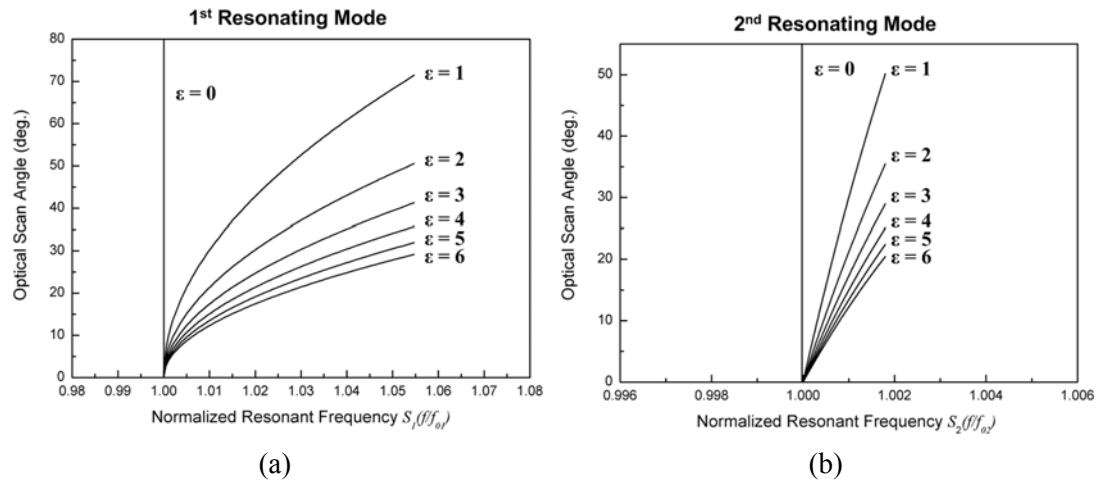


Figure 3.26 Theoretical predictions of the variation of resonant frequency with the optical scan angle of (a) the first and (b) the second resonating mode for different ε values.

It is seen that the resonant frequencies increase with increasing optical scan angle for both resonating modes and the amount of variation of the resonant frequency with the same optical

scan angle increases with increasing ε value due to the greater degree of nonlinearity.

3.5 Summary

In this chapter, optical efficiency, which is a key tenet against the adoption of the grating scanner, was successfully maximized using binary sub-wavelength diffraction grating with an optimized profile. Grating profile optimization through RCWA simulation demonstrated the theoretical possibility of high optical efficiency grating scanning. Fabrication of grating with different groove depth verified experimentally the simulation results. A diffraction efficiency of around 80%, which is closed to a coated mirror, was achieved using a TM-polarized light beam.

Improvements in structural design can increase the optical scanning performance of the vibratory grating scanner. Using the 2-DOF indirect actuation scheme, the scanning amplitude is no longer limited by the travel range of microactuators but by the mode shape design. In particular, the maximum stress in flexural beams can be minimized by using the 2-DOF circular resonator resulting in increased dynamic rotational amplitude. Besides, the singular outer circular resonator configuration eliminates resonant frequency mismatching in 2-DOF LTR resonators.

To assist the modeling and design of the driving resonators, comprehensive dynamic models of 2-DOF LTR and circular resonators were proposed. The model takes into account practical factors, such as weight of suspension springs, fabrication imperfection and large deformation geometrical nonlinearities, and is thus capable of providing accurate predictions of the

dynamic performances efficiently.

Chapter 4 Single-layered vibratory grating scanner: design, fabrication process and characterization

Depending on the location of the diffraction grating platform, MEMS vibratory grating scanners can be classified as being single-layered or double-layered. In a single-layered vibratory grating scanner, the grating platform is suspended by several suspension flexures at its edge and located in the same plane as its driving actuator. The major advantage of single-layered vibratory grating scanners is the simplicity of scanner structure and micromachining process. This chapter will introduce the design, micromachining process and characterization of three prototype single-layered vibratory grating scanners, which are driven by 2-DOF LTR, ELTR and circular resonator, respectively.

4.1 Single-layered grating scanner driven by 2-DOF LTR resonator

In this section, development of single-layered vibratory grating scanner driven by 2-DOF LTR resonator is presented. High optical efficiency of more than 75% is experimentally achieved with a simple gold-coated binary sub-wavelength grating. The prototype scanner with 1mm diameter diffraction grating is capable of achieving an optical scan angle of 13.7° with a 632.8nm wavelength incident laser beam at a scanning frequency of 20353Hz. The scanned beam quality and optical resolution is measured using stroboscopic method. Little dynamic deformation is observed and the measured optical resolution is around 310 pixels per-unidirectional scan. Compared with previous developed grating scanners [40-41], scanning performances, such as optical efficiency, scanning resolution and frequency, have

been significantly improved in this prototype.

4.1.1 Scanner design and simulation

Simplified schematic illustration of the developed single-layered vibratory grating scanner driven by 2-DOF LTR resonator is shown in Figure 4.1.

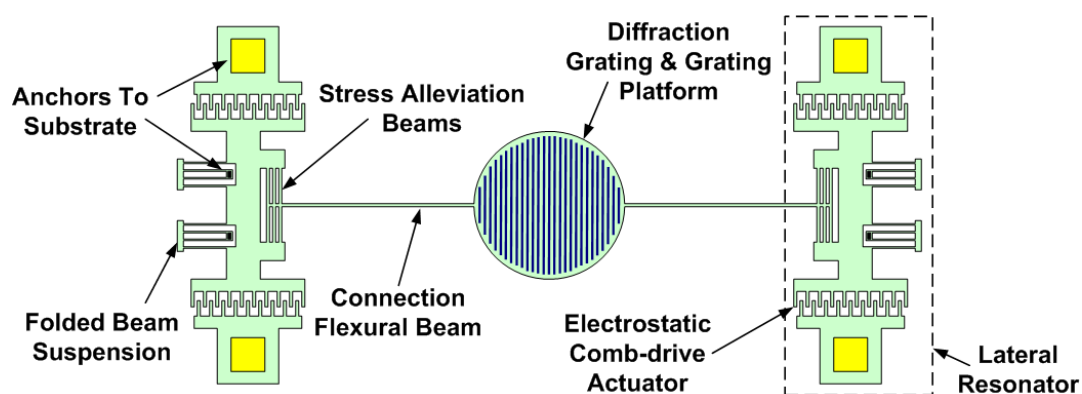


Figure 4.1 Schematic illustration of a single-layered vibratory grating scanner driven 2-DOF LTR resonator.

Two sets of electrostatic comb-driven lateral resonators are attached symmetrically opposite to a platform with a sub-wavelength diffraction grating through flexure suspensions. The diffraction grating has a diameter of 1mm. Each comb-drive resonator has a total number of 216 movable fingers on one side with finger length of $80\mu\text{m}$, width of $6\mu\text{m}$, thickness of $80\mu\text{m}$, finger gap of $3\mu\text{m}$, and initial finger overlap length of $40\mu\text{m}$. The comb-drive resonator is suspended by 23 sets of folded-beam suspensions with beams of length $182\mu\text{m}$, width $7.5\mu\text{m}$, and thickness $80\mu\text{m}$. The flexure suspension connecting the comb-drive resonator to the grating platform consists of a main flexure beam with beam length of $902\mu\text{m}$, width of $27\mu\text{m}$, and thickness of $80\mu\text{m}$, and the stress alleviation beams each having a length

of 376 μm , width of 6 μm , and thickness of 80 μm . The stress alleviation beams are transversely connected to the connection flexural beam allowing it to reduce its axial stress during large deformation, hence reducing the nonlinearity of the laser scanner.

Dynamic performances, such as resonant frequencies and mode shapes of the prototype scanner are predicted by the established comprehensive analytical model (refer to section 3.4.1) and FE simulations (type of analysis: natural frequency extraction, element type: C3D8R, number of elements: 109296, number of DOF: 6) using the commercial software package ABAQUSTM. Material properties of silicon used throughout the dissertation are shown in Table 4.1.

Table 4.1 Material properties of single crystal silicon.

Material	Parameter	Value
Silicon	Young's Modulus	169GPa
	Poisson's Ratio	0.28
	Density	2330Kg·m ⁻³

The prototype scanner is a 2-DOF vibration system, where two resonating modes are expected, namely 1st and 2nd mode. The mode shape can be defined as the ratio of the rotational angle of the grating platform to the lateral displacement of the micro resonator. Figure 4.2 shows FE simulated mode shapes of both resonating modes of the prototype scanner. Due to computing power limitations and the elaborate features in the actual device, the model used in FE simulations is simplified. Each comb-driven lateral resonator was simplified to an equivalent mass (rigid plate) supported by four flexure beams having the

same total spring constant as that of the original 23 sets of folded-beam suspensions. One end of each supporting flexural beams was fixed as the boundary condition in the simulation. The grating platform, flexure beams connecting the resonators to the platform and their associated stress alleviation springs were modeled as with the original device layout.

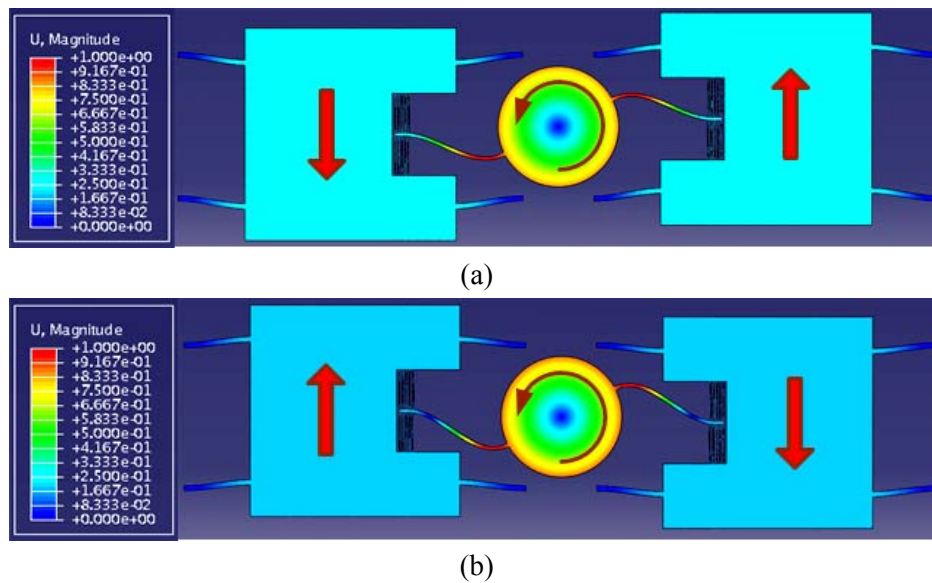


Figure 4.2 Mode shapes of (a) 1st and (b) 2nd resonating mode during vibration obtained using FE simulation.

The analytical predictions and FE simulation results of the natural frequencies and mode shapes of both resonating modes are compared in Table 4.2. Since the influence of the fabrication imperfections are very difficult to be included in FE simulations, analytical predictions with and without considering fabrication imperfections are made for easy comparison. The amount of the fabrication imperfections can be obtained from Figure 3.7. As shown in Table 4.2, theoretical predictions agree well with FE simulation results when the influence of fabrication imperfections is ignored. Moreover, resonant frequencies drop significantly when fabrication errors are considered.

Table 4.2 Comparison between theoretically predicted and FE simulated resonant frequencies as well as mode shapes of a 2-DOF LTR resonator driven single-layered grating scanner.

Mode		Ignoring fabrication imperfections		Theoretical prediction considering fabrication imperfections
		Theoretical prediction	FE simulation	
1 st Mode	Frequency (Hz)	27348	27314	24632
	Mode ratio (°/μm)	0.50	0.40	0.28
2 nd Mode	Frequency (Hz)	31807	31021	28768
	Mode ratio (°/μm)	-0.28	-0.54	-0.56

4.1.2 Fabrication process

The prototype device was fabricated using SOI micromachining technology. Figure 4.3 shows the fabrication process flow. The SOI wafer used in our process consists of an 80μm thick n-type heavily doped silicon device layer, a 2μm thick buried oxide (BOX) layer, and a 650μm thick silicon handle wafer. Total four photo masks were used in the fabrication.

The SOI wafer was firstly coated with a thin positive photoresist layer (resist type: AZ1505, thickness: 500nm) and the grating pattern with a period of 500 nm and grating duty circle of 50% was formed in the photoresist layer using deep-UV lithography. The grating pattern was then transferred to the silicon device layer using timed RIE process. The depth of the grating groove was controlled to around 125 nm to maximize the diffraction efficiency of the first-order diffraction beam. The photoresist layer was then stripped off and a 1μm thick undoped silicate glass (USG) layer was deposited on the SOI wafer surface. Next, the SOI wafer was again coated with photoresist (resist type: AZ6624, thickness: 2.4μm). After a

photolithography pattern transfer process, 1 μ m USG layer was patterned by a RIE process and the etching stopping on silicon device layer. A subsequent DRIE process etched the 80 μ m silicon device layer and stopped at BOX layer, which formed the vibratory grating platform, comb-drive resonators and flexural beams. The SOI wafer was then patterned on the backside, and a following DRIE etching removed completely the exposed silicon substrate stopping on the BOX layer. After that the scanner structure was released by etching the exposed BOX and USG layers using a BOE solution (buffered oxide etchant solution with 6 parts of 40% NH₄F and 1 part of 49% HF). A 20nm/500nm thick Cr/Au (Chromium/gold) layer was then deposited through the shadow mask to the selected areas on the SOI wafer to form the bond pads and electrical routing wires. Finally, a 10nm/80nm thick Cr/Au was sputtered on the wafer surface to enhance the reflectivity of the optical grating.

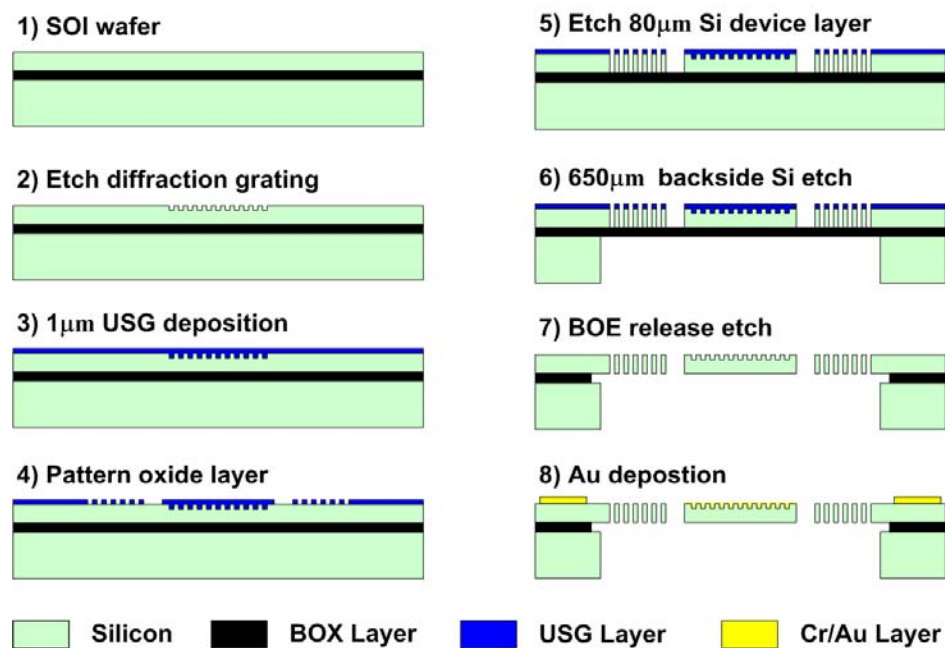


Figure 4.3 Fabrication process of the prototype 2-DOF LTR resonator driven single-layered vibratory grating scanner.

Figure 4.4(a) shows the fabricated sub-wavelength diffraction grating with a period of 500nm and a duty cycle of 50%. SEM image of the fabricated prototype 2-DOF LTR resonator driven single-layered vibratory grating scanner is shown in Figure 4.4(b).

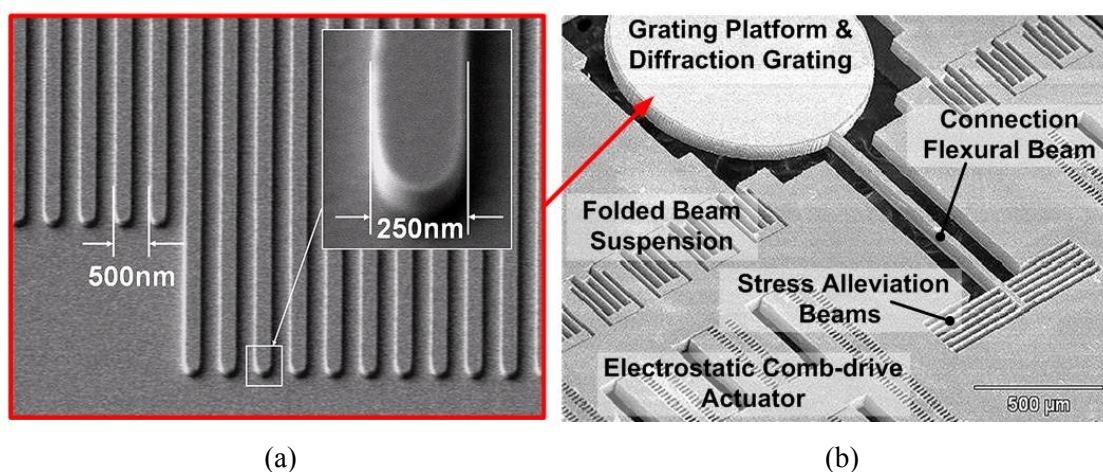


Figure 4.4 SEM images showing (a) sub-wavelength diffraction grating with a period of 500nm and a duty cycle of 50%; (b) center part of the prototype 2-DOF LTR resonator driven single-layered vibratory grating scanner.

4.1.3 Experimental characterizations

The optical performance of the MEMS grating scanner was tested using a linearly polarized 632.8nm wavelength He-Ne laser beam at the optimal bow-free incident angle of 28.4°. High optical efficiency laser scanning (more than 75% of incident beam can be used for laser scanning) was experimentally demonstrated with the TM-polarized laser beam. Figure 4.5 shows a projected scan-line on a screen located at a distance of 200mm from the grating scanner and schematic illustration of the experimental setup. The screen normal was aligned parallel to the direction of the first-order diffracted beam when the grating is at rest. The MEMS grating scanner was operated in air and each comb-drive resonator was driven by a

push-pull mechanism [131] with 45V DC bias and 84V AC peak-to-peak voltages at a driving frequency of 20353Hz (close to the resonant frequency of the first vibration mode). The optical scan angle is estimated to be around 13.7°.

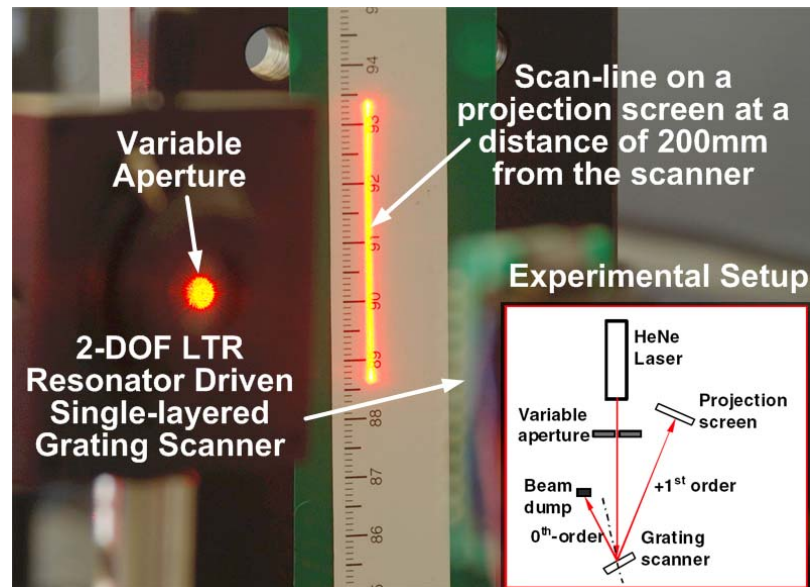


Figure 4.5 Photograph shows the scanning trajectory and the inset shows a schematic illustration of the experimental setup.

As expected, the MEMS grating scanner has two vibration/scanning modes. The measurement results, theoretical predictions by comprehensive analytical model and FE simulation results are summarized in Table 4.3.

As shown in Table 4.3, the measured resonant frequencies are lower than FE simulation results due to the well-known fabrication imperfections. Theoretical predictions considering fabrication imperfections agree well with measurement results, indicating the validity of the comprehensive dynamic model established in section 3.4.1.

Table 4.3 Summary of theoretically predicted, FE simulated and measured resonant frequencies as well as mode shapes of the prototype 2-DOF LTR resonator driven single-layered grating scanner.

Mode		FE simulations ignoring fabrication imperfections	Theoretical predictions considering fabrication imperfections	Experimental measurements
1 st Mode	Frequency (Hz)	27314	24632	20353
	Mode ratio ($^{\circ}/\mu\text{m}$)	0.40	0.28	0.24
2 nd Mode	Frequency (Hz)	31021	28768	25962
	Mode ratio ($^{\circ}/\mu\text{m}$)	-0.54	-0.56	-0.65

The frequency response of the grating scanner was obtained by measuring the length of the scan-line on the projection screen while sweeping the driving frequency around the two resonant frequencies of the device. The DC bias and AC peak-to-peak voltages were fixed at 45 V and 84 V, respectively.

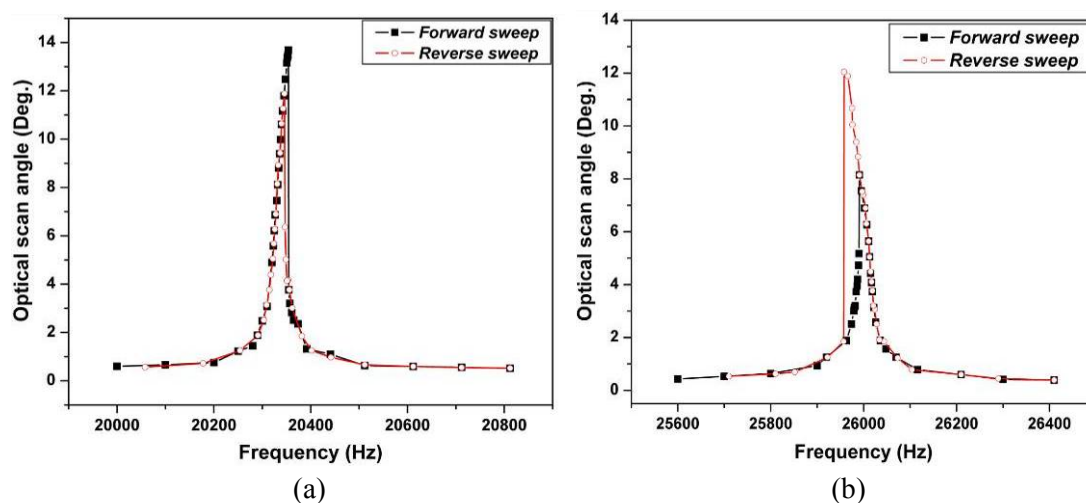


Figure 4.6 Frequency responses of prototype 2-DOF LTR resonator driven single-layered grating scanner at frequency regions near the resonant frequencies of (a) 1st and (b) 2nd resonating modes.

Figures 4.6(a) & (b) show frequency responses of the scanner at frequency regions close to the resonant frequencies of the 1st and 2nd resonating modes, respectively. Although the scanner demonstrated some level of large-deflection vibration nonlinearity, i.e., the optical scan angle is different during forward sweep and reverse sweep, the effectiveness of reducing the large-deflection vibration nonlinearity using stress alleviation beams is apparent, compared to previously developed prototype without stress alleviation beams [41].

The scanned-beam quality and resolution of the prototype scanner is tested using stroboscopic method. The incident laser beam from the He-Ne laser was strobed using an acousto-optic modulator (AOM) to produce light pulses with a full-width-half-maximum (FWHM) pulse duration of 25ns synchronized to the device driving signal to ‘freeze’ the motion of the scanning beam. The schematic illustration of the experimental setup is shown in Figure 4.7.

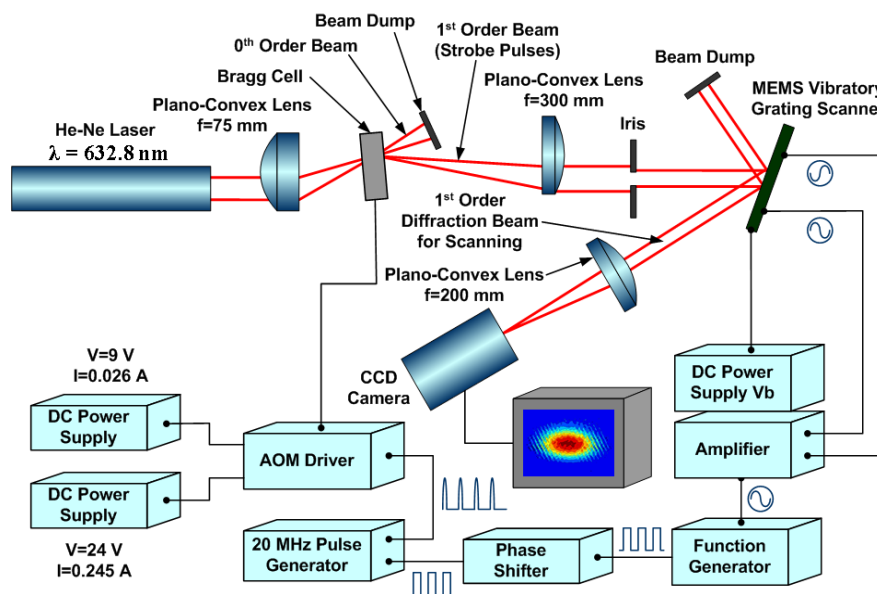


Figure 4.7 Schematic illustration of experimental setup to investigate the scanned-beam quality and optical resolution using stroboscopic method.

To enhance the response time of the AOM, the output beam of the He-Ne laser was focused into the Bragg cell through a 75mm plano-convex lens to reduce the time required for acoustic pulse packets to transmit through the optical beam. The strobed first-order diffraction beam from the Bragg cell was then collimate using a 300mm plano-convex lens and directed to the MEMS grating scanner at the bow-free incident angle of 28.4° . The first-order beam diffracted from the scanner was then focused onto a CCD camera by a 200mm focusing lens. The strobed beam positions were controlled by adjusting the phase difference between the strobe-pulses and the AC driving signal. The scanner was operated in atmosphere and driven by push-pull mechanism with 45 V DC bias and 84 V AC peak-to-peak voltages at the first resonant frequency of 20353Hz. Figure 4.8 shows a photograph of the actual experimental setup.

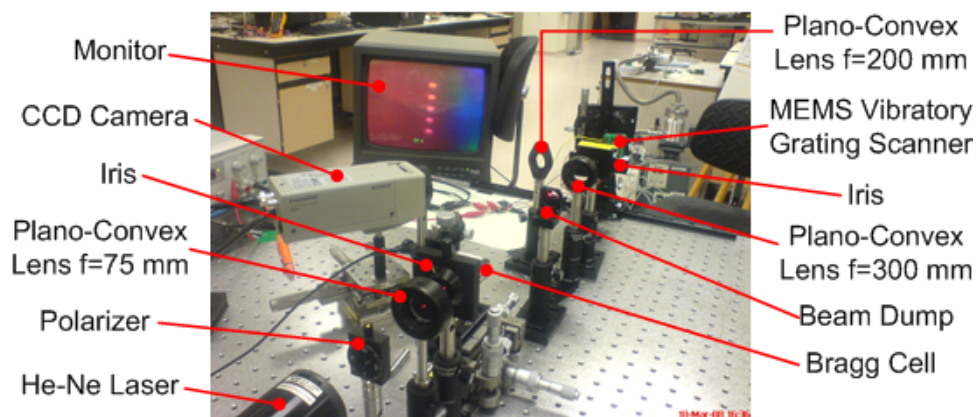


Figure 4.8 Photograph of actual experimental setup investigating the scanned-beam quality and optical resolution using stroboscopic method.

Figure 4.9 shows the two-dimensional contour plots of the light intensity distribution of the focal spots captured by the CCD camera at four different regions along the scan line, namely at the upper extreme position, two-third and one-third of the scan amplitude, and the center of

the scan.

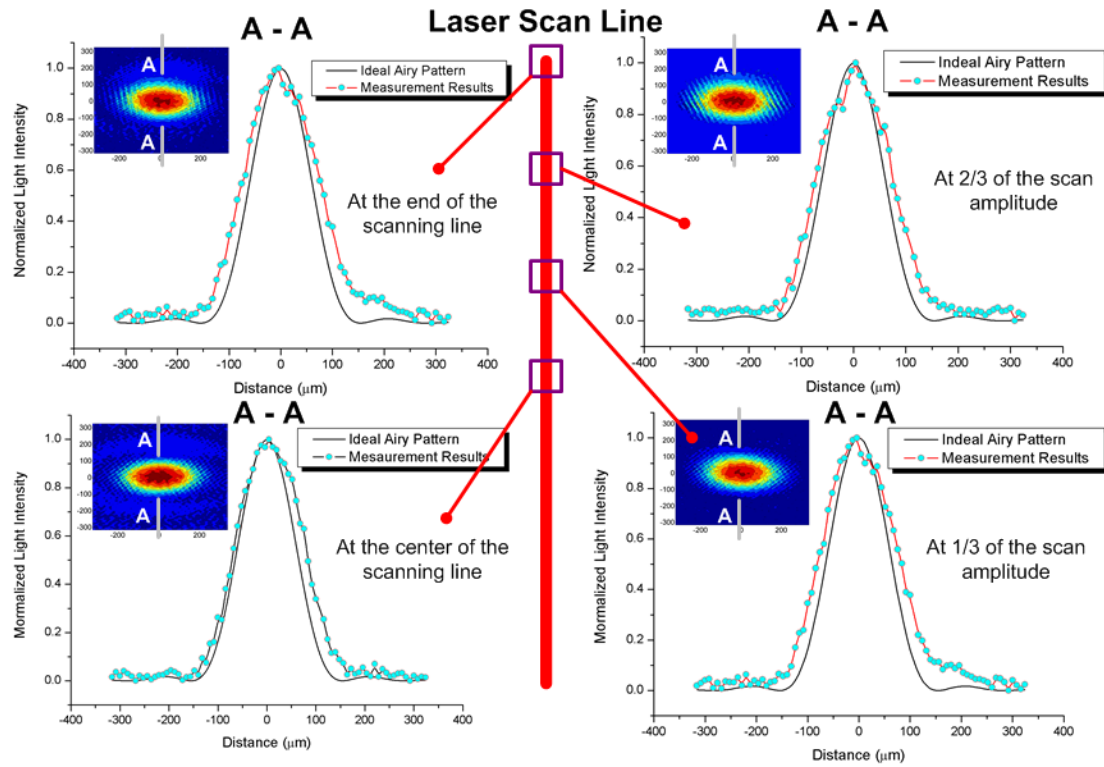


Figure 4.9 Light intensity distribution of the focal spots captured by CCD camera.

Normalized intensity profiles along a vertical line (scan direction) through the center of the strobed spots were also plotted in the figure. It is observed that the size and shape of the laser spots are almost the same at different locations. The intensity profiles of the laser focal spots match closely to the theoretical diffraction pattern calculated assuming a uniform illumination of the diffraction grating with no dynamic deformation. The average FWHM diameter of the focal spots was determined to be about $155\mu\text{m}$ along the scan direction, representing an overall scanned optical resolution of roughly 310 pixels per unidirectional scan.

4.2 Single-layered grating scanner driven by 2-DOF ELTR resonator

To increase the scanning speed, a 2-DOF ELTR resonator driven single-layered vibratory grating scanner with a backside thinned grating platform is developed. The grating platform is thinned by a round cavity and reinforced by a circular frame, which are fabricated using single mask delay etching (SMDE) technique. This section presents the design, simulation, fabrication process and characterization of the high-speed MEMS grating scanner as well as the principle and applications of the SMDE technique. When illuminated with a 635nm wavelength incident laser beam, the prototype scanner with a 1mm diameter diffraction grating is capable of scanning at 50192Hz with an optical scan angle of 14.1°. Compared with the prototype scanner discussed in section 4.1, there is a 1.5 times increase of the scanning speed with the same grating diameter and optical scan angle.

4.2.1 Single mask delay etching technique

The single mask delay etching (SMDE) technique utilizes the non-uniformity of the DRIE process, due to its well-know loading effects, to regulate the etching rate of a prescribed area by using one specially designed photo mask. In the photo mask, the original etching region is partitioned into different sections using some narrow dummy line patterns according to the required etching rate. In order to implement the SMDE technique, etching rates of trenches with different widths using the DRIE process were investigated. Figure 4.10 shows the measured averaging etching rates (over 4 hours) as a function of the trench width, which varies from 20 μ m to 1000 μ m. A masking photoresist layer (MEGAPOSITTM SPRTM 220) with a thickness of 10 μ m was used. The parameters of the DRIE process are summarized in Table

4.4.

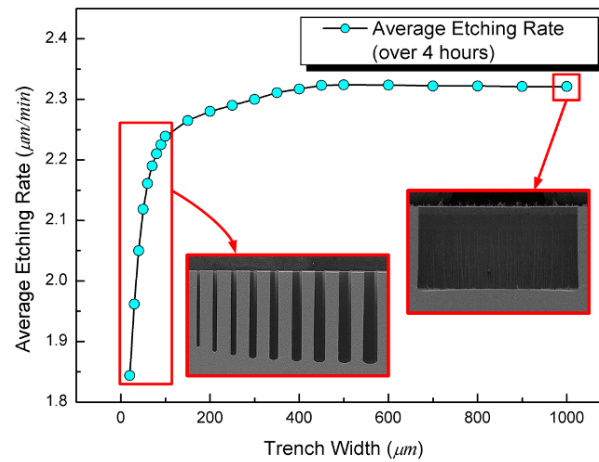


Figure 4.10 Average etching rates (over 4 hours) as a function of the trench width.

Table 4.4 DRIE process parameters of anisotropic silicon etching.

Process Step	Gas Flow (sccm)			Power(W)		Cycle Time (s)
	C ₄ F ₈	SF ₆	O ₂	Coil	Platen	
Etch	0	130	13	600	23	8
Passivate	110	0	0	600	0	5

As shown in Figure 4.10, the average etching rate increases significantly with increasing trench width when the trench width is less than 200μm, and remains unchanged when the trench width is around 200μm to 600μm. Moreover, the average etching rate drops when the trench width is over 600μm. This is because the micro loading is the major effect of the DRIE process while etching narrow trenches. When the etching trench is wide, the macro loading becomes the major effect. Figure 4.11 shows white light interferometer-measured bottom profiles of trenches with different trench widths. As shown in Figure 4.11, when the trench is 100μm wide, the bottom profile is concave shaped. With increasing trench widths, the bottom profiles vary from the concave shape to the convex shape accordingly and the convexity of a

wider trench is more significant.

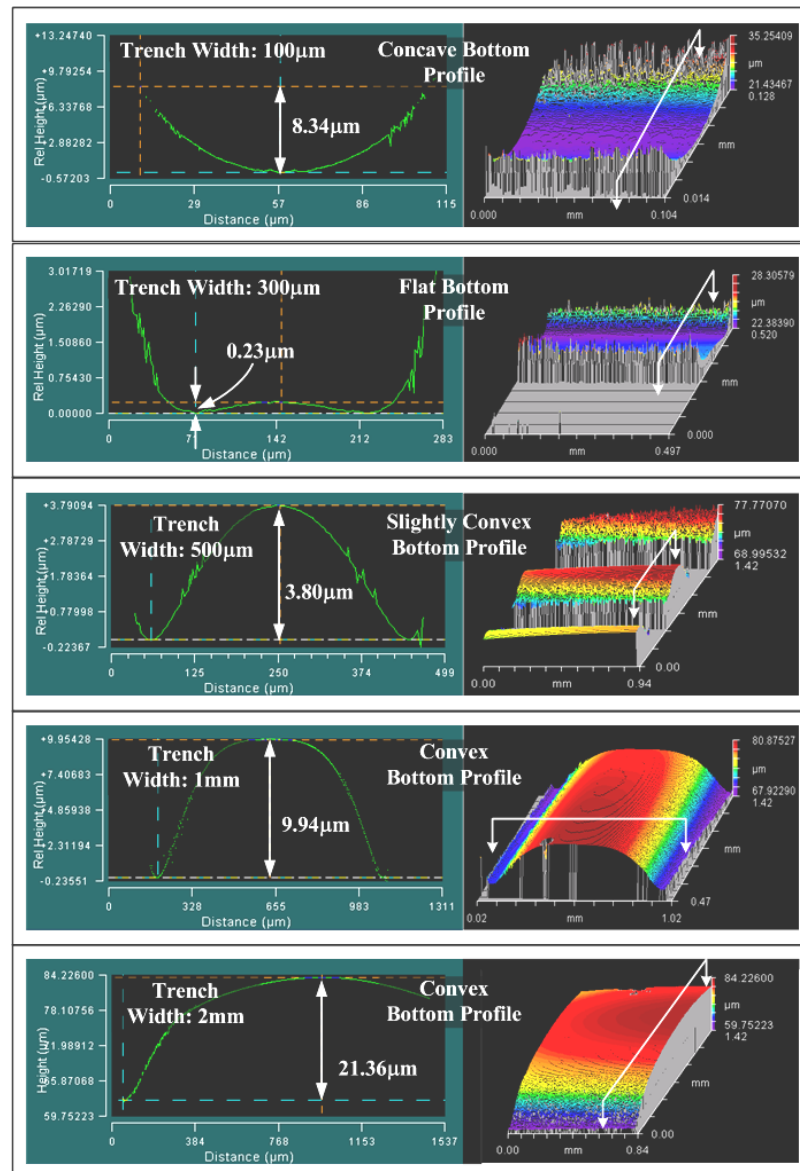


Figure 4.11 White light interferometer measured bottom profiles of trenches with different trench widths, which are formed by a 4 hour DRIE process.

The SMDE technique can be used in the SOI micromachining process to create discrete step structures in a silicon device layer through the multi-step DRIE process. The schematic illustration of the fabrication process is shown in Figure 4.12. As shown in Figure 4.12, the wafer backside is patterned using a specially designed photo mask and etched using the DRIE

process. The whole etching region is partitioned into several sub-regions and each region is further divided by some dummy fin structures. The etching rate of each sub-region is determined by the trench width between the dummy fin structures. Then a recess silicon etching process, which is more isotropic, is used to remove all dummy fin structures. The process parameters of the silicon recess etching are shown in Table 4.5. After that, the multi-step structures are formed and some level of the step structures can be transferred from the silicon substrate to the silicon device layer through a subsequent DRIE process. Finally, the multi-level structure (shown in Figure 4.12, 5th step) can be realized. This process is very useful while fabricating MEMS devices like the micromirror laser scanner, which requires a thin torsional spring but a thick mirror body with a reinforcement frame on its backside. In this study, the SMDE technique was used to form a round cavity to reduce the rotary inertia of the grating platform.

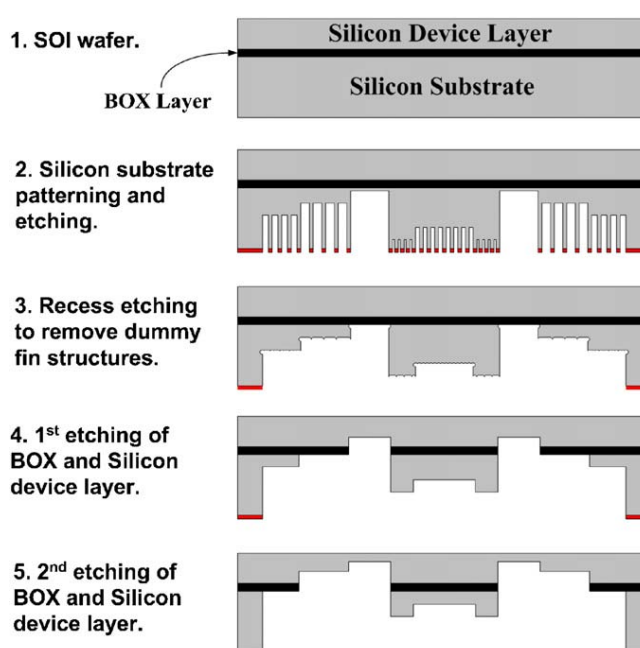


Figure 4.12 Schematic of the multi-level step structures on a SOI wafer formed using the SMDE technique.

Table 4.5 DRIE process parameters of isotropic silicon recess etching.

Process Step	Gas Flow (sccm)			Power(W)		Cycle Time (s)
	C ₄ F ₈	SF ₆	O ₂	Coil	Platen	
Etch	0	250	25	500	30	14
Passivate	110	0	0	500	0	5

The capabilities of forming multi-level step structures using the SMDE technique were experimentally demonstrated. SEM images of fabricated single step circular structures are shown in Figure 4.13.

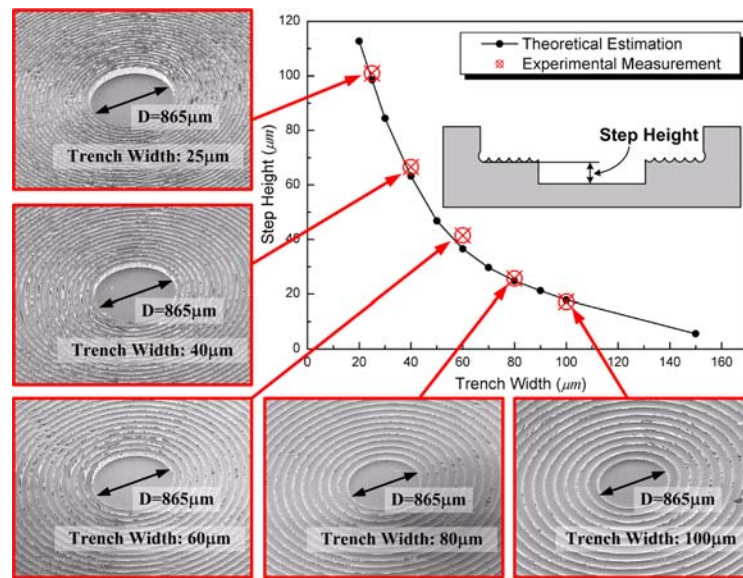


Figure 4.13 Circular cavities with different step heights formed using the SMDE technique.

The step height of each structure was measured using a white light interferometer and compared with its theoretical estimated value. The theoretical estimation was obtained using the product of the relative etching rate and the total etching time. The relative etching rate can be calculated using trench widths and the average etching rate relationship (shown in Figure

4.10). As shown in Figure 4.13, the step height of a formed circular step structure can be controlled by varying the trench width between dummy fin structures and the measurement results agree well with the theoretical estimations. Similarly, multilevel step structures can be easily formed using the SMDE technique by assigning different trench widths. Figure 4.14 shows the SEM image and the measured 3D profile of a fabricated three-level circular step structure.

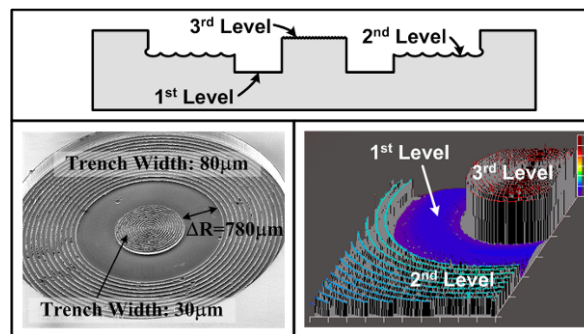


Figure 4.14 Three-level circular step structure formed using the SMDE technique.

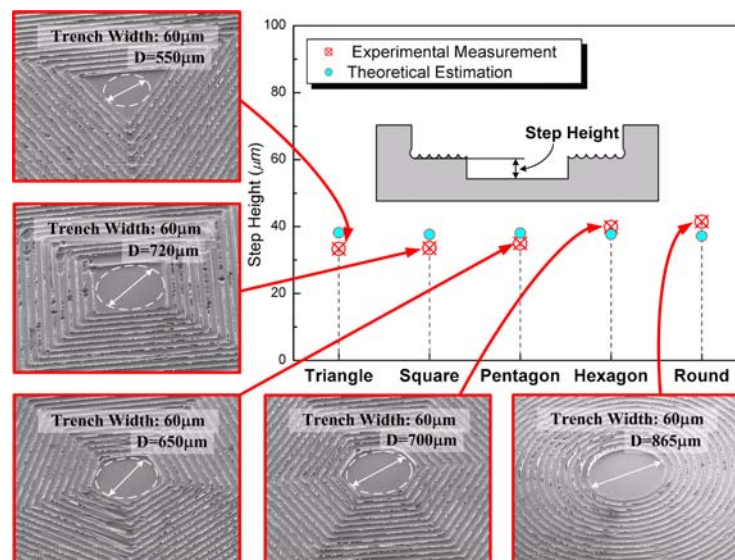


Figure 4.15 Polygonal cavities with different shapes formed using the SMDE technique.

Polygonal step structures can also be formed using the SMDE technique, as shown in Fig 4.15.

The diameter of the polygon's incircle and trench width between dummy fins are used to calculate the relative etching rate, which determines the step height of the structure. The measurement results agree with the theoretical estimations very well.

Moreover, the SMDE technique can be used to improve the uniformity of the etched surface in wide trenches after a time consuming DRIE etching processes. Normally, a wide trench has a convex etched surface and the depth variation can be several tens of micros if the trench width is millimeter level, as shown in Figure 4.11. Figure 4.16 shows an example that the uniformity of the etched surface of a 2mm wide trench can be improved by using the SMDE technique.

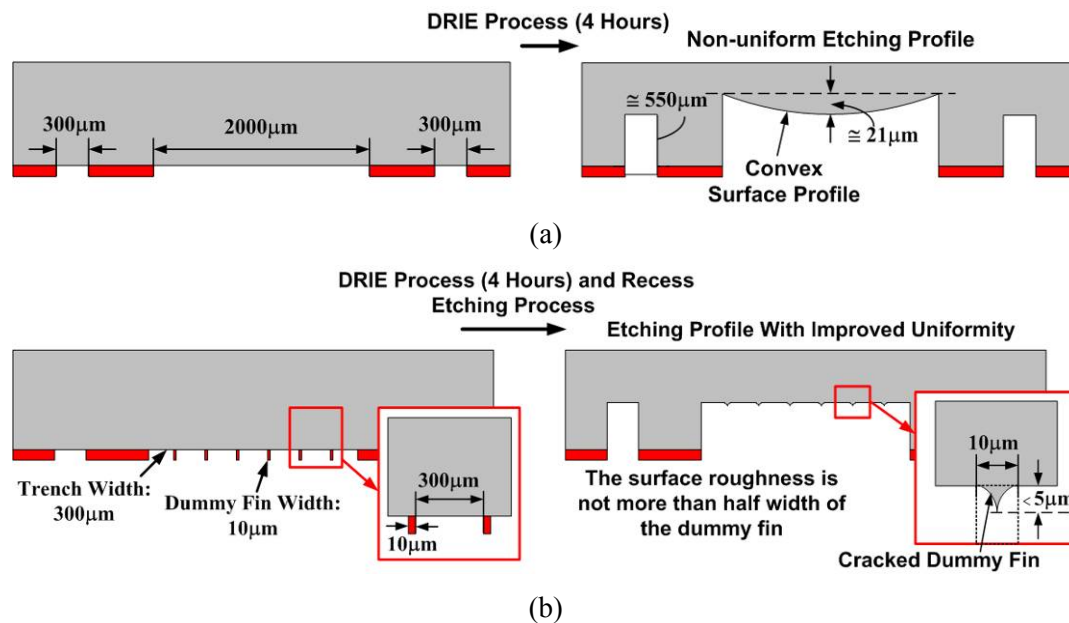


Figure 4.16 An example showing (a) Non-uniform etching profile after a 4 hour DRIE process and (b) uniformity improved etching profile by using the SMDE technique.

As shown in Figure 4.16(a), without using the SMDE technique, the etching profile of a 2mm

wide trench is convex shape and the depth variation is over $20\mu\text{m}$. While using the SMDE technique, the 2mm wide area is partitioned into several $300\mu\text{m}$ wide areas using $10\mu\text{m}$ wide dummy lines before etching. After a 4 hour DRIE process, several $300\mu\text{m}$ wide trenches and $10\mu\text{m}$ wide dummy fin structures are formed. After that, a recess etching process breaks all dummy fin structures and forms the final etched surface. Since the etched profile in a $300\mu\text{m}$ wide trench is flat (referred to Figure 4.11), the surface roughness is determined by the height of the cracked dummy fin structures, as shown in Figure 4.16(b). The height of the residual dummy fin can be considered approximately to be its half width. For example, if the width of the dummy fin is $10\mu\text{m}$, the average roughness of the etched surface can be estimated to be less than $5\mu\text{m}$. Consequently, the uniformity of the final etched surface can be effectively improved using the SMDE technique.

4.2.2 Scanner design and simulation

Figure 4.17 shows a schematic illustration of the 2-DOF ELTR resonator driven single-layered vibratory grating scanner with a backside thinned grating platform. The diffraction grating with a period of 400nm is patterned on a round grating platform with a diameter of 1mm and a thickness of $80\mu\text{m}$. The grating platform is connected to the substrate through 20 supporting flexural beams. Among these beams, 12 of them are designed to be longer than others to save space. As shown in Figure 4.17, a round cavity, which was formed using the SMDE technique, is located at the backside of the grating platform to reduce its rotary inertia. The rigidity of the grating platform is ensured by a circular reinforcement frame at its edge. The designed diameter and the depth of the round cavity are $850\mu\text{m}$ and $65\mu\text{m}$,

respectively. This results in a rotary inertia reduction of 42.4%. In other words, the total stiffness can have a reduction of 42.4%, while maintaining the same scanning speed.

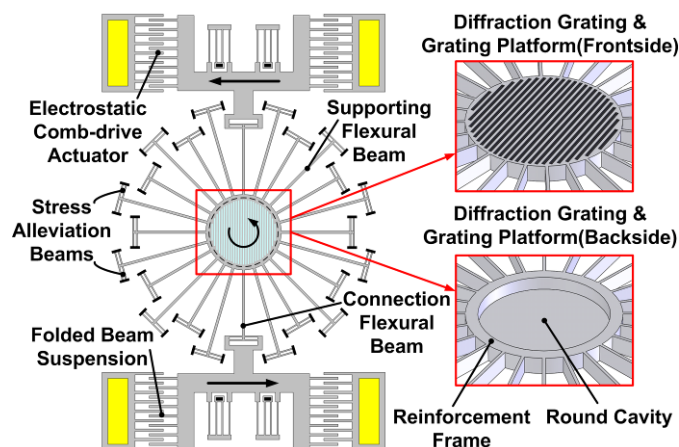


Figure 4.17 Schematic illustration of a 2-DOF ELTR resonator driven single-layered vibratory grating scanner with a backside thinned grating platform.

Table 4.6 Structural parameters of the 2-DOF ELTR resonator driven single-layered vibratory grating scanner.

	Width (μm)	Length (μm)	Thickness (μm)
Longer Supporting Flexural Beam	30	1300	80
Shorter Supporting Flexural Beam	27	1050	80
Connection Flexural Beam	27	1050	80
Stress Alleviation Beam	6	255	80
Folded Beam Suspension	8	170	80
Comb Finger	7	64	80

Two sets of electrostatic comb-drive resonators are configured symmetrically and each of them is attached to the grating platform through one connection flexural beam. Each of the supporting flexural beams and connection beams has two pairs of perpendicularly connected stress alleviation beams, which are used to reduce its axial stress during the operation. The

micro resonator is suspended by 96 sets of folded beam suspensions and actuated by electrostatic comb-drive actuators. Each comb-drive resonator has a total number of 164 movable fingers on one side. The detailed structural parameters of the high-speed MEMS grating scanner are summarized in Table 4.6.

Dynamic performances of the prototype scanner, such as resonant frequencies and mode shapes, are predicted by the established comprehensive analytical model (refer to section 3.4.1) and FE simulations using the commercial software package ABAQUSTM. The prototype scanner can be treated as a 2-DOF vibrating system and two resonating modes are expected. Figure 4.18 shows FE simulated mode shapes of both resonating modes of the prototype scanner.

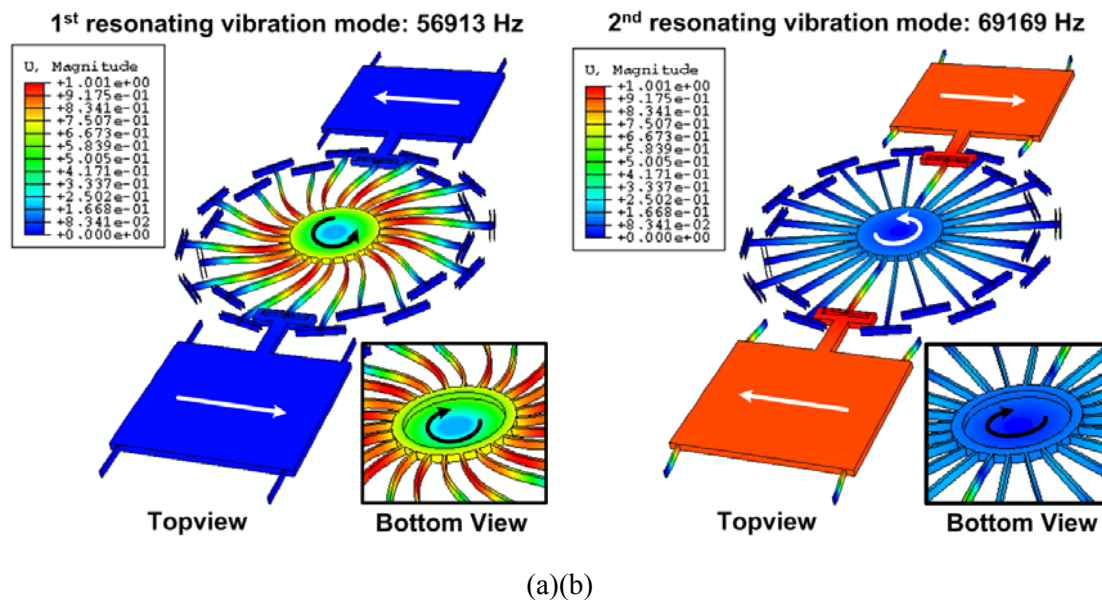


Figure 4.18 FE simulation results showing the resonant frequencies and mode shapes of (a) the 1st and (b) the 2nd resonating mode.

The analytical predictions and FE simulation results of the natural frequencies and mode shapes of both resonating mode are compared in Table 4.7. Since the influence of the fabrication imperfections are very difficult to be included in FE simulations, analytical predictions with and without considering fabrication imperfections are made for easy comparison. As shown in Table 4.7, theoretical predictions agree well with FE simulation results when the influence of fabrication imperfections is ignored.

Table 4.7 Comparison between theoretically predicted and FE simulated resonant frequencies as well as mode shapes of a 2-DOF ELTR resonator driven single-layered grating scanner.

Mode		Ignoring fabrication imperfections		Theoretical prediction considering fabrication imperfections
		Theoretical prediction	FE simulation	
1 st Mode	Frequency (Hz)	60006	56913	52261
	Mode ratio (°/μm)	7.64	7.48	6.51
2 nd Mode	Frequency (Hz)	69972	69169	61189
	Mode ratio (°/μm)	-0.0178	-0.015	-0.017

4.2.3 Fabrication process

SOI micromachining technology and the SMDE technique were combined to fabricate the prototype device. A total of four photo masks were used. The SOI wafer used in our process consists of an 80μm thick n-type heavily doped silicon device layer, a 2μm thick buried oxide (BOX) layer, and a 650μm thick silicon handle wafer. The schematic of the fabrication process flow is shown in Figure 4.19. As shown in Figure 4.19, the binary diffraction grating with a 400 nm grating pitch and a 50% duty cycle was patterned using deep-UV lithography and timed plasma etching. The groove depth of the diffraction grating was controlled to be

150nm for maximum diffraction efficiency.

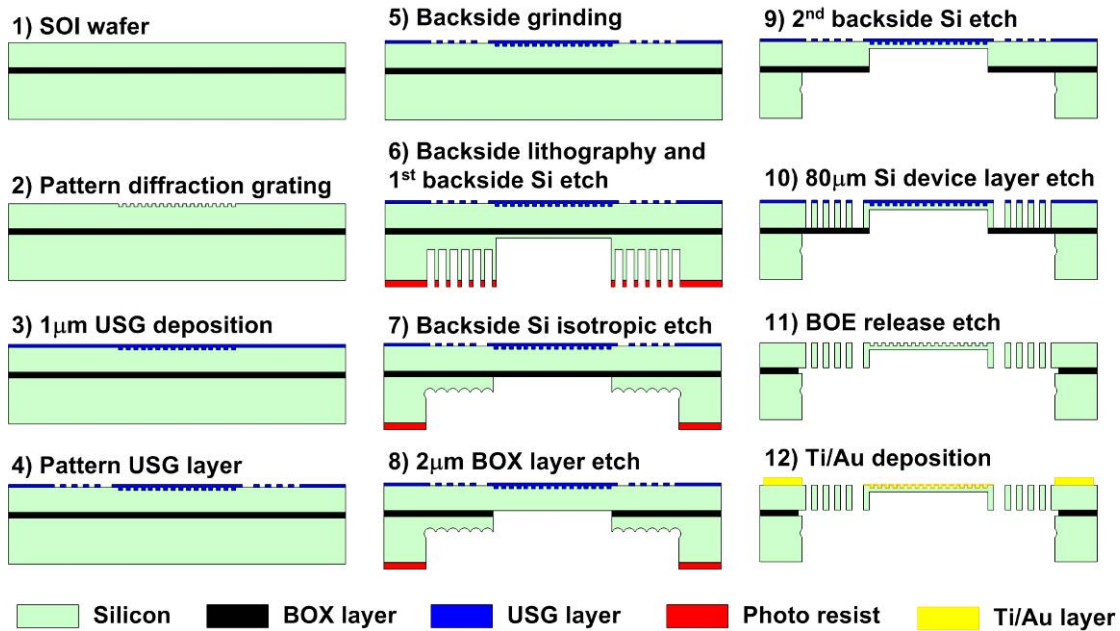


Figure 4.19 Fabrication process of the prototype 2-DOF ELTR resonator driven single-layered vibratory grating scanner.

Then, a 1 μ m USG layer was deposited on the top of the wafer and patterned using the RIE process. The hard mask layer of the grating platform, suspension beams and electrostatic comb-drive actuators was defined in this step for the future process. Next, the backside of the SOI wafer was grinded and polished until the thickness of the silicon substrate is around 500 μ m. After that, the SOI wafer was patterned on the backside using a specially designed mask for the future delay etching. The etching region was partitioned to different sections with different trench widths by a set of concentric circular dummy fin structures. The region of the round cavity of the grating platform has the biggest trench width resulting in highest etching rate. The SOI wafer was then etched from its backside by the first DRIE process until a few microns of silicon are left in the region of the round cavity. The thickness of the

remaining silicon in the etching region was less than $45\mu\text{m}$. Next a plasma recess etching process removed all the dummy fin structures and exposed the BOX layer in the round cavity region. The $2\mu\text{m}$ BOX layer was then etched through by the subsequent RIE process, which stopped at the silicon device layer. Next, the round cavity region and the rest were etched simultaneously by the second DRIE process. The etching process stopped when the depth of the round cavity was around $65\mu\text{m}$. All the BOX layer of the rest of the etching region was exposed and etched in the following RIE process. Subsequently, the $80\mu\text{m}$ thick silicon device layer was etched by another DRIE process to form the grating platform, suspension beams and comb-drive actuators. All structures were then released from the backside using a BOE solution. After that, a $100\text{nm}/500\text{nm}$ thick Ti/Au layer, which is used as the metal pad for wire bonding, was evaporated on the top of the wafer through a shadow mask. Finally, a $10\text{nm}/80\text{nm}$ Ti/Au layer was evaporated on the wafer's top surface to enhance the reflectivity of the diffraction grating.

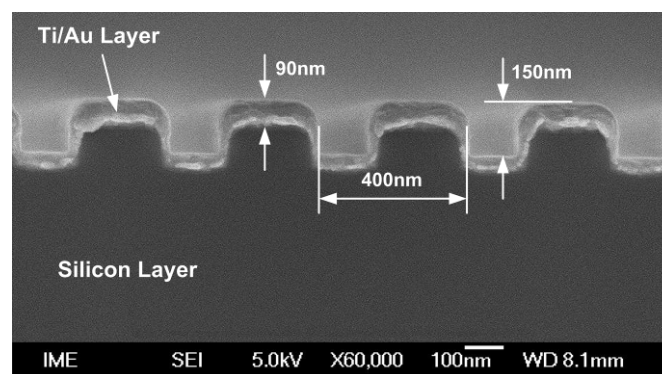


Figure 4.20 SEM image showing the cross-sectional view of the fabricated sub-wavelength diffraction grating with a grating period of 400nm .

Figure 4.20 shows the cross-sectional view of the fabricated sub-wavelength diffraction

grating with a grating period of 400 nm using a SEM image. The whole view of the fabricated device is shown by a microscopic image in Figure 4.21. Figures 4.22(a) & (b) are SEM images showing the top and bottom view of the fabricated device, respectively.

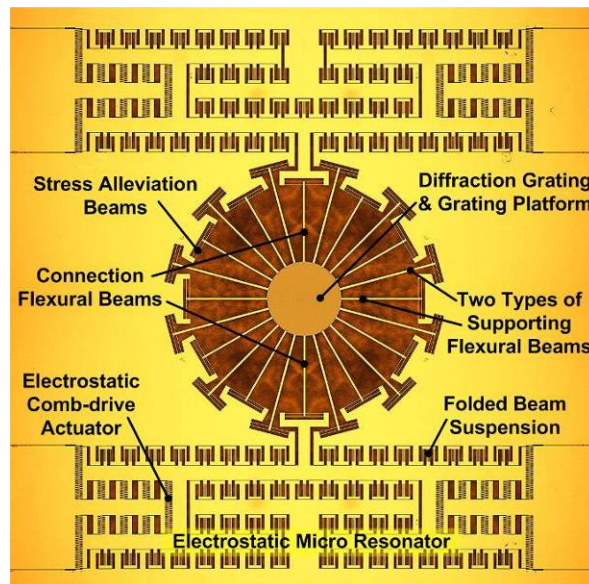


Figure 4.21 Microscopic image showing the whole view of the fabricated device.

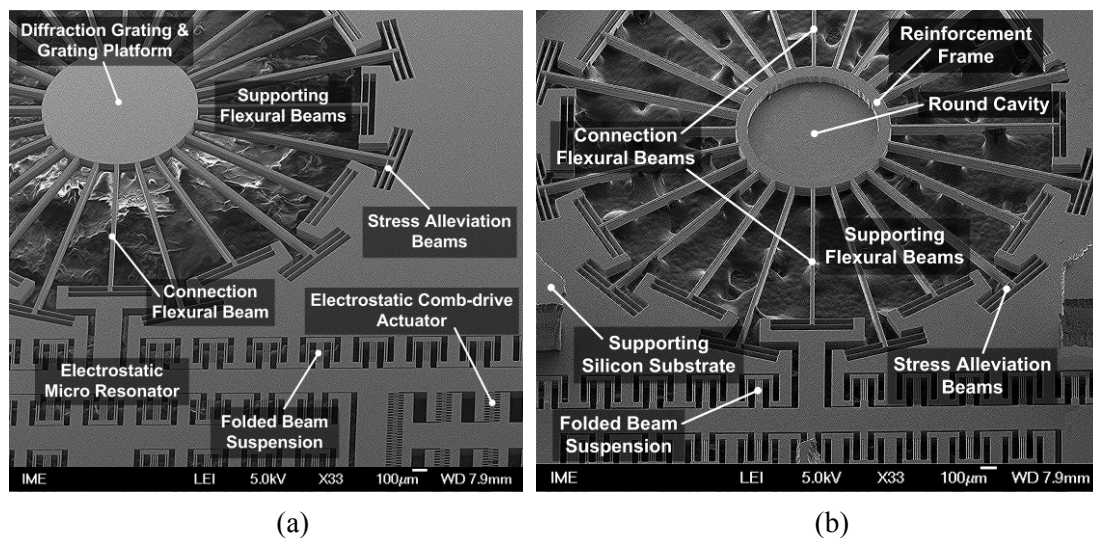


Figure 4.22 SEM images showing the (a) top view and (b) bottom view of the fabricated device.

The backside profile of the grating platform with the round cavity is measured using a white

light interferometer and the measurement results are shown in Figure 4.23. The diameter and the depth of the round cavity are measured to be $842\mu\text{m}$ and $64.85\mu\text{m}$. The measurement results agree well with design parameters showing the feasibility and the reliability of the fabrication process.

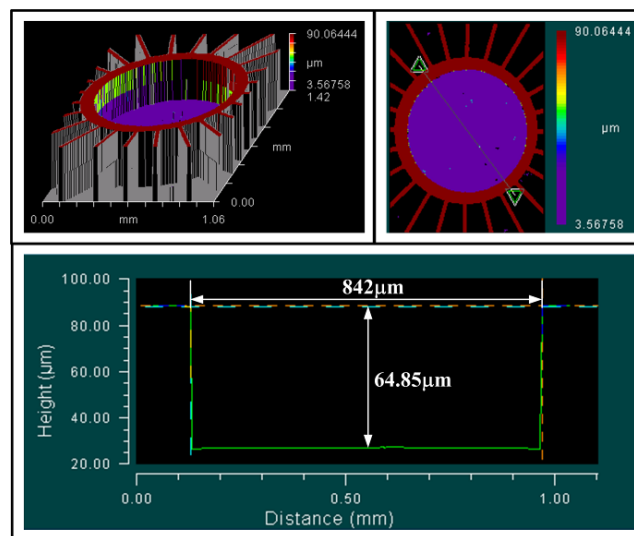


Figure 4.23 White light interferometer measurement results of the round cavity and circular reinforcement frame on the backside of the grating platform.

4.2.4 Experimental characterization

The optical and dynamic performances of the prototype device were tested using a linear polarized laser beam with a wavelength of 635nm from a 5mW laser diode module. The incident angle of the illuminated laser beam was determined to be 73.3° so that the bow-free scanning trajectory can be achieved. The optical efficiency of the 400nm diffraction grating was measured and the experimental setup is shown in Figure 4.24. The incident laser beam firstly went through a tunable polarizer and was then split into two beams by a beam splitter. One beam illuminated on a photo detector and the other beam illuminated on the diffraction

grating. The intensity of the first-order diffraction beam was measured by another photo detector and the zeroth-order beam was dumped. The diffraction efficiency was then calculated according to the readings from the two photo detectors.

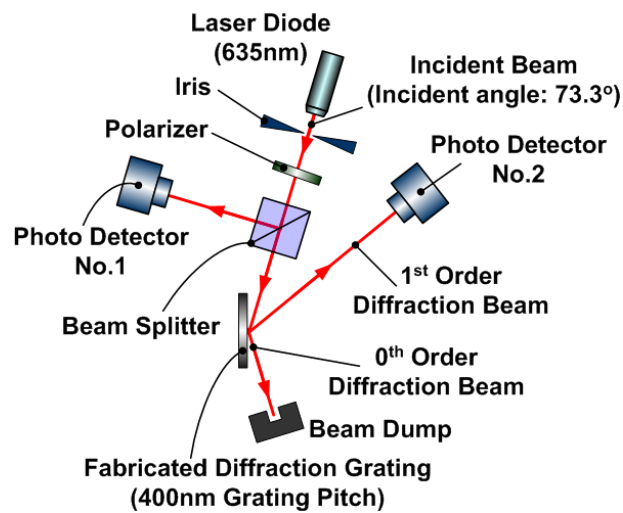


Figure 4.24 Schematic of the experimental setup measuring the diffraction efficiency of the fabricated grating.

Figure 4.25(a) shows the measured first-order diffraction efficiency versus the polarization angle. When the polarization of the incident beam varies from TE polarization (parallel to the grating lines) to TM polarization (perpendicular to the grating lines), the diffraction efficiency increases from 7% to 63%. Therefore, TM polarization is preferred due to higher diffraction efficiency achieved. Since the diffraction efficiency is polarization dependent, the intensity variation of the scanned beam during scanning is also measured. Figure 4.25(b) shows the measured scanned beam efficiency versus the optical scan angle for TM-polarization. The measurement results show that the efficiency decreases slightly from the center to the end of the scan line and the variation is less than 0.85%, which is acceptable for most laser scanning

applications.

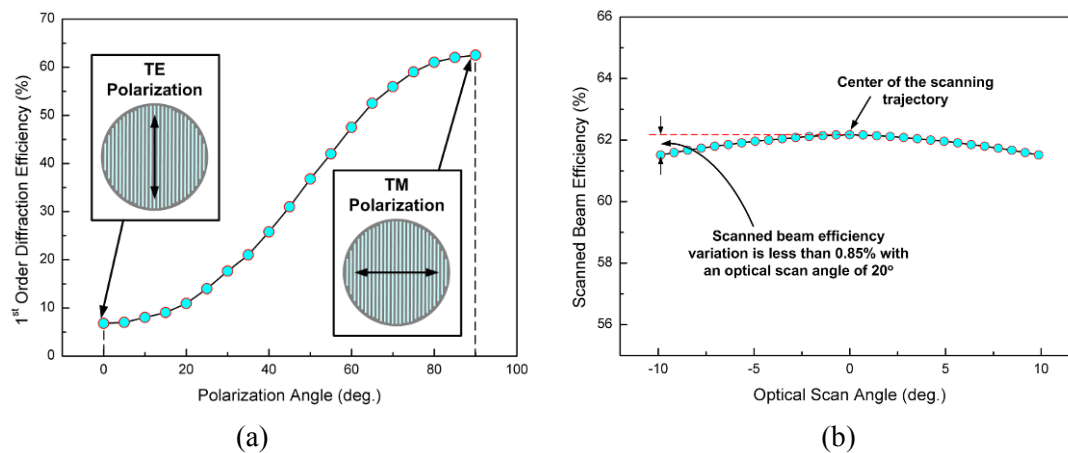


Figure 4.25 (a) Measured 1st order diffraction efficiency versus the polarization angle; (b) measured scanned beam efficiency versus the optical scan angle for TM-polarization.

The experimental setup for the dynamic performance characterization is shown in Figure 4.26.

The prototype scanner was mounted in a vacuum chamber with a vacuum pressure of 0.12mTorr to raise the quality factor. Each electrostatic comb-drive resonator was driven by a push-pull mechanism with a DC bias and an AC sinusoidal signal. A projection screen and a beam dump were aligned perpendicular to the first- and zeroth-order diffracted beams respectively when the diffraction grating remained motionless. After applying voltages to the driving actuators, the grating platform vibrates resonantly and the first-order diffraction beam scans accordingly while the zeroth-order beam remains stationary. The scanning trajectory of the 1st order diffraction beam was projected on the projection screen and the zeroth-order diffraction beam was dumped. The optical scan angle was determined by measuring the length of the projected laser trajectory and the distance between the screen and the device. The prototype scanner with a 1mm diameter diffraction grating was capable of scanning at a frequency of 50192 Hz with an optical scanning angle of 14.1°.

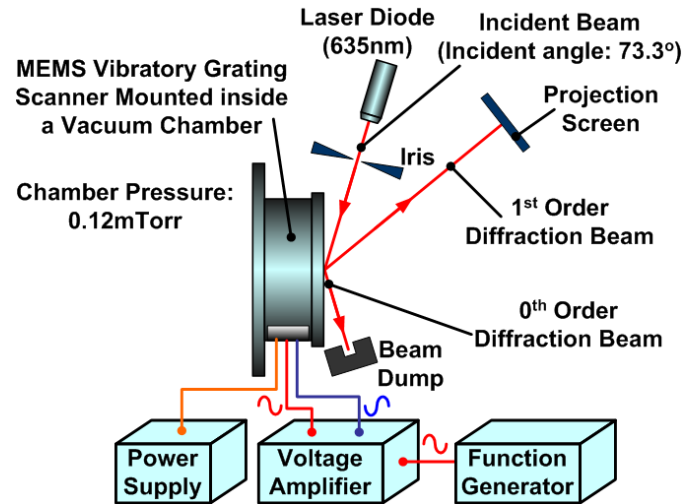


Figure 4.26 Schematic of the experimental setup for measurement of dynamic performances.

As expected, the MEMS grating scanner has two vibration/scanning modes. Since the scanning angle in atmosphere is very small, measurement of the mode shape is very difficult. The measurement results, theoretical predictions by comprehensive analytical model and FE simulation results are summarized in Table 4.8, which again verified the validity of the comprehensive dynamic model established in section 4.1.3.

Table 4.8 Summary of theoretically predicted, FE simulated and measured resonant frequencies as well as mode shapes of the prototype 2-DOF ELTR resonator driven single-layered grating scanner.

Mode		FE simulations ignoring fabrication imperfections	Theoretical predictions considering fabrication imperfections	Experimental measurements
1 st Mode	Frequency (Hz)	56913	52261	50192
	Mode ratio (°/μm)	7.48	6.51	N/A
2 nd Mode	Frequency (Hz)	69169	61189	60273
	Mode ratio (°/μm)	-0.015	-0.017	N/A

The frequency response of the prototype scanner was obtained through sweeping the frequencies of the driving AC sinusoidal signal. Although there are two resonating modes, the 2-DOF ELTR resonator driven single layered grating scanner was designed to scan at frequencies near its first resonating mode. The reason is that the first resonating mode has a higher mode ratio resulting in larger scanning amplitudes, less risk of brittle fracture of the connection flexural beams, compared with the second resonating mode.

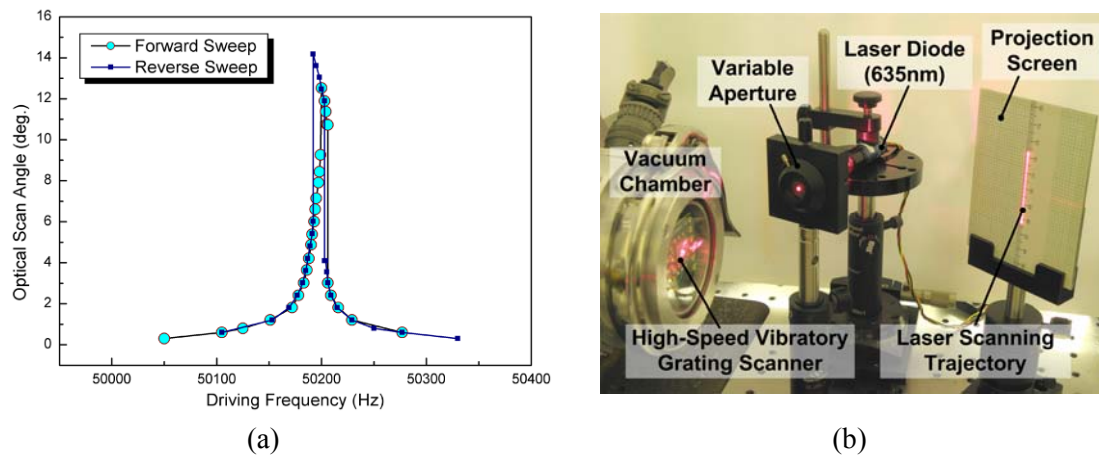


Figure 4.27 (a) Measured frequency response of the prototype scanner in vacuum at the region near its first resonating mode; (b) photograph of the laser scanning trajectory of the prototype scanner on a projection screen.

With driving voltages of 100V DC bias and 200 V AC peak-to-peak voltages, the frequency response of the prototype scanner near the region of its working mode was obtained and shown in Figure 4.27(a). Figure 4.27(b) shows the photograph of the experimental setup and the projected laser scanning trajectory on the screen, which is located at a distance of 200 mm from the scanner.

4.3 Single-layered grating scanner driven by 2-DOF circular resonator

To increase scanning amplitudes, a single-layered grating scanner driven by 2-DOF circular resonator was developed and presented in this section. Multiple-spring suspensions minimize the internal stresses during scanning resulting in large scanning amplitudes. The prototype scanner with a 1 mm diameter diffraction grating is capable of scanning at 20289Hz with an optical scan angle of around 25°. Compared with the prototype scanner discussed in section 4.1, there is an over 80% increase of the optical scan angle while keeping the grating diameter and scanning speed unchanged. Besides, since only one micro resonator rather than previously several symmetrically configured micro resonators is adopted, it will not encounter resonant frequency mismatch problem due to uncertainties and imperfections in the micro fabrication process.

4.3.1 Scanner design and simulation

The schematic illustration of the micromachined 2-DOF circular resonator driven single-layered grating scanner is shown in Figure 4.28. In order to ensure enough beam size of the scanned light, diameter grating with a diameter of 1mm is adopted. The round platform is connected to the outer circular comb-drive resonator through 16 connection flexural beams. The suspension flexural beams were designed to achieve operational scanning frequency and appropriate mode shapes. Among the 16 single beam suspensions, 8 of them are designed to be longer than the others in order to save space. The dimensions of the eight beams are 18 μ m wide and 1400 μ m long and the rest are 15 μ m wide and 1050 μ m long. Each of the connection

flexural beams has 2 pairs of perpendicularly connected stress alleviation beams with a width of $7\mu\text{m}$ and a length of $410\mu\text{m}$, which are used to reduce its axial stress during large deformation. The outer circular comb-drive resonator is suspended by 40 symmetrically configured circular folded beam suspensions with beams of width $18\mu\text{m}$ and length $405\mu\text{m}$ and driven by electrostatic circular comb-drive actuators. There are 264 movable circular fingers for one side driving with finger width $7\mu\text{m}$, finger gap $4\mu\text{m}$ and initial finger overlap angle 1° .

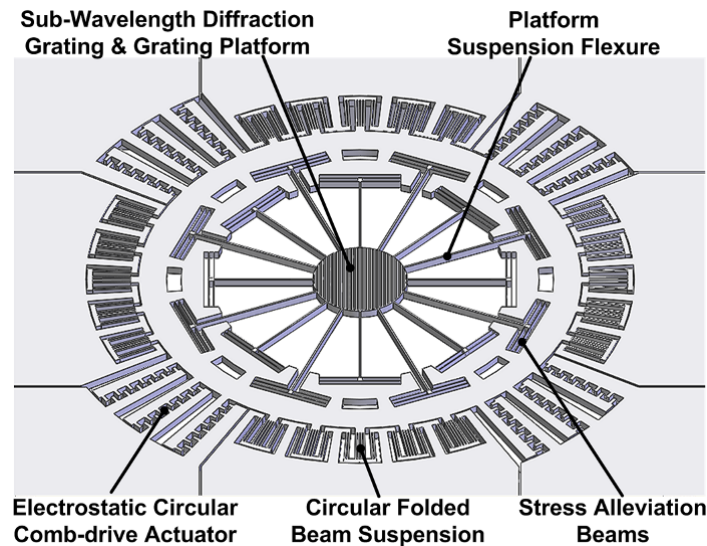


Figure 4.28 Schematic illustration of the micromachined 2-DOF electrical comb driven circular resonator driven in-plane vibratory grating scanner.

Dynamic performances, such as resonant frequencies and mode shapes of the prototype scanner are predicted by the established comprehensive analytical model (refer to section 3.4.2) and FE simulations using the commercial software package ABAQUSTM. In the 2-DOF circular resonator, two resonating modes are expected during vibration, namely 1st and 2nd mode. The mode shape can be defined as the ratio between the rotational angle of the grating

platform and the outer circular resonator. Figure 4.29 shows FE simulated mode shapes of both resonating modes of the prototype scanner.

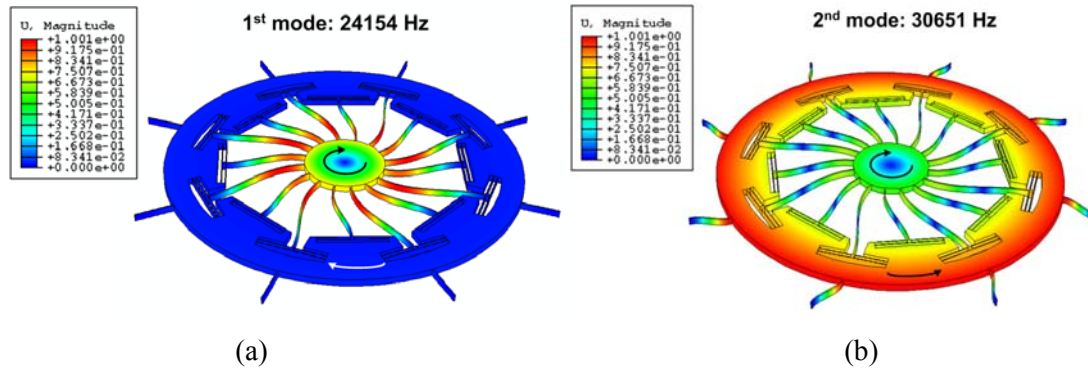


Figure 4.29 Mode shapes of (a) 1st and (b) 2nd resonating mode during vibration obtained using FE simulation.

The analytical predictions and FE simulation results of the natural frequencies and mode shapes of both resonating mode are compared in Table 4.9. As shown in the table, theoretical predictions agree well with FE simulation results when the influence of fabrication imperfections is ignored.

Table 4.9 Comparison between theoretically predicted and FE simulated resonant frequencies as well as mode shapes of a 2-DOF circular resonator driven single-layered grating scanner.

Mode		Ignoring fabrication imperfections		Theoretical prediction considering fabrication imperfections
		Theoretical prediction	FE simulation	
1 st Mode	Frequency (Hz)	24435	24154	20730
	Mode ratio	126.00	122.45	124.19
2 nd Mode	Frequency (Hz)	30928	30651	26171
	Mode ratio	-2.56	-2.59	-2.51

4.3.2 Fabrication process

SOI micromachining technology was used to fabricate the prototype device and four photo masks were used. The fabrication process flow is illustrated in Figure 4.30. The SOI wafer used has an 80 μm thick heavily doped silicon device layer, 2 μm thick BOX layer and a 650 \pm 25 μm thick silicon substrate.

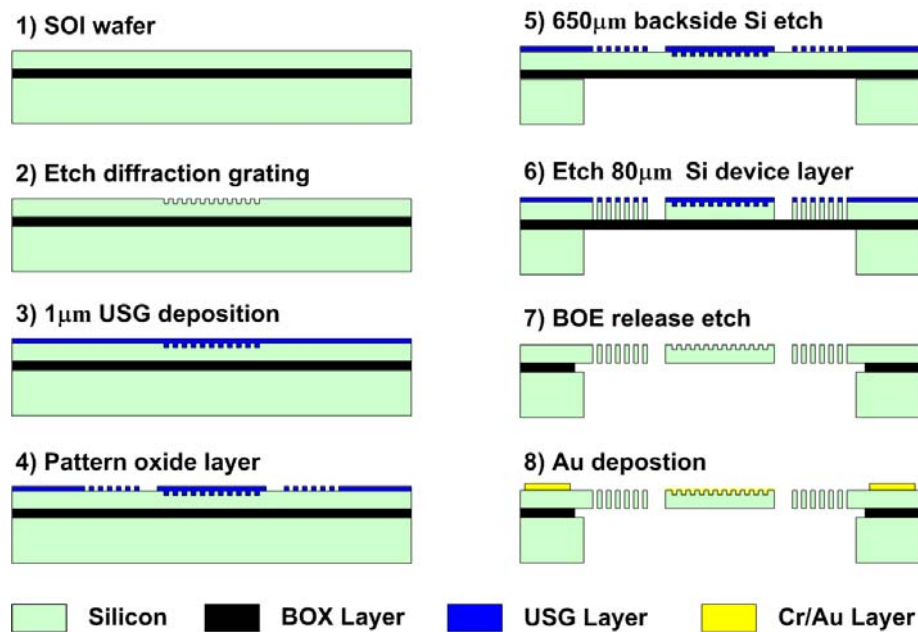


Figure 4.30 Fabrication process flow of the prototype in-plane vibratory grating scanner.

As shown in Figure 4.30, the diffraction grating has similar 400nm grating period and 50% duty cycle with a depth of around 150nm. Then, 1 μm USG layer was deposited and patterned by using RIE process. Next, the SOI wafer was patterned on the backside followed by a DRIE process, which is used to remove silicon and expose the region of all the structures. The etching process stopped at the BOX layer. Subsequently, the 80 μm thick silicon device layer was etched by another DRIE process, which is also stopped at the BOX layer, to form the grating platform, circular comb-drive actuator and suspension beams. After that, the structures

formed in SOI device layer were release from backside by using BOE solution. Then, the metal pads for wire bonding were formed by evaporating 100nm/500nm thick Ti/Au layer through a shadow mask. Finally, a 10nm/80nm Ti/Au layer was evaporated on the wafer surface to enhance the reflectivity of the diffraction grating.

The whole view and the center part of the fabricated device are shown by a microscope image and a SEM image in Figures 4.31(a) & (b), respectively.

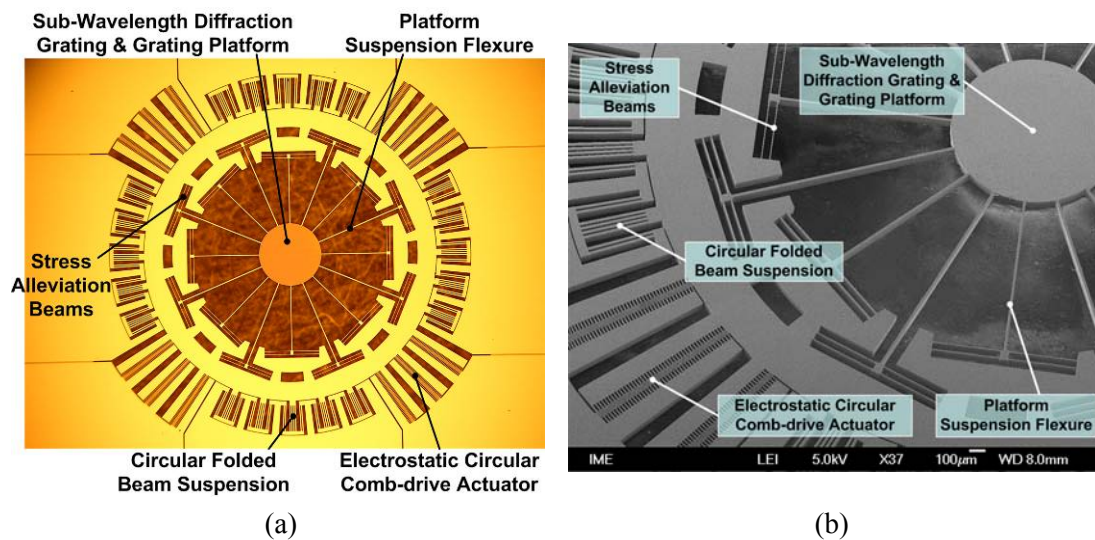


Figure 4.31 (a) Microscopic image showing the whole view and (b) SEM image showing the center part of the fabricated prototype scanner.

4.3.3 Experimental characterizations

The optical performance of the MEMS grating scanner was tested using a linearly TM-polarized He-Ne laser beam with a wavelength of 632.8 nm. Similar experimental setup to the one shown in Figure 4.26 was used by replacing the laser diode with the He-Ne laser source. The incident angle was determined to be 71.8° for a 400nm period diffraction grating

to satisfy bow-free scanning conditions.

The dynamic performance of the prototype scanner was tested in both atmosphere and vacuum. As expected, two resonating modes exist. The optical scan angle was measured through measuring the length of the laser scanning trajectory on the projection screen, which was aligned perpendicularly to the 1st order diffracted beam when the grating is motionless. The outer circular comb-drive resonator was driven by a push-pull mechanism. While tested in atmosphere (760Torr), the driving voltages were fixed at 80V DC bias and 160V AC peak-to-peak. Further increasing the driving power may cause the instability of the electrostatic circular comb-drive actuator. Figure 4.32 (a) & (b) show the measured frequency responses in atmosphere. The resonant frequencies of the 1st and the 2nd resonating modes were experimentally determined as 20182Hz and 21910Hz with an optical scan angle of 20.8° and 18.1°, respectively.

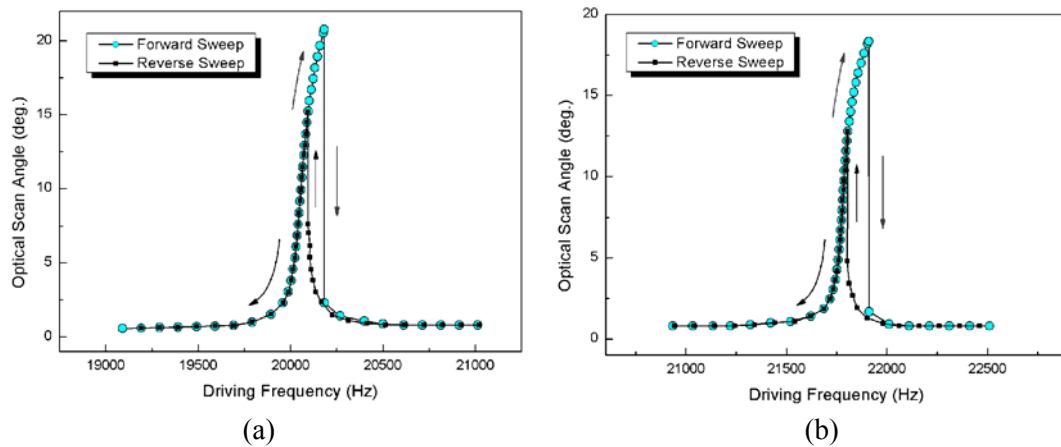


Figure 4.32 Measured frequency responses of the prototype scanner in atmosphere at frequency regions near the resonant frequencies of (a) the 1st and (b) the 2nd modes.

While tested in vacuum (0.12mTorr), the driving voltage was fixed at 15V DC bias and 30 V

AC peak-to-peak. Further increasing the driving power may cause the brittle fracture of the main flexural suspension beams. Figure 4.33 (a) & (b) show measured frequency responses in vacuum. The resonant frequencies of the 1st and 2nd resonating modes were experimentally determined as 20289Hz and 21918Hz with an optical scan angle of 24.8° and 18.2° respectively.

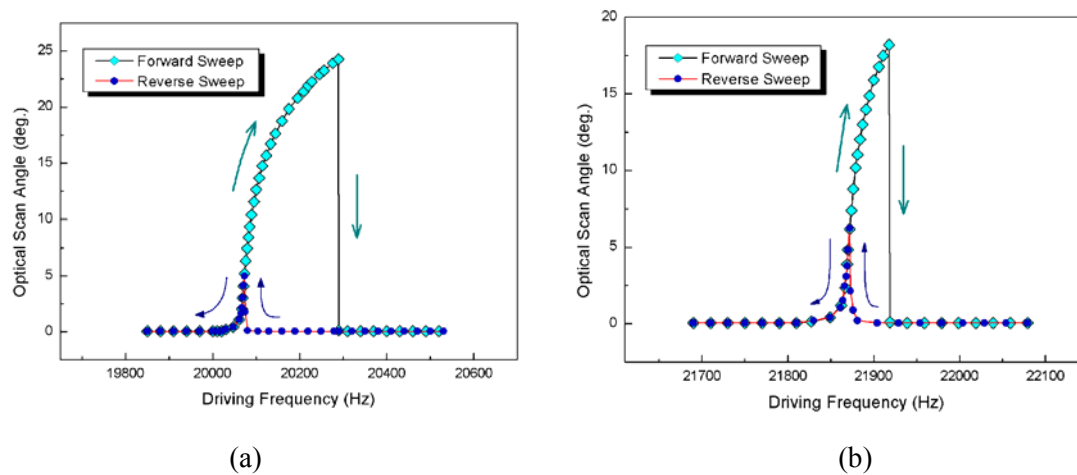


Figure 4.33 Measured frequency responses of the prototype scanner in vacuum at frequency regions near the resonant frequencies of (a) the 1st and (b) the 2nd modes.

The scanner demonstrated some level of large-deflection nonlinearity during vibration. For example, the scanner's optical scanning angle is different during the forward and backward driving frequency sweeping. Besides, there are slight differences between measured resonant frequencies in atmosphere and vacuum. The linearity of the vibration can be further improved by reducing the stiffness of the stress alleviation beams along the axial direction.

According to the dynamic testing results, operating in vacuum and scanning at the frequency near the resonant frequency of the 1st resonating mode are preferred due to lower driving

voltage, higher scanning amplitude and less risk of brittle fracture of the main flexural suspension beams. High-speed laser scanning was experimentally demonstrated and Figure 4.34 shows a photograph of the projected laser scanning trajectory on a projection screen, which is located at a distance of 100mm from the grating scanner.

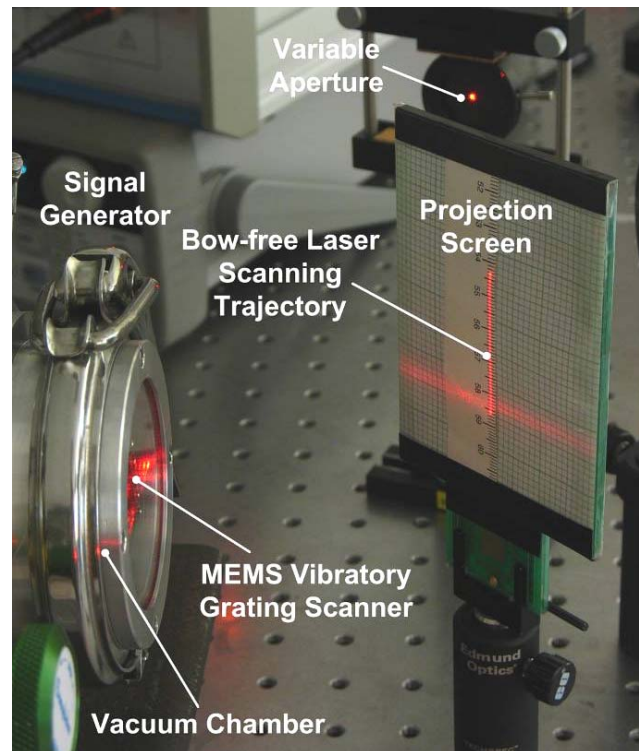


Figure 4.34 Photograph of the experimental setup for the prototype scanner.

The resonant frequencies and mode shapes of the prototype scanner were also measured on probe station under microscope in atmosphere. The driving power was selected to be 50V DC bias and 100V AC peak-to-peak voltages to avoid large-deflection nonlinearity during the vibration. The measured resonant frequencies and mode shapes of the prototype device are compiled in Table 4.10, which shows the comparisons between theoretical analyses and experimental results.

Table 4.10 Summary of theoretically predicted, FE simulated and measured resonant frequencies as well as mode shapes of the prototype 2-DOF circular resonator driven single-layered grating scanner.

Mode		Predictions		Measurements		
		FE simulation	Theoretical Model	In atmosphere (50V DC bias and 100V _{pp} AC)	In atmosphere (80V DC bias and 160V _{pp} AC)	In Vacuum (15VDC bias and 30V _{pp} AC)
1 st Mode	Frequency (Hz)	24154	20730	20095	20182	20289
	Mode shape	122.45	124.19	94.76	N/A	N/A
2 nd Mode	Frequency (Hz)	32013	26171	21806	21910	21918
	Mode shape	-2.59	-2.59	-18	N/A	N/A

As shown in Table 4.10, the comprehensive dynamic model for 2-DOF circular resonator (established in section 3.4.2) could provide accurate prediction of both resonant frequencies and mode shapes. The deviations between the theoretical and experimental results are acceptable and mainly due to the uncertainty in fabrication process, material properties and imperfect boundary conditions of the suspension. Besides, the measured resonant frequencies vary with different driving conditions, which is mainly due to the large-deflection nonlinearity during the vibration and different viscous damping while testing.

4.4 Summary

In this chapter, three single-layered vibration grating scanners were demonstrated. Design and modeling using the established comprehensive dynamic model were performed. The validity of the analytical model was verified by comparing the theoretical predictions, FE simulation

results and experimental measurements. The salient performance parameters of the developed scanners are summarized in Table 4.11.

Table 4.11 Performance parameters of the developed single-layered vibratory grating scanners.

	Grating diameter	Optical scan angle	$\theta_{\text{Opt}}D$	Scanning frequency
2-DOF LTR resonator driven	1mm	13.7°	13.7 deg·mm	20353Hz
2-DOF ELTR resonator driven	1mm	14.1°	14.1 deg·mm	50192Hz
2-DOF circular resonator driven	1mm	25°	25 deg·mm	20289Hz

The prototype grating scanner driven by a 2-DOF LTR resonator with a 1mm diameter grating is able to achieve an optical scan angle of 13.7° with a scanning frequency of 20353Hz in air. Compared with the previously developed grating scanner, there is a 70% and 1.4 times increase in optical resolution and scanning speed, respectively. The good scanned beam quality was experimentally verified by the stroboscopic method.

A novel SMDE technique was proposed and applied to further improve the performance of the vibratory grating scanner. A single-layered grating scanner driven by the 2-DOF ELTR resonator was successfully fabricated. The prototype scanner with a backside thinned grating platform and thick suspension springs is capable of achieving an optical scan angle of 14.1° and a scanning frequency of 50192Hz in vacuum. Compared with the previously developed single-layered 2-DOF LTR resonator driven grating scanner, there is a 1.5 times increase in

scanning speed while keeping the scanning amplitude the same.

The single-layered grating scanner driven by the 2-DOF circular resonator was developed to further increase the scanning amplitudes. Multiple-spring suspensions reduce internal stress level in flexural beams resulting in an increase of the maximum scanning amplitude. In addition, configuration of a single outer resonator eliminates the resonant frequency mismatching issue, which is common in 2-DOF LTR resonator driven scanners. The prototype scanner with a 1 mm diameter diffraction grating is capable of scanning at 20289Hz in vacuum with an optical scan angle of around 25°. Compared with the previously developed 2-DOF LTR resonator driven single-layered grating scanner, there is an over 80% increase of the optical resolution while keeping the scanning speed unchanged.

Chapter 5 Double-layered vibratory grating scanner: design, fabrication process and characterization

A grating scanner can be configured either single- or double-layered, as discussed in previous chapters. Compared with single-layered grating scanners, double-layered scanners, in which the diffraction grating and its driving actuator are located in different layers, have the potential to scan at large amplitudes at high scanning speeds with large aperture sizes. To further enhance the optical resolution, a double-layered vibratory grating scanner driven by 2-DOF circular resonator is developed and presented in this chapter in detail. The prototype scanner with a 2mm diameter diffraction grating is capable of achieving an optical scan angle of 33.5° at a scanning frequency of 21591Hz. This results in a $\theta_{Opt}D$ product of 67 deg-mm. Compared with previously developed single-layered grating scanner driven by 2-DOF circular resonator, there is a large increase of $\theta_{Opt}D$ product with a similar scanning speed.

5.1 Double-layered configuration

Three prototype single-layered vibratory grating scanners (shown in Figure 5.1(a)), where the grating platform and its driving actuator are located in the same plane, have been demonstrated in the previous chapter. Although adopting the single-layered configuration makes the fabrication process simple, further improvements of the optical performance are hindered. As the rotation angle of the grating platform is inversely proportional to the diameter of the diffraction grating platform, the aperture size and the optical scan angle cannot be increased simultaneously for a given maximum allowable deformation of the

platform suspension flexures. In addition, increasing the diameter of the grating platform will increase its rotational inertia and the stiffness of the suspension flexures would have to be increased by either widening or shortening the flexures to maintain the same scanning frequency. This will induce excessive stress in the suspension flexures and reduce the scanning amplitude.

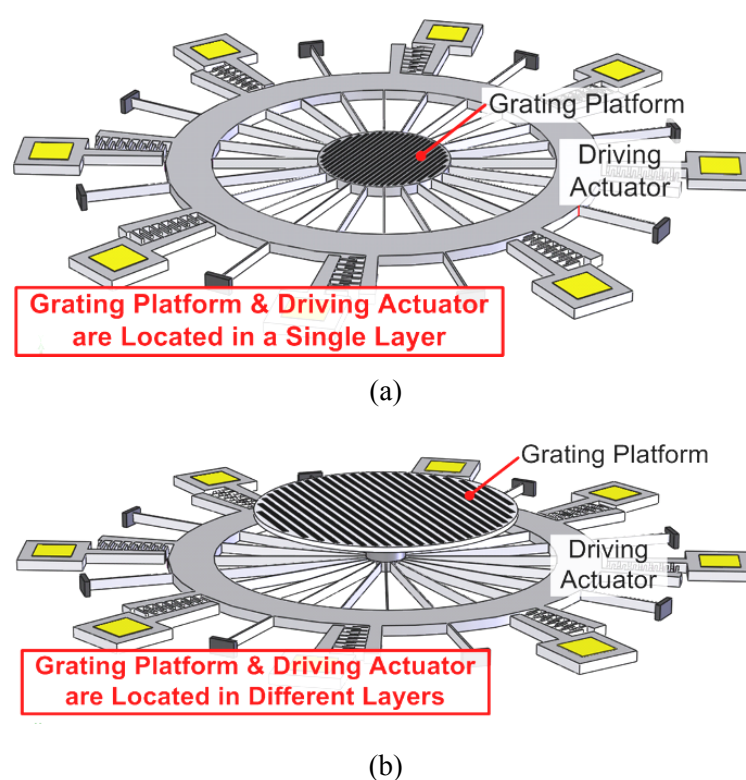


Figure 5.1 Schematic illustration of grating scanners with (a) single-layered and (b) double-layered configurations.

Double-layered vibratory grating scanners, in which the grating platform and its driving actuator are located in different layers, are proposed to improve the optical performance instead. As shown in Figure 5.1(b), the grating platform is located at the top layer and connected to a connection platform through a round pillar at its center. The connection

platform and driving actuator are located in a separate layer below the grating and are supported by several flexures. Under this configuration, the rotation angle of the grating platform is no longer determined by the size of the diffraction grating but by the diameter of the connection platform. Therefore, the size of the diffraction grating can be increased and the size of the connection platform can be reduced to a minimum, thus increasing the aperture size and the scanning amplitude simultaneously. This configuration significantly boosts its optical resolution. Furthermore, the double-layered configuration allows the thickness of the grating platform and suspension flexures to be independent of each other. This is highly advantageous for high-speed scanning. It is well-known that increasing the diameter of the grating platform will increase its rotational inertia. However, high-speed resonant scanning can be maintained by either thinning the grating platform or thickening the suspension flexures together with the driving comb-drives. The former is not likely to result in dynamic deformation of the grating platform and the latter will reduce the stress level in the suspension flexures. Consequently, double-layered vibratory grating scanners are capable of scanning at high speeds with large scanning amplitudes and having large grating aperture sizes.

5.2 Scanner design and simulation

Different ways can be used to fabricate the electrostatic double-layered vibratory grating scanner, such as the multi-layer surface micromachining process [47], the wafer bonding process [64] and the post assembly process. In this study, a combination of the bulk micromachining process and the post assembly process to fabricate the device was adopted. The proposed fabrication scheme not only reduces the complexities and difficulties of the

device fabrication but also supplies enough flexibility to the device design. The schematic illustration of the assembled double-layered vibratory grating scanner is shown in Figure 5.2.

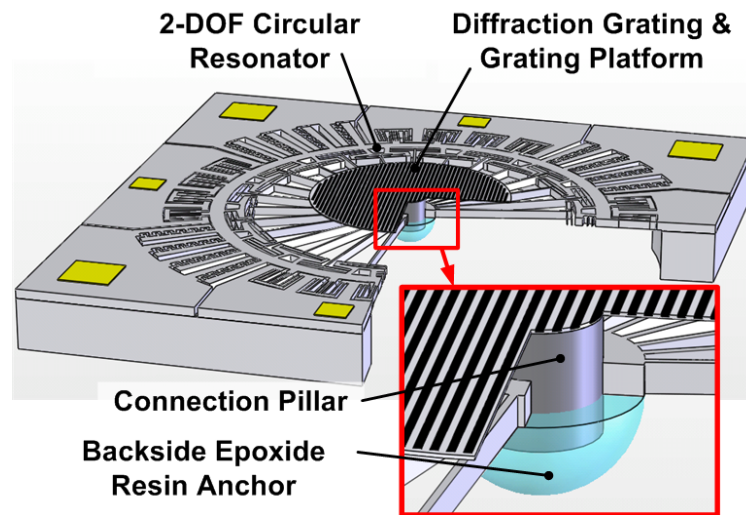


Figure 5.2 Schematic illustration of an assembled double-layered vibratory grating scanner.

The grating platform with diffraction grating on its top and the connection pillar on its back as well as the driving actuator are designed and fabricated separately using the bulk micromachining process. The grating platform with the connection pillar is schematically shown in Figure 5.3.

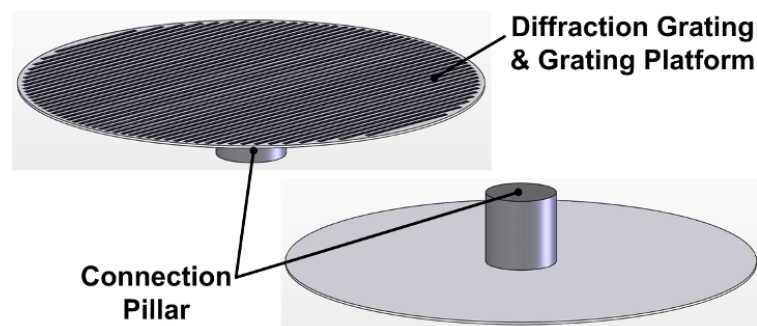


Figure 5.3 Schematic illustration of the grating platform with connection pillar.

The diffraction grating, with a 400nm grating pitch and 2mm diameter, is patterned on the front side of the circular grating platform, which has a radius and thickness of 1010 μm and 10 μm respectively. The connection pillar is attached to the backside of the grating platform at its center. Its radius and the thickness are 150 μm and 200 μm respectively.

The schematic illustration of the 2-DOF electrostatic comb-driven circular resonator, which acts as the driving actuator, is shown in Figure 5.4.

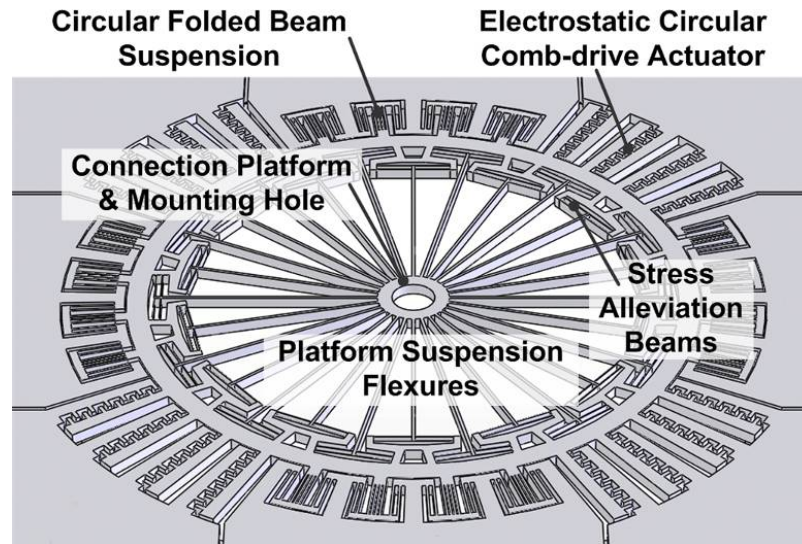


Figure 5.4 Schematic illustration of the electrostatic 2-DOF circular resonator.

The circular connection platform, with a mounting hole at its center, is connected to an outer comb-driven circular resonator through 28 connection flexural beams. Each of them has two pairs of perpendicularly connected stress alleviation beams. The radius of the connection platform and the mounting hole are 250 μm and 150 μm , respectively. Among the 28 connection flexural beams, 14 beams are 21 μm wide and 1300 μm long and the rest are 23 μm

wide and 1500 μm long. Each stress alleviation beam has a width of 6 μm and a length of 255 μm . The outer circular resonator is suspended by 32 sets of circular folded beam suspensions with beams of width 17 μm and length 340 μm . There are 280 movable circular fingers for one-side driving with finger width 7 μm , finger gap 4 μm and initial finger overlap angle 0.7°. The thickness of all the structures in the driving actuator layer is 80 μm .

The fabricated grating platform as well as the 2-DOF circular driving resonator are assembled together manually by using an in-house developed manual aligner and bonded together using the epoxide resin. The manual assembly process is developed for proof-of-concept and it can be replaced by a customized semi-auto or auto machinery assembly process for mass production, such as the die attachment process in photonics packaging. The detailed fabrication and manual assembly processes will be discussed in detail in the next section.

FE simulations were conducted to examine the scanner's resonant frequencies and mode shapes using the commercial software package ABAQUSTM without considering geometric nonlinearity of the connection flexural beams. The mode shape is defined as the ratio of the rotational angle of the diffraction grating to the outer resonator. Figure 5.5 shows the simulation results. For the 1st resonating mode, the diffraction grating and the driving resonator rotates in a same direction with a ratio of 88.73 at a frequency of 26204Hz. For the 2nd resonating mode, the diffraction grating rotates in the opposite direction from the driving resonator. The resonant frequency is 42670Hz and the mode shape is -1.17. The scanner is designed to work at the 1st resonating mode due to its higher mode ratio, which results in

larger scanning amplitudes with less risk of brittle fracture of the platform suspension flexures comparing to the second resonant mode. For the second resonant mode, due to the small travel range of the circular comb-drive actuator coupled with the low mode ratio, the scanning amplitude obtainable is very small and further increasing the driving power may cause instability of the circular comb-drive actuator.

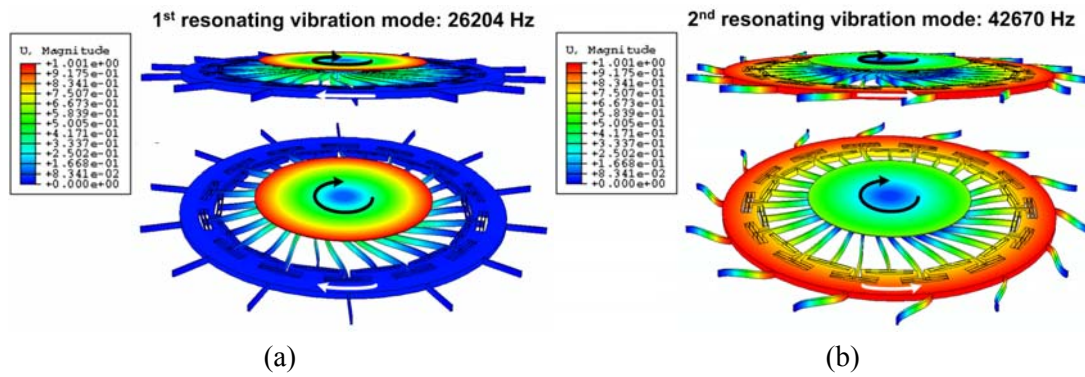


Figure 5.5 FE simulation results showing the resonant frequencies and mode shapes of (a) the 1st and (b) the 2nd resonating mode.

Large deformation geometric nonlinearity of connection beams is expected, which can cause the resonant frequency to vary with different scanning amplitudes. The frequency shifting can be predicted using the analytical model of the 2-DOF circular resonator developed in section 3.4.3, which considers the geometrical nonlinearity. Resonant frequencies are normalized by their linear resonant frequencies for easy comparison. Figure 5.6 shows the prediction of resonant frequency variations of the 1st resonating mode, which is the working mode of the scanner.

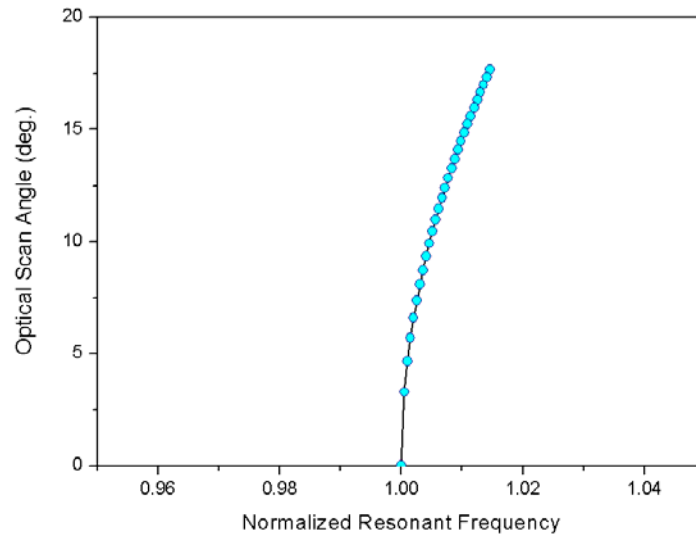


Figure 5.6 Theoretical predictions of resonant frequency variations of the 1st resonating mode.

5.3 Fabrication process

5.3.1 Diffraction grating, grating platform and connection pillar

The most straight forward method to fabricate the thin diffraction grating platform and its backside pillar is using SOI wafers. The schematic illustration of the fabrication process flow is shown in Figure 5.7. SOI wafers with a 10 μ m thick silicon device layer, a 2 μ m thick BOX layer and a 750 μ m thick silicon substrate were used in the fabrication process.

As shown in Figure 5.6, a 200nm low-pressure chemical vapor deposition (LPCVD) silicon nitride layer was first deposited on both sides of the SOI wafer. The top layer was then removed by a RIE process. Next, the diffraction grating with a 400nm grating period and 50% duty cycle was patterned using deep-UV lithography and a timed RIE process. The depth of the grating groove is controlled to be 150nm for maximum diffraction efficiency. The 10 μ m thick silicon device layer was patterned and etched through to form the grating platform by using DRIE process, which stopped at the BOX layer. A 2.4 μ m thick photoresist layer (resist

type: AZ6624) was used as the masking layer. Then LPCVD silicon nitride layer on the backside of the SOI wafer, which served as the hard mask for the following wet-etching process, was patterned using RIE. Subsequently, a 550 μm deep square cavity, which thinned down the silicon substrate to 200 μm , was formed by wet anisotropic Si etch in KOH solution (35 wt%, 75°C). After that, a 1 μm plasma-enhanced chemical vapor deposition (PECVD) USG layer was deposited onto the SOI wafer's backside and the bottom of the etched cavity and patterned using RIE process. The connection pillar was then formed by another DRIE process, which stopped at the BOX layer. Finally, the exposed BOX layer was etched from the backside by using BOE solution.

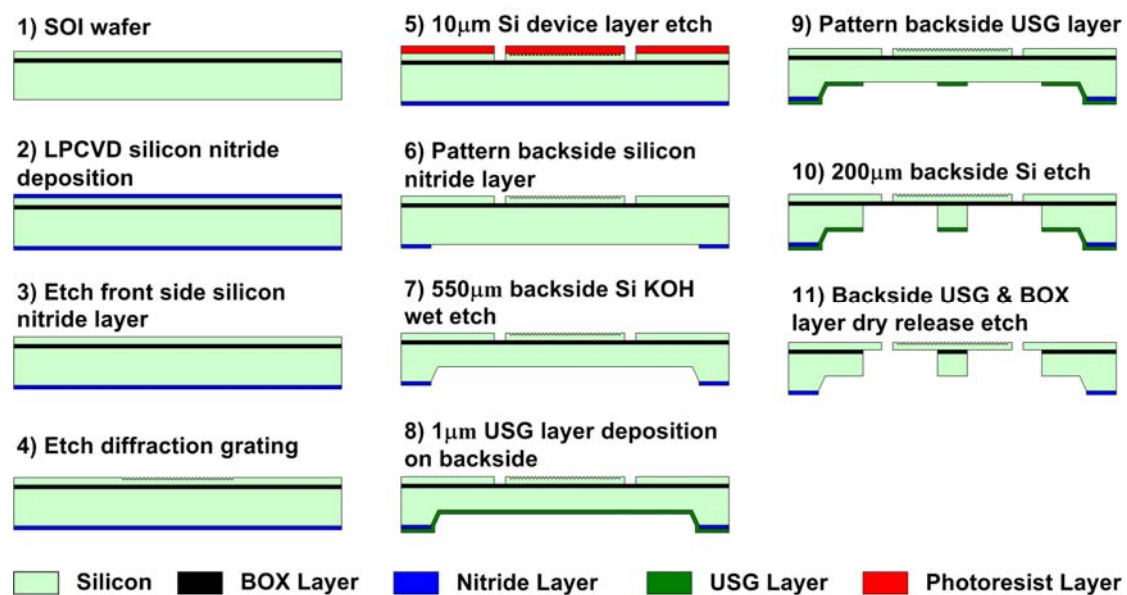


Figure 5.7 Initial micromachining process used to fabricate the grating platform with the diffraction grating and the connection pillar.

The thickness of the grating platform was accurately defined by the thickness of the silicon device layer and the thickness of the connection pillar is defined by the depth of the backside

cavity, formed by wet anisotropic Si etch which has excellent etching uniformity. Grating platforms and connection pillars with different dimensions can be easily fabricated by simply choosing SOI wafers of the required specifications and tuning process parameters.

Although using the fabrication process based on SOI wafer is simple and offers precise control of the thickness of the grating platform, the residual stress in the BOX layer deforms the thin grating platform statically. Figure 5.8 shows a measured profile of the grating platform using a white light interferometer.

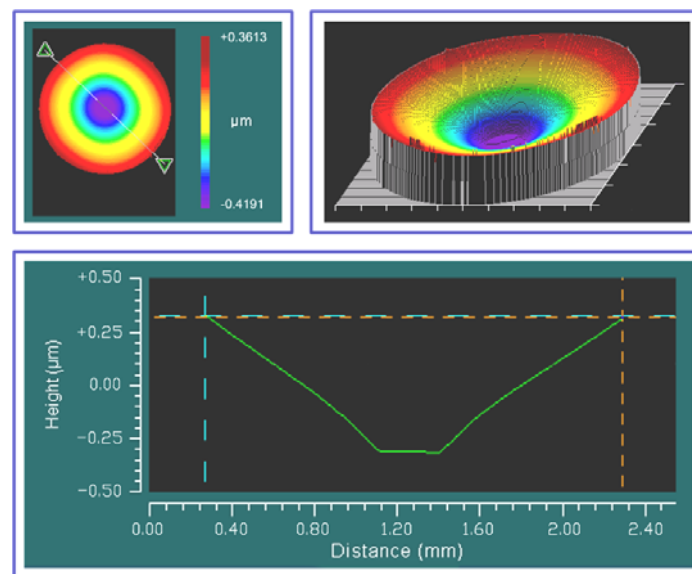


Figure 5.8 White light interferometer measured surface profile of the diffraction grating fabricated using SOI wafers.

Since small deformations of the grating platform will bring about significant aberration to the optical system and degrade the optical performance, the thickness of the grating platform has to be thick enough to eliminate this effect, which unfortunately increases the rotational inertia. This prevents the potential advantages of the double-layered configuration to be fully utilized.

Besides, the usage of SOI wafers may increase the total cost.

To eliminate the influence of the residual stress in the BOX layer and further reduce the total cost, an improved micromachining process based on normal bulk silicon wafers has been developed. Compared with SOI wafers, bulk silicon wafers are much cheaper and without any residual stress problem, yielding flatter grating platform with higher optical quality.

In the modified process, the thickness of the grating platform is determined by the process parameters, which offers flexibility in choosing the thickness of the grating platform. Figure 5.9 shows the schematic of the improved micromachining process to fabricate the diffraction grating, grating platform and backside pillar. Normal single-side polished bulk silicon wafers with a thickness of $750\mu\text{m}$ were used in the fabrication process.

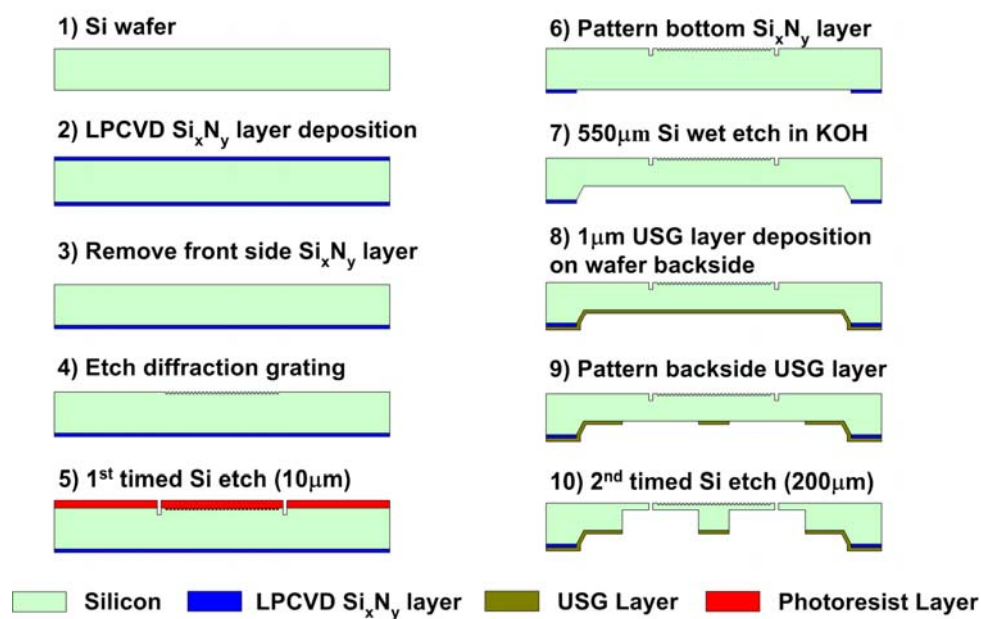


Figure 5.9 Improved micromachining process used to fabricate the diffraction grating, grating platform and connection pillar.

As shown in Figure 5.9, a 200nm thick LPCVD silicon nitride layer was deposited on both sides of the wafer and the top layer was removed by a following RIE process. Then, the diffraction grating was patterned and etched using deep-UV lithography and timed RIE process. The depth of the grating groove is controlled to be 150nm for maximum diffraction efficiency. Next, the grating platform was formed by a 1st DRIE process. The depth is controlled to be 10 μ m, which defines the thickness of the grating platform and serves as an etching stop mark for the following process. A 2.4 μ m thick photoresist layer (resist type: AZ6624) was used as the masking layer. The LPCVD layer on wafer's backside was patterned using RIE and a 550 μ m deep square cavity was formed by wet anisotropic Si etch in KOH solution (35 wt%, 75°C). A 1 μ m PECVD USG layer was deposited onto the wafer's backside and patterned using RIE. Finally, the connection pillar was formed and the grating platform was released by the 2nd timed DRIE process which stopped when trenches formed by the 1st DRIE process were fully exposed. Figure 5.10(a) shows a SEM image of the fabricated grating platform and connection pillar. The improvement on static flatness was verified by white light interferometer measurement result, as shown in Figure 5.10(b).

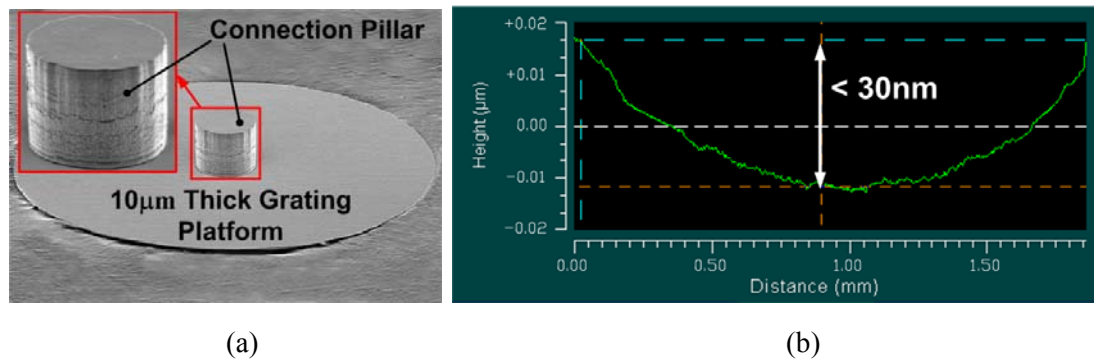


Figure 5.10 (a) SEM image of the fabricated grating platform and the connection pillar; (b) white light interferometer measurement static deformation of the diffraction grating.

5.3.2 Electrostatic comb-driven 2-DOF circular resonator

The electrostatic comb-driven 2-DOF circular resonator was fabricated using SOI micromachining technology. The SOI wafer has a 80 μm thick heavily doped silicon device layer, a 2 μm thick BOX layer and a 650 μm thick silicon substrate. The fabrication process flow is illustrated in Figure 5.11.

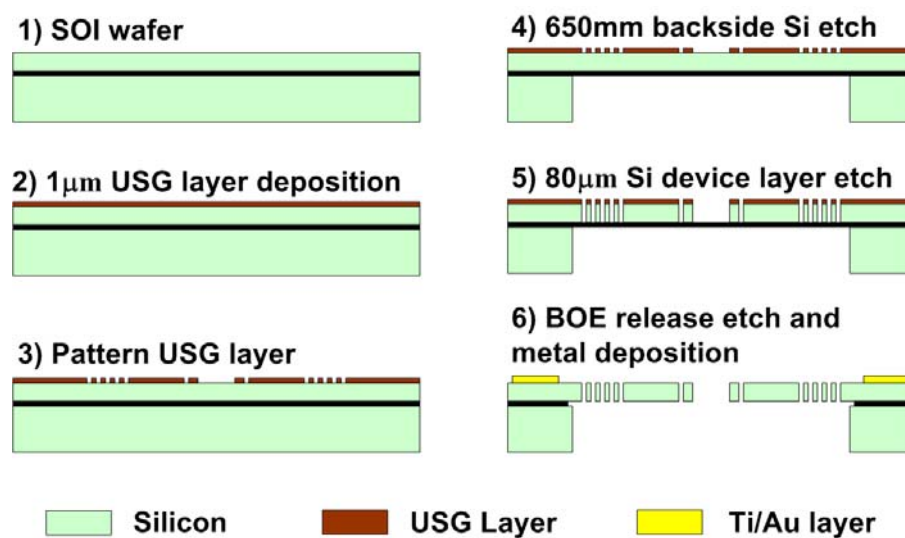


Figure 5.11 Fabrication process flow of the electrostatic comb-driven 2-DOF circular resonator.

As shown in Figure 5.11, a 1 μm PECVD USG layer was deposited onto the SOI wafer's front side and patterned by using a RIE process. It was subsequently used as the hard mask for the following DRIE etching process. The SOI wafer was patterned on its backside and the 650 μm thick silicon substrate was etched through by a following DRIE process to expose the region encompassing all the structures. The BOX layer was used as a stop layer for the DRIE etching process. Next, the 80 μm thick silicon device layer was etched through from the wafer's front side by another DRIE process, which is also stopped at the BOX layer. After this step, the

connection platform with a mounting hole, the circular comb-drive actuator and suspension flexures were formed. The USG layer on the wafer's front side and the exposed BOX layer were etched away in BOE solution so that all the structures formed in the silicon device layer were released. Finally, the metal pads for wire bonding were formed by evaporating 100nm/500nm thick Ti/Au layer through a shadow mask. Figure 5.12 shows a microscopic image of the fabricated 2-DOF electrostatic comb-driven circular resonator.

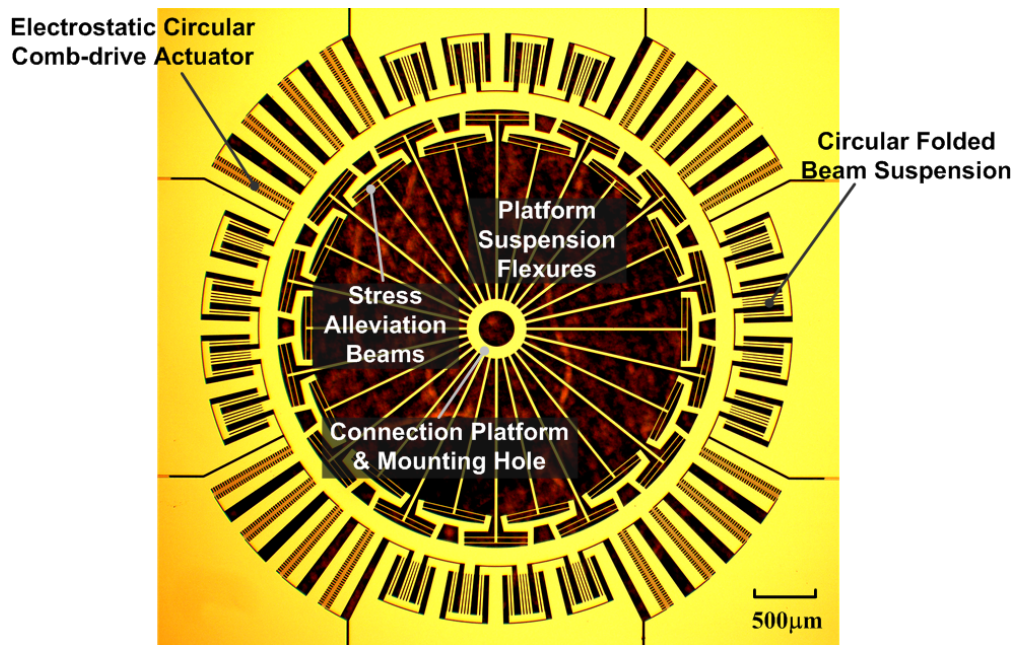


Figure 5.12 Microscopic image of the fabricated electrostatic comb-driven 2-DOF circular resonator.

5.3.3 Manual assembly process

After the grating platform and its driven 2-DOF circular resonator have been fabricated, they were assembled manually using an in-house developed manual aligner, as shown in Figure 5.13. Figure 5.14 shows a schematic illustration of the manual assembly process.

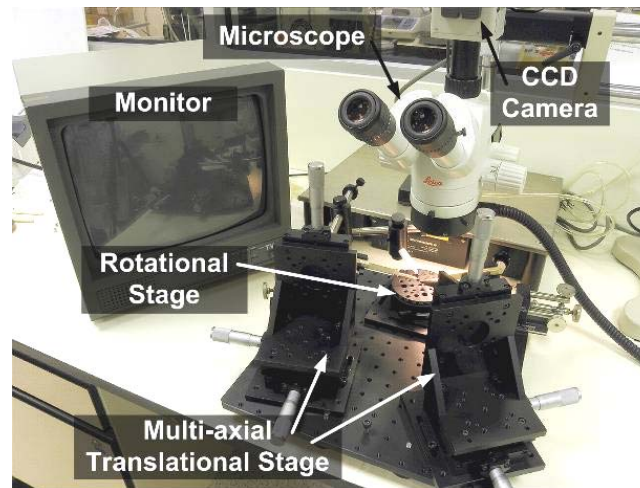


Figure 5.13 Photograph of the in-house developed manual aligner.

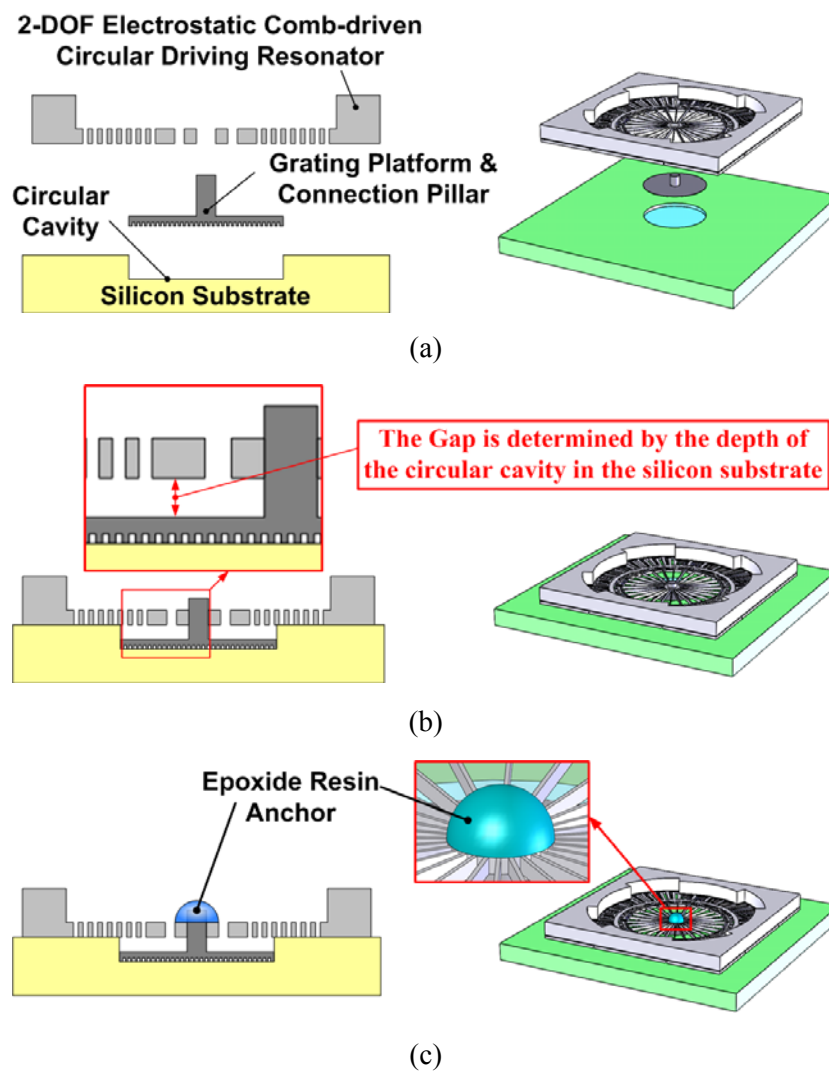


Figure 5.14 Schematic illustration of the manual assembly process.

As shown in 5.14(a), both the grating platform and 2-DOF electrostatic comb-driven circular resonator were turned upside down before assembly. A silicon substrate with a circular cavity located at its center, which acts as a mold during the manual assembly process, was designed and fabricated using the bulk micromachining process. The circular cavity having diameter 2050 μm and depth 90 μm was formed by a timed DRIE process, ensuring that the bottom of the cavity is parallel to the surface of the substrate. Then the grating platform was placed inside the circular cavity with connection pillar facing upwards. The driving resonator was held by a gripper attached to a 3-axes precision positioner. The 2-DOF circular resonator was then aligned under a microscope so that the mounting hole and the connection pillar were concentric. Next, the 2-DOF circular resonator was pressed tightly until it contacts the surface of the fixed silicon substrate. Meanwhile, the connection pillar was inserted into the mounting hole, as shown in Figure 5.14(b). The gap between the grating platform and the 2-DOF circular resonator was determined by the depth of the circular cavity in the silicon substrate. The parallelism between the diffraction grating and its driving actuator was ensured by the accuracy of the fabricated silicon substrate. Finally, the connection pillar and the connection platform were bonded together by AralditeTM 2012 Epoxy Adhesive (as shown in Figure 5.14(c)) and cured in an oven with a temperature of 40°C for 2 hour to achieve full strength of 25 to 30MPa. Figure 5.15 shows the whole view and the part of the assembled electrostatic double-layered vibratory grating scanner through photographic and SEM images.

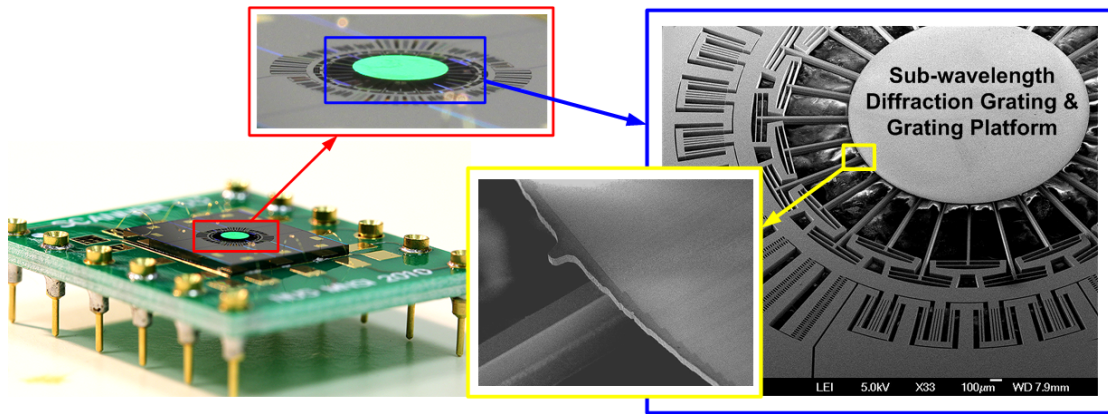


Figure 5.15 Images of the assembled prototype double-layered vibratory grating scanner.

The backside view of the assembled device and the magnified view of the epoxide resin anchor are shown in Figure 5.16.

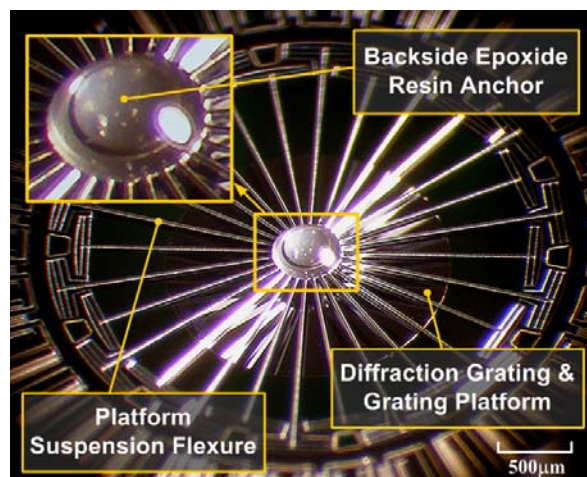


Figure 5.16 Microscopic images showing the backside of the assembled double-layered grating scanner and the magnified view of the epoxide resin anchor.

Since the MEMS vibratory grating scanner utilizes the in-plane rotational motion of a diffraction grating to scan the laser beam, the parallelism between the diffraction grating and the rotational plane is a very important factor that influences the quality of the laser scanning trajectory. To evaluate the accuracy of the proposed manual assembly process, the parallelism

of the diffraction grating and its driving actuator was measured using a white-light interferometer, as shown in Figure 5.17. The measurement result shows that the slope angle of the diffraction grating relative to its driving actuator is only 0.0297° , a value so small that it has negligible effect on the quality of the laser scanning trajectory. This indicates that the proposed manual assembly process is sufficiently accurate for the proposed electrostatic double-layered vibratory grating scanner.

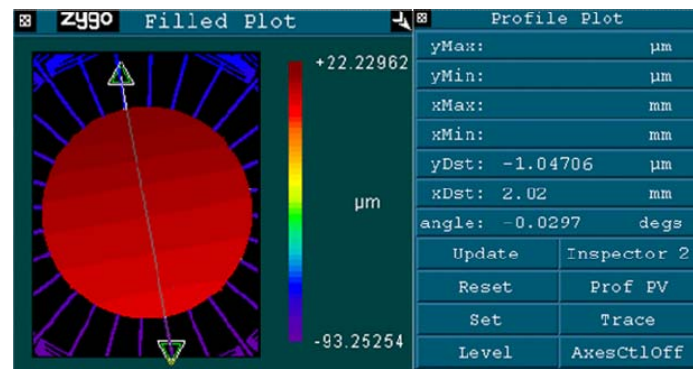


Figure 5.17 White light interferometer measurement result of the parallelism between the diffraction grating and its driving actuator.

5.4 Experimental characterizations

5.4.1 Dynamic characterizations

The dynamic performance of the prototype electrostatic double-layered vibratory grating scanner was tested using a linearly polarized He-Ne laser beam with a wavelength of 632.8nm. The experimental setup is schematically illustrated in Figure 5.18.

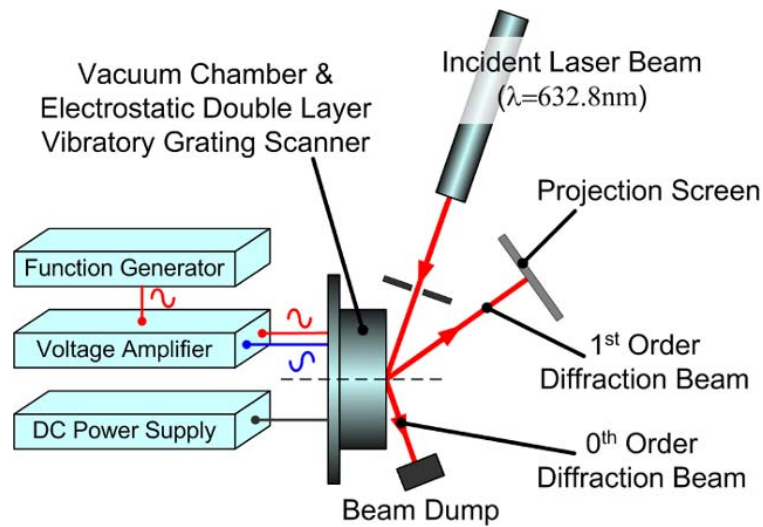


Figure 5.18 Schematic illustration of the experimental setup for dynamic characterization.

The incident angle of the illuminated laser beam was determined to be 71.8° to achieve bow-free scanning for a 400nm pitch diffraction grating. The prototype grating scanner was mounted in a vacuum chamber and tested under both atmospheric and vacuum pressure (0.12mTorr). The electrostatic 2-DOF circular resonator was driven by a push-pull mechanism. A projection screen was placed 100mm away and aligned perpendicular to the direction of the 1st order diffracted beam when the grating is stationary. The optical scan angle was obtained through measuring the length of the scanning trajectory. Figure 5.19 shows a photograph of the projected laser scanning trajectory on a projection screen. While tested in atmosphere, the driving voltages were fixed at 100V DC bias and 200V AC peak-to-peak voltages. The prototype device with a 2mm diameter diffraction grating was capable of scanning at 21336Hz with an optical scan angle of 21° , resulting in $\theta_{opt}D$ product of 42 deg·mm. While tested in vacuum condition with a pressure of 0.12mTorr, the driving voltages were fixed at 65V DC bias and 130V AC peak-to peak voltages. The scanning amplitude of the prototype scanner was measured around 33.5° with a scanning frequency of 21591 Hz.

The resultant $\theta_{opt}D$ product is 67 deg·mm.

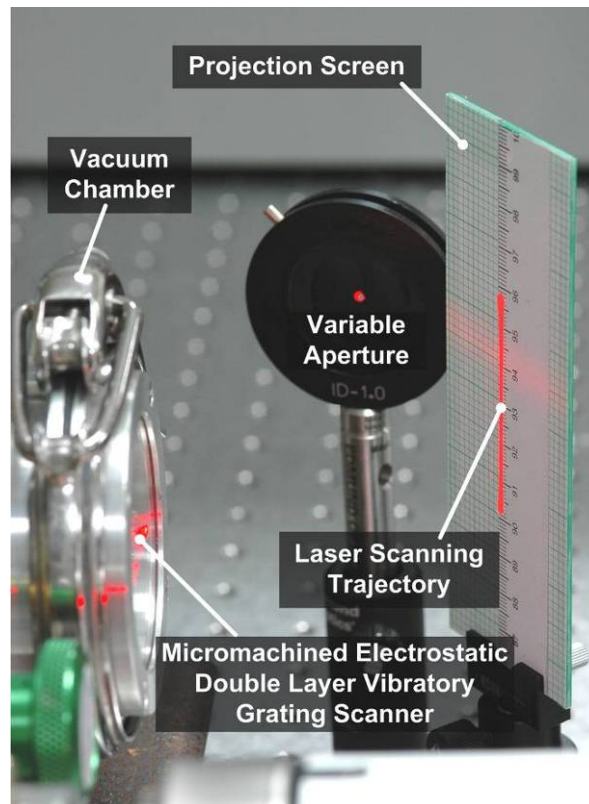


Figure 5.19 Photograph of the laser scanning trajectory of the prototype scanner on a projection screen.

The frequency response of the prototype scanner near its first resonating mode obtained in vacuum is shown in Figure 5.20. As expected, the dynamic performance of the prototype scanner demonstrated some level of large-deflection nonlinearity. For example, the scanning amplitudes were different during the forward and backward frequency sweeps, the amplitude jumping phenomena was observed and the resonant frequency depended on the scanning amplitude.

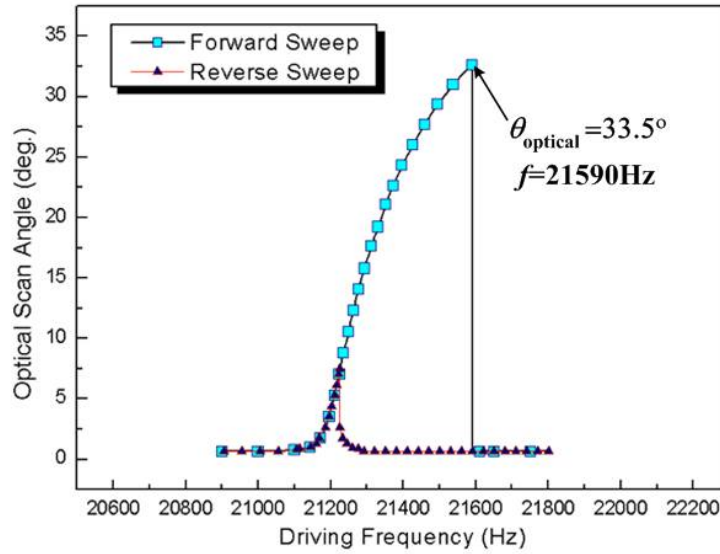


Figure 5.20 Measured frequency response of the prototype scanner in vacuum at frequency regions near the resonant frequencies of its 1st resonating mode.

By gradually increasing the driving voltages from 5 V dc bias and 10 V ac peak-to-peak voltages to 65 V dc bias and 130 V ac peak-to-peak voltages, the resonant frequencies at different scanning amplitudes were determined by recording the frequencies at which the forward-sweeping amplitude jumping occurred. Then those recorded frequencies are normalized by the smallest value. Figure 5.21 shows the comparison between the theoretical predictions and experimental measurements of the variations of the normalized resonant frequencies as a formulation of optical scan angle. The theoretical predictions were based on Eq. 3.53 in Section 3.4.3. It can be seen that there is a good agreement when the scanning amplitude is small. The error increases as the scanning amplitude increases. This is because only first order of the parameter “ ϵ ” was considered in the theoretical model derived in Section 3.4.3. The theoretical calculation accuracy could be improved with higher order of “ ϵ ” but numerical methods have to be involved to obtain the solution..

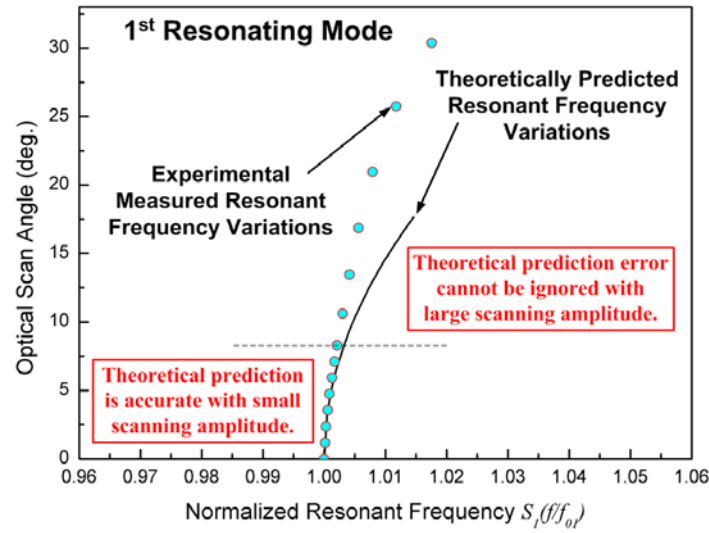


Figure 5.21 Comparison of theoretical and experimental measured variations of normalized resonant frequencies with optical scan angles.

5.4.2 Optical quality of the scanned beam

Characterization experiments to determine the scanned-beam quality and optical resolution were conducted in atmosphere rather than vacuum. This is to avoid the disturbance of the multiple-reflections brought by the uncoated thick glass plate on the vacuum chamber.

The quality of the scanned-beam was measured with an in-house developed cyclic lateral shearing interferometer [132] and a Mach-Zehnder interferometer respectively. The cyclic lateral shearing interferometer is a common-path interferometer. One of the major advantages of using a common-path interferometer is that the obtained interferogram is capable of resisting external vibrations resulting in high signal-to-noise ratio. However, the information obtained with lateral shearing interferometers is implicit and require some computation to reconstruct the deformed wavefront. The Mach-Zehnder interferometer is an open-path interferometer. The incident light beam was separated into two beams: one is used as a

reference beam and the other one illuminates the surface under test. The reference beam and the beam under test are then combined to form an interferogram. The major advantage of Mach-Zehnder is that the information obtained is explicit and the deformed wavefront is easy to be reconstructed. However, open-path interferometers are sensitive to vibrations resulting in a low signal-to-noise ratio. Hence, these interferometers have higher vibration isolation requirements of the experimental environments as compared with the common-path interferometers.

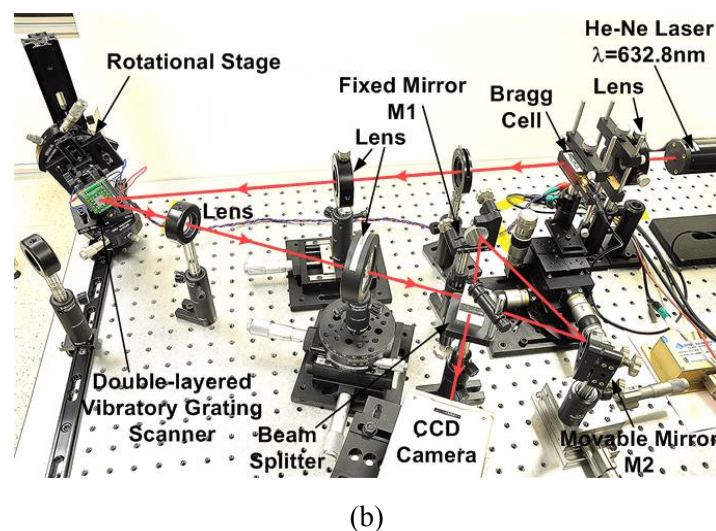
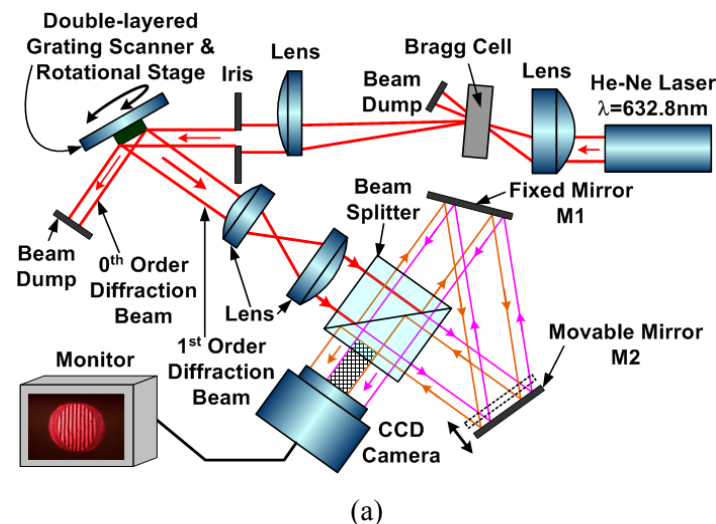


Figure 5.22 (a) Schematic and (b) photograph showing the experimental setup to investigate the scanned-beam quality using an in-house developed cyclic lateral shearing interferometer.

The quality of the scanned-beam was firstly measured by a cyclic lateral shearing interferometer and the schematic illustration and photograph of the experiment setup are shown in Figures 5.22(a) & (b). The incident laser beam was strobed using an acousto-optic modulator (AOM) to produce light pulses with a full-width-half-maximum (FWHM) pulse duration of 25ns, which was synchronized to the driving signal to “freeze” the motion of the scanned beam. To shorten the response time of the AOM, the He-Ne laser beam was focused into the Bragg cell through a 75mm plano-convex lens. The strobed 1st order diffraction beam from the Bragg cell was then collimated using a 300mm plano-convex lens and directed onto the grating scanner with an incident angle of 71.8° . The strobed beam positions were controlled by adjusting the phase difference between the strobe pulses and the ac driving signal and brought to the same horizontal plane by rotating the rotational stage, which the device is mounted. The 1st order diffraction beam from the scanner was expanded to 2.5 times of its original size using 50mm and 125mm achromatic lenses. The expanded beam was then directed to a cyclic lateral shearing interferometer, which is constitute of a beam splitter, a fixed mirror M1 and a movable mirror M2. In the interferometer, the expanded beam was split into two beams traveling in opposite directions and then merged together to form an interference pattern, which is captured by a CCD camera. The amount of the lateral shearing is controlled by the movable mirror M2. A small amount of defocusing was introduced to the system by tuning the lenses, which are used to expand the incident beam, so that the lateral shearing interference pattern for an aberrationless wavefront is some straight fringes with uniform gaps. The number of the fringes is determined by the amount of the defocusing introduced. Larger amount of defocusing will result in smaller gaps between

fringes.

Figure 5.23 shows interferograms captured at four different regions along the scan line, namely at center, one-third and two-thirds of the scan amplitude and extreme position. The interferogram at the center of the scan line mainly reflects the static flatness of the grating platform at this position, as the acceleration force is zero. While the interferogram at the extreme position of the scan line mainly reflects the dynamic flatness as the grating platform experiences the maximum acceleration force at this position. As shown in Figure 5.23, there is no significant distortion observed in the interference patterns, which indicates the good quality of the scanned beam. This is because the optical interferometer is very sensitive and little amount of aberrations of the wavefront will severely distort the interference pattern.

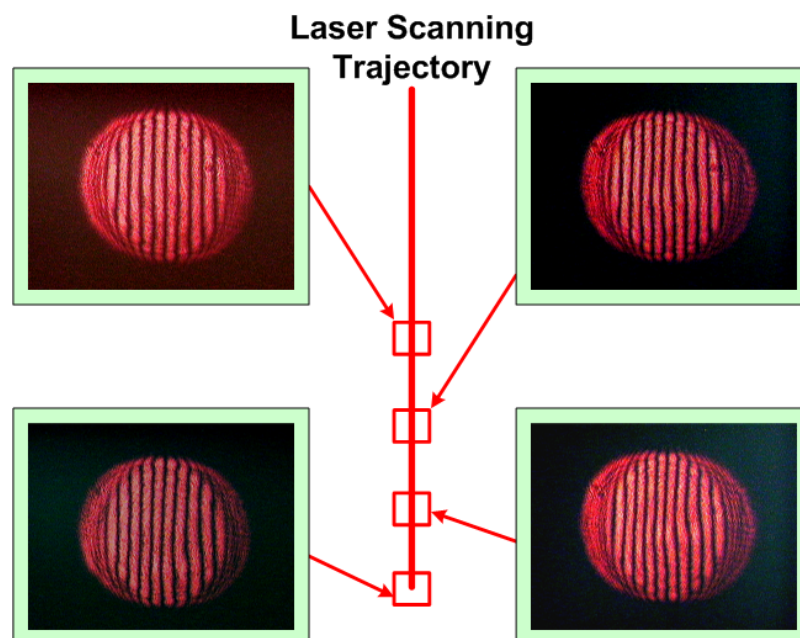


Figure 5.23 Measured interferograms of the strobed spots at four different positions of the scan line using cyclic lateral shearing interferometer.

The quality of the scanned-beam was also measured by an in-house developed Mach-Zehnder interferometer. Figures 5.24(a) & (b) show the schematic illustration and photograph of the experiment setup, respectively.

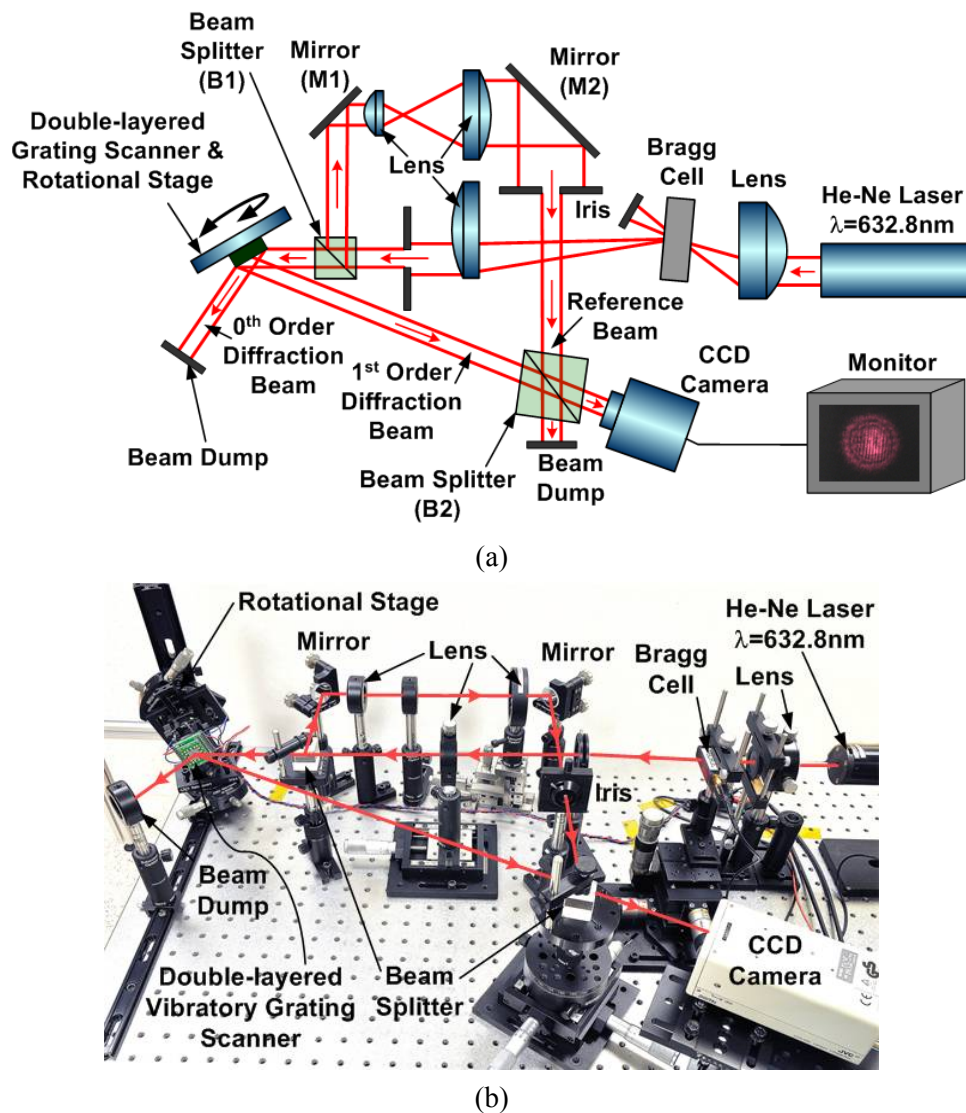


Figure 5.24 (a) Schematic illustration and (b) photograph showing the experimental setup to investigate the scanned-beam quality using an in-house developed Mach-Zehnder interferometer.

Similar to the experimental setup shown in Figure 5.22(a), the incident laser beam was

strobed using the AOM to “freeze” the motion of the scanned beam. The strobed beam was then collimated and directed into the Mach-Zehnder interferometer, where the collimated laser beam was split into 2 beams by the beam splitter B1. One beam illuminates the grating scanner with the incident angle of 71.8° . The other beam, which can be treated as the reference beam, was reflected by the mirror M1 and expanded to 2 times of its original size using 50mm and 100mm achromatic lenses. Then the expanded beam was reflected by the mirror M2 and went through an iris to have its size regulated. After that the reference beam and the 1st order diffraction beam from the grating scanner were merged together by the beam splitter B2 to form an interference pattern and captured by a CCD camera. The reference beam and the 1st order diffraction beam were merged with a small angle intentionally so that the interference pattern for an aberrationless wavefront consists of uniform distributed straight fringes. The gap between the fringes is determined by the angle between the reference beam and the diffraction beam and larger angle will result in smaller fringe gaps.

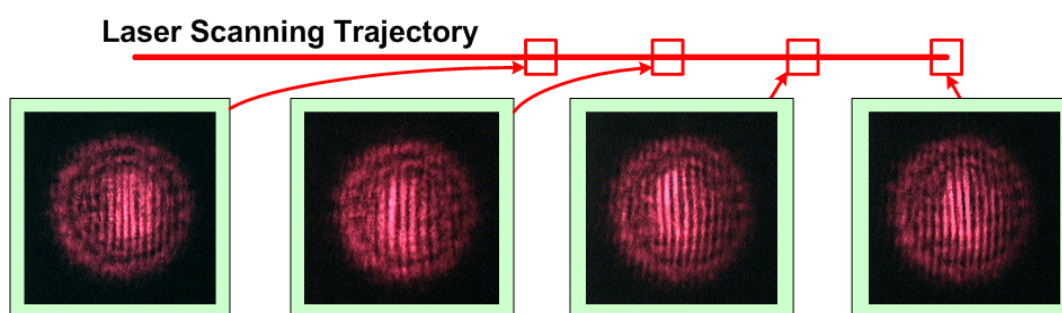


Figure 5.25 Measured interferograms of the strobed spots at different positions of the scan line using a Mach-Zehnder interferometer.

Similarly, the interferograms were captured at the center, one-thirds, two-thirds and extreme positions of the scan line shown in Figure 5.25. The measurement again results show little

distortion of the interference pattern also indicating the good quality of the scanned beam at high speed.

To measure the optical resolution, the strobed 1st order diffraction beam from the scanner was focused to a CCD camera using a 500mm plano-convex lens. Figures 5.26(a) & (b) show the schematic illustration and photograph of the experiment setup.

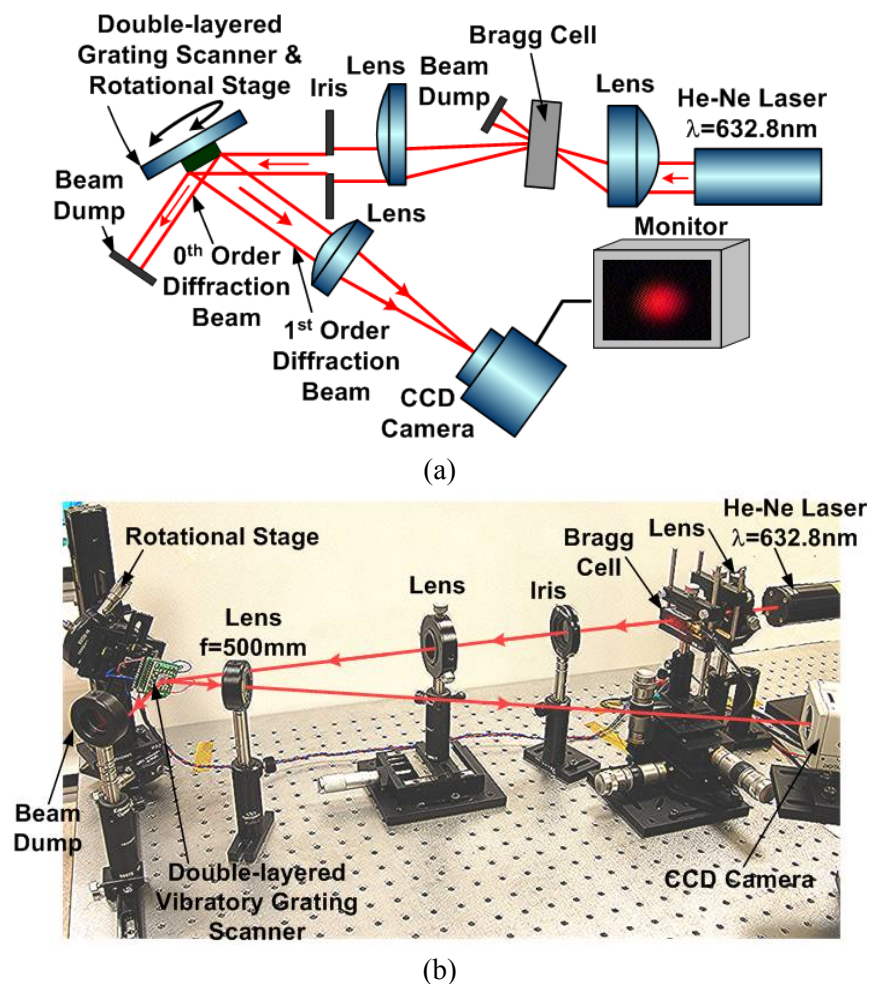


Figure 5.26(a) Schematic illustration and (b) photograph showing the experimental setup to investigate the optical resolution.

The captured light intensity distributions of the focal spots at different positions of the scan line are shown in Figure 5.27. The FWHM diameter of the focal spots was determined to be around $200\mu\text{m}$ along the scan direction. This indicates an optical resolution of 916 pixels per-unidirectional-scan when the vibratory grating scanner is operated in atmosphere. When the vibratory grating is operated in vacuum condition with an optical scan angle of 33.5° , the optical resolution can be estimated to be 1460 pixels per-unidirectional-scan according to the experimentally measured spot size.

Laser Scanning Trajectory

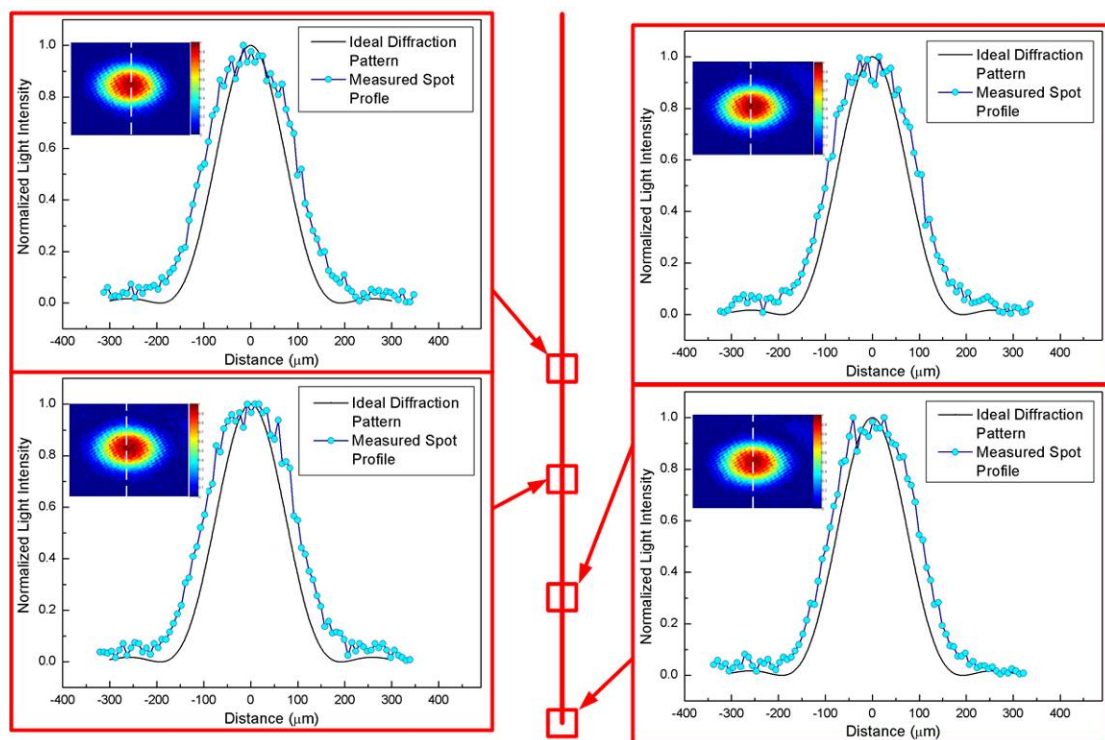


Figure 5.27 CCD camera captured light intensity distribution of the focal spots at different positions of the scan line.

5.5 Summary

A double-layered vibratory grating scanner driven by the 2-DOF circular resonator was successfully fabricated and demonstrated in this chapter. Double-layered grating scanners have the potential to scan at large amplitudes at high scanning speeds with large aperture sizes.

The prototype double-layered grating scanner was fabricated using a hybrid scheme, which combined the bulk micromachining process and the post assembly process. The advantages of the hybrid scheme are the reduced complexities and difficulties of fabrication process and increased flexibility to the device design. The grating platform and driving actuators were designed and fabricated separately. They were then assembled together by a post-assembly process.

The diffraction grating and its platform were initially fabricated using SOI wafers. Although the SOI wafer based fabrication process could offer precise control of the grating platform's thickness, the residual stress in the BOX layer will deform the grating platform statically, which is not acceptable. Then an improved fabrication process based on bulk silicon wafer was developed to overcome this problem.

The double-layered grating scanner was successfully fabricated and assembled. The prototype scanner with a 2mm diameter diffraction grating is able to scan at 21591Hz with an optical scan angle of 33.5° in vacuum. The resultant $\theta_{Opt}D$ product is 67 deg·mm. Compared with

previously developed single-layered grating scanner driven by 2-DOF circular resonator, there is a 1.7 times increase of $\theta_{opt}D$ product with a similar scanning speed.

The scanned beam quality was verified to be good using a cyclic lateral shearing interferometer and a Mach-Zehnder interferometer. The optical resolution of the scanner was experimentally measured to be 916 pixels per unidirectional scan while scanning in atmosphere. While scanning in vacuum condition, the optical resolution can be estimated to be 1460 pixels per-unidirectional-scan.

Chapter 6 Synchronized laser scanning of multiple MEMS diffraction gratings

This chapter presents an effective method to achieve synchronized laser scanning of multiple beams by using MEMS diffraction gratings with resonant frequency fine-tuning mechanisms. Multiple gratings are actuated in-plane by a common electrostatic comb-driven resonator and their resonant frequencies can be fine-tuned to compensate the micromachining process errors. Continuous and reversible resonant frequency tuning was achieved. The resonant frequencies of vibratory diffraction gratings can be gradually tuned up to a few hundred Hertz with tuning voltages increased from 0V to 5V. Synchronized laser scanning of multiple beams was experimentally demonstrated using stroboscopic method.

6.1 Background

Laser scanning using a diffraction grating has the potential to achieve high scanning rate without optical performance degradation due to dynamic aberration, which has been proven experimentally in previous chapters. This is attributed to the adoption of the in-plane rotation of a diffraction grating instead of out-of-plane deflection of a reflective surface to scan the laser beam. Our reported prototype scanners have shown promise for many narrow-band laser scanning applications, such as monochromatic laser scanning displays. However, due to the dispersive grating used, they are not suitable for applications that require multiple-wavelength collinear scanning, such as miniaturized raster-scanning color displays, laser color printers, and laser cameras. For example, in miniaturized color displays, in order to scan a color image,

the scan lines of different wavelengths (primary colors: red, green, and blue) have to be essentially collinear. In other words, the red, green, and blue laser spots must be always at the same location and scan at the same velocity. Since a diffraction grating is a dispersive element, different wavelengths leave the diffraction grating at different diffraction angles and may have different scanning velocities. Consequently, a MEMS vibratory structure having one diffraction grating cannot be used for multi-wavelength collinear scanning applications such as color displays.

To achieve multi-wavelength collinear scanning, synchronized motion of multiple gratings has to be realized. This can be achieved by either configuring different grating elements on a common platform or on multiple grating platforms with synchronized motion, as shown in Figure 6.1.

The collinear scanning scheme using multiple grating elements on a common platform has been demonstrated by G. Zhou et al. in 2006, as shown in Figure 6.1(a) [41]. The scheme is simple and easy to be implemented. However, the aperture size of each grating elements is limited. Although the total area of the diffraction grating platform can be increased using double-layered configuration, the moment of inertia of the grating platform will be increased significantly, which could reduce the scanning frequency and amplitudes.

The multi-wavelength collinear scanning can also be realized by using multiple gratings configured on different platforms with synchronized in-plane rotational motion, as shown in

Figure 6.1(b).

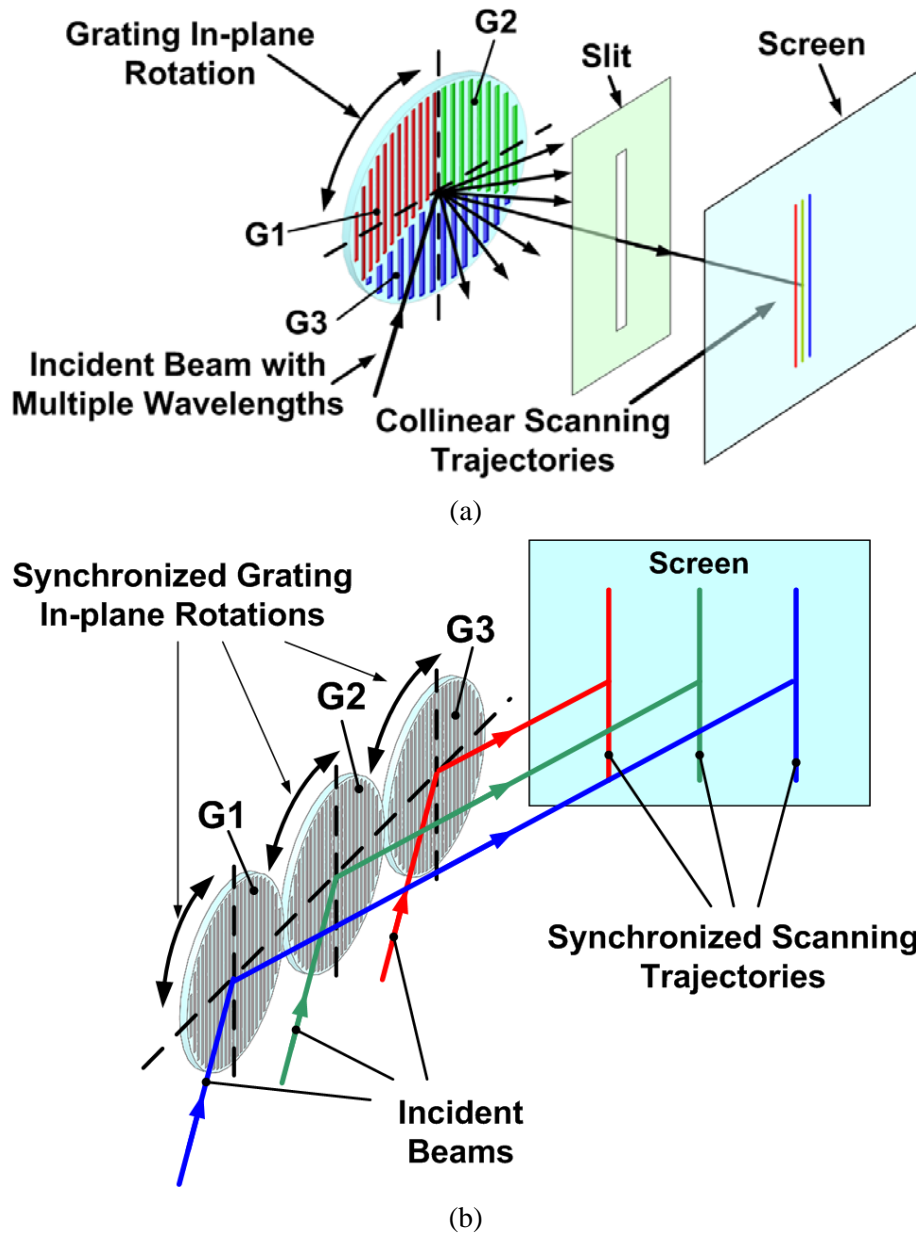


Figure 6.1 Schematic illustration of multi-wavelength collinear scanning of laser beams using multiple grating elements configured on (a) a common grating platform with and (b) multiple grating platforms with synchronized rotational motion.

The major advantage of this scheme is that adequate aperture size can be achieved for each grating element, resulting in higher optical efficiency and resolution. Synchronized motion

can be achieved by using phase-locked-loop (PLL) control, which requires integrated angular position sensors in the scanner and complicated control electronics.

In this chapter, an effective method to achieve synchronized laser scanning of multiple beams using mechanically synchronized multiple gratings on different grating platform, which are actuated by a common driving resonator and vibrated at resonance. The vibrating amplitudes of each grating can be adjusted through tuning its resonant frequency by its frequency tuning mechanism. The mechanical synchronization scheme is based on multi-DOF resonant vibration system, as shown in Figure. 6.2.

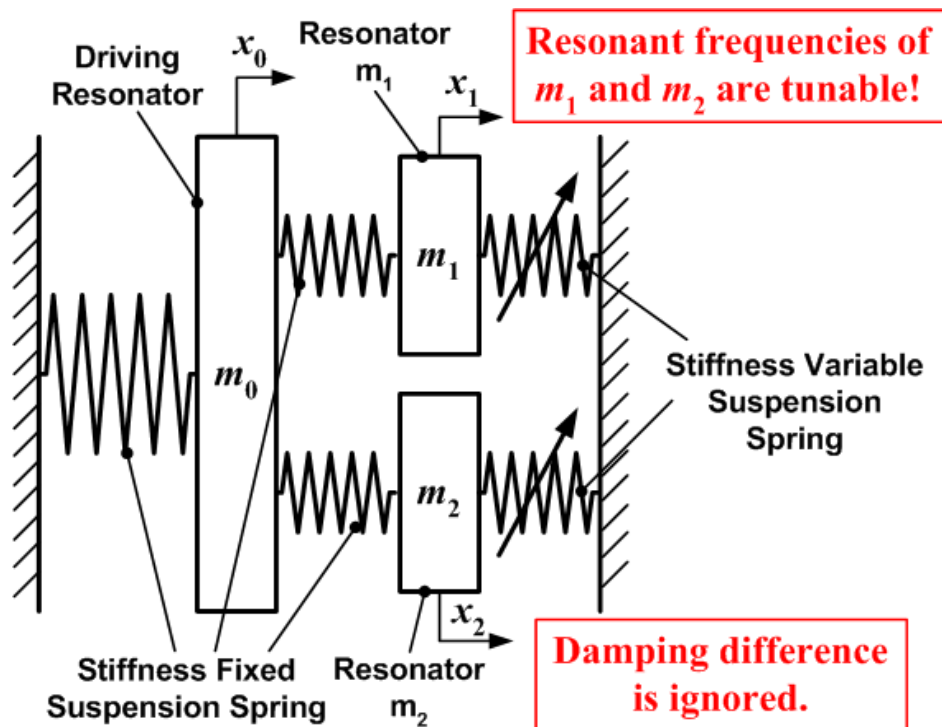


Figure 6.2 Schematic illustration of a mechanical synchronization scheme.

As shown in Figure 6.2, multiple working resonators are attached to a common driving

resonator. The geometric dimensions of all working resonators are designed to be the same, so that the viscous damping difference can be ignored. When all working resonators have the same resonant frequencies, the multi-DOF vibration system can be reduced to a 2-DOF vibration system. All working resonators will vibrate at the same frequency with the same phase in resonance. However, due to the imperfections of the fabrication process, there are small deviations of suspensions among the resonators, which will cause amplitude difference between the resonators. This can be solved by adding a frequency tuning mechanism in each working resonator. This is used to compensate for the fabrication errors by tuning the stiffness of the resonator's suspensions.

Different reversible frequency tuning methods have been investigated in the literature, such as utilizing the electrostatic spring effect [133-134], localized thermal stressing effect [135] and mechanically stiffening effect of a torsional spring [136]. In this work, we utilize an electro-thermal bent-beam actuator to fine-tune the stiffness of a T-shaped flexure through mechanical stretching.

6.2 Design and fabrication

Figure 6.3 shows a schematic illustration of the MEMS vibratory grating scanner with two diffraction gratings and their integrated resonant frequencies fine-tuning mechanisms. All the structures have a same thickness of 80 μ m. The diffraction grating has a diameter of 1mm and grating pitch of 400nm. Each diffraction grating platform is suspended and connected to the substrate by four circular fold-beam suspensions with a beam width of 12 μ m and a beam

length of $500\mu\text{m}$. Each grating platform is connected to the common electrostatic comb-driven lateral resonator through a connection flexural beam with a width of $23\mu\text{m}$ and a length of $1000\mu\text{m}$. Two pairs of stress alleviation beams are perpendicularly connected to the bottom of each connection beam with a width of $6\mu\text{m}$ and a length of $300\mu\text{m}$. The common resonator is suspended by 92 sets of folded beam suspensions with beam width of $8\mu\text{m}$ and length of $260\mu\text{m}$. A total of 212 movable fingers are configured on one side of the common resonator with finger length of $105\mu\text{m}$, width of $7\mu\text{m}$, finger gap of $4\mu\text{m}$ and initial finger overlap of $50\mu\text{m}$.

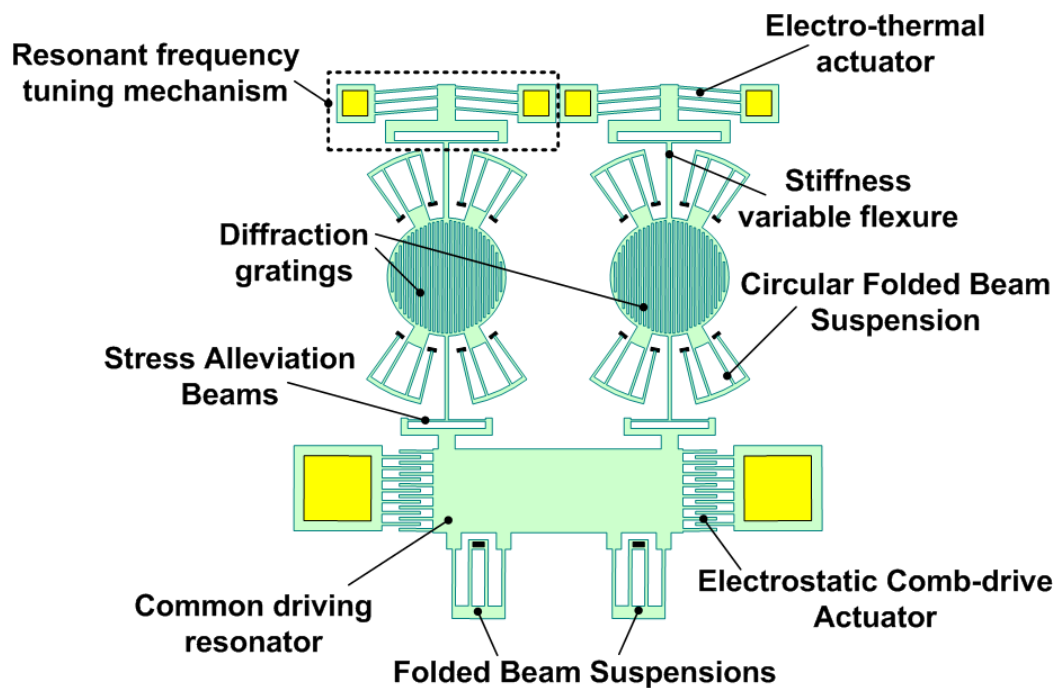


Figure 6.3 Schematic illustration of MEMS vibratory grating scanner with two diffraction gratings and their integrated resonant frequencies fine-tuning mechanisms.

Each grating platform is connected in turn individually to an electrothermal bent-beam tuning actuator through a T-shaped spring, as shown in Figure 6.4(a). In the tuning mechanism, the

T-shaped spring is connected to a movable block, which is suspended by four sets of folded beam suspensions with beam width of $8\mu\text{m}$ and length of $210\mu\text{m}$. The position of the movable block is controlled by an electrothermal bent-beam actuator, which consists of 43 pairs of bent beams with beam width of $8\mu\text{m}$, length of $700\mu\text{m}$ and an inclined angle of 0.6° . To minimize the influence of the heat generated from the electrothermal actuator, thermal isolation hole structures are configured on the movable block to increase the thermal resistance. The working principle of the T-shaped stiffness variable spring is shown in Figure 6.4(b). As shown in the figure, the spring consists of one main flexural beam and a pair of perpendicularly attached beams namely “a” and “b” respectively. While applying the tuning voltages, the flexure “b” will deform and the total rotational spring constant of the T-shaped spring changes accordingly.

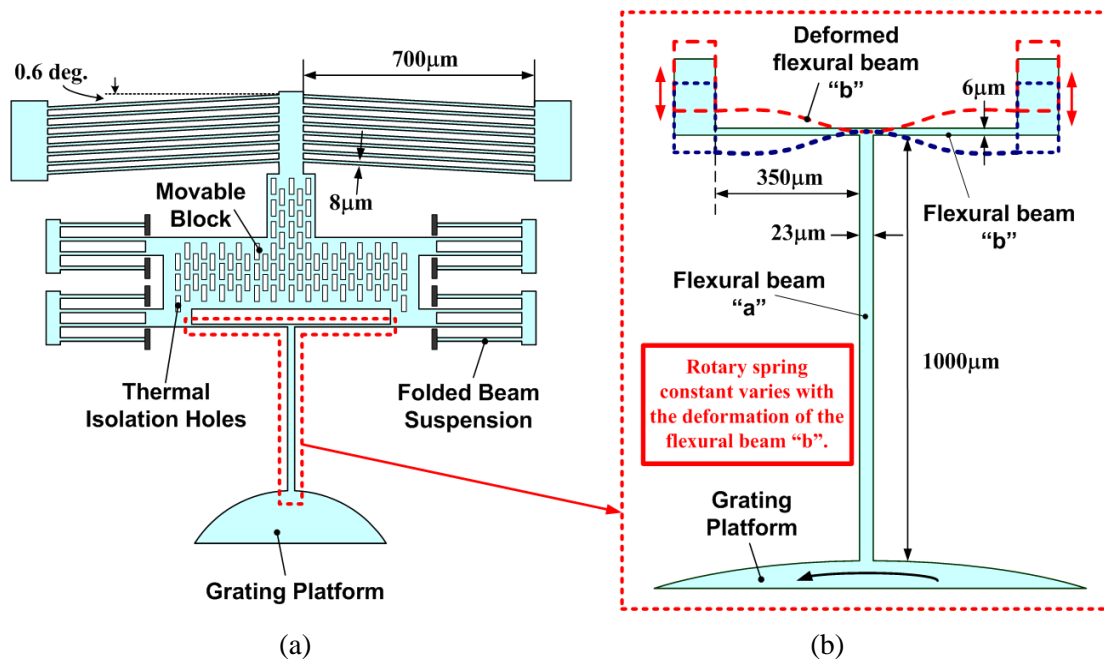


Figure 6.4 Schematic illustrations of (a) the electrothermal driven resonant frequency fine-tuning mechanism and (b) working principle of the T-shaped stiffness variable flexure.

The prototype scanner was fabricated using SOI micromachining technology and the process flow is shown in Figure 6.5. SOI wafers with 80 μm thick device layer, 2 μm BOX layer and 650 μm silicon substrate were adopted. As shown in Figure 6.5, two diffraction gratings with a period of 400nm were first patterned. Then a 1 μm thick USG layer was deposited on the wafer's top and patterned through a PECVD and RIE process. This was used as the hard mask layer for the following etching process. After that, the 650 μm thick silicon substrate is etched through from wafer backside using a DRIE process. The etching stopped at the BOX layer. The 80 μm thick silicon device layer was then etched through by another front side DRIE process. Diffraction grating platforms, suspension springs, electrostatic comb-drive actuators and electrothermal bent-beam actuators were formed. Next a wet etching process using BOE solution released all the structures. Finally, the metal pads and reflection layer on the grating were formed by a 2-step metal deposition process.

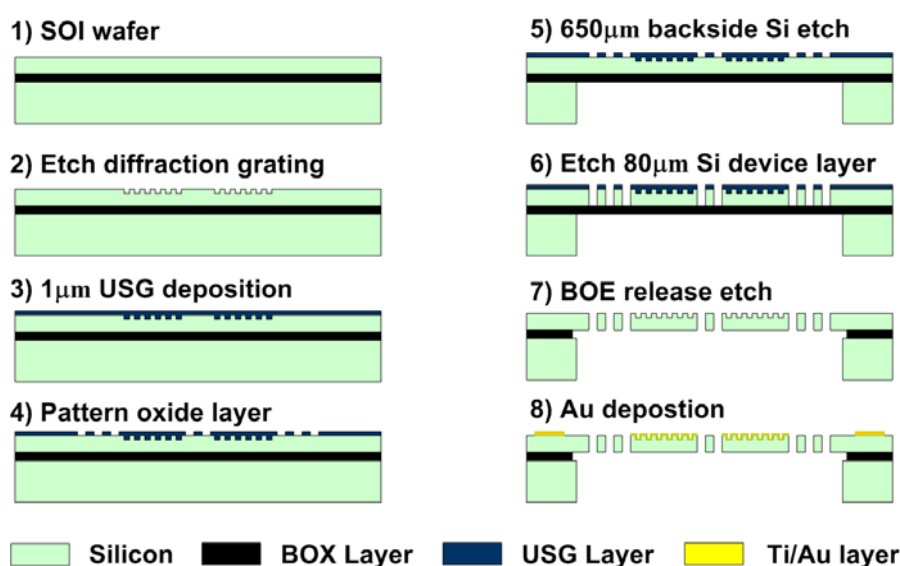


Figure 6.5 Schematic illustration of the process flow fabricating the prototype scanner with two diffraction gratings.

Figure 6.6 is a microscope image showing the whole view of the fabricated scanner. Figures 6.7 (a) & (b) show the magnified views of the common electrostatic comb-driven resonator with one diffraction grating and both diffraction gratings with their resonant frequencies fine-tuning mechanisms, respectively.

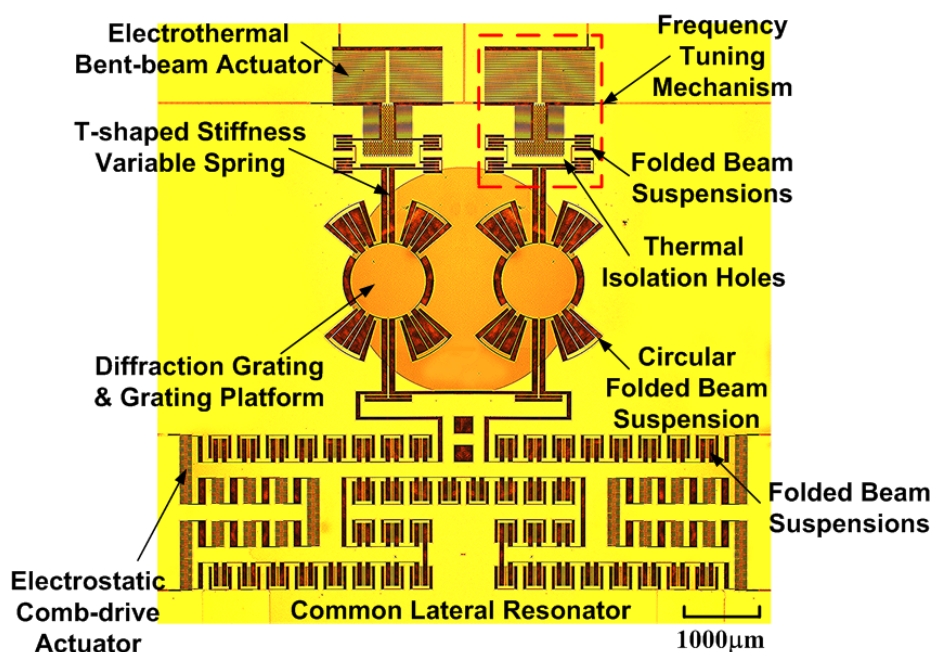


Figure 6.6 Microscopic image showing the whole view of the fabrication prototype scanner.

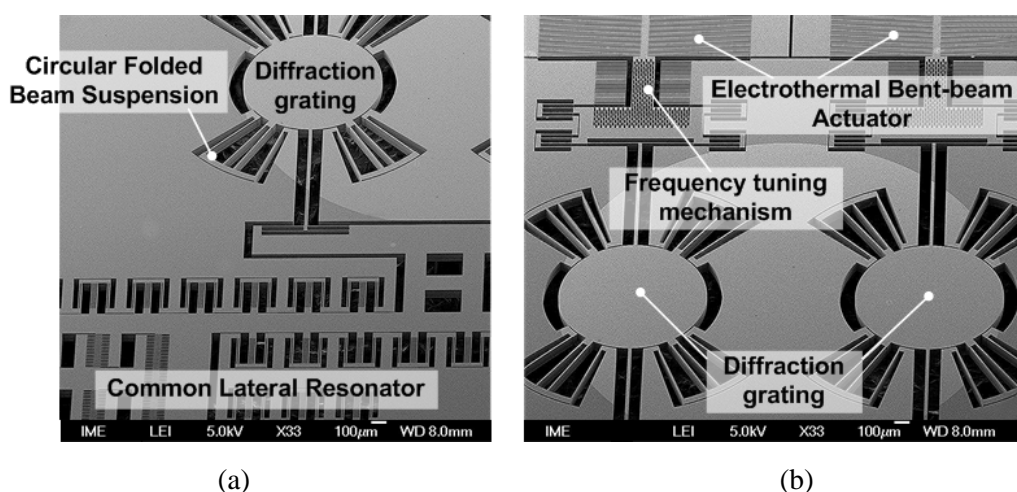


Figure 6.7 SEM images of the prototype device showing (a) common electrostatic comb-driven resonator with one diffraction grating and (b) diffraction gratings with their resonant frequencies fine tuning mechanisms.

6.3 Characterization

The variation of the resonant frequency of a grating with different tuning voltages was measured using a He-Ne laser beam in atmosphere. The schematic of the experimental setup is shown in Figure 6.8.

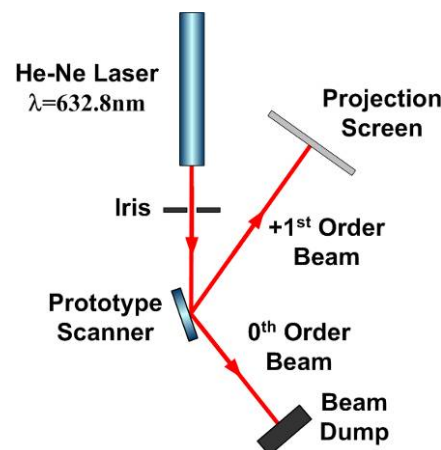


Figure 6.8 Schematic illustration of the experimental setup measuring the resonant frequency tuning capabilities.

The incident angle of the laser beam was fixed at 71.8° to achieve a straight scanning trajectory. A projection screen was aligned perpendicularly with the 1st order diffraction beam when the grating is stationary and placed a certain distance from the scanner. The optical scan angle was obtained by measuring the length of the scanning line on the screen.

Measurement result of variation of the resonant frequency of a grating with different tuning voltages is shown in Figure 6.9. As tuning voltages increased from 0V to 5V, the resonant frequency gradually decreased from 19870 Hz to 19588 Hz and the tuning range is 282 Hz. By design, we expect a resonant frequency increase through the spring stiffening effect.

However, in experiment the resonant frequency decreases with the increasing tuning voltages. This may be due to the initial deformation of the T-shaped spring caused by residual stress during the microfabrication process. In future, the influence of the residue stress can be compensated in the design stage. A required tuning trend and tuning range can be obtained through a proper design.

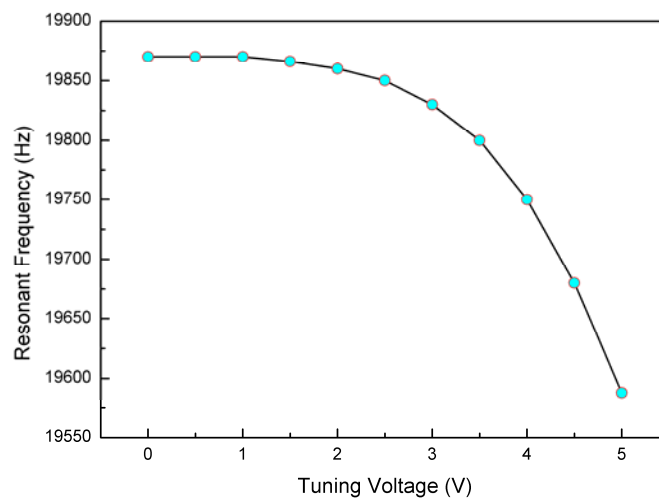


Figure 6.9 Measured variations of the resonant frequency with respect to different tuning voltages.

The synchronized laser scanning of two beams was demonstrated using the stroboscopic method and the schematic of the experiment setup is shown in Figure 6.10. The incident laser beam was strobed by the AOM with a FWHM of 25ns to “freeze” the motion of the scanned beam. The incident beam was focused before entering the Bragg cell to shorten the response time. The strobed light beam was then collimated and illuminated on the grating scanner. The diameter of the collimated beam was large enough to cover both diffraction gratings. 1st order diffraction beams from both diffraction gratings were focused by a plano-convex lens. A CCD

camera was placed at a small distance away from the focal plane of the focusing lens and aligned perpendicularly to the diffraction beam when the gratings were stationary. This configuration was used to separate the scanning trajectories for easy visual observation. A photograph of the actual setup is shown in Figure 6.11.

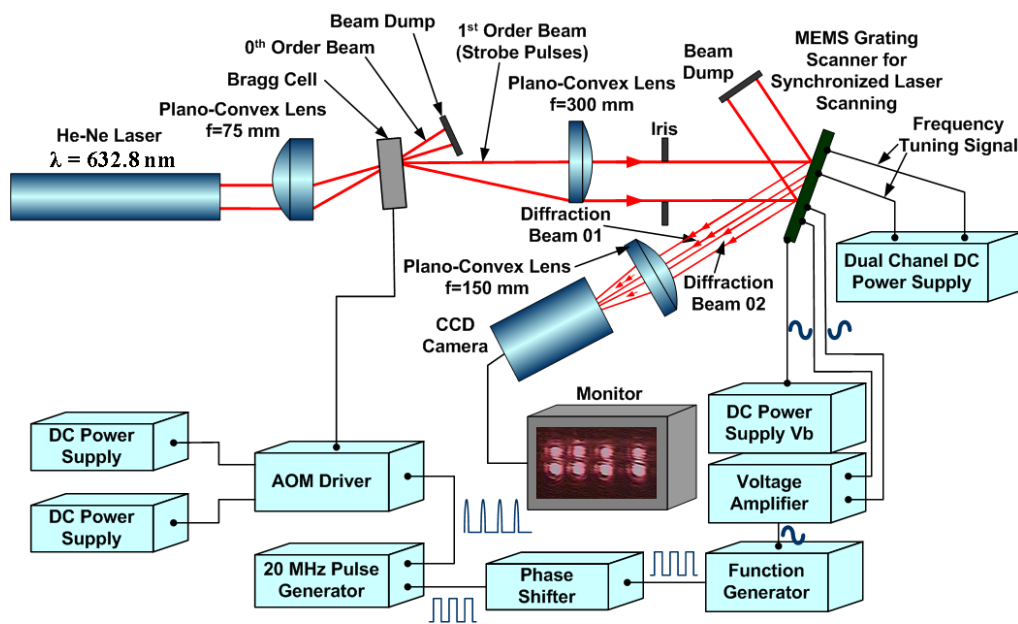


Figure 6.10 Schematic illustration of the experimental setup investigating the synchronized laser scanning of two beams using the stroboscopic method.

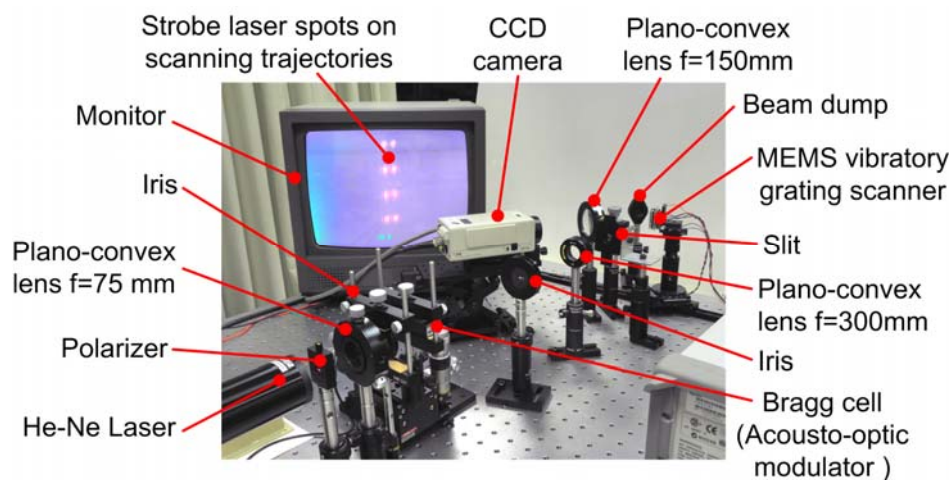


Figure 6.11 Photograph of the actual experimental setup investigating the synchronized laser scanning of two beams using the stroboscopic method.

Figures 6.12 (a) & (b) show the strobe spots from different positions of scanning trajectories before and after the resonant frequency fine-tuning respectively. Before frequency tuning, the scanning amplitudes of the two gratings were not equal because their resonant frequencies were different due to fabrication errors. Upon applying tuning voltages of 0V and 3.87V for the two tuning actuators, respectively, the scanning amplitudes were adjusted to be equal. Thus synchronized laser scanning of two laser beams was experimentally demonstrated.

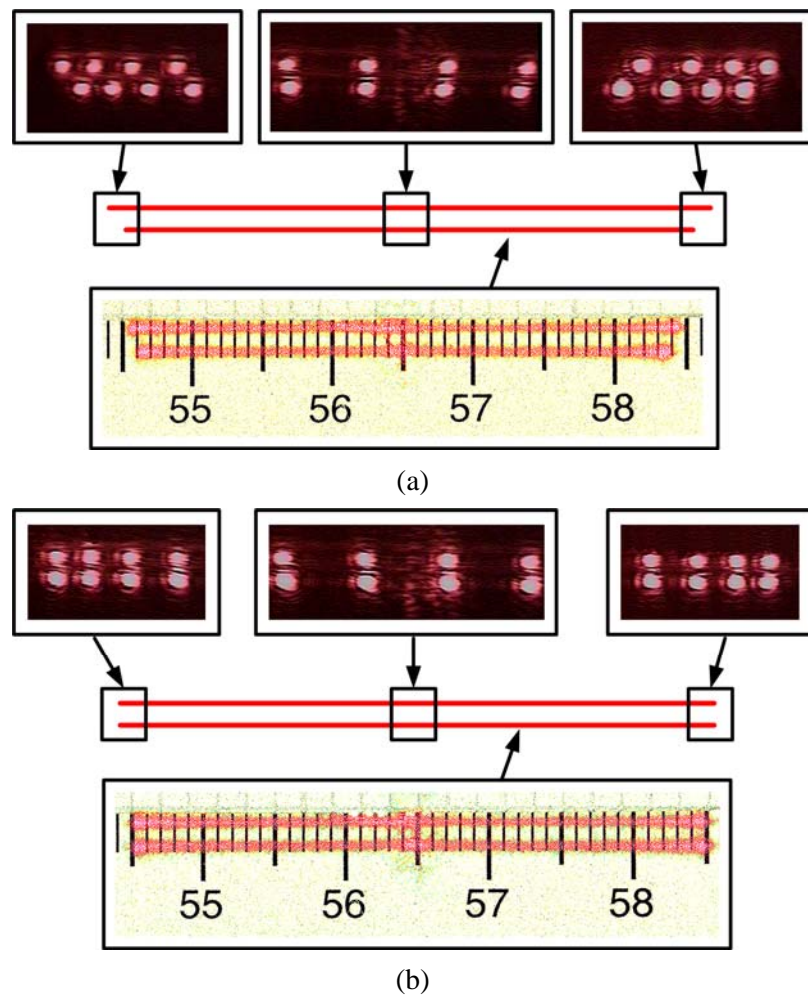


Figure 6.12 Strobe spots from different positions of scanning trajectories (a) before and (b) after the resonant frequency tuning with tuning voltages of 0V and 3.87 V for two tuning actuators.

6.4 Summary

Synchronized collinear scanning of beams with multiple wavelengths is desired by many applications, such as colored projection displays. A simple synchronization scheme based on mechanical resonant vibration of multi-DOF vibration system was proposed and a prototype scanner with two diffraction gratings was fabricated successfully. In the prototype device, two grating platforms were connected to a common driving resonator through single beam flexures. Each grating platform has its own resonant frequency tuning mechanism to compensate the fabrication errors. Reversible resonant frequency tuning and synchronized laser scanning of two beams were experimentally demonstrated using a stroboscopic method.

Chapter 7 Conclusion

High speed laser scanning has been widely implemented in numerous applications including manufacturing, medicine, military hardware, information and communication systems. Many of these applications require both high-speed and high-resolution scanning. The electrostatic in-plane vibratory grating scanner, which is subject to less dynamic deformation, has been shown to be highly suitable for next-generation miniaturized laser scanning technology. However, low optical efficiency, low scanning resolution and insufficient scanning frequency of the initial devices did not satisfy the requirements to be used as a high performance optical scanner. The objective of this dissertation is to further enhance the performance of the micromachined high-speed vibratory grating scanner through optical design, scanner structure optimization and novel micromachining process development. Significant progress has been made during this study in improving and overcoming the initial performance limitations.

Through careful design of the gratings, high optical efficiencies close to that of a coated mirror had been demonstrated to be possible. Using RCWA simulations, the grating period and grating groove depth can be optimized to achieve around 80% optical efficiency. We achieved experimentally verified results which demonstrated both the modeling and the accuracy of the fabrication process.

Optimizing the mechanical design of the resonators typically would involve simplified analytical models or finite element simulations. For better accuracy in predicting performance,

the simplified models are often insufficient. On the other hand, FE modeling is too time-consuming in return for higher accuracy. This study established a comprehensive dynamic model that can take several practical factors into consideration into a single model. This basic framework was successfully used in all subsequent design iterations to better predict fabrication outcomes with reliable accuracy.

Scanning performances, such as optical resolution (represented by $\theta_{\text{opt}}D$ product) and scanning frequency, of the vibratory grating scanners have been significantly improved, which is summarized in Figure 7.1.

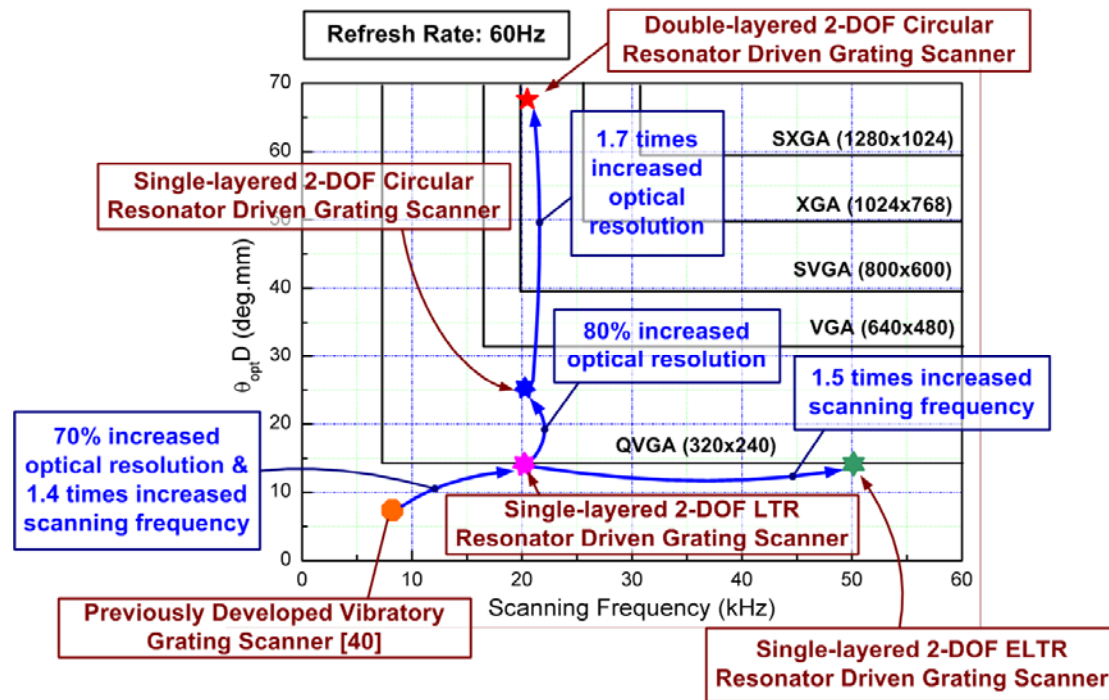


Figure 7.1 Summarization of the scanning performances of developed vibratory grating scanners.

Innovative mechanical structure designs are used to improve the grating scanner's

performance. Two main approaches were successfully demonstrated in this study. Using 2-DOF resonators rather than 1-DOF resonators can assist in overcoming travel range limitations of the electrostatically driven comb-drive actuators. At the same time, better stability of the in-plane rotational motion can also be achieved. For example, the developed single-layered grating scanner driven by the 2-DOF LTR resonator with a 1mm diameter grating is capable of scanning at 20353Hz with an optical scan angle of 13.7°. The resulting $\theta_{\text{Opt}}D$ product is 13.7 deg·mm. Compared with the previously developed grating scanner, there is a 70% increase in optical resolution and 1.4 times increase in scanning frequency.

The other approach is to utilize a circular resonator rather than the previous lateral designs. This has the advantage of increasing the total stiffness of the suspensions without inducing excessive stress. Large in-plane rotation angles were achieved through this design. The prototype single-layered 2-DOF circular resonator driven grating scanner is capable of achieving an optical scan angle of around 25° with a 1mm diameter grating platform and the resultant $\theta_{\text{Opt}}D$ product is 25 deg·mm. There is a 80% increase in optical resolution compared to the 2-DOF LTR resonator driven single-layered scanner.

Generally, increasing the scanning frequency and amplitude at the same time is challenging. Higher scanning frequency requires stiffer suspension springs, which could introduce higher stress level in the flexural beams and reduce the scanning amplitude. Thus a thin grating platform with thick suspension springs and driving actuators is desired. A novel SMDE technique was developed to achieve this in a single etching step. This simple and low-cost

method was utilized to fabricate improved high speed vibratory grating scanners capable of achieving an optical scan angle of 14.1° with a scanning frequency of 50192Hz. Compared with the single-layered 2-DOF LTR resonator driven grating scanner, this prototype has a 1.5 times increase in scanning frequency while keeping the same optical resolution performance.

A high performance optical scanner would require large aperture and large scanning amplitude. Such a design consideration in single-layer grating scanners is often contradictory. Large grating platforms mean greater displacement is necessary at the outer resonators to achieve similar rotational angles. The solution proposed in this study is then to decouple them through separating the grating platform and the actuating resonators into a two layers. This novel double-layer vibratory grating scanner design fundamentally allows the aperture size and the scanning angle to be optimized simultaneously, paving the way for higher optical resolution capabilities. A prototype double-layered 2-DOF circular resonator driven grating scanner was successfully demonstrated. The prototype scanner is capable of achieving an optical scan angle of 33.5° with a 2mm diameter diffraction grating and the resultant $\theta_{\text{Opt}}D$ product is 67 deg-mm. Compared with single-layered grating scanner driven by 2-DOF circular resonator, there is a 1.7 times increase in optical resolution. Grating scanner with the double-layered configuration has the potential to fulfill the requirements of XGA format (even SXGA format) through structure optimization in the future.

Finally, display applications require synchronized scanning of multiple wavelengths. In the case of grating scanners, multiple devices would need to be synchronized. An electro-thermal

frequency tuning mechanism is developed as a means of mechanical synchronization. This mechanism was successfully demonstrated with two diffraction gratings performing synchronized laser scanning.

In summary, grating optimization, theoretical modeling and mechanical design optimization had been carried out in this study to significantly enhance the performance of the vibratory grating optical scanner. High performance laser scanning was demonstrated to be feasible with several innovations.

Further development can still be done to improve the scanner's performance. For example, the double-layer design enables a clear platform for further progress to be made in terms of improving the optical resolution and the scanning frequency. Both can be further increased in a double-layered vibratory grating scanner by using larger diffraction gratings and thicker suspensions and driving actuators. This development is important on many fronts. Imaging applications such as a spectral imager will be able to take advantage of a larger aperture to increase the signal-to-noise ratio. Laser display applications will also be able to use it to achieve higher resolutions. Angular positioning sensors can be integrated in the future so that precise closed-loop control of laser scanning is feasible. Coupled with the preliminary synchronization study, the closed-loop control will allow applications which require multiple grating scanners such as a laser display to be realized.

References

- [1] H. Urey, D. Wine, and J. R. Lewis, "Scanner design and resolution tradeoffs for miniature scanning displays" *Flat Panel Display Technology and Display Metrology, Proc. SPIE*, San Jose, CA, vol. 3636, pp. 60-68, (1998).
- [2] H. Urey, "Torsional MEMS scanner design for high-resolution display systems" *Optical Scanning II, Proc. SPIE*, Seattle, Washington, vol. 4773, pp. 27-37, (2002).
- [3] H. Urey, D. Wine, and T. Osborn, "Optical performance for MEMS scanner based microdisplays" *MOEMS Miniaturized Systems, Proc. SPIE* vol. 4178, pp. 176-185, (2000).
- [4] D. Wine, M. P. Helsel, L. Jenkins, H. Urey, and T. D. Osborn, "Performance of a bi-axial MEMS-based scanner for microdisplay applications" *Proc. SPIE*, vol. 4178, pp. 186-196, (2000).
- [5] R. B. Sprague, T. Montague, and D. Brown, "Bi-axial magnetic drive for scanned beam display mirrors," *MOEMS Display and Imaging Systems III, Proc. SPIE*, vol. 5721, pp. 1-13, (2005)
- [6] G. J. Brakenhoff, P. Blom, and P. Barends, "Confocal Scanning Light Microscopy with High Aperture Immersion Lenses" *Journal of Microscopy*, vol. 117, pp. 219-232, (1979).
- [7] J. B. Pawley (ed.), "Handbook of Biological Confocal Microscopy" *New York: Plenum Press*, (1995).
- [8] C. J. R. Sheppard and D. M. Shotton, "Confocal Laser Scanning Microscopy" *Oxford, United Kingdom: BIOS Scientific Publishers*, (1997).
- [9] T. R. Corle and G. S. Kino, "Confocal Scanning Optical Microscopy and Related Imaging Systems" *New York: Academic Press*, (1996).
- [10] T. Wilson (ed.), "Confocal Microscopy", *New York: Academic Press*, (1990).

-
- [11] G. J. Tearney, M. E. Brezinski, B. E. Bouma, S. A. Boppart, C. Pitris, J. F. Southern, and J. G. Fujimoto, "In Vivo Endoscopic Optical Biopsy with Optical Coherence Tomography" *Science*, vol. 276, pp. 2037-2039, (1997).
- [12] F. Feldchtein, G. Gelikonov, V. Gelikonov, R. Kuranov, A. Sergeev, N. Gladkova, A. Shakhov, N. Shakhova, L. Snopova, A. Terent'eva, E. Zagainova, Y. Chumakov, and I. Kuznetzova, "Endoscopic applications of optical coherence tomography" *Optics Express*, vol. 3, n 6, pp. 257-270, (1998).
- [13] G. J. Tearney, S. A. Boppart, B. E. Bouma, M. E. Brezinski, N. J. Weissman, J. F. Southern, and J. G. Fujimoto, "Scanning single-mode fiber optic catheter-endoscope for optical coherence tomography" *Optics Letters*, vol. 21, n 7, pp. 543-545, (1996).
- [14] V. X. D. Yang, Y. X. Mao, N. Munce, B. Standish, W. Kucharczyk, N. E. Marcon, B. C. Wilson, and I. A. Vitkin, "Interstitial Doppler optical coherence tomography" *Optics Letters*, vol. 30, n 14, pp. 1791-1793, (2005).
- [15] Y. Pan, H. Xie, and G. K. Fedder, "Endoscopic optical coherence tomography based on a microelectromechanical mirror" *Optics Letters*, vol. 26, n 24, pp. 1966-1968, (2001).
- [16] H. Xie, Y. Pan and G.K. Fedder, "A SCS micromirror for optical coherence tomographic imaging" *Sensors and Actuators A: Physics*, vol. A103, n 1-2, pp. 237-241, (2003).
- [17] T. Xie, H. Xie, G.K. Fedder, and Y. Pan, "Endoscopic Optical Coherence Tomography with a Modified MEMS Mirror for Detection of Bladder Cancers" *Applied Optics*, vol. 42, n 31, pp. 6422-6426, (2003).
- [18] T. Matsuda, F. Abe, and H. Takahashi, "Laser printer scanning system with a parabolic mirror" *Applied Optics*, vol. 17, n 6, pp. 878-884, (1978).
- [19] P.J. Watt and D.N.M. Donoghue, "Measuring forest structure with terrestrial laser scanning" *International Journal of Remote Sensing*, vol. 26, n 7, pp. 1437-1446, (2005).
- [20] M.H. Kiang; O. Solgaard, R.S. Muller, K.Y. Lau, "Micromachined polysilicon microscanners for barcode readers" *IEEE Photonics Technology Letters*, vol. 8, n 12, pp. 1707-1709, (1996).

-
- [21] R.D. Richmond, S.C. Cain, "Direct-Detection LADAR Systems" *SPIE Press Book*, (2010).
- [22] P.K. Venuvinod and W. Ma, "Rapid prototyping : laser-based and other technologies" *Boston : Kluwer Academic*, (2004).
- [23] L. Beiser, "Unified optical scanning technology" *John Wiley & Sons, Inc.*, (2003).
- [24] R.A. Gerald, "Overview of a high performance polygonal scanner sub-system" *Proceedings of SPIE-The International Society for Optical Engineering*, vol. 1454, pp. 102-110, (1991).
- [25] M.F. Gerald, R.A. Gerald, "Polygonal scanners for television and high-definition television laser projectors: spatial and temporal tolerances versus resolution" *Journal of Electronic Imaging*, vol. 3, n 3, pp. 318-327, (1994).
- [26] M. Ketabchi, M. Bering, C. Deter, "Polygonal scanner subsystem for laser display" *Proceedings of the SPIE-The International Society for Optical Engineering*, vol. 3131, pp. 20-29, (1997).
- [27] C.S. Ih, L.Q. Xiang, "Compound holographic scanners" *Proceedings of the SPIE-The International Society for Optical Engineering*, vol. 498, pp. 191-198, (1984).
- [28] R.D. Richard, H.L. Gerald, "holographic scanners for machine vision, printing nad barcode applications" *Proceedings of SPIE-The International Society for Optical Engineering*, vol. 747, pp. 17-24, (1987).
- [29] C.S. Ih, L.Q. Xiang, "Advanced holographic scannings and applications" *Proceedings of the SPIE-The International Society for Optical Engineering*, vol. 673, pp. 296-302, (1987).
- [30] J.F. Lotspeich, "Electrooptic light-beam deflection" *IEEE Spectrum*, vol. 5, n 2, pp. 45-52, (1968).
- [31] T.C. Lee, J.D. Zook, "Light beam deflection with electrooptic prisms" *IEEE Journal of Quantum Electronics*, vol. 4, n 7, pp. 442-454, (1968).

-
- [32] G.A. Coquin, J.P. Griffin and L.K. Anderson, "Wideband acoustooptic deflectors using acoustic beam steering" *IEEE Trans. Sonics & Ultrasonics*, SU-17(1), pp. 34-40, (1970).
- [33] M. Gottlieb, C.L.M. Ireland, J.M. Ley, "Electro-optic and acousto-optic scanning and deflection" *New York, Marcel Dekker, Inc.*, (1983).
- [34] E. Job, S. Vincent, W. Steve, "Microsystems technology (MST) and MEMS applications-An overview" *MRS Bulletin (0883-7694)*, vol. 26, n 4, pp. 312-315, (2001).
- [35] R.S. Muller and K.Y. Lau, "Surface micromachined micro optical elements and systems" *Proceedings of the IEEE*, vol. 86, pp. 1705-1720, (1998).
- [36] Y. Xu, J. Singh, C.S. Premachandran, A. Khairyanto, K.W.S. Chen, N. Chen, C.J.R. Sheppard and M. Olivo, "Design and development of a 3D scanning MEMS OCT probe using a novel SiOB package assembly" *Journal of Micromechanics and Microengineering*, vol. 18, 125005, (2008).
- [37] O. Cakmakci and J. Rolland, "Head-Worn Displays: A Review" *Journal of display technology*, vol. 2, n 3, pp. 199-216, (2006).
- [38] G. Zhou, k.K.L. Cheo, F.E.H. Tay, and F.S. Chau, "Neural network approach for linearization of the electrostatically actuated double-gimballed micromirror", *Analog Integrated Circuits and Signal Processing*, vol. 40, n 2, pp. 141-153, (2004).
- [39] R.A. Conant, J.T. Nee, K.Y. Lau, and R.S. Muller, "Dynamic deformation of scanning mirrors" *IEEE/LEOS International Conference on Optical MEMS (Hawaii, USA)*, pp. 49-50, (2000).
- [40] G. Zhou, L. Vj, F. S. Chau, and F. E. H. Tay, "Micromachined in-plane vibrating diffraction grating laser scanner" *IEEE Photonics Technology Letters*, vol. 16, n 10, pp. 2293-2295, (2004).
- [41] G. Zhou and F.S. Chau, "Micromachined vibratory diffraction grating scanner for multiwavelength collinear laser scanning" *IEEE Journal of Microelectromechanical Systems*, vol. 15, n 6, pp. 1777-1788, (2006).

-
- [42] D.J. Bell, T.J. Lu, N.A. Fleck and S.M. Spearing, "MEMS actuators and sensors: observations on their performance and selection for purpose" *Journal of Micromechanics and Microengineering*, vol. 15, n 7, pp. 153-164, (2005).
- [43] K.E. Petersen, "Silicon torsional scanning mirror" *IBM Journal of Research and Development*, vol. 24, n 5, pp. 631-637, (1980).
- [44] V.A. Aksyuk, F. Pardo, C.A. Bolle, S. Arney, C.R. Giles, and D.J. Bishop, "Lucent Microstar micromirror array technology for large optical crossconnects" *Proceedings of the SPIE - The International Society for Optical Engineering*, vol. 4178, pp. 320-324, (2000).
- [45] J. Tsai and M.C. Wu, "Gimbal-less MEMS two-axis optical scanner array with high fill-factor" *Journal of Microelectromechanical Systems*, vol. 14, n 6, pp. 1323-1328, (2005).
- [46] V. Milanovic, G.A. Matus and D.T. McCormick, "Gimbal-Less Monolithic Silicon Actuators for Tip-Tilt-Piston Micromirror Applications" *IEEE Journal of Selected Topics in Quantum Electronics*, vol. 10, n 3, pp. 462-471, (2004).
- [47] J. Tsai and M.C. Wu, "Design, Fabrication, and Characterization of a High Fill-Factor, Large Scan-Angle, Two-Axis Scanner Array Driven by a Leverage Mechanism" *Journal of Microelectromechanical Systems*, vol. 15, n 5, pp. 1209-1213, (2006).
- [48] J. Singh, T. Gan, A. Agarwal, Mohanraj, and S. Liw, "3D free space thermally actuated micromirror device" *Sensors and Actuators A: Physics*, vol. 123-124, pp. 468-475, (2005).
- [49] S.H. Sadat, D. Kamiya, and M. Horie, "Large-Deflection Spiral-Shaped Micromirror Actuator" *Journal of Microelectromechanical Systems*, vol. 18, n 6, pp. 1357-1364, (2009).
- [50] E.T. Carlen, K.H. Heng, S. Bakshi, A. Pareek and C.H. Mastrangelo, "High-Aspect Ratio Vertical Comb-Drive Actuator With Small Self-Aligned Finger Gaps" *Journal of Microelectromechanical Systems*, vol. 14, n 5, pp. 1144-1155, (2005).

-
- [51] H. Toshiyoshi, W. Piyawattanametha, C.T. Chan and M.C. Wu, "Linearization of electrostatically actuated surface micromachined 2-D optical scanner" *Journal of Microelectromechanical Systems*, vol. 10, n 2, pp. 205-214, (2001).
- [52] G.D.J Su, H. Toshiyoshi and M.C. Wu, "Surface-micromachined 2-D optical scanners with high-performance single-crystalline silicon micromirrors" *IEEE Photonics Technology Letters*, vol. 13, n 6, pp. 606-608, (2001).
- [53] G. Zhou, F.E.H. Tay, and F.S. Chau, "Modeling of a two-axis torsional micromirror using AHD" *International Journal of Computational Engineering Sciences (IJCES)*, vol. 4, n 3, pp. 593-596, (2003).
- [54] G. Zhou, F.E.H. Tay, and F.S. Chau, "Macro-modelling of a double-gimballed electrostatic torsional micromirror" *Journal of Micromechanics and Microengineering*, vol. 13, n 5, pp. 532-547, (2003).
- [55] T.S. Kim, S.S. Lee; Y. Yee, J.U. Bu, C.G. Park and M.H. Ha, "Large tilt angle electrostatic force actuated micro-mirror" *IEEE Photonics Technology Letters*, vol. 14, n 11, pp. 1569-1571, (2002).
- [56] S. Kwon, V. Milanovic and L.P. Lee, "Large-Displacement Vertical Microlens Scanner With Low Driving Voltage" *IEEE Photonics Technology Letters*, vol. 14, n 11, pp. 1572-1574, (2002).
- [57] V. Milanovic, S. Kwon and L. P. Lee, "High Aspect Ratio Micromirrors With Large Static Rotation and Piston Actuation" *IEEE Photonics Technology Letters*, vol. 16, n 8, pp. 1891-1893, (2004).
- [58] S. Kwon, V. Milanovic and L.P. Lee, "Vertical Combedrive Based 2-D Gimbaled Micromirrors With Large Static Rotation by Backside Island Isolation" *IEEE Journal of Selected Topics in Quantum Electronics*, vol. 10, n 3, pp. 498-504, (2004).
- [59] V. Milanovic, "Multilevel Beam SOI-MEMS Fabrication and Applications" *Journal of Microelectromechanical Systems*, vol. 13, n 1, pp. 19-30, (2004).

-
- [60] J.H. Lee, Y.C. Ko, B.S. Choi, J.M. Kim and D.Y. Jeon, "Bonding of silicon scanning mirror having vertical comb fingers" *Journal of Micromechanics and Microengineering*, vol. 12, n 6, pp. 644-649, (2002).
- [61] Q.X. Zhang, A.Q. Liu, J. Li and A.B. Yu, "Fabrication technique for Microelectromechanical Systems Vertical Comb-drive Actuators on a Monolithic Silicon Substrate" *Journal of Vacuum Science Technology: B*, vol. 23, n 1, pp. 32-41, (2005).
- [62] U. Krishnamoorthy, D. Lee and O. Solgaard, "Self-aligned Vertical Electrostatic Comb-drives for Micromirror Actuation" *Journal of Microelectromechanical Systems*, vol. 12, n 4, pp. 458-464, (2003).
- [63] C. Tsou, W.T. Lin, C.C. Fan and B.C.S. Chou, "A novel self-aligned vertical electrostatic comb-drives actuator for scanning micromirrors" *Journal of Micromechanics and Microengineering*, vol. 15, n 4, pp. 855-860, (2005).
- [64] I.W. Jung, U. Krishnamoorthy and O. Solgaard, "High fill-factor two-axis gimbaled tip-tilt-piston micromirror array actuated by self-Aligned vertical electrostatic comb-drives" *Journal of Microelectromechanical Systems*, vol. 15, n 3, pp. 563-571, (2006).
- [65] D. Hah, C.A. Choi, C.K. Kim and C.H. Jun, "A Self-aligned vertical comb-drive actuator on an SOI wafer for a 2D scanning micromirror" *Journal of Micromechanics and Microengineering*, vol. 14, n 6, pp. 1148-1156, (2004).
- [66] D. Hah, S.T.Y. Huang, J.C. Tsai, H. Toshiyoshi and M.C. Wu, "Low-Voltage, Large-Scan Angle MEMS Analog Micromirror Arrays With Hidden Vertical Comb-Drive Actuators" *Journal of Microelectromechanical Systems*, vol. 13, n 2, pp. 279-289, (2004).
- [67] <http://www.mems.sandia.gov/> [Online].
- [68] M.C. Wu and W.L. Fang, "Design and fabrication of MEMS devices using the integration of MUMPs, trench-refilled molding, DRIE and bulk silicon etching process" *Journal of Micromechanics and Microengineering*, vol. 15, n 12, pp. 535-542, (2004).

-
- [69] M.C. Wu, H.Y. Lin and W.L. Fang, "A Poly-Si-Based Vertical Comb-Drive Two-Axis Gimbaled Scanner for Optical Applications" *IEEE Photonics Technology Letters*, vol. 18, n 20, pp. 2111-2113, (2006).
- [70] K.H. Jeong and L.P. Lee "A novel micro fabrication of a self-aligned vertical comb drive on single SOI wafer for optical MEMS applications" *Journal of Micromechanics and Microengineering*, vol. 15, n 2, pp. 277-281, (2005).
- [71] M. Sasaki, D. Briand, W. Noell, N.F. Rooij and K. Hane, "Three-Dimensional SOI-MEMS Constructed by Buckled Bridges and Vertical Comb Drive Actuator" *IEEE Journal of Selected Topics in Quantum Electronics*, vol. 10, n 3, pp. 455-461, (2004).
- [72] H. Xie, Y.T. Pan and G.K. Fedder, "A CMOS-MEMS Mirror With Curled-Hinge Comb Drives," *Journal of Microelectromechanical Systems*, vol. 12, n 4, pp. 450-457, (2003).
- [73] D. Hah, P.R. Patterson, H.D. Nguyen, H. Toshiyoshi, M.C. Wu, "Theory and Experiments of Angular Vertical Comb-Drive Actuators for Scanning Micromirrors" *IEEE Journal of Selected Topics in Quantum Electronics*, vol. 10, n 3, pp. 505-513, (2004).
- [74] M. Fujino, P.R. Patterson, H. Nguyen, W. Piyawattanametha and M.C. Wu, "Monolithically Cascaded Micromirror Pair Driven by Angular Vertical Combs for Two-Axis Scanning," *IEEE Journal of Selected Topics in Quantum Electronics*, vol. 10, n 3, pp. 492-497, (2004).
- [75] H.D. Nguyen, D. Hah, P.R. Patterson, R. Chao, W. Piyawattanametha, E.K. Lau and M.C. Wu, "Angular Vertical Comb-Driven Tunable Capacitor With High-Tuning Capabilities" *Journal of Microelectromechanical Systems*, vol. 13, n 3, pp. 406-413, (2004).
- [76] W. Piyawattanametha, P.R. Patterson, D. Hah, H. Toshiyoshi and M.C. Wu, "Surface-and Bulk-Micromachined Two-Dimensional Scanner Driven by Angular Vertical Comb Actuators," *Journal of Microelectromechanical Systems*, vol. 14, n 6, pp.1329-1338, (2005).

-
- [77] J. Kim, D. Christensen and L. Lin, "Micro vertical comb actuators by selective stiction process" *Sensors and Actuators A: Physics*, vol. 127, n 2, pp. 248-254, (2006).
- [78] J. Kim, H. Choo, L. Lin and R.S. Muller "Microfabricated Torsional Actuator Using Self-Aligned Plastic Deformation of Silicon" *Journal of Microelectromechanical Systems*, vol. 15, n 3, pp. 553-562, (2006).
- [79] J. Kim, D. Christensen and L. Lin, "Monolithic 2-D Scanning Mirror Using Self-Aligned Angular Vertical Comb Drives," *IEEE Photonics Technology Letters*, vol. 18, n 20, pp. 2111-2113, (2006).
- [80] P.J. Resnick and P.J. Clews, "Whole wafer critical point drying of MEMS devices," *Proceedings of the International Society for Optical Engineering*, vol. 4558, pp. 189-196, (2001).
- [81] H. Schenk, P. Durr, T. Haase, D. Kunze, U. Sobe, H. Lakner and H. Kuck, "Large Deflection Micromechanical Scanning Mirrors for Linear Scans and Pattern Generation" *IEEE Journal of Selected Topics in Quantum Electronics*, vol. 6, n 5, pp. 715-722, (2000).
- [82] H. Schenk, P. Durr, D. Kunze, H. Lakner and H. Kuck, "Design and modeling of large deflection micromechanical 1D and 2D scanning mirrors" *Proceedings of the SPIE - The International Society for Optical Engineering*, vol. 4178, pp. 116-125, (2000).
- [83] H. Schenk, P. Durr, D. Kunze, H. Lakner and H. Kuck, "A resonantly excited 2D-micro-scanning-mirror with large deflection" *Sensors and Actuators A: Physics*, vol. 89, n 1-2, pp. 104-111, (2001).
- [84] M.H. Kiang, D.A. Francis, C.J. Chang-Hasnain, O. Solgard, K.Y. Lau and R.S. Muller, "Actuated polysilicon micromirrors for raster-scanning displays" *Transducers 97. 1997 International Conference on Solid-State Sensors and Actuators. Digest of Technical Papers (Cat. No.97TH8267)*, vol.1, pp. 323-326, (1997).

-
- [85] M.H. Kiang, O. Solgard, K.Y. Lau and R.S. Muller, "Micromachined microscanners for optical scanning" *Proceedings of the SPIE-The International Society for Optical Engineering*, vol. 3008, pp. 82-90, (1997).
- [86] M.H. Kiang, O. Solgard, K.Y. Lau and R.S. Muller, "Polysilicon optical microscanners for laser scanning displays" *Sensors and Actuators A: Physicis*, vol. A70, n 1-2, pp. 195-199, (1998).
- [87] M.H. Kiang, O. Solgard, K.Y. Lau and R.S. Muller, "Electrostatic combdrive-actuated micromirrors for laser-beam scanning and positioning" *Journal of Microelectromechanical Systems*, vol. 7, n 1, pp. 27-37, (1998).
- [88] V. Milanovic, M. Last and K.S.J. Pister, "Laterally actuated torsional micromirrors for large static deflection" *IEEE Photonics Technology Letters*, vol. 15, n 2, pp. 245-247, (2003).
- [89] L. Zhou, J.M. Kahn and K.S.J. Pister, "Scanning micromirrors fabricated by an SOI/SOI wafer-bonding process" *Journal of Microelectromechanical Systems*, vol. 15, n 1, pp. 24-32, (2006).
- [90] J.D. Grade and H. Jerman, "MEMS electrostatic actuators for optical switching applications" *Conference on Optical Fiber Communication, Technical Digest Series*, vol. 54, n 3, pp. WX2/1-WX2/3, (2001).
- [91] J.D. Grade, K.Y. Yasumura, and H. Jerman, "Micromachined actuators with braking mechanisms" *Sensors and Actuators A: Physical*, vol. 122, n 1, pp. 1-8, (2005).
- [92] M.T.K. Hou, J.Y. Huang, S.S. Jiang and J.A. Yeh, "In-plane rotary comb-drive actuator for a variable optical attenuator" *Journal of Microlithography, Microfabrication, and Microsystems*, vol. 7, n 4, pp. 043015 (6 pp.), (2008).
- [93] J. Tsaur, Z.J. Wang, L. Zhang, M. Ichiki,; J.W. Wan, and R. Maeda, "Preparation and application of lead zirconate titanate (PZT) films deposited by hybrid process: Sol-gel method and laser ablation" *Japanese Journal of Applied Physics, Part 1: Regular Papers and Short Notes and Review Papers*, vol. 41, n 11B, pp. 6664-6668, (2002).

-
- [94] T. Kobayashi, J. Tsaur and R. Maeda, "Fabrication of optical micro scanner driven by PZT actuators" *Japanese Journal of Applied Physics, Part 1: Regular Papers and Short Notes and Review Papers*, vol. 44, n 9B, pp. 7078-7082, (2005).
- [95] F. Filhol, E. Defay, C. Divoux, C. Zinck and M.T. Delaye, "Resonant micro-mirror excited by a thin-film piezoelectric actuator for fast optical beam scanning" *Sensors and Actuators A: Physical*, vol. 123-124, pp. 483-489, (2005).
- [96] Y. Yasuda, M. Akamatsu, M. Tani, T. Iijima and H. Toshiyoshi, "Piezoelectric 2D-optical micro scanners with PZT thick films" *Integrated Ferroelectrics*, vol. 80, pp. 341-353, (2006).
- [97] J.H. Park, J. Akedo and H. Sato, "High-speed metal-based optical microscanner using stainless-steel substrate and piezoelectric thick films prepared by aerosol deposition method" *Sensors and Actuators A: Physical*, vol. 135, n 1, pp. 86-91, (2007).
- [98] K.H. Koh, T. Kobayashi, F.L. Hsiao and C. Lee, "Characterization of piezoelectric PZT beam actuators for driving 2D scanning micromirrors" *Sensors and Actuators A: Physical*, vol. 162, n 2, pp. 336-347, (2010).
- [99] S. Schweizer, S. Calmes, M. Laudon and P. Renaud, "Thermally actuated optical microscanner with large angle and low consumption" *Sensors and Actuators A: Physical*, vol. A76, n 1-3, pp. 470-477, (1999).
- [100] A. Jain, A.Kopa, Y. Pan, G.K. Fedder and H. Xie, "A two-axis electrothermal micromirror for endoscopic optical coherence tomography," *IEEE Journal of Selected Topics in Quantum Electronics*, vol. 10, n 3, pp. 636-642, (2004).
- [101] A. Jain and H. Xie, "single-crystal silicon micromirror for large bi-directional 2D scanning applications" *Sensors and Actuators A: Physical*, vol. 130-131, pp. 454-460, (2006).
- [102] J. Singh, J.H.S. Teo, Y. Xu, C.S. Premachandran, N. Chen, R. Kotlanka, M. Olivo and C. J. R. Sheppard, "A two axes scanning SOI MEMS micromirror for endoscopic

- bioimaging,” *Journal of Micromechanics and Microengineering*, vol. 18, n 12, pp. 025001 (9 pages), (2008).
- [103] Y. Xu, J. Singh, T. Selvaratnam and N. Chen, “Two-Axis Gimbal-Less Electrothermal Micromirror for Large-Angle Circumferential Scanning” *IEEE Journal of Selected Topics in Quantum Electronics*, vol. 15, n 5, pp. 1432-1438, (2009).
- [104] B. Wagner and W. Benecke, “Microfabricated actuator with moving permanent magnet” *Proceedings of IEEE Microelectromechanical Systems: An Investigation of Micro Structures, Sensors, Actuators, Machines and Robots (Cat. No.91CH2957-9)*, pp. 27-32, (1991).
- [105] C.H. Ji, Y.K. Kim and G.B. Chung “Design and fabrication of electromagnetic micromirror with bulk silicon mirror plate and aluminum spring” *Japanese Journal of Applied Physics, Part 1: Regular Papers, Short Notes & Review Papers*, vol. 39, n 12B, pp. 7138-7141, (2000).
- [106] C.H. Ji and Y.K. Kim, “Electromagnetic micromirror array with single-crystal silicon mirror plate and aluminum spring” *Journal of Lightwave Technology*, vol. 21, n 3, pp. 584-590, (2003).
- [107] Y. Jun, S. Luanava and V. Casasanta, “Magnetic actuation for MEMS scanners for retinal scanning displays” *Proceedings of the SPIE-The International Society for Optical Engineering*, vol. 4985, pp. 115-120, (2003).
- [108] Y.H. Jang and Y.K. Kim, “Design, fabrication and characterization of an electromagnetically actuated addressable out-of-plane micromirror array for vertical optical source applications” *Journal of Micromechanics and Microengineering*, vol. 13, n 6, pp. 853-863, (2003).
- [109] M. Prasciolu, A. Carpentiero, R. Kumar, D. Cojoc, S. Cabrini, L. Businaro, F. Romanato,; E.D. Fabrizio, D. Recchia and G. Parmigiani, “Electromagnetically Actuated Surface Micromachined Free Standing Torsion Beam Micromirror Made by

- Electroplated Nickel” *Japanese Journal of Applied Physics, Part 1: Regular Papers and Short Notes and Review Papers*, vol. 43, n 1, pp. 418-423, (2004).
- [110] H. Urey, A.D. Yalcinkaya, T. Montague, D. Brown, R. Sprague, O. Anac, C. Ataman and I. Basdogan, “Two-axis MEMS scanner for display and imaging applications” *IEEE/LEOS Optical MEMS 2005: International Conference on Optical MEMS and Their Applications*, pp. 17-18, (2005).
- [111] A.D. Yalcinkaya, H. Urey, D. Brown, T. Montague and R. Sprague, “Two-axis electromagnetic microscanner for high resolution displays” *Journal of Microelectromechanical Systems*, vol. 15, n 4, pp. 786-794, (2006).
- [112] C.H. Ji, M. Choi, S.C. Kim, K.C. Song, J.U. Bu and H.J. Nam, “Electromagnetic two-dimensional scanner using radial magnetic field” *Journal of Microelectromechanical Systems*, vol. 16, n 4, pp. 989-996, (2007).
- [113] K.H. Kim, B.H. Park, G.N. Maguluri, T.W. Lee, F.J. Rogomentich, M.G. Bancu, B.E. Bouma, B. De, F. Johannes and J.J. Bernstein, “Two-axis magnetically-driven MEMS scanning catheter for endoscopic high-speed optical coherence tomography” *Optics Express*, vol. 15, n 26, pp. 18130-18140, (2007).
- [114] H. Urey, S. Holmstrom and A.D. Yalcinkaya, “Electromagnetically actuated FR4 scanners” *IEEE Photonics Technology Letters*, vol. 20, n 1, pp. 30-32, (2008).
- [115] S.O. Isikman and H. Urey, “Dynamic modeling of soft magnetic film actuated scanners” *IEEE Transactions on Magnetics*, vol. 45, n 7, pp. 2912-2919, (2009).
- [116] I.J. Cho and E. Yoon, “A low-voltage three-axis electromagnetically actuated micromirror for fine alignment among optical devices” *Journal of Micromechanics and Microengineering*, vol.19, n 8, pp. 085007 (8 pages), (2009).
- [117] K. Hane and M. Sasaki, “Comprehensive Microsystems, Volume 3: Optical Systems, Micro-Mirrors” *Netherlands, Elsevier B.V.*, (2008).

-
- [118] R.A. Conant, J.T. Nee, K.Y. Lau and R.S. Muller, "A flat high-frequency scanning micromirror" *Technical Digest of Solid-State Sensor and Actuator Workshop (TRF Cat. No.00TRF-0001)*, pp. 6-9, (2000).
- [119] H.Y. Lin and W. Fang, "A rib-reinforced micro torsional mirror driven by electrostatic torque generators" *Sensors and Actuators A: Physical*, vol. 105, n 1, pp. 1-9, (2003).
- [120] C.H. Ji, M. Choi, S.C. Kim, S.H. Lee, S.H. Kim, Y. Yee and J.U. Bu, "An electrostatic scanning micromirror with diaphragm mirror plate and diamond-shaped reinforcement frame" *Journal of Micromechanics and Microengineering*, vol. 16, n 5, pp. 1033-1039, (2006).
- [121] A. Wolter, T. Klose, S.T. Hsu, H. Schenk and H. Lakner, "Scanning 2D micromirror with enhanced flatness at high frequency" *Proceedings of the SPIE-The International Society for Optical Engineering*, vol. 6114, pp. 61140L 1-8, (2006).
- [122] S. Hsu, T. Klose, C. Drabe and H. Schenk, "Fabrication and characterization of a dynamically flat high resolution micro-scanner" *Journal of Optics A: Pure and Applied Optics*, vol. 10, n 4, pp. 044005 (8 pages), (2008).
- [123] A.A. Yasseen, S.W. Smith, F.L. Merat and M. Mehregany, "Diffraction Grating Scanners Using Polysilicon Micromotors" *IEEE Journal of Selected Topics in Quantum Electronics*, vol. 5, n 1, pp. 75-82, (1999).
- [124] G. Zhou, L. Vj, F.E.H. Tay and F.S. Chau, "Diffraction grating scanner using a micromachined resonator," *Proceeding of 17th IEEE International Conference on Microelectromechanical Systems (MEMS 2004)*, pp. 45-48, (2004).
- [125] L. Beiser, "Holographic Scanning", *New York: Wiley*, (1988).
- [126] M.G. Moharam and T.K. Gaylord, "Rigorous coupled-wave analysis of planar grating diffraction" *Journal of the Optical Society of America*, vol. 71, n 7, pp. 811-818, (1981).

-
- [127] M.A. Ordal, L.L. Long, R.J. Bell, S.E. Bell, R.R. Bell, R.W. Alexander and C.A. Ward, "1983 Optical properties of the metals Al, Co, Cu, Au, Fe, Pb, Ni, Pd, Pt, Ag, Ti, and W in the infrared and far infrared" *Applied Optics*, vol. 22, n 7, pp. 1099-1019, (1983).
- [128] R.W. Johnstone, M. Parameswaran, "An Introduction to Surface-Micromachining". Norwell, Massachusetts: Kluwer Academic Publishers, (2004).
- [129] J. Li, Q. Zhang, A. Liu, W. L. Goh, and J. Ahn, "Technique for preventing stiction and notching effect on silicon-on-insulator microstructure", *Journal of Vacuum Science Technology: B*, vol. 21, n 6, pp. 2530-2539, (2003).
- [130] N. Minorsky, "Nonlinear Oscillations" Princeton: Van Nostrand, (1962).
- [131] W.C. Tang, T.C.H. Nguyen, M.W. Judy and R.T. Howe, "Electrostatic comb-drive of lateral polysilicon resonators" *Sensors and Actuators A: Physical*, vol. A21, n 1-3, pp. 328-331, (1990).
- [132] D. Malacara, "Optical Shop Testing, 3rd edition" Wiley, 2007.
- [133] K. Lee and Y. Cho, "A triangular electrostatic comb array for micromechanical resonant frequency tuning" *Sensors and Actuators A: Physical*, vol. A70, n 1-2, pp. 112-117, (1998).
- [134] K. Lee, L. Lin and Y. Cho, "A closed-form approach for frequency tunable comb resonators with curved finger contour" *Sensors and Actuators A: Physical*, vol. 141, n 2, pp. 523-529, (2008).
- [135] T. Remtema and L. Lin, "Active frequency tuning for micro resonators by localized thermal stressing effects" *Sensors and Actuators A: Physical*, vol. 91, n 3, pp. 326-332, (2001).
- [136] J. Lee, S. Park, Y. Eun, B. Jeong and J. Kim, "Resonant frequency tuning of torsional micro scanner by mechanical restriction using MEMS actuator" *Proceedings of the IEEE International Conference on Micro Electro Mechanical Systems (MEMS 2009)*, pp. 164-167, (2009).